Publication No. U-3548

RE-ENTRY AND SPACE SYSTEMS PROGRAMS

N68 23669

FINAL REPORT

STUDY OF A PASSIVE DAMPER FOR ATMOSPHERIC ENTRY BODIES

Prepared for: National Aeronautics and Space Administration
Ames Research Center
Moffett Field, California

Under Contract: NAS2-3274

Prepared by: Richard R. Auelmann, Program Engineer
Andrew B. Bauer
Richard A. DuPuis
Joyce M. Roberts

18 April 1966

AERONUTRONIC
DIVISION OF PHILCO CORPORATION
A SUBSIDIARY OF Ford Motor Company,
FORD ROAD/NEWPORT BEACH, CALIFORNIA

62381

CONTENTS (Continued)

SECTION		PAGE
7	DIGITAL COMPUTER PROGRAMS	
	7.1 Three Dimensional Program	7-1
	7.2 Planar Program	7-17
8	INTERNAL DAMPER DYNAMICS	
	8.1 Flow Model	8-1
	8.2 Relating C_D - R_d Curve to Drag and Velocity	8-5
	8.3 Heating Parameter	8-5
	8.4 Experimental Considerations	8-8
	8.5 Experimental Facilities	8-12
	8.6 Experimental Results	8-21
	8.7 Sliding Friction Corrections	8-32
	8.8 Conclusions	8-34

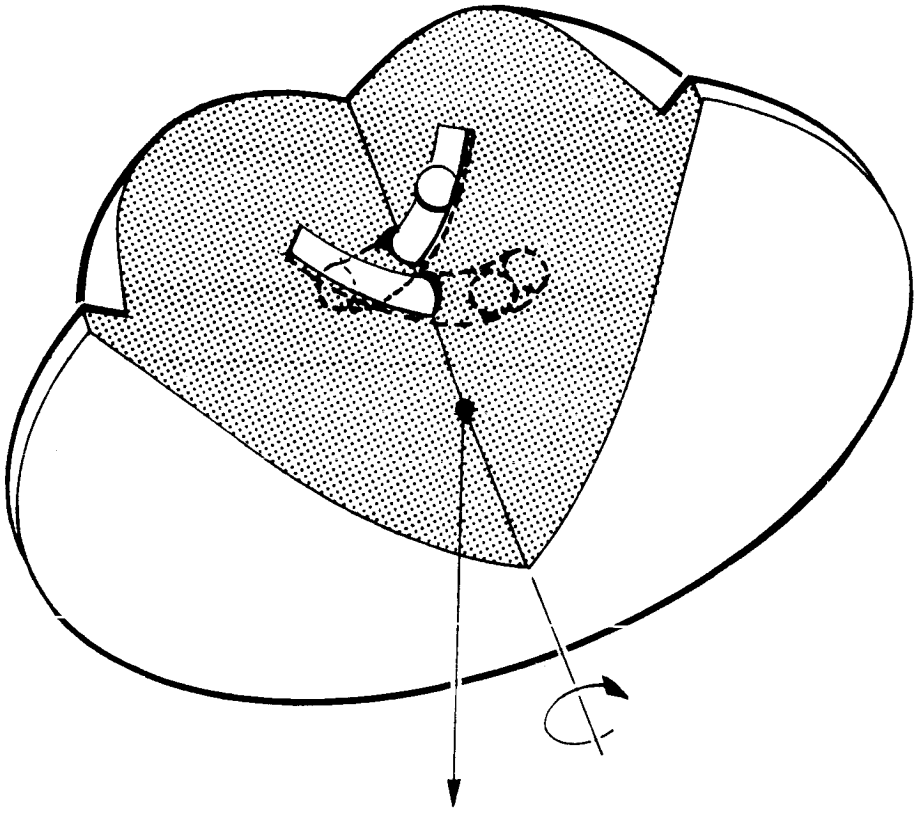

F03446 U

AMES MARS ATMOSPHERIC PROBE WITH DAMPERS

SUMMARY

The design and operation of a passive damper for use on spinning and nonspinning entry bodies is examined in this report. The damper is a constant curvature tube which contains a high density ball and a fluid. Two such dampers are orthogonally mounted with respect to the vehicle centerline with the convex edges facing forward. Oscillations of the vehicle cause the balls to move in their tubes. The ball motions are opposed by the fluid, energy is dissipated, and the vehicle angle of attack is damped.

The basic damper parameters are the mass, the tube radius of curvature, the location of the tube, the tube length, elasticity of the tube stops, and the fluid drag. All other factors being equal, the damper performance is limited by the available mass. The results given in this report are for dampers which weigh between 5 and 10 percent of the vehicle weight. This suggests that passive dampers are not practical for vehicles which weigh in excess of 100 pounds, active systems being more competitive.

For a "tuned" damper, the damper and vehicle pitch frequencies are equal. The frequency ratio depends only on the tube curvature and not on the damper mass. Linear theory indicates that the optimum tube curvature is that which "tunes" the damper. Runs made for blunt vehicles indicate that the tuning curvature is optimum even when gross nonlinearities are taken into consideration. However, for slender vehicles

with large angular motions and finite tube lengths, the optimum tube curvature was found to be two to four times larger than the tuning curvature.

The damper location is also a critical factor. As a rule, the damper should be placed as far aft as possible, certainly behind the vehicle center of mass. This has the effect of telescoping the effective damper moment arm.

The tube length is restricted either by the dimensions of the vehicle or by limits on the slope at the ends of the tubes. Curvatures measured from the vehicle centerline should not exceed 60 degrees. For values approaching 90 degrees, the balls tend to "linger" near the stops; and for values exceeding 90 degrees, the motion may be temporarilly unstable.

For nonspinning vehicles, the tube stops should be made as inelastic as possible: first, because some energy will be dissipated on impact; and second, the transients to motion are minimized. The elasticity of the tube stops is not an important factor for spinning vehicles.

The fluid drag parameters are selected last. Damper performance is relatively insensitive to changes by a factor of two in the fluid drag. Ballpark values are established by trial and error. The gap between the ball and the tube is the main factor in determining fluid drag. An analytical model of the fluid drag is developed and confirmed by extensive testing. Curves are presented which relate the fluid drag coefficient and Reynold's number for selected gap ratios. It is established that a gas can provide ample drag for ball speeds encountered in practical damper designs. This finding is significant because the weight of the fluid, being a gas, is negligible.

The external-vehicle damper dynamics was modeled and programmed for solution on a digital computer. Actually, two programs were written: a planar program which applies only to nonspinning bodies, and a

three-dimensional program which applies to both spinning and non-spinning bodies. The planar model was used to investigate vehicle response and damper tradeoffs for the Goddard Mars atmospheric probe. The three-dimensional model was used to conduct similar studies for the Ames Mars atmospheric probe and a slender Earth re-entry body, both spin-stabilized.

For spinning bodies, the angle of attack is damped to a small trim angle and holds constant until impact. The trim angle increases as the fluid drag increases. On the other hand, the dynamic pressure at which trim occurs increases with fluid drag.

The damper also causes the spin rate to decrease until the angle of attack is trimmed. The spin rate stabilizes beyond this point. The spin reduction is small for blunt bodies, on the order of 5 percent for the Ames probe. Significant spin changes were observed for the slender Earth re-entry body. The changes were the smallest when the fluid drag was the largest.

The damper also damps the precession rate of the symmetry axis about the velocity vector. For slender bodies, the precession rate is driven to zero at about the same point that the angle of attack is trimmed. For blunt bodies, the precession rate decay is much slower.

The damper is shown to be an effective device for damping the angle of attack envelope and the precession rate for spinning and nonspinning entry bodies. It does not introduce any instabilities. However, there is no evidence and, indeed, we doubt that the damper can prevent the phenomena of roll resonance, of current interest to the industry.

NOTATION*

a_i	coefficients in the series approximation for the axial force coefficient
b^2	basic damper parameter, $5I/(7MR\ell)$
b_A^2	ratio of damper axial frequency to vehicle pitch frequency
b_N^2	ratio of damper normal frequency to vehicle pitch frequency
C_A	axial force coefficient
C_m	pitch moment coefficient
C_N	normal force coefficient
C_i	coefficients in fluid drag approximation
CC	center of curvature
CM	center of mass
CP	center of pressure
c	entry rate parameter, $\beta v \sin \gamma$
D	distance between the CC and the CM
D_α	fluid drag force
d	ball diameter
E	energy
E_1, E_2	computer parameters used to remove dampers
E_3	computer parameter used to eliminate the lift force effect on $\overline{v}$
$\dot{E}_D$	damper energy dissipation rate

*The symbols used in Section 8 are listed at the end of that section.

F_A	axial force
F_D	drag force
F_L	lift force
F_N	normal force
F_T	tangential force on ball
G	aerodynamic moment
$\bar{G}'$	moment due acceleration of the CM
h	altitude
h^*	reference altitude
I	pitch and yaw inertias, when equal
I_1	moment of inertia about x
I_2	moment of inertia about y
J	moment of inertia about the symmetry axis
K_a	$a_1+2a_2k_z+a_3(4k_z^2-1)+4a_4k_z(2k_z^2-1)$
K_m	$m_1+2m_2k_z+m_3(4k_z^2-1)+4m_4k_z(2k_z^2-1)$
K_n	$n_1+2n_2k_z+n_3(4k_z^2-1)+4n_4k_z(2k_z^2-1)$
k	damper inertia ratio, mR^2/I
k^*	effective inertia ratio, $\frac{7}{5}k\left[\frac{5}{7}(\lambda-1)+b_N^2\right]^2$
k_1	mR^2/I_1
k_2	mR^2/I_2

k_3	mR^2/J
$\bar{k}$	a unit vector along the velocity vector
ℓ	reference length
M	vehicle mass
m	mass of a single damper ball
m_i	coefficients in the series approximation for the pitch moment coefficient
n	vehicle inertia ratio, J/I
n_i	coefficients in the series approximation for the normal force coefficient
Q'_α	constraint moment about the CC due to the acceleration of the CM
Q_θ	pitch moment
Q_θ	constraint moment about the CM due to the acceleration of the CM
q	dynamic pressure
p_i	ball rates, $\dot{\alpha}_i$
p_α	ball rate, $\dot{\alpha}$
p_θ	angle of attack rate, $\dot{\theta}$
R	ball path radius
R_d	Reynold's number
$\bar{r}$	radius vector from the CM to the ball
r_b	ball radius
S	reference area
T	kinetic energy
t	time

U	ball speed in tube
$\bar{v}$	velocity of the CM
X,Z	inertial coordinates in the planar model
x,y,z	body fixed coordinate system with z along the symmetry axis
x^*,y^*,z^*	nonrotating coordinate system with origin at the CM
α,α_i	ball angles
α_L	maximum value for α
α_M	computer parameter relating to α_L
β	reciprocal of the atmospheric scale height
γ	angle between $\bar{v}$ and the local horizontal
δ	fluid drag function
ϵ	impact elasticity factor
ζ	$1-\cos\alpha$
η	$\cos\alpha - \lambda$
θ	total angle of attack
θ_b	angle of rotation of ball about its center
θ_e	θ envelope
λ	D/R
λ_g	gap ratio (labeled λ in Section 8)
μ	kinematic viscosity of fluid
μ_i	coefficients in fluid drag function δ
ρ	atmospheric density

ρ_*	reference density
ρ_X, ρ_Z	position coordinates of the CM in the planar model
τ	nondimensional parameter, $2\Omega/c$
ν	linear pitch frequency
ϕ	precession angle of symmetry axis about $\bar{v}$
ψ	relative precession angle of body with respect to the nodal axis
Ω	$\sqrt{qS\ell/I}$
$\bar{\omega}$	angular velocity of the body about the CM

CONTENTS

SECTION		PAGE
1	INTRODUCTION	1-1
2	DAMPER DESIGN AND OPERATION	
	2.1 Basic Concepts	2-1
	2.2 Nonlinear Effects	2-23
3	AMES MARS ATMOSPHERIC PROBE	
	3.1 Vehicle Description and Entry Dyanmics	3-1
	3.2 Damper Design and Tradeoffs	3-10
4	THE GODDARD MARS ATMOSPHERIC PROBE	
	4.1 Vehicle Description and Dynamics	4-1
	4.2 Damper Design	4-10
5	SMALL EARTH RE-ENTRY CONE	
	5.1 Vehicle Description and Dynamics	5-1
	5.2 Damper Design and Performance	5-3
6	MODEL FOR THE VEHICLE-DAMPER DYNAMICS	
	6.1 Introduction	6-1
	6.2 Geometry and Forces	6-3
	6.3 Planar Model	6-8
	6.4 Three Dimensional Model	6-13
	6.5 Model Extensions	6-21

SECTION 1

INTRODUCTION

Figure 1-1a shows a pendulum of mass M and a damper which are acted on by gravity g. The damper is a curved tube which contains a small ball and a viscous fluid. Oscillations of the pendulum about the pivot excite the ball which motion is opposed by the fluid. As a result, energy is dissipated from the system, and the motions of the pendulum and ball are damped to the vertical. These comments seem self-evident; however, the skeptic may prove them either mathematically or by test.

The gravity model is but an analogy to the model of the spherical entry body and damper shown in Figure 1.1b. Here the vehicle acceleration $\dot{v}$ replaces gravity. The body oscillates about its offset center of mass and the ball damps the oscillations to the velocity vector. All this points to the possibility of using a passive damper to accelerate the convergence of the angle of attack envelope for atmospheric entry bodies.

Early in 1965 a study* was conducted at Aeronutronic which showed that a passive damper could provide a significant reduction in the angle of attack envelope for only a small fraction of the vehicle weight. The damper was similar to the ball-fluid-tube configuration shown in Figure 1-1. In this early study, it was assumed that the vehicle did not

*Auelmann, R. R., "Passive Damping of the Angle of Attack Envelope During Re-Entry," Aeronutronic Publication No. U-3108, 18 May 1965.

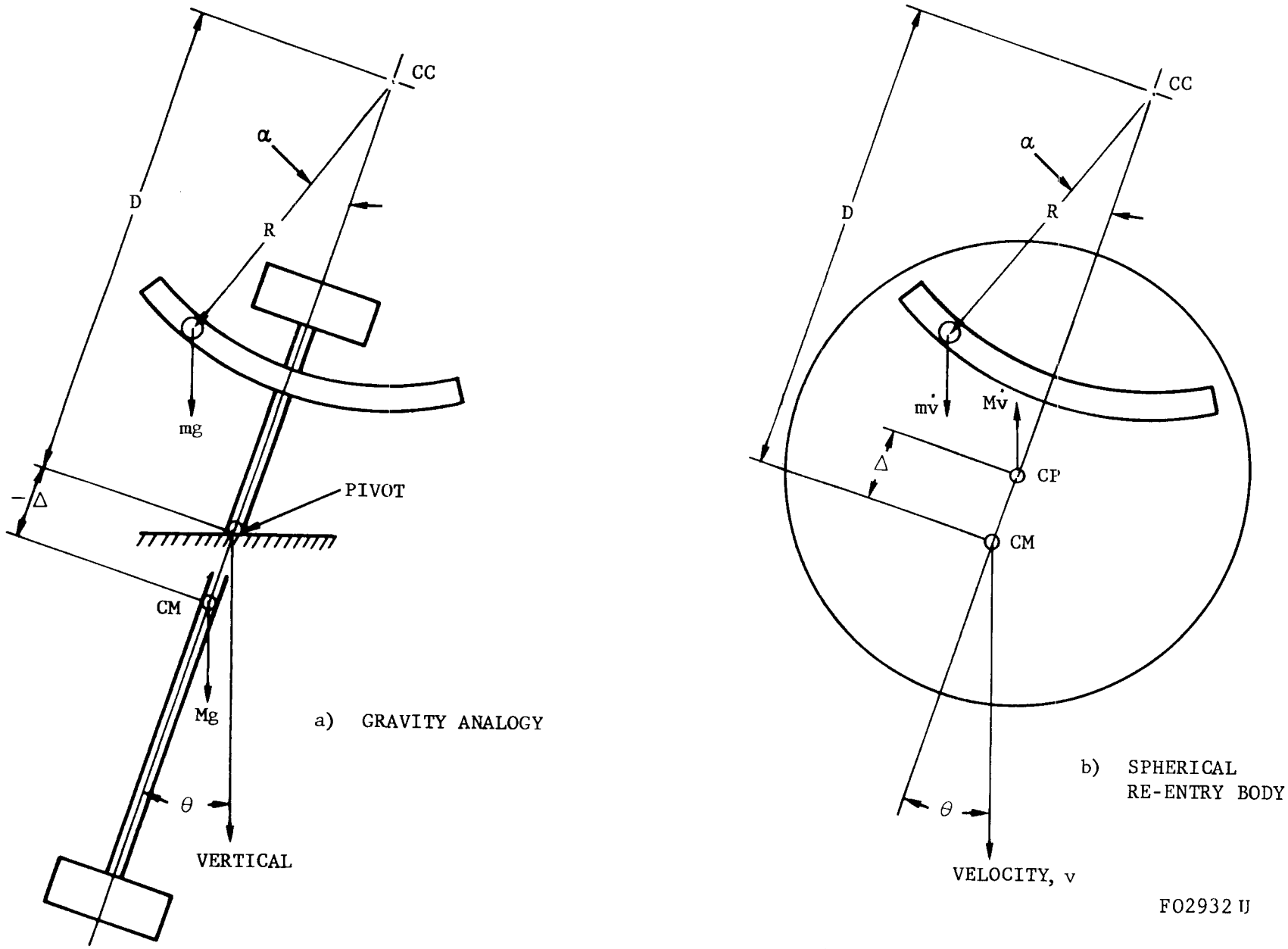

FIGURE 1-1. GRAVITY ANALOGY TO A SPHERICAL RE-ENTRY BODY

spin, the vehicle and ball motions were coplanar, the angles were small, and the fluid drag was viscous. Having obtained encouraging results, it became important to investigate the damper capabilities for a wider range of applications using a more precise model. The objectives of the current study were:

(a) to develop a model of the external vehicle-damper dynamics applicable to spinning entry bodies, large angular motions and other nonlinearities.

(b) to develop a model of the fluid forces on the ball for the expected speed regime, and to establish whether sufficient forces can be obtained using a gas.

(c) to investigate the use of the damper on selected vehicle configurations.

Prior to this study, there was no evidence that a pendulum damper would work on a spinning entry body. It was reasoned, that two dampers, orthogonally mounted with respect to the vehicle centerline, would simultaneously damp the pitch and yaw oscillations. However, there were several unknowns; would the precession rate be damped along with the angle of attack, would the spin rate be affected, or would the damper introduce an instability or some other unexpected response. Possibly the damper would be suitable for one class of vehicles but not for another.

SECTION 2

DAMPER DESIGN AND OPERATION

2.1 BASIC CONCEPTS

2.1.1 PLANAR MODEL

The basic concepts of the pendulum damper are explained using a planar model in which the re-entry body and a single damper oscillate in a fixed plane. The vehicle-damper geometry is shown in Figure 2-1. The damper ball of mass m travels in a tube with mean path radius R. The center of curvature (CC) of the tube is located a distance D behind the vehicle center of mass (CM). The angle α locates the ball within the tube relative to the vehicle symmetry axis. The angle α_L is the maximum value for α determined by the length of the tube. The angle θ between the vehicle symmetry axis and the vehicle velocity vector $\bar{v}$ is the total angle of attack. The angles θ and α specify the system.

The vehicle experiences an axial force component F_A and a normal component F_N acting through the center of pressure (CP) as shown in Figure 2-1. These forces are given by

$$F_A = qSC_A$$

$$F_N = qSC_N$$

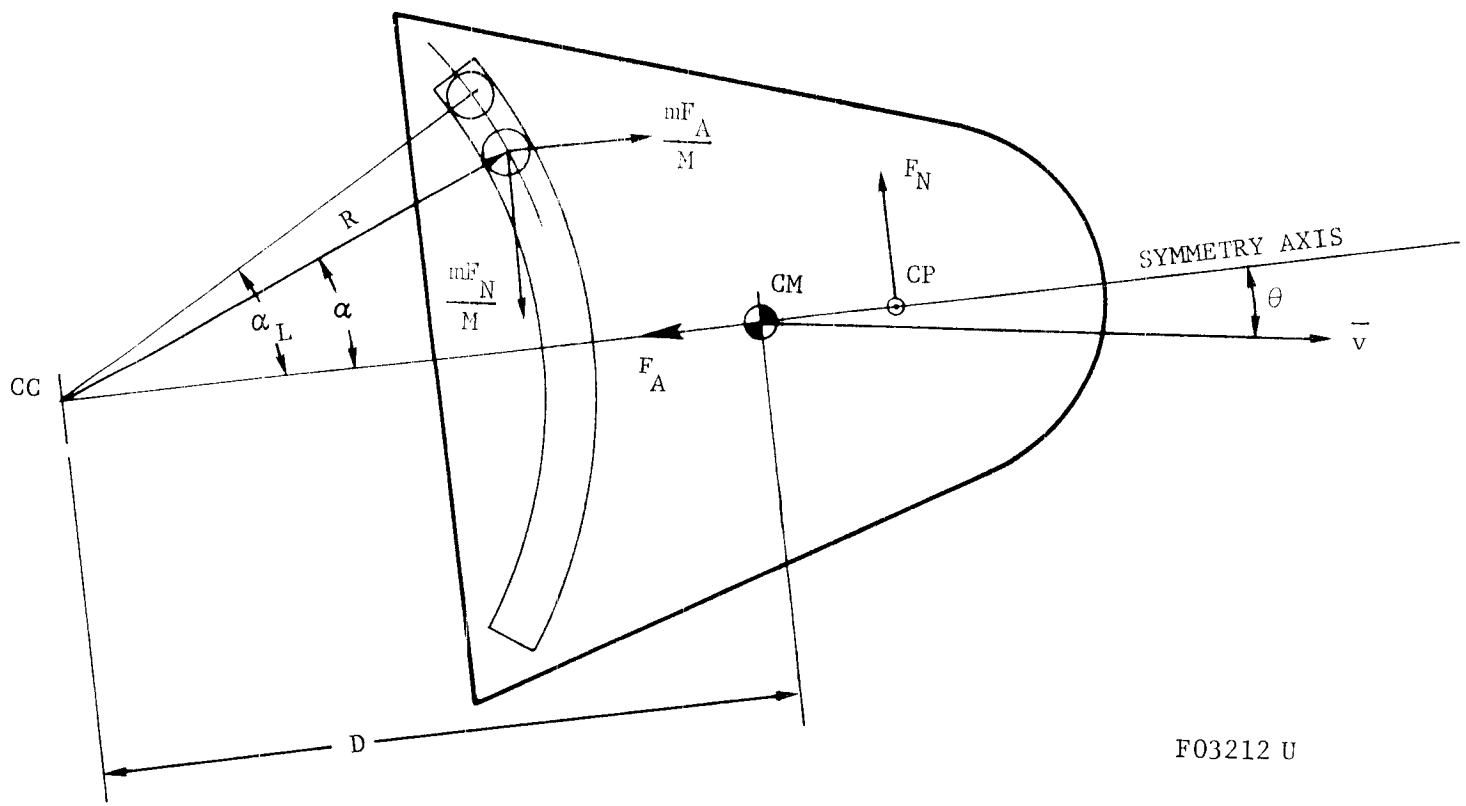

FIGURE 2-1. VEHICLE-DAMPER CONFIGURATION

where q is the dynamic pressure, S is the vehicle reference area, C_A is the axial force coefficient, and C_N is the normal force coefficient. C_A and C_N are functions of θ, and q is a function of time. An equivalent force system is obtained by shifting F_N to the CM and introducing the torque

$$Q_\theta = qS\ell C_m$$

where ℓ is the vehicle reference length and C_m is the moment coefficient. The inertia characteristics of the vehicle are represented by its mass M and moment of inertia I.

Relative to the CM, the damper mass experiences the inertial force components $-mF_A/M$ in the axial direction and $-mF_N/M$ in the normal direction because of the acceleration of the CM. In addition, the motion of the ball is resisted by the force D_α because of the fluid in the tube. D_α is assumed to be a cubic function of the relative speed $R\dot{\alpha}$, which we represent by

$$D_\alpha = C_1 R \dot{\alpha} + C_2 R^2 \dot{\alpha} |\dot{\alpha}| + C_3 R^3 \dot{\alpha}^3$$

where the C_i are constant coefficients.

The following assumptions are made. First, the velocity vector $\bar{v}$ is fixed in direction. Second, m is very small compared to M so that CM is the effective center of mass of the system. Third, the ball rolls in the tube without slipping. With these assumptions, the equations which describe the vehicle-damper dynamics are

$$\ddot{\theta} - \Omega^2 C_m = -k \Big[(1 - 2\lambda \cos \alpha + \lambda^2) \ddot{\theta} + \zeta \ddot{\alpha} + \lambda (2\dot{\theta} + \dot{\alpha}) \dot{\alpha} \sin \alpha + \frac{7}{5} b^2 \Omega^2 (C_A \sin \alpha + C_N \eta) \Big] \tag{2-1}$$

$$\ddot{\alpha} + 2\delta + b^2 \Omega^2 (C_A \sin \alpha + C_N \cos \alpha) = -\frac{5}{7} (\zeta \ddot{\theta} - \lambda \dot{\theta}^2 \sin \alpha) \tag{2-2}$$

where

$$k = \frac{mR^2}{I}$$

$$\Omega^2 = \frac{qS\ell}{I}$$

$$b^2 = \frac{5I}{7MR\ell}$$

$$\delta = \frac{5D_\alpha}{7mR^2}$$

$$\lambda = \frac{D}{R}$$

$$\eta = \cos\alpha - \lambda$$

$$\zeta = 1 - \lambda\cos\alpha$$

These equations are derived in Section 6. The $\frac{7}{5}$ appearing in certain terms is due to constraint of rolling without slipping. For statically stable bodies, C_m is negative, at least in the region of small θ. The function δ can be represented by the expression

$$\delta = \mu_1 \dot{\alpha} + \mu_2 \dot{\alpha}\,|\dot{\alpha}| + \mu_3 \dot{\alpha}^3$$

where

$$\mu_1 = \frac{5C_1}{14m}$$

$$\mu_2 = \frac{5C_2R}{14m}$$

$$\mu_3 = \frac{5C_3R^2}{14m}$$

Before Equations (2-1) and (2-2) can be solved, it is necessary to specify the functional relations between the aerodynamic coefficients (C_A, C_N, and C_m) and θ, and between Ω^2 and time. The latter relation is determined by the motion of the vehicle mass center.

The basic damper parameters are m, R, D, and the C_i. This set may be replaced by an equivalent set k, b^2, λ, and the μ_i. In addition to these basic parameters, there are α_L and the impact elasticity factor ϵ, which ranges between 1 for a perfectly elastic collision and 0 for a completely inelastic collision. The discontinuities relating to α_L and ϵ must be treated by side conditions on the basic equations.

The nonlinear Equations (2-1) and (2-2) provide little insight into how the various damper parameters affect damper performance. The important tradeoffs are more readily established from the following linear equations:

$$\ddot{\theta} + \nu^2 \theta = -k \left[(1-\lambda)^2 \ddot{\theta} + (1-\lambda) \ddot{\alpha} + \frac{7}{5} \nu^2 \left(b_A^2 \alpha + b_N^2 \theta - \lambda b_N^2 \theta \right) \right] \tag{2-3}$$

$$\ddot{\alpha} + 2\mu_1 \dot{\alpha} + \nu^2 b_A^2 \alpha = -\frac{5}{7} (1-\lambda) \ddot{\theta} - \nu^2 b_N^2 \theta \tag{2-4}$$

where

$$\nu^2 = \Omega^2 \left(-C_m'\right)_{\theta=0}$$

$$b_A^2 = b^2 \frac{\left(C_A\right)_{\theta=0}}{\left(-C_m'\right)_{\theta=0}}$$

$$b_N^2 = b^2 \frac{\left(C_N'\right)_{\theta=0}}{\left(-C_m'\right)_{\theta=0}}$$

with primes denoting derivatives with respect to θ.

2.1.2 TRANSIENT RESPONSE

The characteristic roots of linear Equations (2-3) and (2-4) define the transient response for a given value of the frequency ν. The roots s to the linear set are defined by the characteristic equation

$$\begin{vmatrix} \left[1 + k\,(1 - \lambda)^2\right] s^2 + \nu^2 & \left[1 + \frac{7}{5}\,k\,b_N^2\,(1 - \lambda)\right] \\ \frac{5}{7}\,(1 - \lambda)\,s^2 + b_N^2\,\nu^2 & k\,(1 - \lambda)\,s^2 + \frac{7}{5}\,k\,b_A^2\,\nu^2 \\ & s^2 + 2\mu_1\,s + b_A^2\,\nu^2 \end{vmatrix} = 0 \tag{2-5}$$

which expands as

$$d_4\,s^4 + d_3\,s^3 + d_2\,s^2 + d_1\,s + d_0 = 0 \tag{2-6}$$

where

$$d_4 = 1 + \frac{2}{7}\,k\,(1 - \lambda)^2$$

$$d_3 = 2\mu_1\left[1 + k\,(1 - \lambda)^2\right]$$

$$d_2 = \nu^2\left[1 + b_A^2 + k\,(1 - \lambda)\left(\frac{2}{5}\,b_N^2 - \lambda\,b_A^2\right)\right]$$

$$d_1 = 2\mu_1\,\nu^2\left[1 + \frac{7}{5}\,k\,(1 - \lambda)\,b_N^2\right]$$

$$d_0 = b_A^2\,\nu^2\left(1 - \frac{7}{5}\,k\,\lambda\,b_N^2\right)$$

Equation (2-6) can be regrouped in the form

$$\frac{\frac{d_3}{d_4}\,s\left(s^2 + \frac{d_1}{d_3}\right)}{s^4 + \frac{d_2}{d_4}\,s^2 + \frac{d_0}{d_4}} = -1 \tag{2-7}$$

which is suitable for generating the root locus as a function of the gain d_3/d_4. The zeros z_i are the root solutions for the numerator to vanish and the poles p_i are the root solutions for the denominator to vanish. By inspection we have

$$
\left.
\begin{aligned}
z_1 &= 0 \\
z_{2,3} &= \pm i \sqrt{d_1/d_3} \\
p_{1,2} &= \pm i \sqrt{\frac{d_2}{2d_4} + \frac{1}{2}\sqrt{\left(\frac{d_2}{d_4}\right)^2 - 4\,\frac{d_0}{d_4}}} \\
p_{3,4} &= \pm i \sqrt{\frac{d_2}{2d_4} - \frac{1}{2}\sqrt{\left(\frac{d_2}{d_4}\right)^2 - 4\,\frac{d_0}{d_4}}}
\end{aligned}
\right\} \qquad (2\text{-}8)
$$

When the d_i are introduced into Equation (2-8), one finds that the poles and zeros (with the exception of $z_1 = 0$) are proportional to ν and independent of μ_1. Thus, as ν changes during re-entry, because of the change in dynamic pressure, the poles and zeros maintain their relative locations in complex space, usually on the imaginary axis.

Consider the special case when the damper mass passes through the CM, that is, when $\lambda = 1$. The coefficients d_i then reduce to

$$
\begin{aligned}
d_4 &= 1 \\
d_3 &= 2\mu_1 \\
d_2 &= \nu^2 \left(1 + b_A^2\right) \\
d_1 &= 2\mu_1\, \nu^2 \\
d_0 &= b_A^2\, \nu^2 \left(1 - \frac{7}{5}\, k\, b_N^2\right)
\end{aligned}
$$

and the zeros and poles become

$$
\left.
\begin{aligned}
z_1 &= 0 \\
z_{2,3} &= \pm i\nu \\
p_{1,2} &= \pm i\nu \sqrt{\frac{1}{2}\left(1 + b_A^2\right) + \frac{1}{2}\sqrt{\left(1 - b_A^2\right)^2 + \frac{28}{5} k\, b_A^2\, b_N^2}} \\
p_{3,4} &= \pm i\nu \sqrt{\frac{1}{2}\left(1 + b_A^2\right) - \frac{1}{2}\sqrt{\left(1 - b_A^2\right)^2 + \frac{28}{5} k\, b_A^2\, b_N^2}}
\end{aligned}
\right\} \quad (2\text{-}9)
$$

For given damper mass m, the relative locations of the poles and zeros are fixed by R. Experience has shown that R should be selected so as to maximize the spread between the poles and zeros. This is accomplished by "tuning" R with the equation

$$
b_A^2 = 1 \qquad (2\text{-}10)
$$

When Equation (2-10) is satisfied the poles are located at

$$
\left.
\begin{aligned}
p_{1,2} &= \pm i\nu \sqrt{1 + \sqrt{\frac{7}{5} k\, b_N^2}} \\
p_{3,4} &= \pm i\nu \sqrt{1 - \sqrt{\frac{7}{5} k\, b_N^2}}
\end{aligned}
\right\} \quad (2\text{-}11)
$$

The effect of varying R while holding m fixed is demonstrated below for the special case of a spherical re-entry body with offset CM. In this case, $b_N^2 = b_A^2$. Now k is proportional to R^2 while b_A^2 is proportional to R^{-1}. In our example, $k = 0.0698$ when $b_A^2 = 1$. The poles p_1 and p_3 are plotted as functions of b_A^2 in Figure 2-2 for the stated conditions. With zeros at $i\nu$ and 0, the maximum spread in poles and zeros occurs in the immediate vicinity of $b_A^2 = 1$.

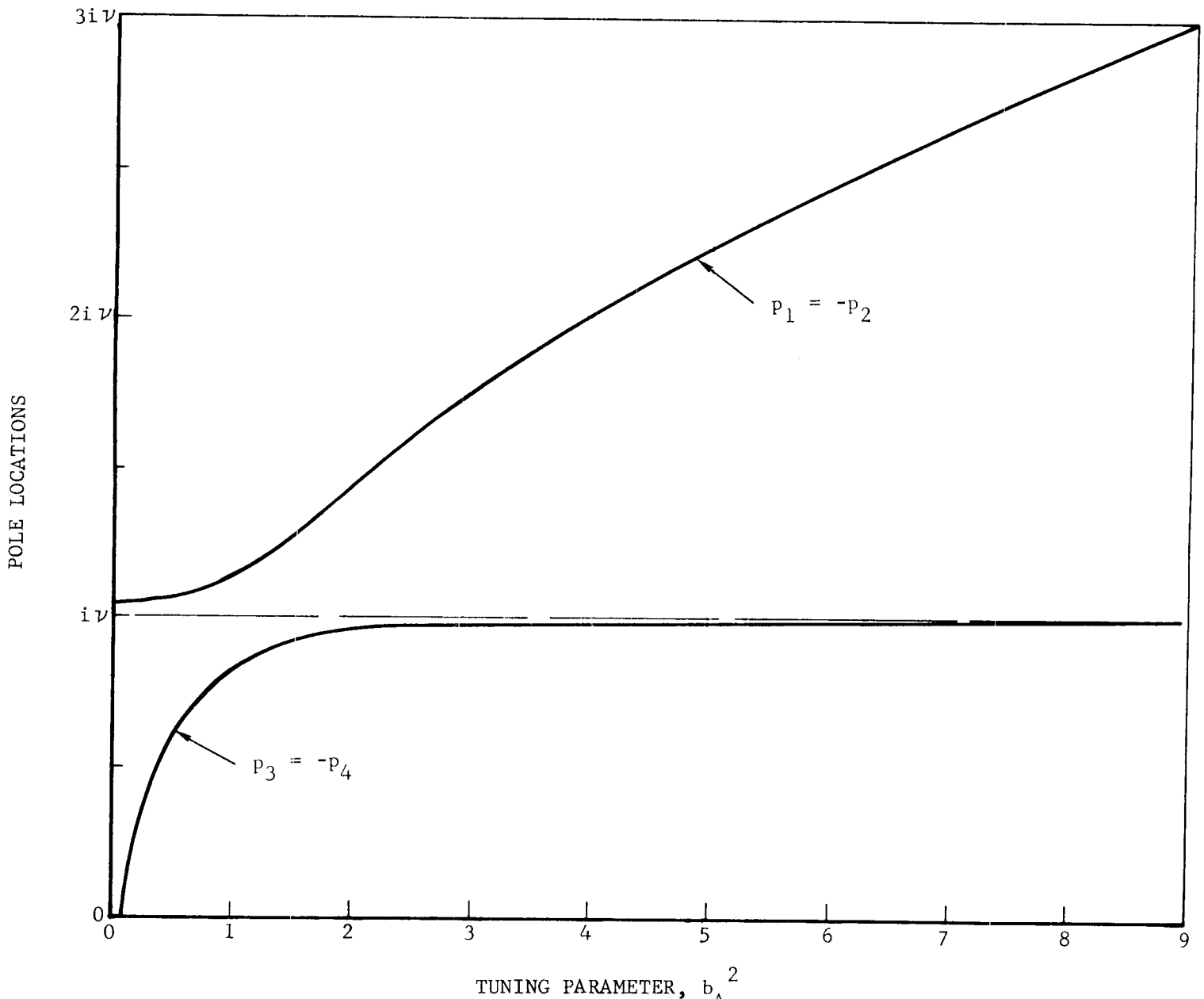

F03213 U

FIGURE 2-2. POLES AS FUNCTIONS OF b_A^2 FOR FIXED DAMPER MASS

Root locus diagrams for the gain $2\mu_1$ are sketched in Figure 2-3 for $b_A^2 = 0.25$, 1 and 4. These sketches illustrate the significance of spreading adjacent poles and zeros. We define the optimum gain $2\mu_1$ for given frequency ν as the one which maximizes the real part of the least stable root of the system. For $b_A^2 = 0.25$, the high frequency pole p_1 is nearly equal to z_2. In this case, the real part of the least stable root (with optimum gain) is only 0.0275 second. For $b_A^2 = 4$, the low frequency pole p_3 is close to z_2. In this case, the real part of the least stable root (with optimum gain) is only $-0.017\ \nu$. For $b_A^2 = 1$, the poles p_1 and p_3 are nearly equidistant from z_2. Consequently, the real part of the least stable root (with optimum gain) is approximately $-0.11\ \nu$. The transient response for $b_A^2 = 1$ is 4 times faster than for $b_A^2 = 0.25$ and 6.5 times faster than for $b_A^2 = 4$.

Unlike the poles and zeros, the characteristic roots do not maintain the same relative positions as ν changes during re-entry. The reason is that the root locations depend on the damping coefficient μ_1, which is independent of ν. The sketches in Figure 2-4 show the relative root locations as functions of ν for two different μ_1. The solid lines are root locus plots for the gain $2\mu_1$ with $b_A^2 = 1$ for four different ν. The dashed lines join the root locations for two specific μ_1. These sketches show that the smaller μ_1 provides faster damping at small ν and slower damping at large ν.

2.1.3 ENERGY SINK APPROXIMATION

The transient analysis of the previous section gives no indication of the response when ν is a function of time. To do so one must integrate a linear set of equations with time variable coefficients. Under the assumption of slowly varying ν, we obtain approximate solutions to Equations (2-3) and (2-4). We call this method the energy-sink approximation.

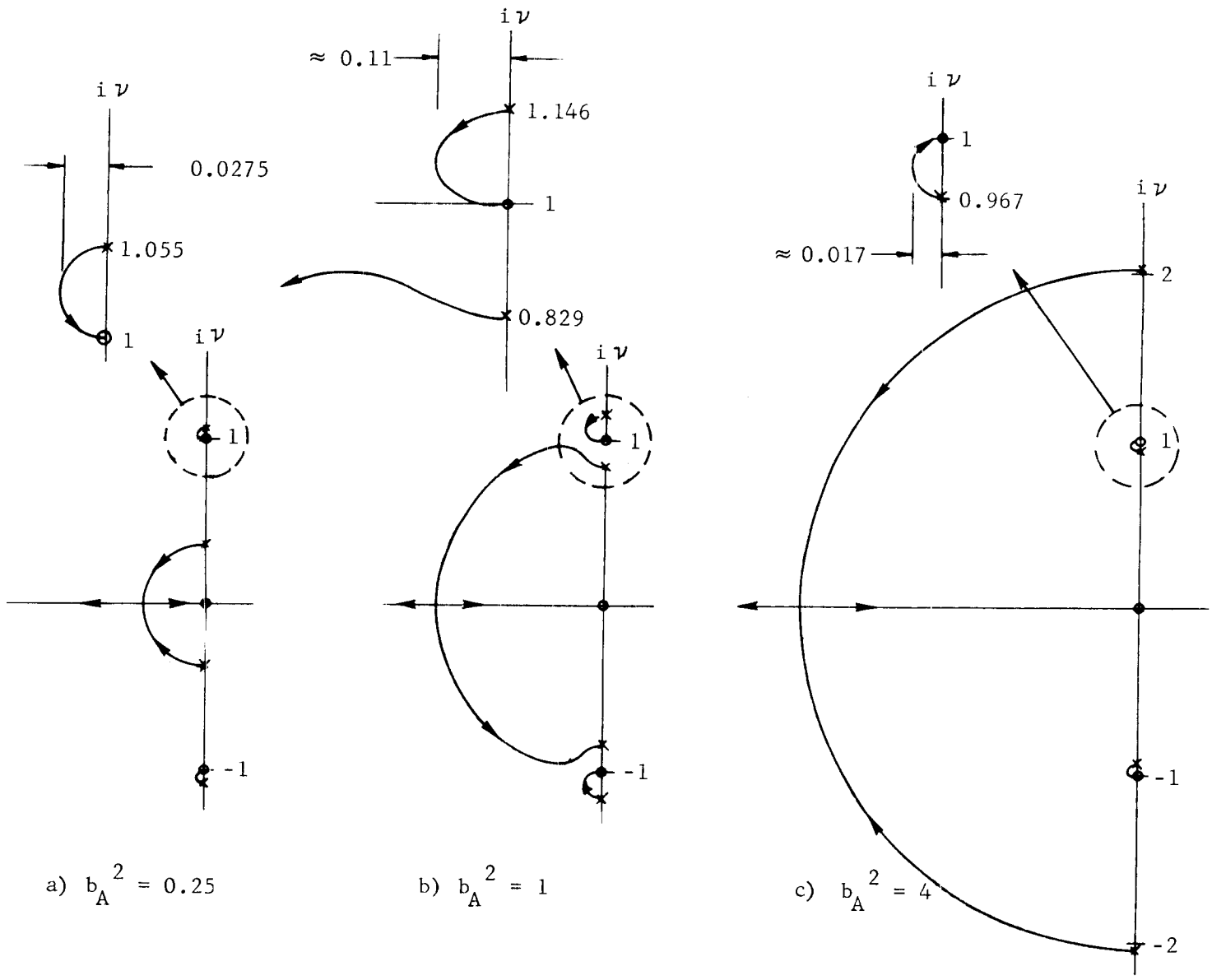

FIGURE 2-3. ROOT LOCUS PLOTS FOR $b_A^2 = 0.25$, 1 AND 4
(SAME DAMPER MASS IN EACH PLOT)

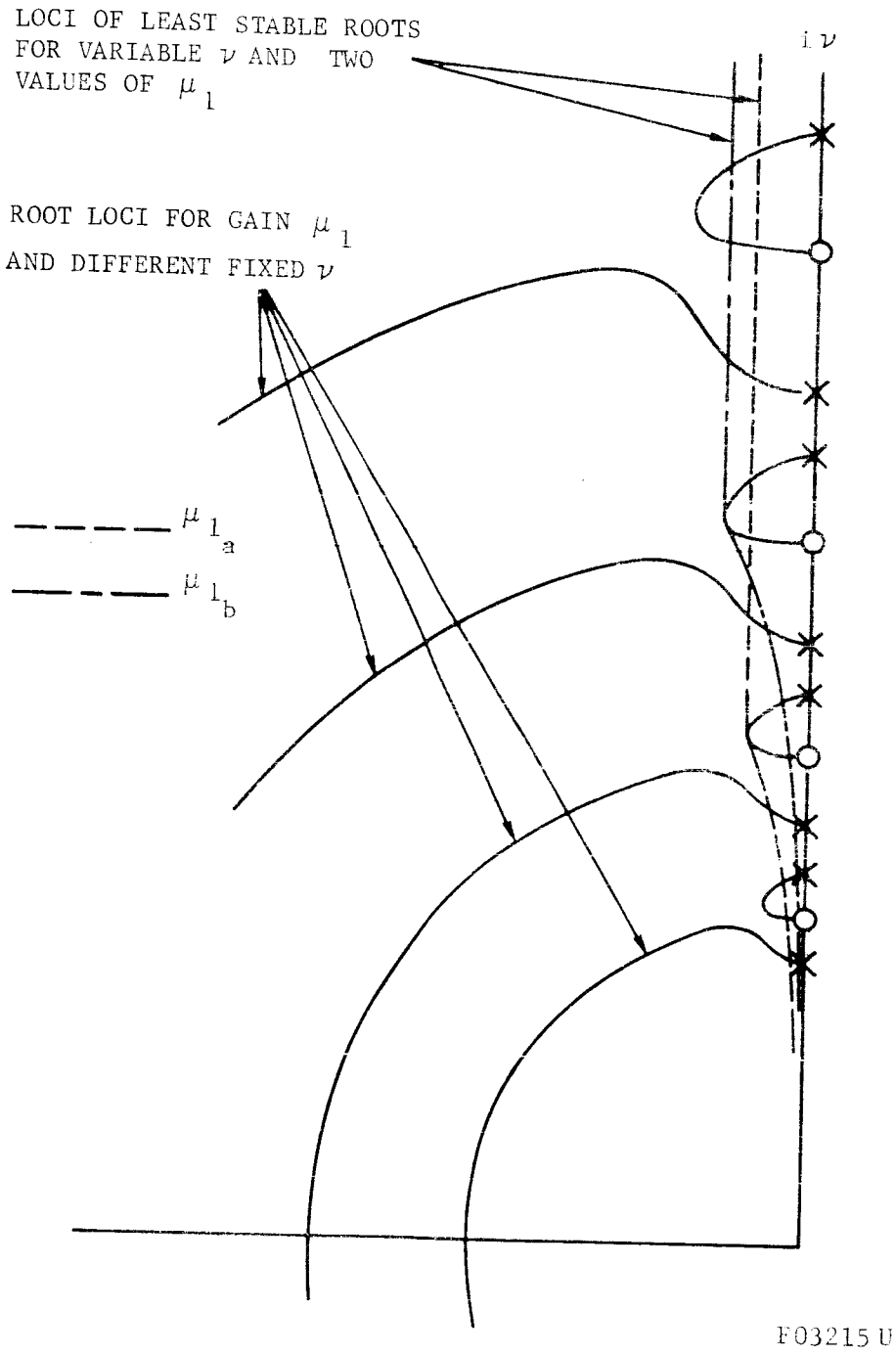

FIGURE 2-4. LOCI OF LEAST STABLE ROOTS FOR VARIABLE ν AND TWO FIXED VALUES OF μ_1

First we assume that the stored energy in the damper is negligible compared to the vehicle energy

$$E = \frac{1}{2} I \left(\dot{\theta}^2 + \nu^2 \theta^2\right) \tag{2-12}$$

The time rate of change of energy can be expressed as

$$\dot{E} = I \nu \dot{\nu} \theta^2 + \dot{E}_D \tag{2-13}$$

where $\dot{E}_D$ is the rate of energy dissipation caused by the damper.

When $k << 1$, a solution to Equation (2-3), which is valid for short periods of time, can be obtained by setting $k = 0$. One then has

$$\begin{aligned} \theta &= \theta_e \cos(\nu t + \chi) \\ \dot{\theta} &= -\nu \theta_e \sin(\nu t + \chi) \end{aligned} \tag{2-14}$$

where θ_e is the maximum displacement of θ during an oscillation and χ is the phase angle. The average values for E and $\dot{E}$ are defined by

$$\left.\begin{aligned} \langle E \rangle &= \frac{1}{2\pi} \int_0^{2\pi} E \, d(\nu t) \\ \langle \dot{E} \rangle &= \frac{1}{2\pi} \int_0^{2\pi} \dot{E} \, d(\nu t) \end{aligned}\right\} \tag{2-15}$$

Introducing Equation (2-14) into (2-15) we obtain

$$\langle E \rangle = \frac{1}{2} I \nu^2 \theta_e^2 \tag{2-16}$$

$$\langle \dot{E} \rangle = \frac{1}{2} I \nu \dot{\nu} \theta_e^2 + \langle \dot{E}_D \rangle \tag{2-17}$$

Differentiating $\langle E \rangle$ with respect to time and equating the result to Equation (2-17) we obtain

$$\dot{\theta}_e = -\frac{\dot{\nu}}{2\nu} \theta_e + \frac{\langle \dot{E}_D \rangle}{I \nu^2 \theta_e} \tag{2-18}$$

The first term on the right-hand side gives the envelope decay rate caused by the change in ν, while the second term gives the envelope decay rate caused by the damper.

The damper dissipates energy at the rate

$$\dot{E}_D = -C_1 R \dot{\alpha}^2 = -\frac{14}{5} m R^2 \mu_1 \dot{\alpha}^2 \tag{2-19}$$

To evaluate $\dot{\alpha}$, we first use the short-term solutions, Equation (2-14), to express the right-hand side of Equation (2-4) as an explicit function of time:

$$\ddot{\alpha} + 2\mu_1 \dot{\alpha} + b_A^2 \nu^2 \alpha = -K \theta_e \cos(\nu t + \chi) \tag{2-20}$$

where

$$K = \left[\frac{5}{7}(\lambda - 1) + b_N^2\right] \nu^2$$

The steady-state solution to Equation (2-20) is

$$\alpha = -K \theta_e \left[\frac{\left(b_A^2 - 1\right) \nu^2 \cos(\nu t + \chi) + 2\mu_1 \nu \sin(\nu t + \chi)}{\left(b_A^2 - 1\right)^2 \nu^4 + 4\mu_1^2 \nu^2}\right] \tag{2-21}$$

$$\dot{\alpha} = K \theta_e \nu \left[\frac{\left(b_A^2 - 1\right) \nu^2 \sin(\nu t + \chi) - 2\mu_1 \nu \cos(\nu t + \chi)}{\left(b_A^2 - 1\right)^2 \nu^4 + 4\mu_1^2 \nu^2}\right] \tag{2-22}$$

The average value of the steady state solution $\dot{\alpha}$ is given by

$$\begin{aligned} \langle \dot{\alpha}^2 \rangle &= \frac{K^2 \theta_e^2/2}{\left(b_A^2 - 1\right)^2 \nu^2 + 4\mu_1^2} \\ &= \frac{\left[\frac{5}{7}(\lambda - 1) + b_N^2\right]^2 \nu^4 \theta_e^2/2}{\left(b_A^2 - 1\right)^2 \nu^2 + 4\mu_1^2} \end{aligned} \tag{2-23}$$

In the energy-sink approximation, $\dot{\alpha}^2$ in Equation (2-19) is replaced by $\langle\dot{\alpha}^2\rangle$. So doing we obtain

$$\langle\dot{E}_D\rangle = -\frac{\frac{7}{5}\, m\, R^2 \left[\frac{5}{7}(\lambda - 1) + b_N^2\right]^2 \mu_1 \nu^4\, \theta_e^2}{\left(b_A^2 - 1\right)^2 \nu^2 + 4\mu_1^2} \tag{2-24}$$

Using this relation, Equation (2-18) provides

$$\dot{\theta}_e = -\left\{\frac{\dot{\nu}}{2\nu} + \frac{\frac{7}{5}\, k \left[\frac{5}{7}(\lambda - 1) + b_N^2\right]^2 \mu_1 \nu^2}{\left(b_A^2 - 1\right)^2 \nu^2 + 4\mu_1^2}\right\} \theta_e \tag{2-25}$$

To solve Equation (2-25), it is necessary to specify the functional relation between ν and t. Above the point of peak dynamic pressure, the vehicle velocity $\bar{v}$ can be treated as a constant. For an exponential atmosphere ν^2 can be expressed as

$$\nu^2 = \nu_o^2\, e^{ct} \tag{2-26}$$

where

$$c = \beta\, v \sin\gamma$$

β is the reciprocal of the atmospheric scale height and γ is the angle between $\bar{v}$ and the horizontal. Differentiating ν we get

$$\dot{\nu} = \frac{1}{2}\, c\, \nu \tag{2-27}$$

which, together with Equation (2-26), can be used to obtain

$$\frac{d\,\theta_e}{d\nu} = -\left\{\frac{1}{2\nu} + \frac{\frac{7}{5}\, k \left[\frac{5}{7}(\lambda - 1) + b_N^2\right]^2 (2\mu_1/c)\nu}{\left(b_A^2 - 1\right)^2 \nu^2 + 4\mu_1^2}\right\} \theta_e \tag{2-28}$$

Equation (2-28) is of the form

$$\frac{d\,\theta_e}{\theta_e} = -\left(\frac{1}{2\nu} + \frac{h\nu}{\nu^2 + a^2\,\mu_1^2}\right) d\nu \tag{2-29}$$

where

$$h = \frac{\frac{7}{5}\,k\left[\frac{5}{7}\,(\lambda - 1) + b_N^2\right](2\mu_1/c)}{\left(b_A^2 - 1\right)^2}$$

$$a^2 = \frac{16}{\left(b_A^2 - 1\right)^2}$$

The solution for θ_e is

$$\frac{\theta_e}{\theta_{e_0}} = \left(\frac{\nu_0}{\nu}\right)^{1/2}\left[\frac{1 + (a\mu_1/\nu_0)^2}{(\nu/\nu_0)^2 + (a\mu_1/\nu_0)^2}\right]^{h/2} \tag{2-30}$$

where the zero subscript denotes initial values.

The solution is indeterminate when $b_A^2 = 1$, the tuning condition for the mean path radius R. In this singular case, we replace Equation (2-29) by

$$\frac{d\,\theta_e}{\theta_e} = -\left(\frac{1}{2\nu} + p\nu\right) d\nu \tag{2-31}$$

where

$$p = \frac{\frac{7}{5}\,k\left[\frac{5}{7}\,(\lambda - 1) + b_N^2\right]^2}{8\mu_1 c}$$

The solution to Equation (2-31) is

$$\frac{\theta_e}{\theta_{e_o}} = \left(\frac{\nu_0}{\nu}\right)^{1/2} e^{-\frac{p}{2}\left(\nu^2 - \nu_0^2\right)} \tag{2-32}$$

Comparisons were made between the envelope solutions predicted by the energy-sink approximation and numerical solutions to Equations (2-3) and (2-4). The vehicle considered was a sphere with offset CM. Figure 2-5 shows the comparison before the damper is added to the vehicle. The predicted envelope is the familiar quarter-power decay with dynamic pressure. The agreement is excellent. Figure 2-6 shows the comparison when a nonresonant damper $\left(b_A^2 = 1.52\right)$, passing through the CM ($\lambda = 1$), is added to the vehicle. The agreement is good. Figure 2-7 shows the comparison when a resonant damper $\left(b_A^2 = 1\right)$, also passing through the CM, is added to the vehicle. Again, the agreement is good. The values for k, μ_1, c, and ν_0 are listed in the figures.

The parameters k, λ, and b_N^2 only enter into Equations (2-30) and (2-32) through the factor

$$k^* = \frac{7}{5} k \left[\frac{5}{7} (\lambda - 1) + b_N^2\right]^2 \tag{2-33}$$

which should be maximized to obtain the fastest convergence for θ_e. If k^* is negative, θ_e will diverge. The form of k^* indicates that the damper should be located as far aft of the CM as possible, that is, λ should be maximized. The size of k is determined by m and R^2, but R enters through other terms in Equations (2-30) and 2-32). In fact, the transient analysis of Paragraph 2.1.2 indicates that R should be picked to satisfy $b_A^2 = 1$. This means that k can only be increased by increasing m. The only other parameter in k^* is b_N^2. For a spherical re-entry body $b_N^2 = b_A^2$ while for a slender cone with half-cone angle θ_c, $b_N^2 = b_A^2 \cot^2 \theta_c$ using Newtonian theory.

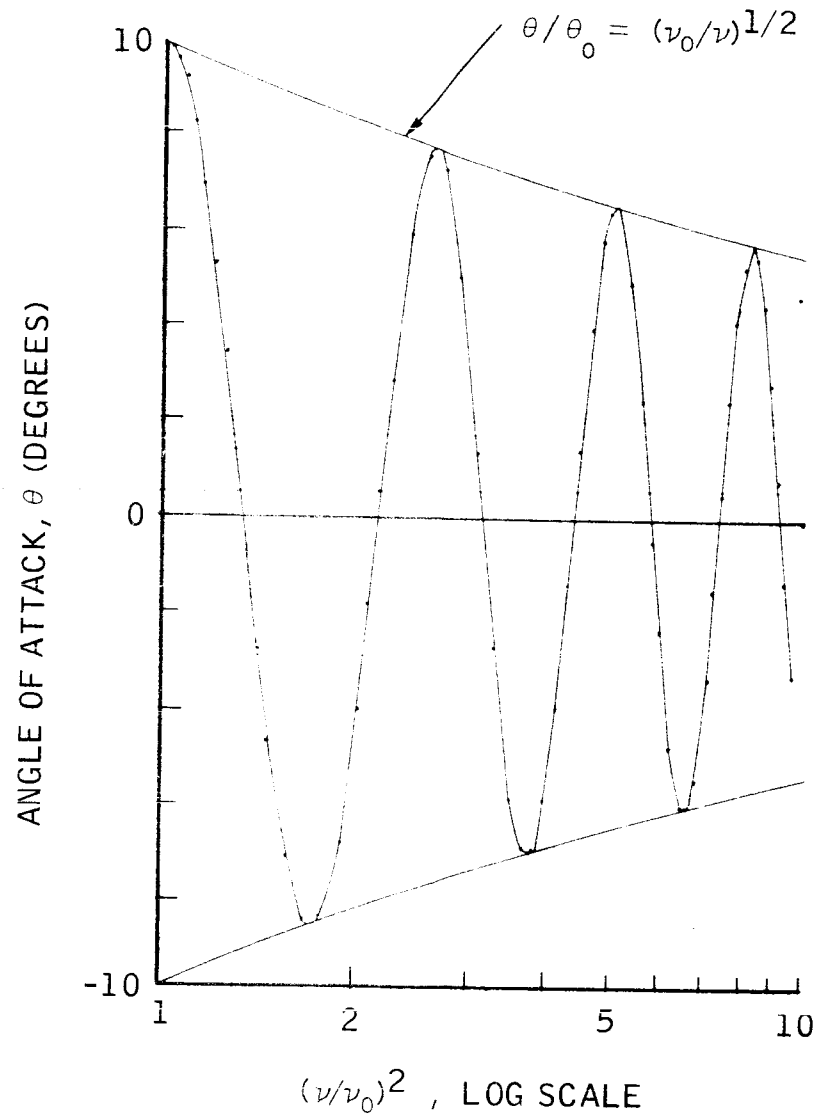

F03359 U

FIGURE 2-5 COMPARISON BETWEEN ANALYTIC AND NUMERICAL SOLUTIONS FOR A SPHERE WITHOUT DAMPER ($\nu_0 = 10\ \mathrm{sec}^{-1}$, RUN 14)

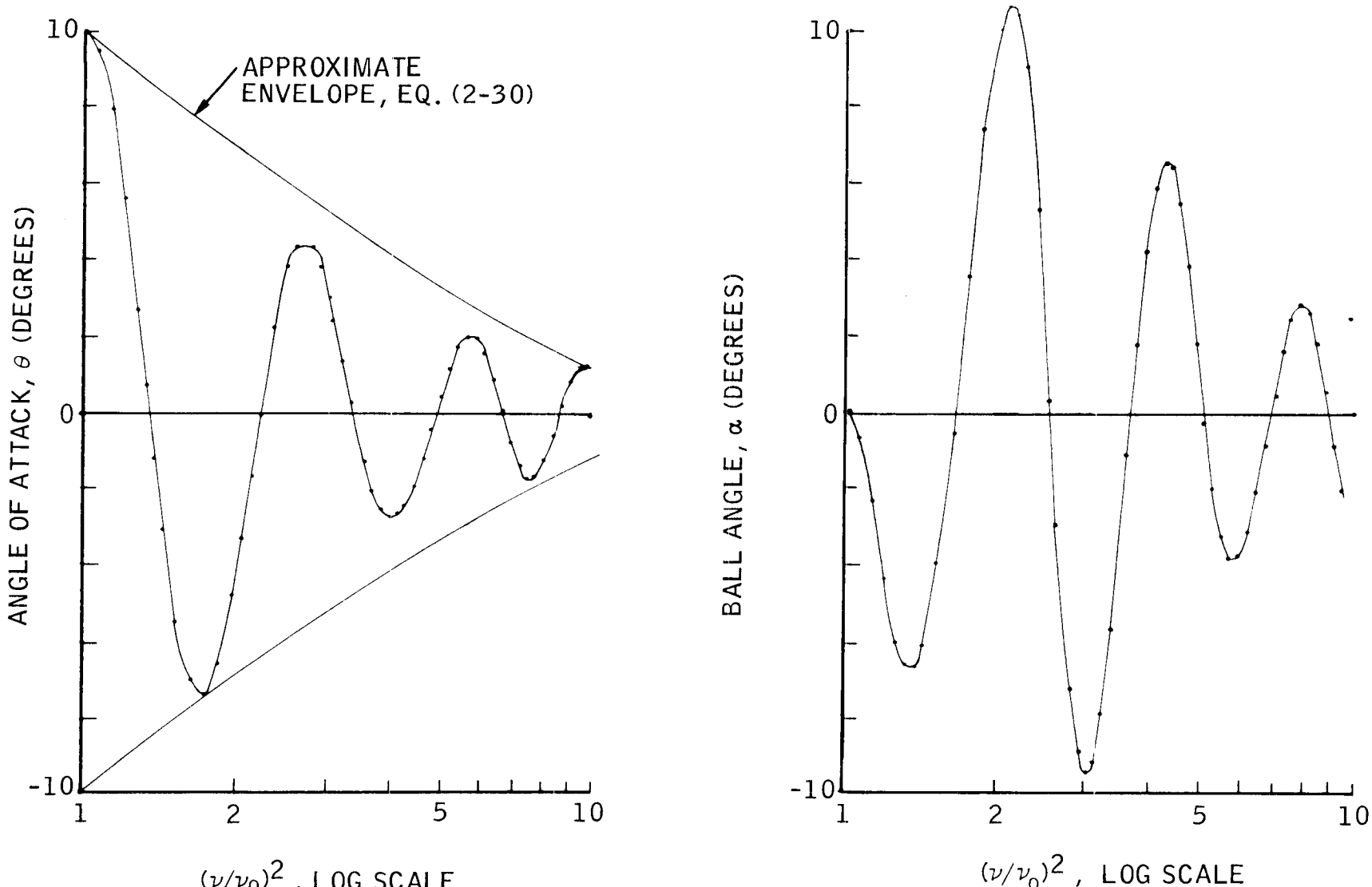

F03360 U

FIGURE 2-6 COMPARISON BETWEEN ANALYTIC AND NUMERICAL SOLUTIONS FOR A SPHERE
($k = 0.0698$, $b^2 = 1.52$, $\lambda = 1$, $\mu_1 = 2.4\ \text{sec}^{-1}$, $c = 1\ \text{sec}^{-1}$, $\nu_0 = 10\ \text{sec}^{-1}$, RUN 12)

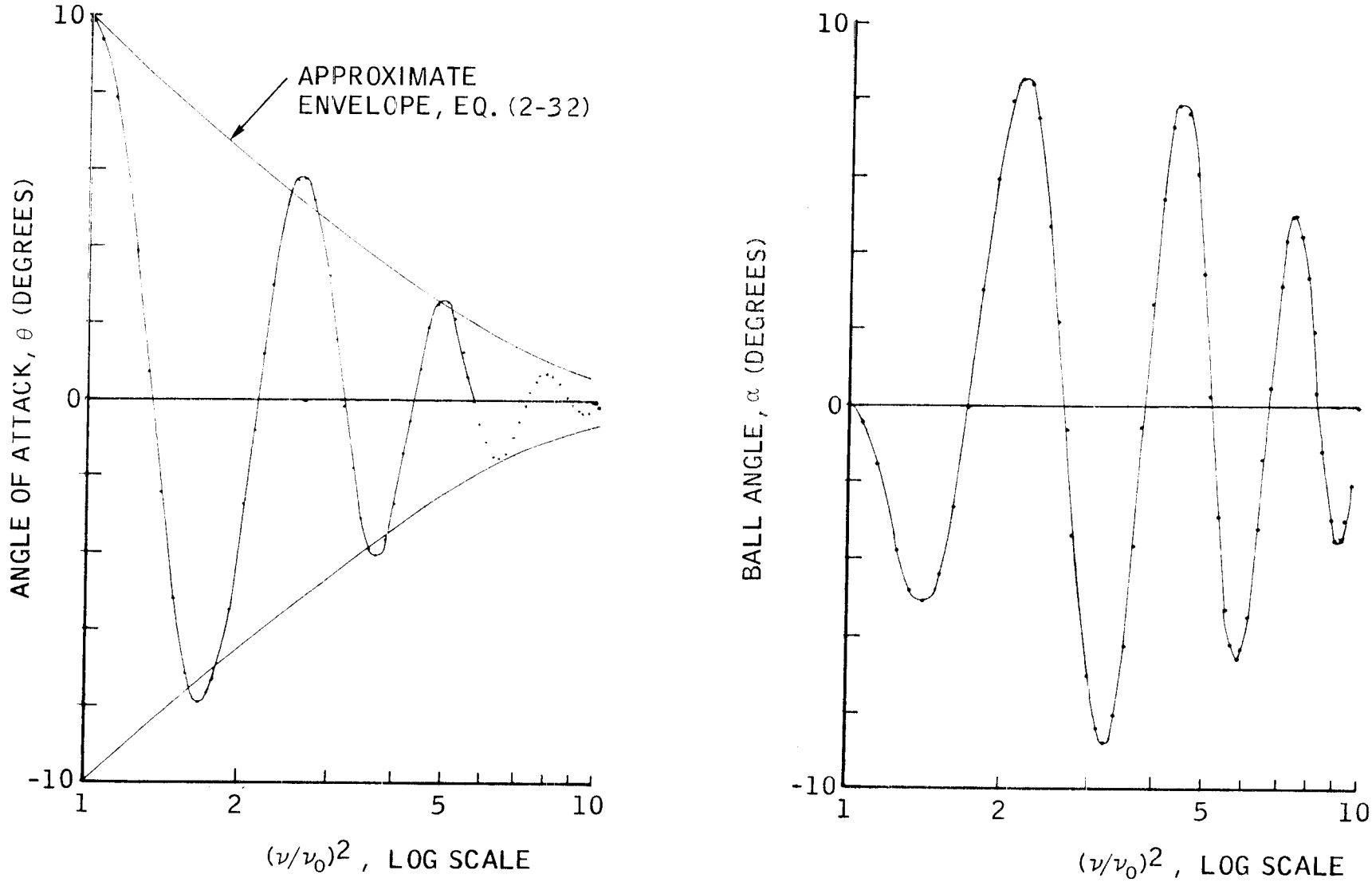

F03361 U

FIGURE 2-7 COMPARISON BETWEEN ANALYTIC AND NUMERICAL SOLUTIONS FOR A SPHERE ($k = 0.0698$, $b^2 = 1$, $\lambda = 1$, $\mu_1 = 2.45\ \text{sec}^{-1}$, $c = 1\ \text{sec}^{-1}$, $\nu_0 = 10$, RUN 11)

Now consider the effect which μ_1 has on the motion. Equation (2-32) says that the decay rate increases when μ_1 decreases. However, this relation cannot be carried to the limit, $\mu_1 = 0$. In obtaining the solutions of Equations (2-30) and (2-32) we approximated the complete solution to Equation (2-20) by the steady-state portion of the solution. This approximation is valid only if the transient response caused by the change in ν is rapidly damped, implying a lower limit on μ_1.

This difficulty arises only for the resonant solution. Equation (2-30) does not suggest that μ_1 be made arbitrarily small. Rather it shows that for small μ_1, θ_e converges rapidly at low ν and slowly at large ν; and conversely for large μ_1. This effect is illustrated in Figure 2-8 where solutions are shown for three cases. The cases differ only in the relative size of μ_1, which is successively doubled in Cases A, B, and C. This result is qualitatively predicted by the transient analysis (see Figure 2-4).

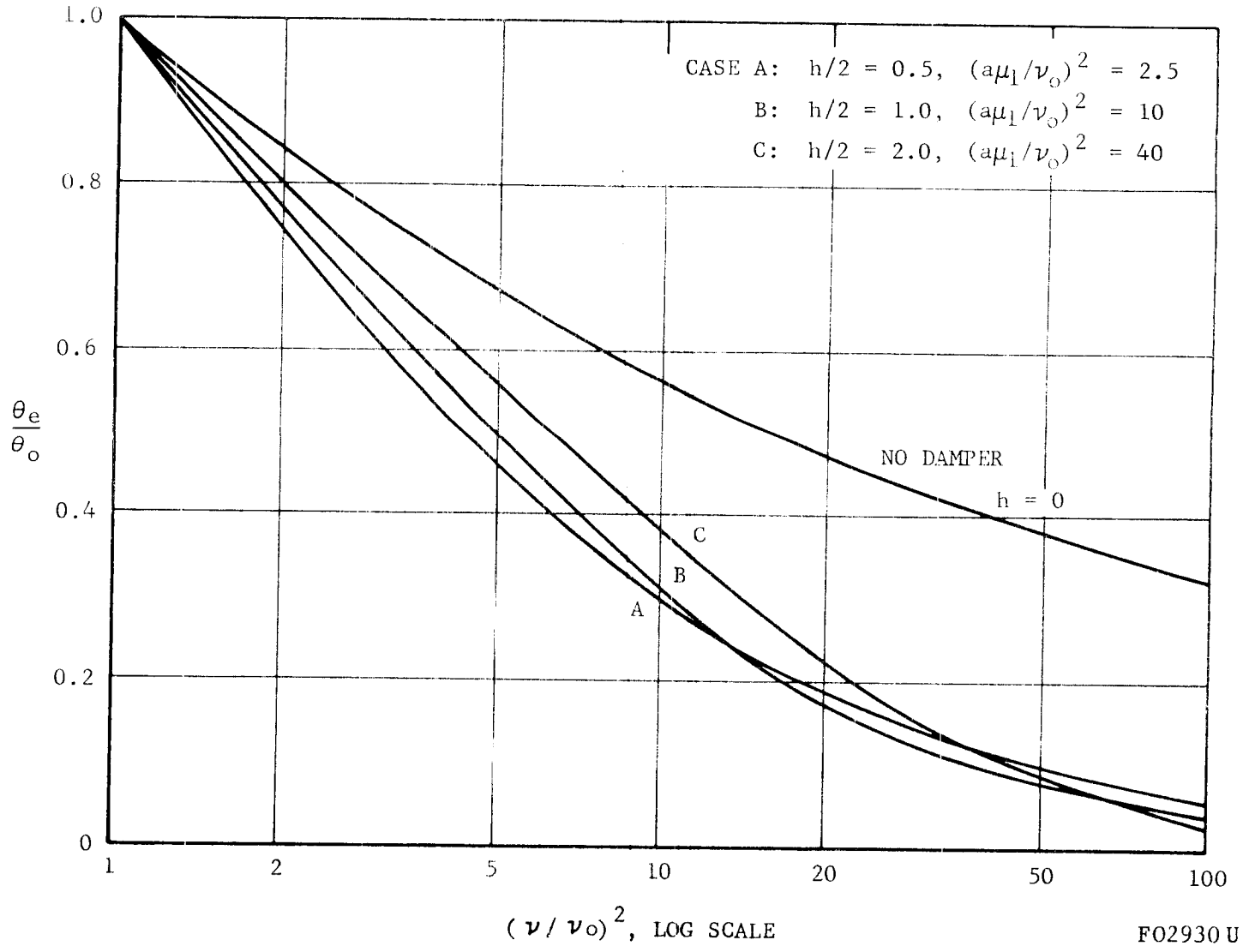

FIGURE 2-8. EFFECT OF VARYING THE μ_1 BASED ON EQUATION (2-30)

2.2 NONLINEAR EFFECTS

2.2.1 LARGE ANGLES AND IMPACT DISCONTINUITIES

The linear model suggests that a damper be designed along the following guidelines:

(1) The mean path radius R should be selected so as to satisfy the condition $b_A^2 = 1$. This condition amounts to "tuning" the damper natural frequency to the vehicle natural frequency ν.

(2) The damper should be located as far aft of the CM as possible, that is, λ should be maximized.

(3) No optimum condition for the damping coefficient μ_1 can be specified, because μ_1 is independent of ν. Rather small μ_1 tends to be more effective at small ν and vice versa.

When θ and α are large, these guidelines may not be entirely correct. The aerodynamic coefficients C_A, C_N, and C_m are nonlinear functions of θ. The fact that C_A may increase by factors of three or four, or may change sign, suggests that "tuning" is not as important as indicated by the linear model.

The angle θ indirectly affects the amplitude of the ball oscillations. Practical considerations dictate that an upper limit α_L be placed on the ball displacement angle α. When θ is large, the ball will impact the ends of the tube, thereby introducing transients into the system. This effect can be quite detrimental, especially for nonspinning entry bodies.

The impact discontinuities are handled in the digital programs (Section 7) by the side condition

$$\dot{\alpha} = -\epsilon\,\dot{\alpha} \tag{2-34}$$

at the limits. The constant ϵ ranges between 0 for an inelastic collision and 1 for an elastic collision. Intermediate values for ϵ can be assigned.

In all cases the best performance results when $\epsilon = 0$. This seems logical; first because transients are minimized, and second because the energy dissipated upon impact is maximized.

The effects of large θ are illustrated for the vehicle-damper combination shown in Figure 2-9. The vehicle is a 2-foot diameter sphere which weighs 25 pounds. The pitch inertia I is 0.5 slug ft^2. C_A and C_N are equal to 1 for a sphere. Taking the reference length ℓ as the distance between the CP and the CM, we have $\ell = 0.2$ ft and $C_m = -1$. With this choice of ℓ, the parameter b_A^2 is given by

$$b_A^2 = b^2 = \frac{5I}{7\ MR\ell}$$

The tuning condition, $b_A^2 = 1$, is satisfied by R = 2.29 ft. Since the ball passes through the CM, $\lambda = 1$. The ball weighs 0.43 pound, fixing k at 0.0698. The angle limit $\alpha_L = 23$ degrees is set so that the tube does not extend beyond the sphere. The impact parameter ϵ is 0 and the linear damping coefficient μ_1 is 2 sec^{-1}.

To integrate Equations (2-1) and (2-2), it is necessary to specify the relation between Ω^2 and time. For a constant velocity through an exponential atmosphere, Ω^2 is of the form

$$\Omega^2 = \Omega_o^2\ e^{ct}$$

In this example, we set $\Omega_o^2 = 0.1$ and $c = 1$ sec^{-1}.

The ball starts at rest in the center of the tube and the vehicle starts at an initial angle of attack of 150 degrees. The resulting vehicle and damper motions are plotted in Figures 2-10 and 2-11, respectively. Two scales for the independent variable are shown; a linear scale for the non-dimensional time ct, and a logarithmetic scale for the $\tau = 2\Omega/c$. Despite the impact discontinuities, evident in Figure 2-11, the damper effectively reduces the angle of attack oscillations. This may be seen by comparing θ with the envelope curve when the damper is removed.

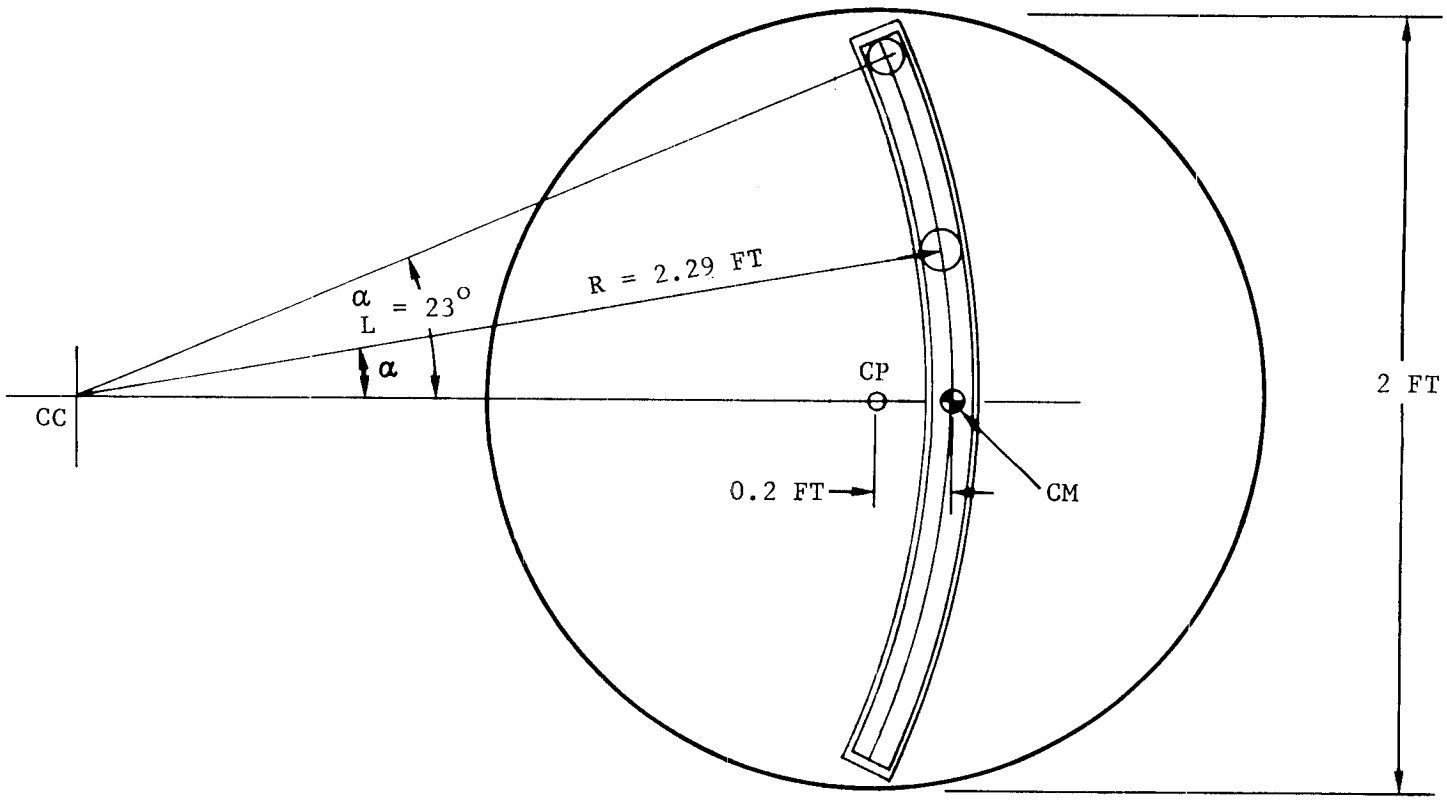

F03216 U

FIGURE 2-9. SPHERICAL ENTRY BODY WITH OFF-SET CM AND A PASSIVE DAMPER PASSING THROUGH THE CM.

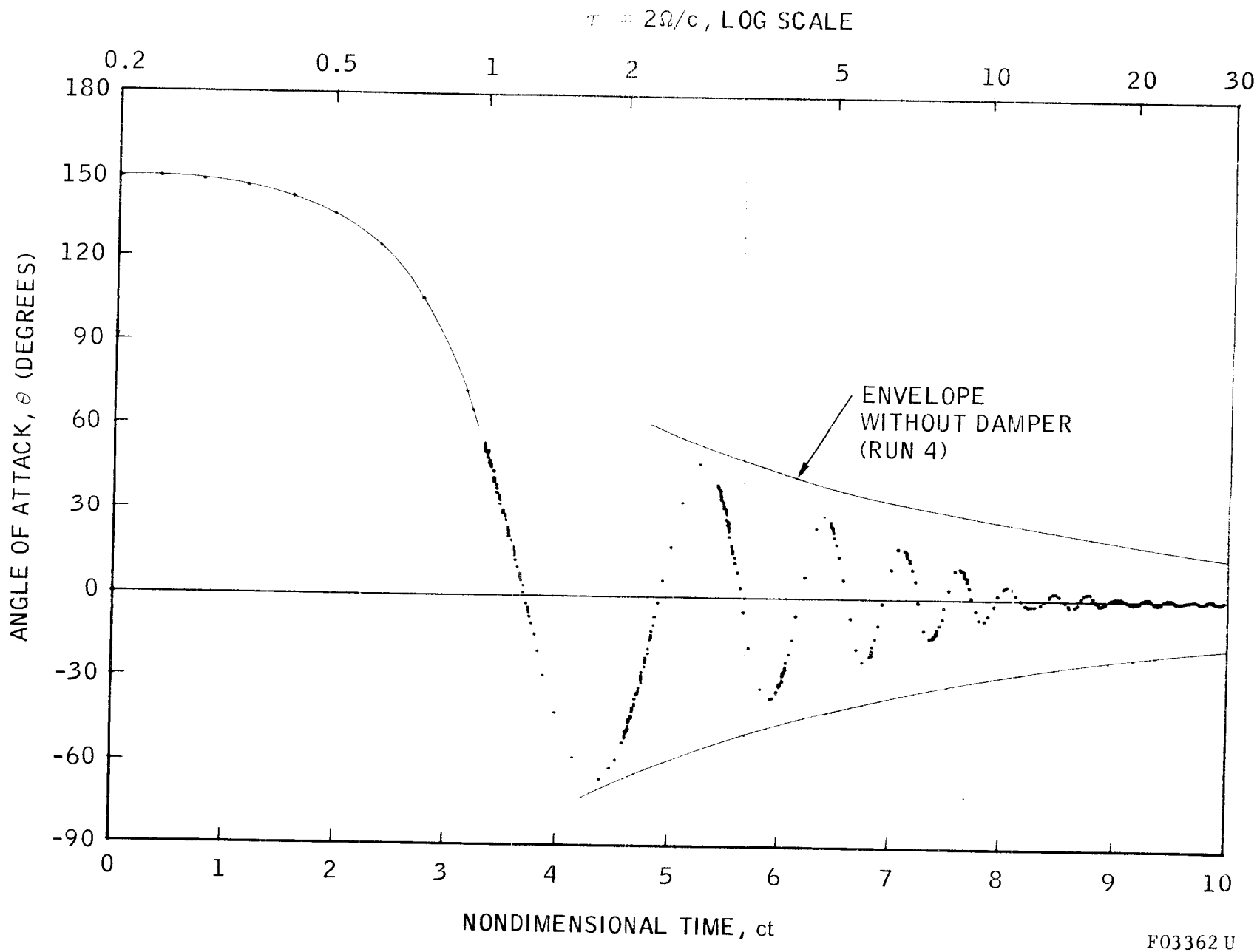

FIGURE 2-10 ANGLE OF ATTACK HISTORY FOR A SPHERE WITH A LINEAR DAMPING LAW
($k = 0.0698$, $b^2 = 1$, $\lambda = 1$, $\mu_1/c = 2$, RUN 3)

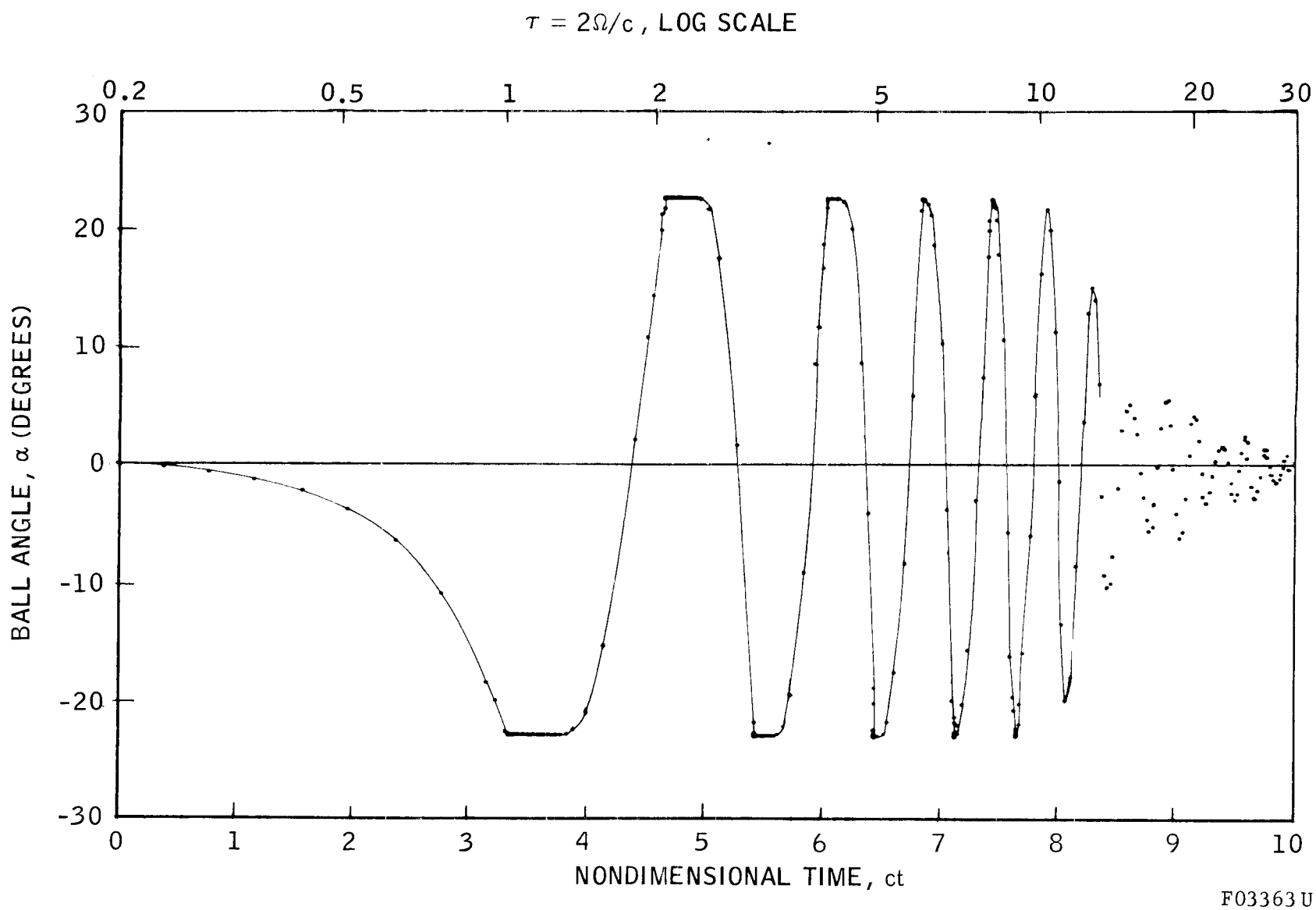

FIGURE 2-11 BALL OSCILLATION (RUN 3)

The values of R which satisfy $b_A^2 = 1$ tend to be very small (even on the order of the ball diameter) for slender re-entry bodies. Here the linear model is completely inadequate, because even moderate values of θ tend to drive α past 90 degrees. Since the motion can be unstable for α greater than 90 degrees, and since the response tends to be slow near 90 degrees, it is expedient to limit α to approximately 60 degrees.

Unfortunately, when R is very small, the path length between stops is too short to be effective. The only recourse is to discard the tuning constraint, $b_A^2 = 1$, and to select a larger value for R. The linear model indicates that the damper performance will drop decisively if this is done. Consequently, one might conclude that the pendulum damper is better suited to blunt vehicles than to slender vehicles. That this conclusion is not necessarily correct may be seen by examining k* defined in Equation (2-33). Here b_N^2 and λ are seen to be as important as R. First, b_N^2 may be an order of magnitude larger for a slender body than for a blunt body. Second, the geometry of a slender body permits large values for λ, while the geometry for a blunt body does not.

2.2.2 EFFECT OF VEHICLE SPIN

A principal objective of the study was to demonstrate the use of two orthogonally mounted pendulum dampers on a spinning re-entry body. This problem is dealt with specifically in Sections 3 and 5.

At the beginning of entry, when the dynamic pressure q is small, the centrifugal force forces the damper balls to the ends of their respective tubes. The force driving the ball against the limit is given by

$$F_T = m\left[\left(\omega_z^2 R \sin\alpha_L - \frac{q\,S}{M}\,C_N\right)\cos\alpha_L \sin\psi - \frac{q\,S}{M}\,C_A \sin\alpha_L\right] \qquad (2\text{-}35)$$

where ω_z is the component of angular velocity about the symmetry axis, and ψ is the angle between the damper plane and the plane of the angle of attack. The terms dependent on ψ are almost periodic, ψ being a monotonically increasing or decreasing function of time.

When F_T becomes negative, the ball moves off the limit and begins to oscillate about $\alpha = 0$. This point depends on q, θ, and α_L. Once the ball begins to oscillate, it will only occasionally return to the limits and then with low velocity. Consequently, the nature of the impact, as characterized by ϵ, is less critical for spinning bodies than for nonspinning bodies.

As long as F_T is positive the ball sits on the limit. In this condition the balls and the vehicle move as a single rigid body with a principal axis misalignment and a center of mass displacement. The principal axis misalignment causes the vehicle to cone about the instantaneous angular momentum vector. The cone angle may be quite large if the dampers are located far aft of the CM, as would normally be true.

In most cases, the effect of the CM displacement is unnoticable. However, it could be more serious than a principal axis misalignment. Pettus* and other investigators have shown that a CM offset can cause a roll resonance and a divergence of the angle of attack envelope. The point of instability is predicted by the equation

$$\nu^2 = \left(1 - \frac{J}{I}\right) \omega_z^2 \tag{2-36}$$

where J is the moment of inertia about the symmetry axis and ν^2 is proportional to q. A potential instability exists if Equation (2-36) is satisfied while F_T is positive. However, even under these conditions the instability is probabalistic in that certain phase relations must also be satisfied.

---

*Pettus, J. J., "Persistent Re-entry Roll Resonance," AIAA Preprint No. 66-49, AIAA Third Aerospace Sciences Meeting, New York, January 1966.

If the initial coning motion caused by the principal axis misalignment is unacceptable or if the instability condition cannot be avoided, the balls can be caged in the centers of their tubes until q is sufficiently large that the balls will not return to the limits when uncaged. This expedient eliminates both problems, but it also adds some complexity to the damper system.

2.2.3 NONLINEAR FLUID DRAG

The drag on the damper ball as it moves through the fluid in the tube can be expressed as

$$D_\alpha = \frac{1}{2} \rho U^2 \pi \left(\frac{d}{2}\right)^2 C_D$$

where ρ is the density of the fluid, $U = R \dot{\alpha}$ is the relative ball speed, d is the ball diameter and C_D is the drag coefficient. For the speeds U encountered with practical damper designs, C_D depends only on the gap ratio

$$\lambda_g = \frac{\text{Inside tube diameter} - d}{d}$$

and the Reynold's number

$$R_d = \frac{U d}{\mu}$$

where μ is the kinematic viscosity of the fluid.

For viscous drag C_D is inversely proportional to U, and D_α is directly proportional to U. The assumption of viscous drag is only realistic for low Reynold's numbers. Since Reynold's numbers as large as 10^4 are reached in practical damper designs, it was necessary to determine the C_D - R_d relations for different gap ratios λ_g. An analytical and experimental program (Section 8) was undertaken with this objective in mind. The C_D - R_d curves of immediate interest to us are plotted in Figures 8-1, 8-8, and 8-9. For $\lambda_g < 0.04$ the theory and the experimental results are in close agreement. For convenience we have used the theoretical (solid line) curves in our calculations.

The procedure for selecting λ_g and the coefficients μ_i is described as follows:

(1) Compare damper performance for different μ_1, with μ_2 and μ_3 set in equal to zero, using the digital program.

(2) Select the near optimum μ_1 and note the maximum ball velocity. Calculate C_1 and plot $D_\alpha = C_1 U$ to the maximum value for U.

(3) Select a gas at a given temperature. This fixes ρ and μ.

(4) Using Figures 8-1, 8-8 and 8-9, select the gap ratio λ_g and generate the actual (nonlinear) D_α curve which approximately fits the linear D_α curve.

(5) Select C_1, C_2, and C_3 which provide the best cubic fit to the actual nonlinear D_α curve. Convert the C_i to the μ_i for use in the computer program.

(6) Compare damper performance using the linear and the cubic drag laws.

This procedure was followed in this report. The performance differences between the linear and cubic damping law proved to be small in all the cases. Furthermore, we found the damper performance to be relatively insensitive to the μ_i; deviations on the order of the coefficients being acceptable.

There is a practical lower limit on λ_g, near 0.003, because of fabrication difficulties. If this limit is approached, it would be desirable to use a more viscous fluid or to pressurize the gas. This was unnecessary in the cases considered.

Again consider the vehicle-damper combination shown in Figure 2-9. The run shown in Figures 2-10 and 2-11 was based on the linear drag law $D_\alpha = C_1 U$ where $C_1 = 0.075$ lb sec/ft. The maximum ball speed was 13.4 ft/sec. Using air with a density $\rho = 0.00237$ lb sec^2/ft and a kinematic viscosity $\mu = 1.52 \times 10^{-4}$ ft^2/sec, and a gap ratio $\lambda_g = 0.01$, we obtained the nonlinear drag law shown in Figure 2-12. A cubic fit to the nonlinear law also shown in Figure 2-12 is given by $D_\alpha = C_1 U + C_2 U |U| + C_3 U^3$ where $C_1 = 0.04$ lb sec/ft, $C_2 = 0.004$ lb sec^2/ft^2 and $C_3 = 2 \times 10^{-5}$ lb sec^3/ft^3. The corresponding values $\mu_1 = 1.07$ sec^{-1}, $\mu_2 = 0.245$ and $\mu_3 = 0.0028$ sec were used to generate the vehicle-damper performance curves in Figures 2-13 and 2-14. The differences between these results and those given in Figures 2-10 and 2-11 are negligible.

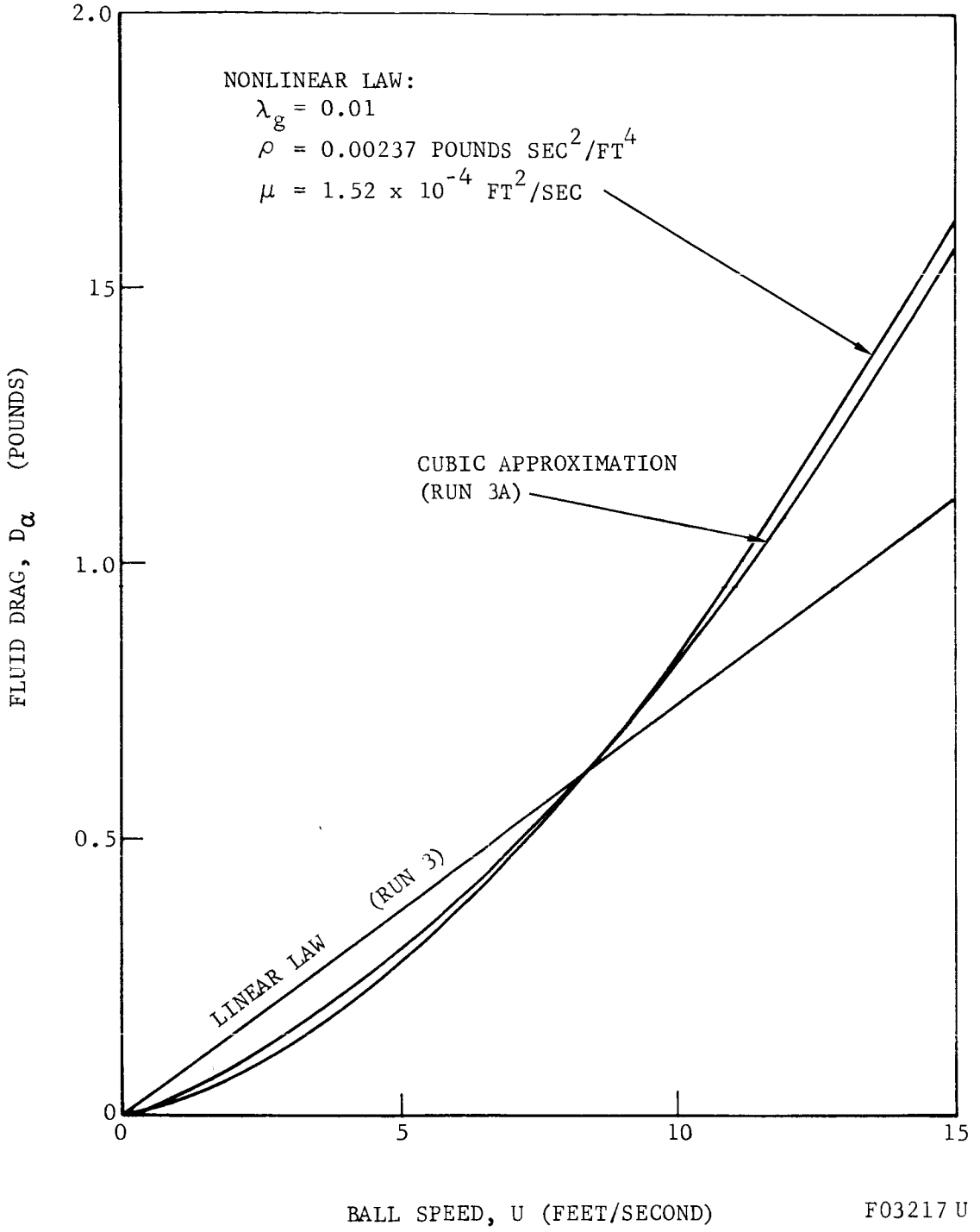

FIGURE 2-12. LINEAR AND NONLINEAR FLUID DRAG LAWS

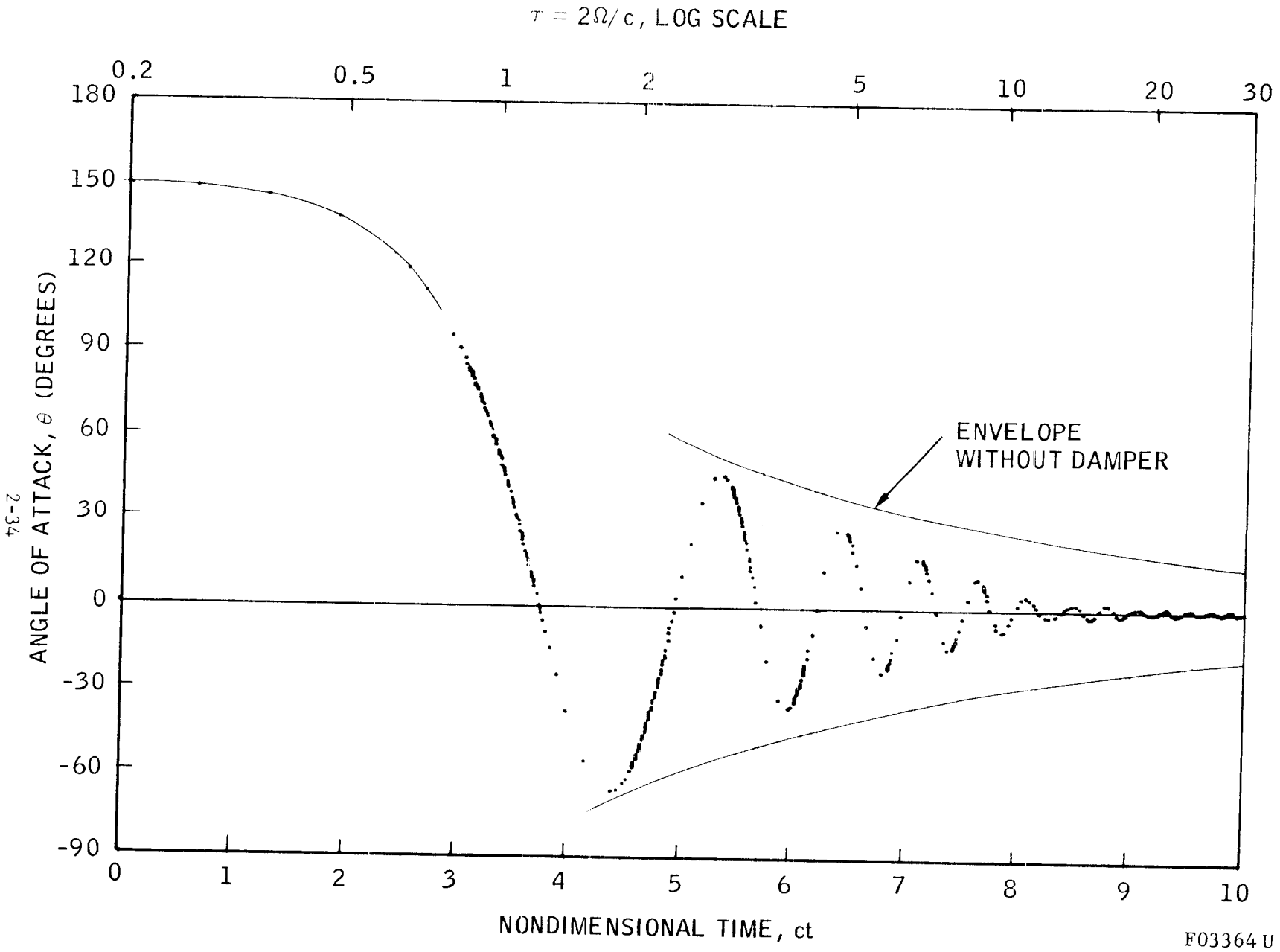

FIGURE 2-13 ANGLE OF ATTACK HISTORY FOR A SPHERE WITH A NONLINEAR DAMPING LAW

($k = 0.0698$, $b^2 = 1$, $\lambda = 1$, $\mu_1/c = 1.07$, $\mu_2/c^2 = 0.245$, $\mu_3/c^3 = 0.0028$, RUN 3A)

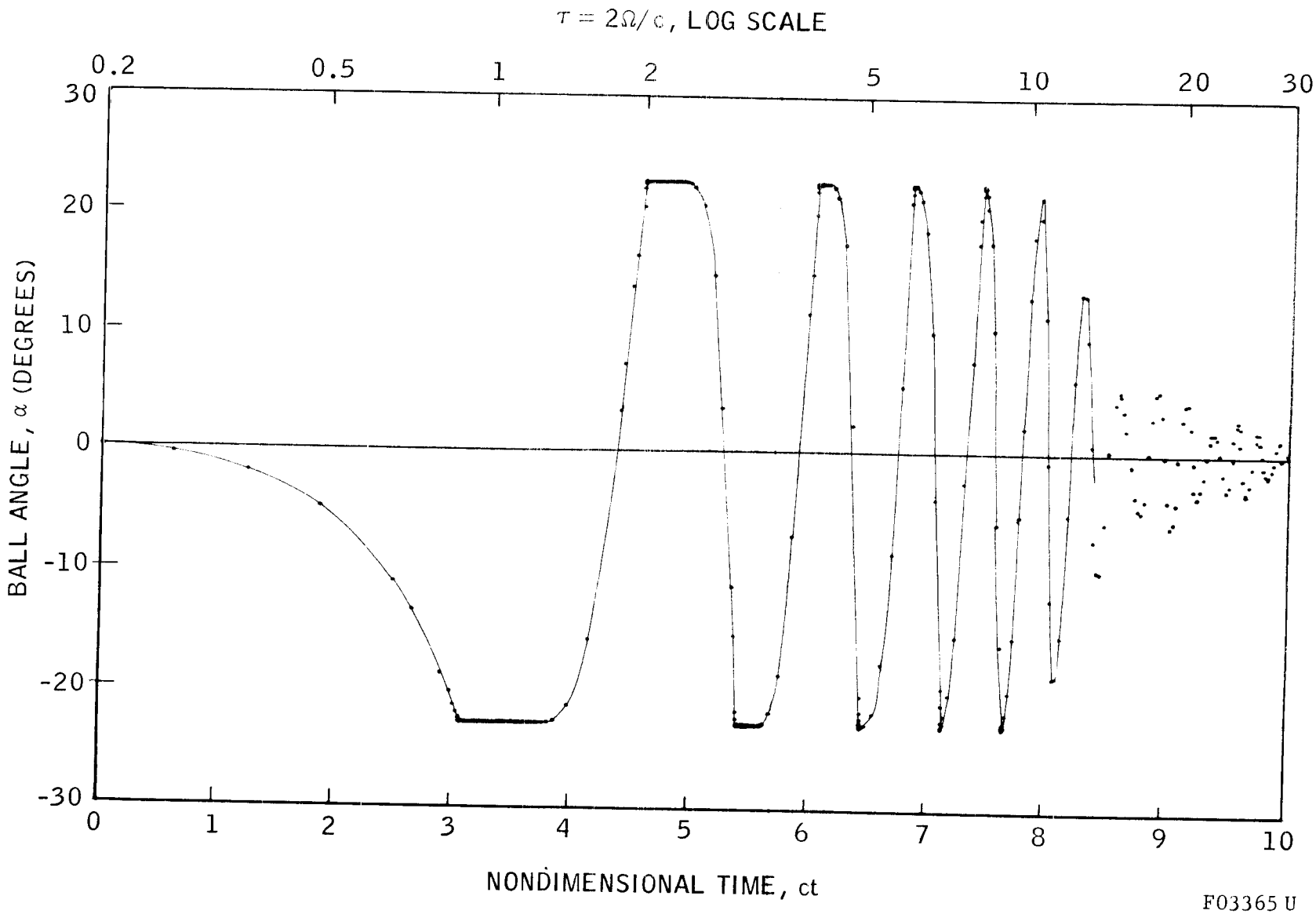

F03365 U

FIGURE 2-14 BALL OSCILLATION (RUN 3A)

SECTION 3

AMES MARS ATMOSPHERIC PROBE

3.1 VEHICLE DESCRIPTION AND ENTRY DYNAMICS

In 1965, A. Seiff and D. E. Reese Jr., of Ames Research Center (NASA) described the use of a spherical entry body as probe for determining the characteristics of the Mars atmosphere.* The "Ames probe" has since evolved into the design shown in Figure 3-1. The vehicle mass M is 1.18 slugs, the roll moment of inertia J is 0.624 slug ft^2 and the pitch (and yaw) moment of inertia I is 0.472 slug ft^2.

The axial force coefficient C_A, the normal force coefficient C_N, and the moment coefficient C_m with respect to the vehicle mass center are plotted as functions of the angle of attack θ in Figures 3-2a, b, and c, respectively. The reference area S is 5.07 ft^2 and the reference length ℓ is 2.54 ft. The dashed curves in these figures are the trigonometric approximations

$$C_A = 1.31 - 1.184 \sin\theta + 0.072 \sin 2\theta + 0.3233 \sin 3\theta - 0.05 \sin 4\theta$$

*Seiff, A., and Reese, D. E., Jr., "Defining Mars' Atmosphere - A Goal for Early Missions," Astronautics and Aeronautics, February, 1965, pp 16-21.

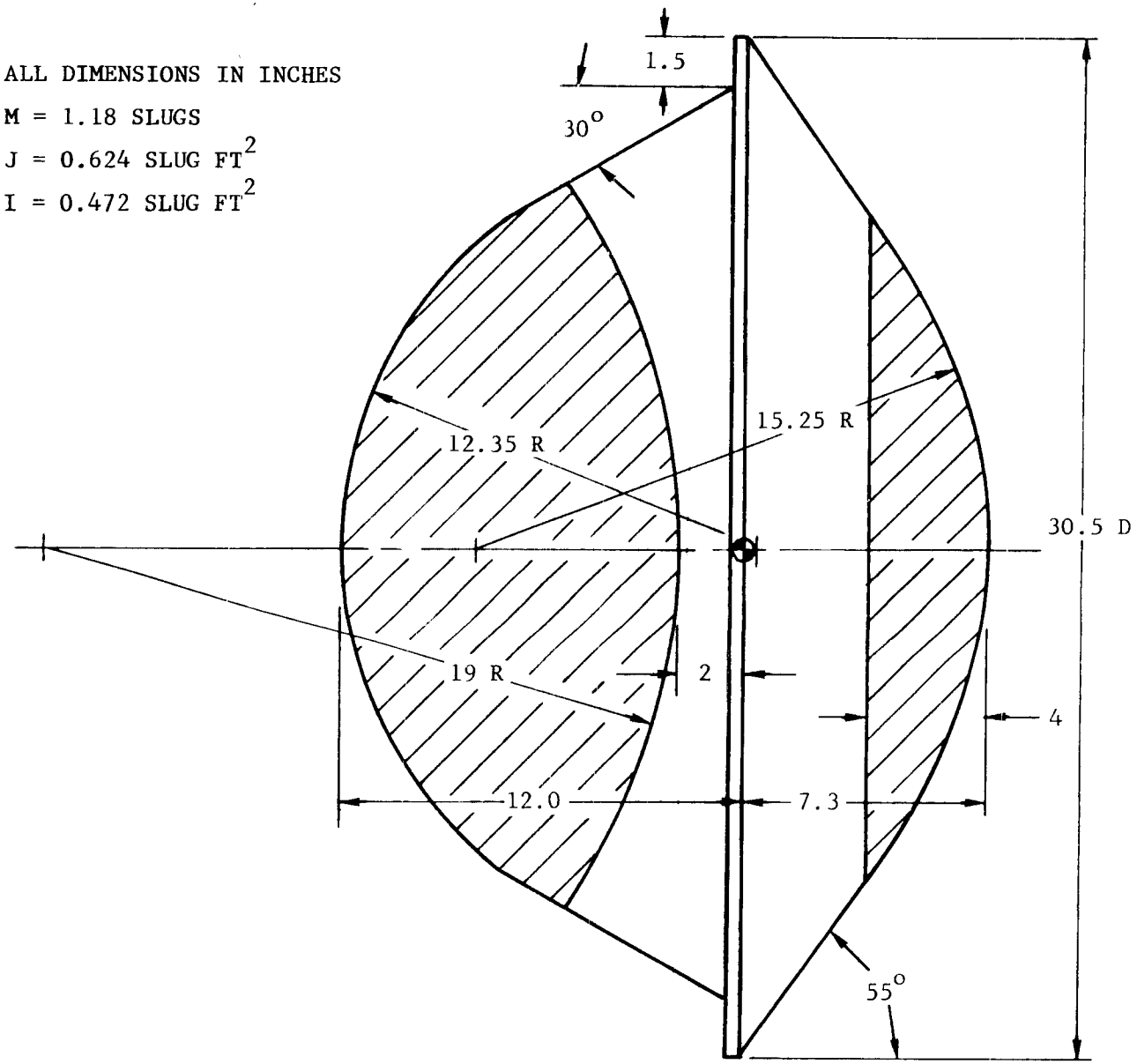

F02920 U

FIGURE 3-1. AMES MARS ATMOSPHERIC PROBE GEOMETRY

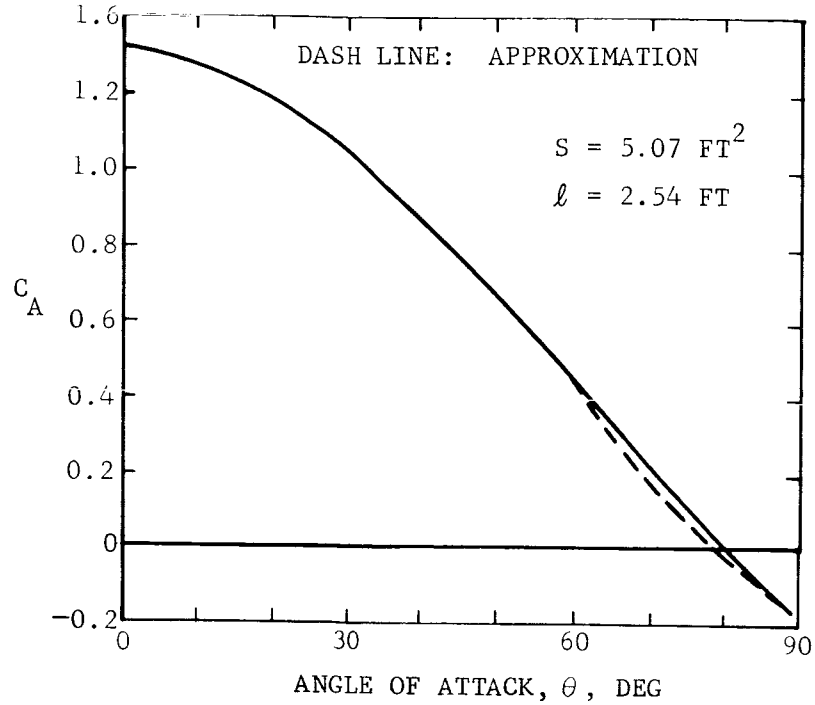

FIGURE 3-2a. AXIAL FORCE COEFFICIENT (AMES PROBE)

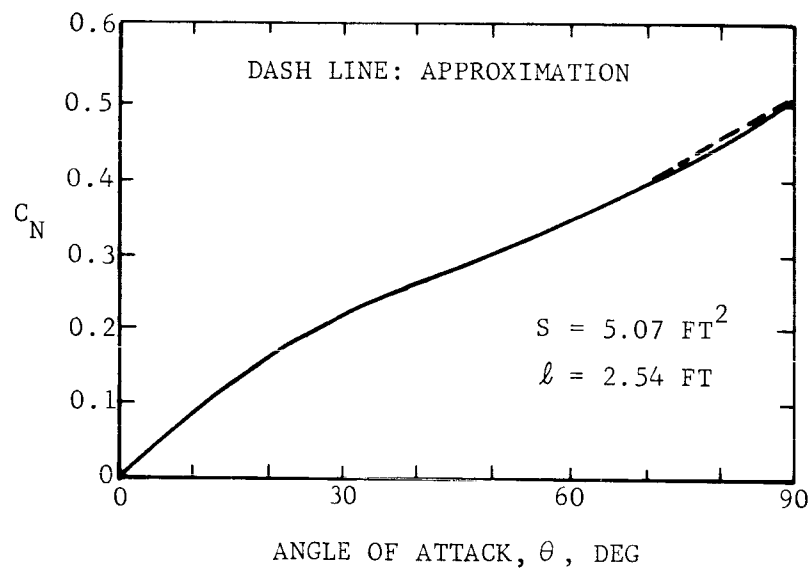

F02928 U

FIGURE 3-2b. NORMAL FORCE COEFFICIENT (AMES PROBE).

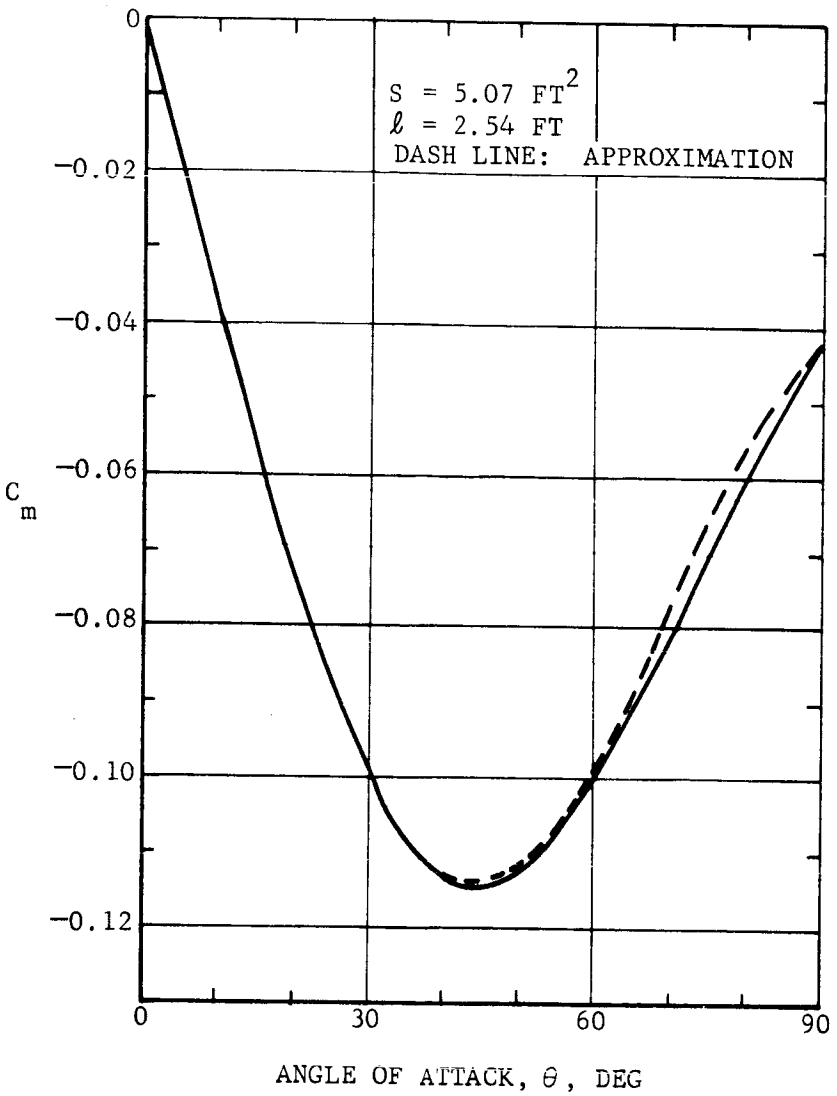

F02927 U

FIGURE 3-2c. MOMENT COEFFICIENT WITH RESPECT TO THE MASS CENTER (AMES PROBE)

$$C_N = 0.4485 \sin\theta - 0.0595 \sin 3\theta + 0.06 \sin 4\theta$$

$$C_m = -0.116 \sin\theta + 0.019 \sin 2\theta - 0.073 \sin 3\theta + 0.0185 \sin 4\theta$$

used in the computer program.

The contractor has furnished two models for the Mars atmosphere; a minimum density "A" atmosphere with surface density $\rho_* = 1.3 \times 10^{-5}$ slug/ft^3 and scale height $\beta^{-1} = 21{,}300$ ft, and a maximum density "B" atmosphere with surface density $\rho_* = 6 \times 10^{-5}$ slug/ft^3 and scale height $\beta^{-1} = 45{,}900$ ft. The density profiles for the A and B model atmospheres along with NASA Model 3 atmosphere (from NASA TN D2525) are shown in Figure 3-3.

Three entry conditions were considered:

(1) A direct entry into the A atmosphere with
$v_o = 21{,}300$ ft/sec, $\gamma_o = 90$ degrees and,
$h_o = 291{,}080$ ft.

(2) An indirect entry into the B atmosphere with
$v_o = 21{,}300$ ft/sec, $\gamma_o = 50$ degrees and,
$h_o = 746{,}820$ ft.

(3) An orbital entry into the A atmosphere with
$v_o = 12{,}000$ ft/sec, $\gamma_o = 20$ degrees, and
$h_o = 315{,}000$ ft.

All three entry conditions satisfy the relation $2\Omega/c = 1$.

The vehicle spins at 30 rpm and has an initial angle of attack of 40 degrees. The velocity v, the dynamic pressure q, and the angle of attack θ are plotted as functions of altitude in Figures 3-4, 3-5, and 3-6 for the above three entry conditions. The angle of attack is seen to converge with increasing q and diverge with decreasing q.

The use of a passive damper to accelerate the convergence of the θ envelope is examined in Paragraph 3.2.

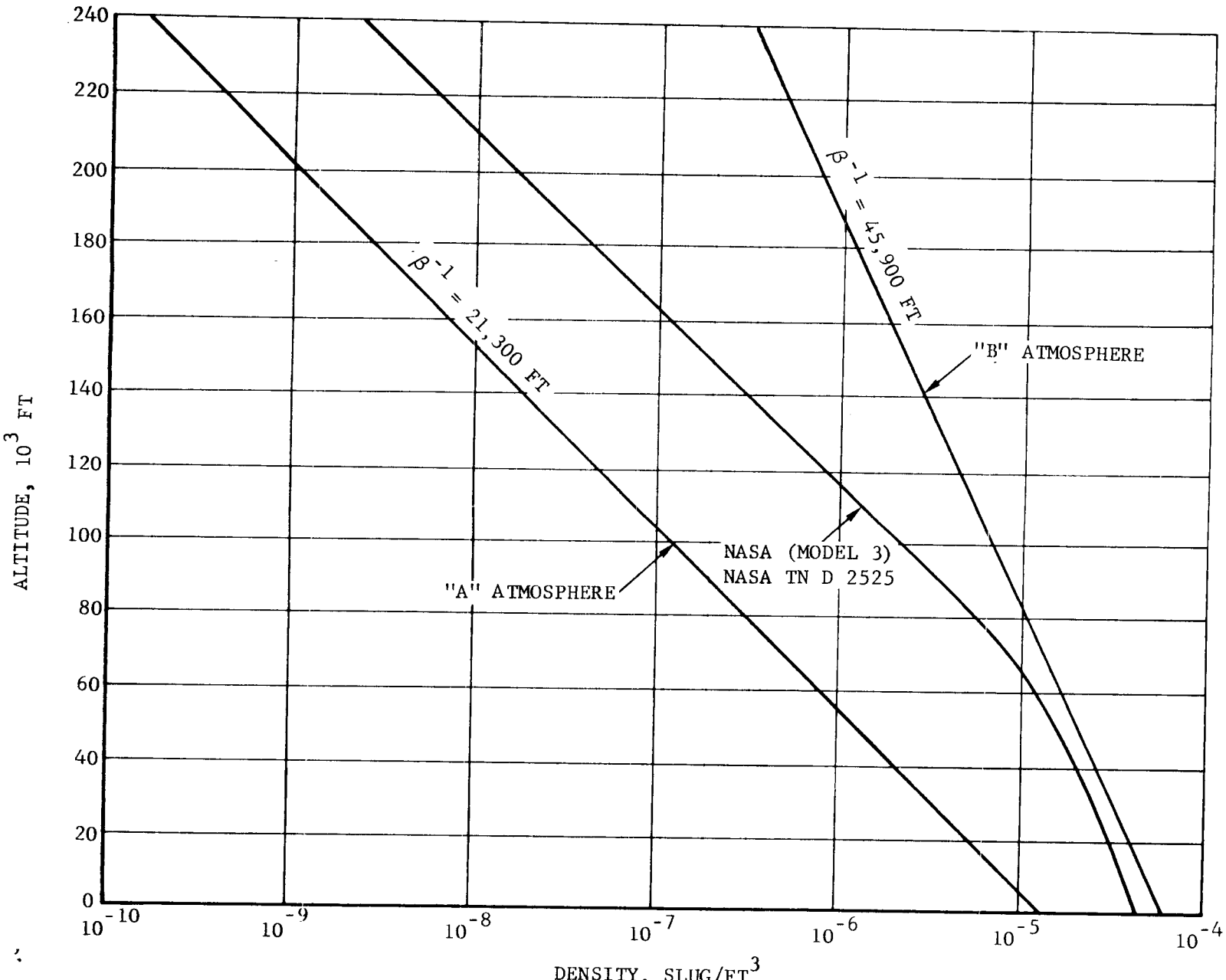

F02924 U

FIGURE 3-3. MODELS FOR THE MARS ATMOSPHERE

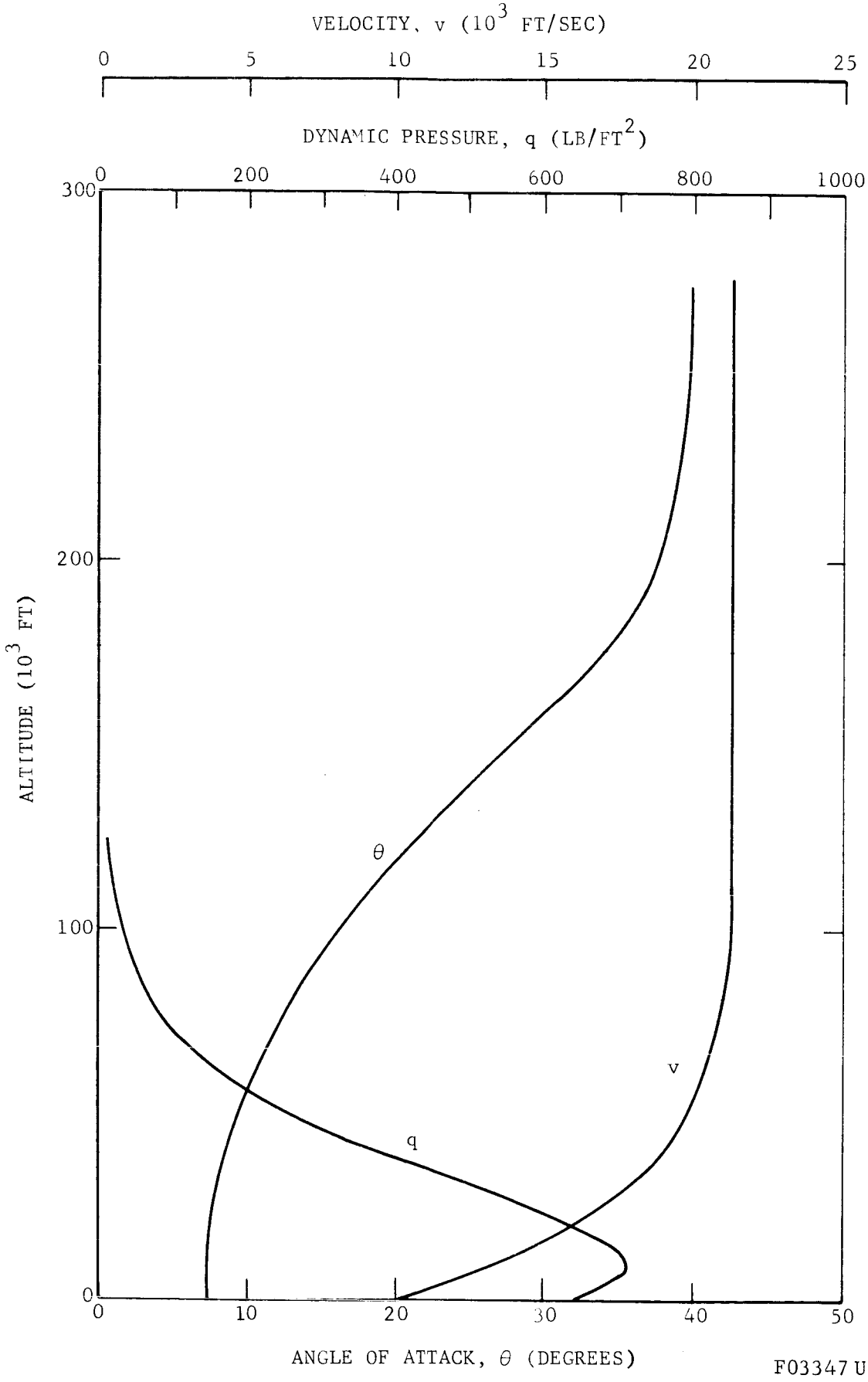

FIGURE 3-4. VELOCITY, DYNAMIC PRESSURE AND ANGLE OF ATTACK PROFILES FOR A DIRECT ENTRY INTO THE ATMOSPHERE

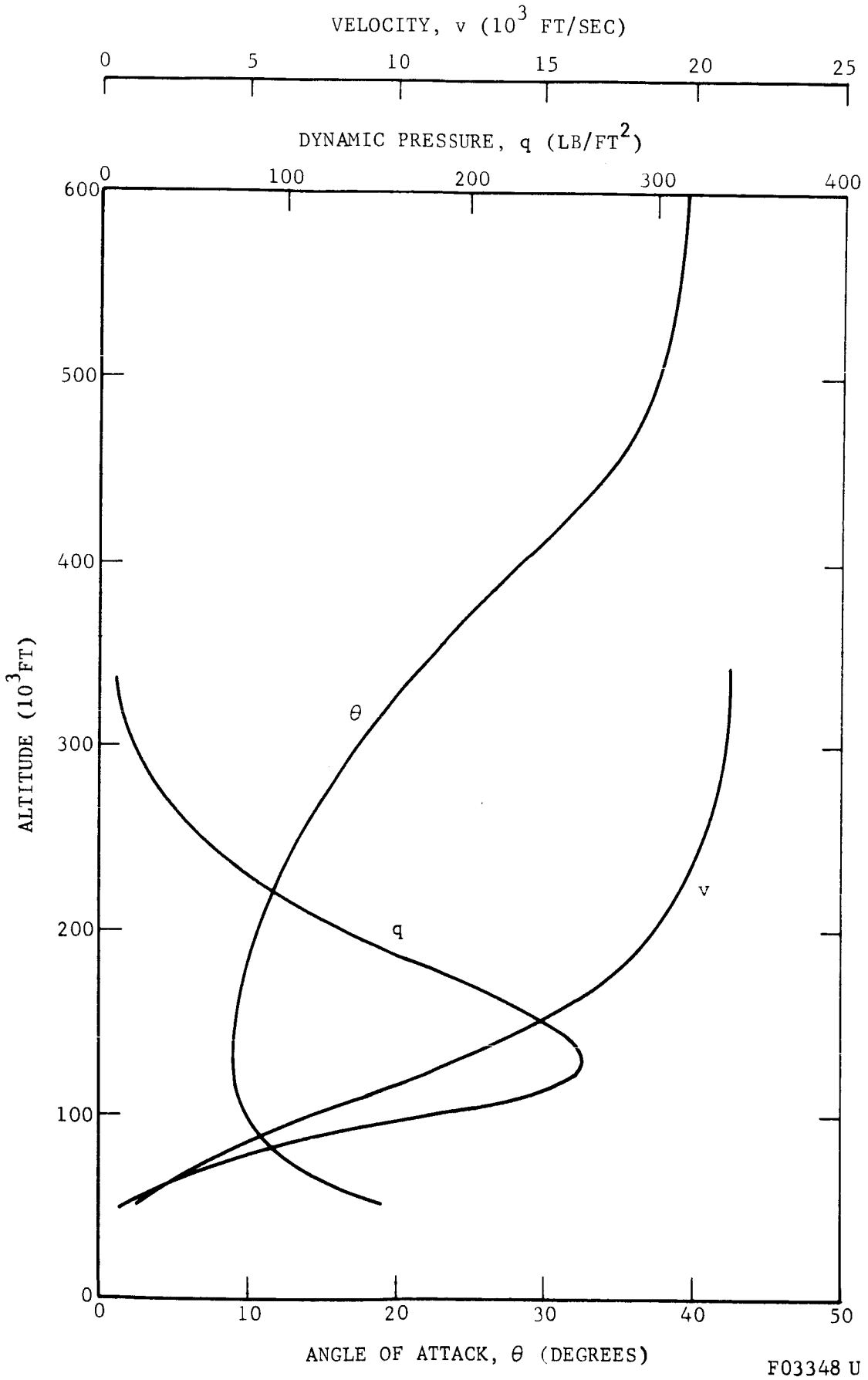

FIGURE 3-5. VELOCITY, DYNAMIC PRESSURE, AND ANGLE OF ATTACK PROFILES FOR AN INDIRECT ENTRY INTO THE ATMOSPHERE

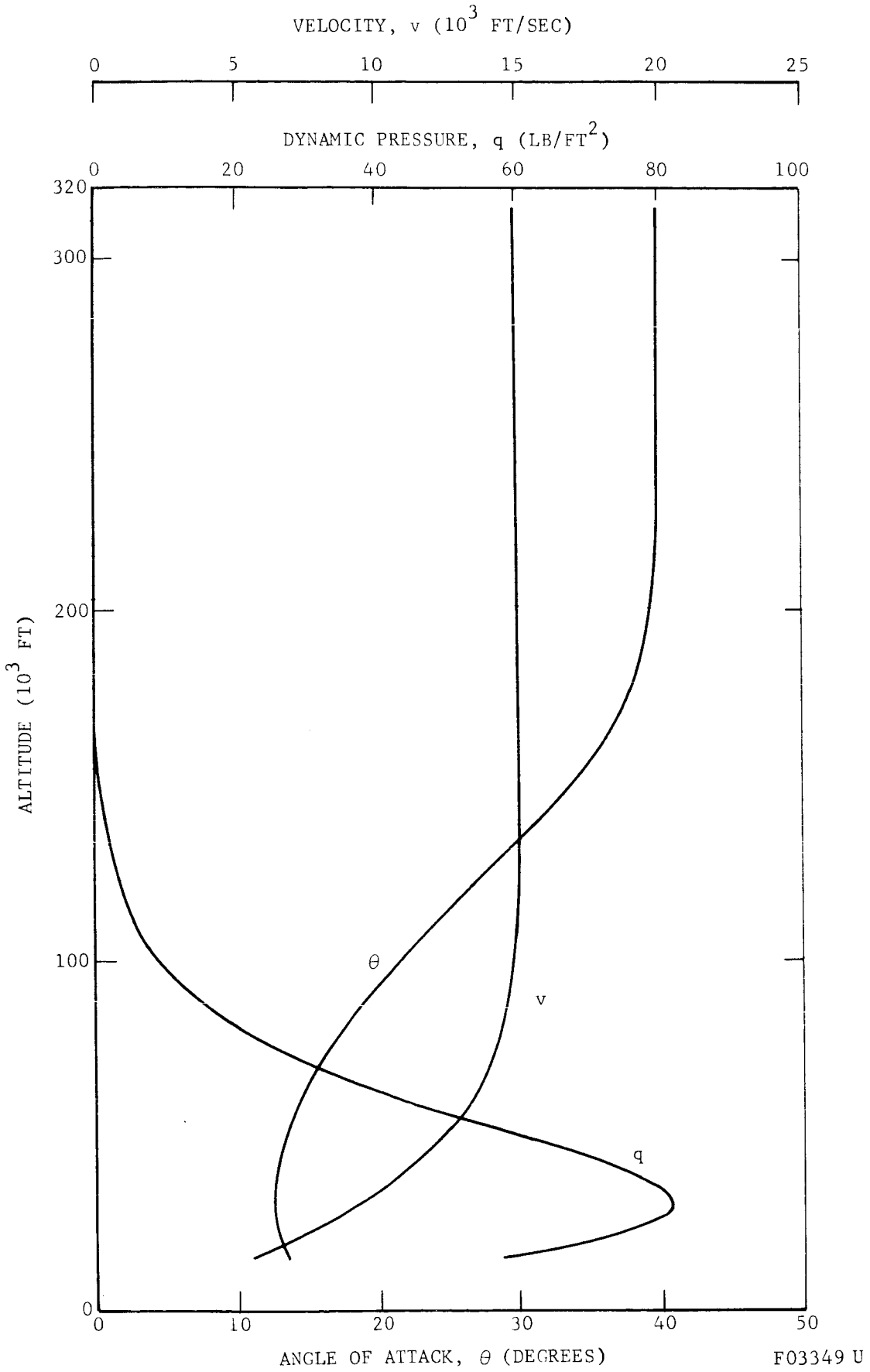

FIGURE 3-6. VELOCITY, DYNAMIC PRESSURE, AND ANGLE OF ATTACK PROFILES FOR ORBITAL ENTRY INTO THE ATMOSPHERE

3.2 DAMPER DESIGN AND TRADEOFFS

3.2.1 NOMINAL DESIGN AND DAMPER LOCATION

The nominal damper design for the Ames probe has two tuned dampers orthogonally mounted with respect to the vehicle centerline. Both dampers are identical. A full-scale drawing of one damper is shown in Figure 3-7. A 1.52 inch tungsten-carbide ball moves along a mean path radius $R = 7.05$ inches in a tube which length is a little more than 8 inches. The angle limit α_L is 25 degrees and the end restraints are inelastic ($\epsilon = 0$).

The estimated weight of each damper is 1.22 pounds. The ball weighs 1 pound based on a density of 0.545 lb/in.^{3}. An 8 inch length of 0.03 inch aluminum tubing weighs 0.17 pound and the end stops weigh 0.05 pound.

The nominal design has an inertia ratio $k = 0.0227$ and a frequency ratio $b^2 = 0.191$. The near optimum linear damping coefficient μ_1 was found to be 2 sec^{-1}.

Four damper locations, specified by D = 2.74, 7.05, 11.05, and 15.7 inches, are pictured in Figure 3-7. In Paragraph 2.1.3 we showed that the damper performance is related to the effective inertia ratio

$$k^* = \frac{7}{5} k \left[\frac{5}{7}(\lambda - 1) + b_n^2\right]^2 \qquad (2\text{-}33)$$

where $b_n^2 = 0.437$ for the Ames probe. For the nominal damper design and the four damper locations we have

D = 2.74 in.	$\lambda = 0.388$	$k^* = 0$
D = 7.05 in.	$\lambda = 1$	$k^* = 0.00617$
D = 11.05 in.	$\lambda = 1.565$	$k^* = 0.0224$
D = 15.70 in.	$\lambda = 2.27$	$k^* = 0.057$

Linear analysis predicts that a damper at the forward location ($\lambda = 0.388$) would have no effect, and that damper performance improves as the damper is moved rearward. The nominal damper location in this study is defined

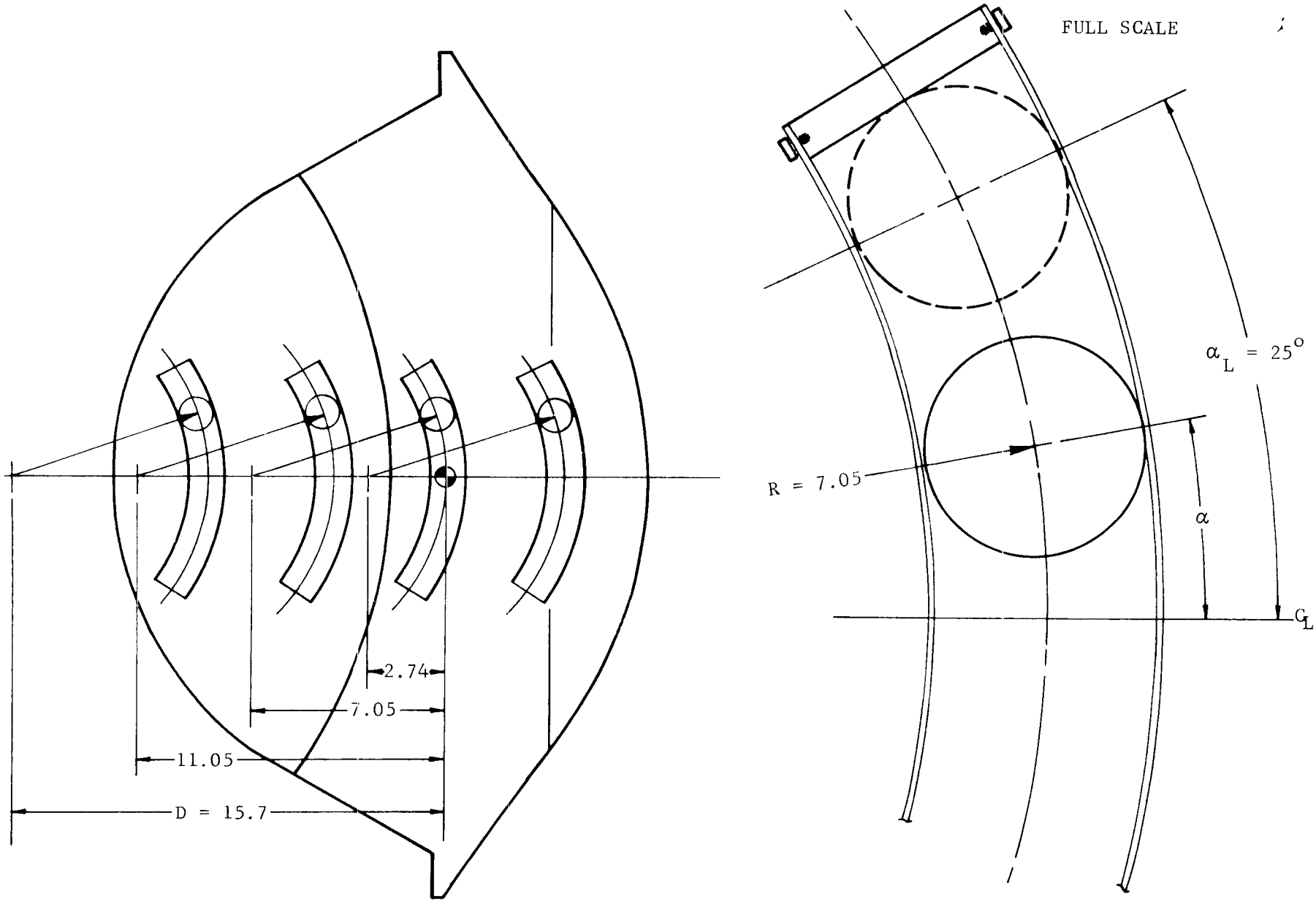

FO2922 U

FIGURE 3-7. DAMPER DESIGN FOR THE AMES PROBE AT FOUR LOCATIONS

by $\lambda = 1.565$. There is some question whether more rearward locations could be adapted.

In a two-tube design, one damper must be forward of the other damper, that is, $\lambda_1 \neq \lambda_2$. However, in all but one run, we made the approximation that $\lambda_1 = \lambda_2$. In the one exception (Run 25) we set $\lambda_1 = 1.565$ and $\lambda_2 = 1.765$ to provide the proper tube offset. The difference between Run 25 and the corresponding Run 13 with $\lambda_1 = \lambda_2 = 1.565$ was negligible.

The damper performances at the above four locations are compared in Figure 3-8 for a vertical entry into the A atmosphere. In this figure, the total angle of attack θ is plotted as a function of altitude. These results substantiate that performance improves as the damper is moved rearward.

The ball motions α_1 and α_2 are plotted as functions of altitude in Figures 3-9 (a through d). The balls leave their limits ($\alpha_L = 25$ degrees) at approximately 160,000 feet and do not return to the stops, which indicates that the choice of the impact parameter ϵ is academic. The ball motions are larger for larger λ, as would be expected.

Returning to Figure 3-8, we note that the vehicle undergoes a large amplitude oscillation above 160,000 feet. Furthermore, the amplitude of the oscillation varies directly with λ and changes phase at $\lambda = 1$. This wobbling is due to the effective principal axis misalignment when the balls are at the limits. The initial amplitudes agree exactly with the predicted free coning motions of an Euler top. This effect can be reduced by reducing λ to 1 or by reducing α_L. Both "fixes" adversely affect the damper performance at low altitudes.

In Paragraph 2.2.2, we commented that roll resonance is a possibility if the balls have not left their stops when the linear pitch frequency ν satisfies the relation

$$\nu^2 = \left(1 - \frac{J}{I}\right) \omega_z^2 \qquad (2\text{-}36)$$

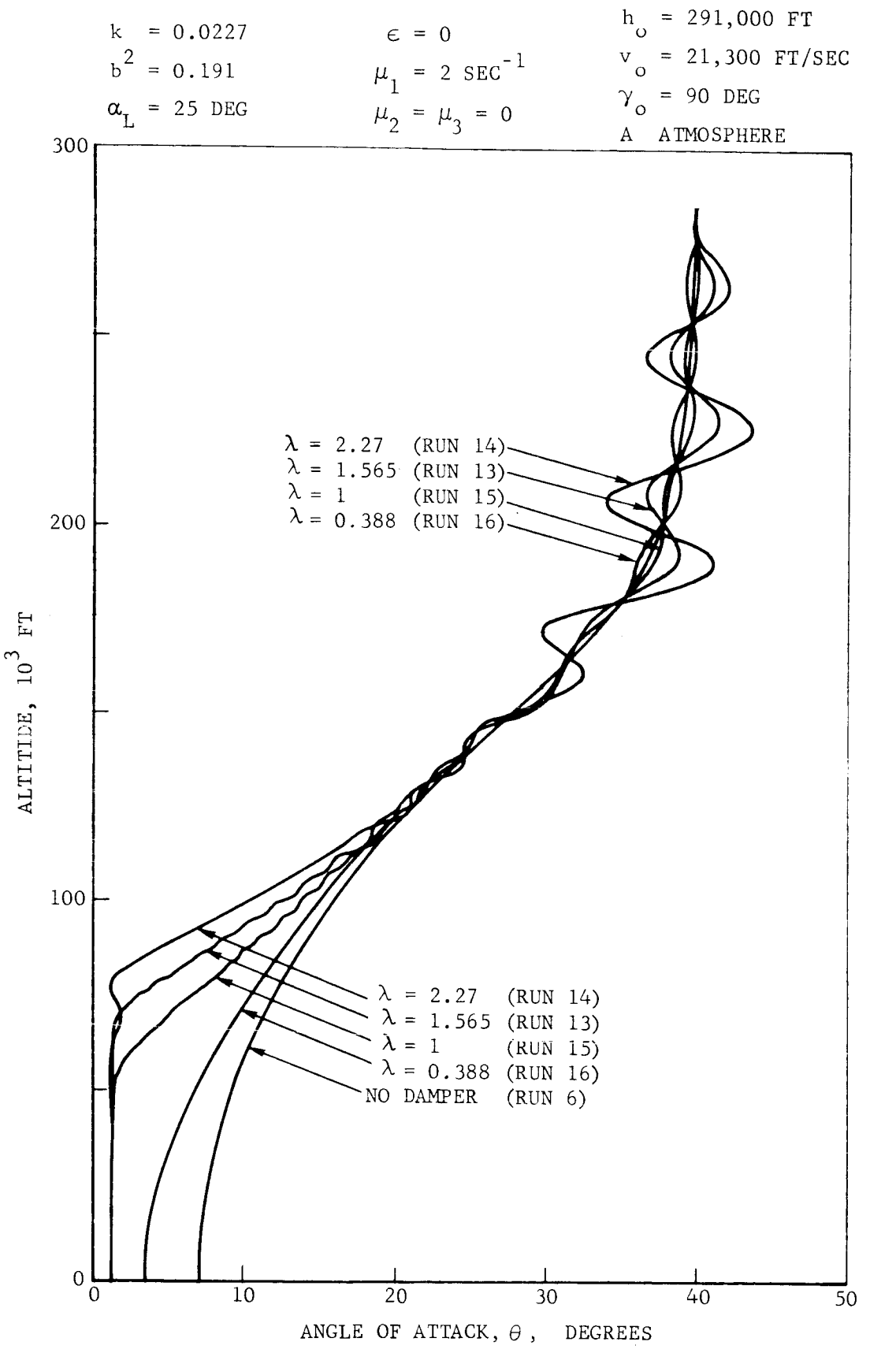

F02923 U

FIGURE 3-8. EFFECT OF VARYING THE DAMPER LOCATION

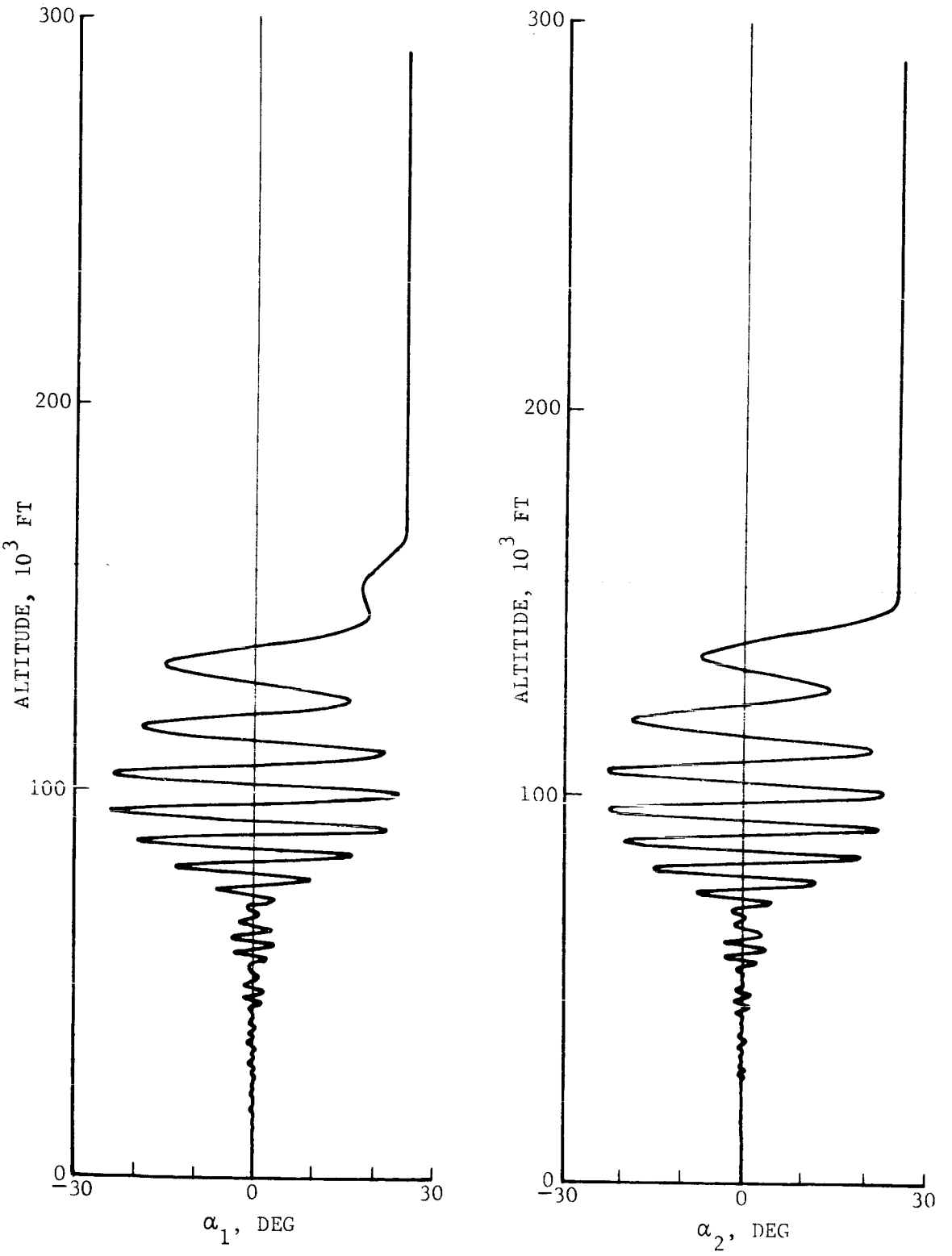

F02921 U

FIGURE 3-9 a. BALL MOTIONS FOR λ = 2.27 (RUN 14)

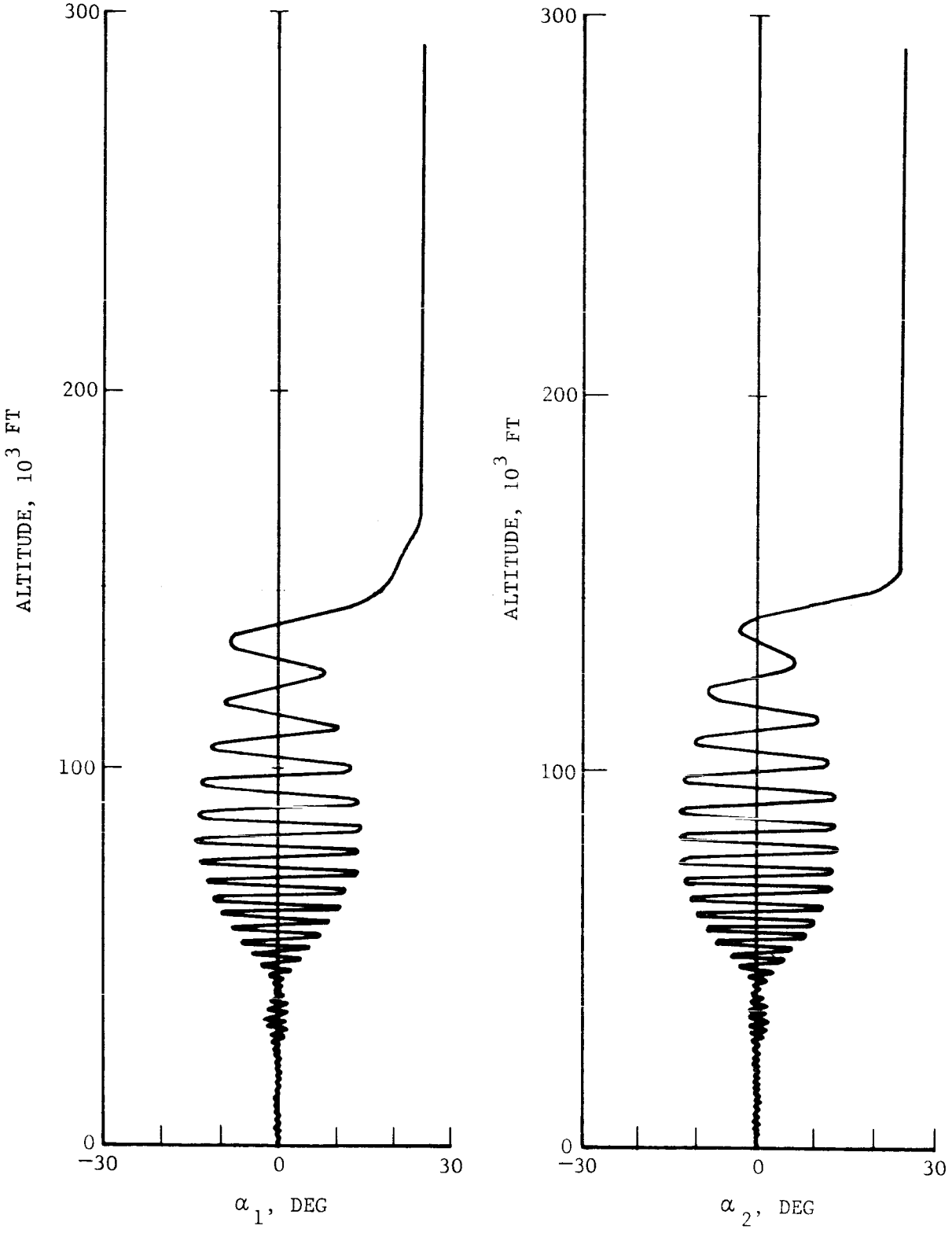

F02938 U

FIGURE 3-9c. BALL MOTIONS FOR λ = 1 (RUN 15)

PRECEDING PAGE BLANK NOT FILMED.

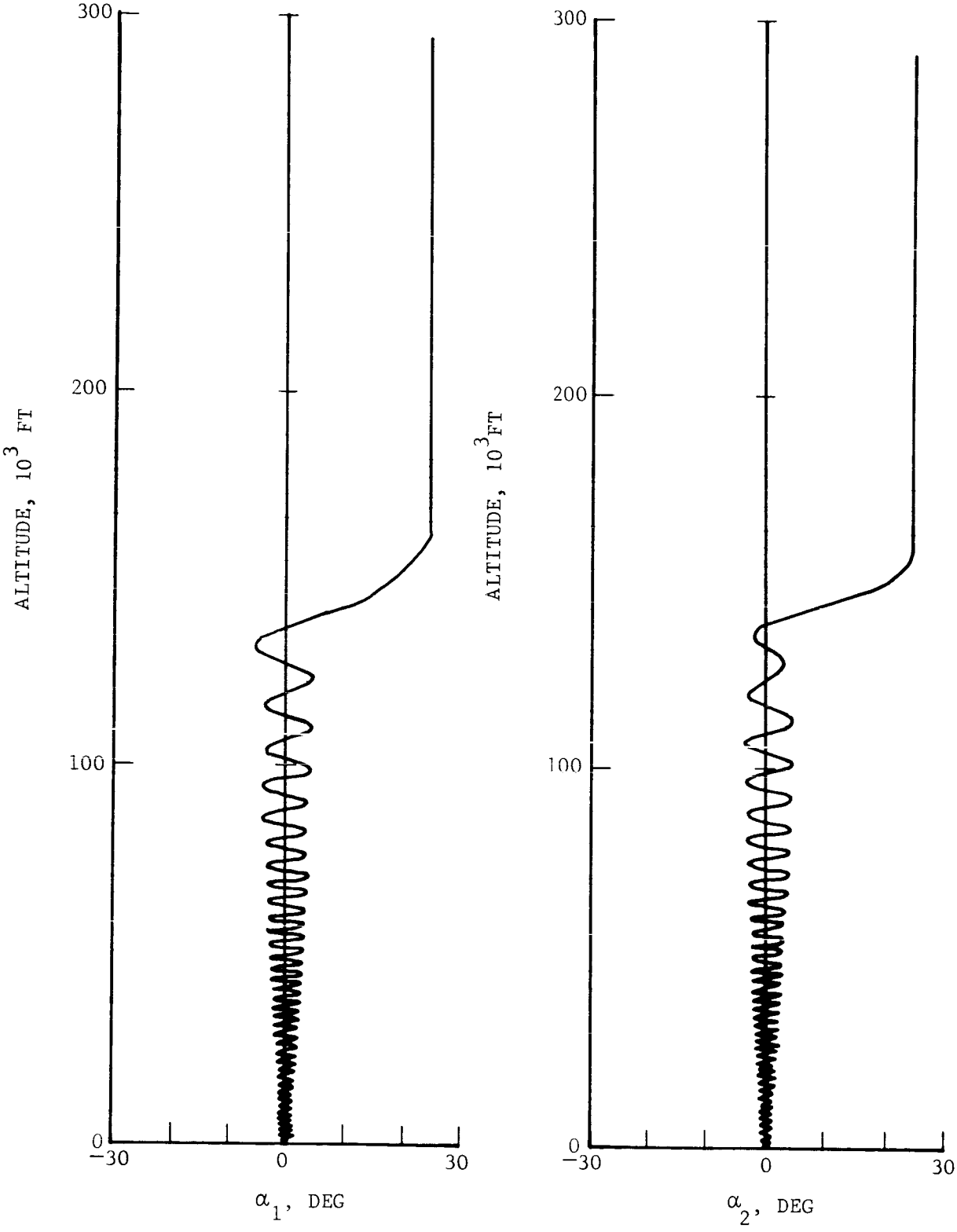

F02937 U

FIGURE 3-9d. BALL MOTIONS FOR λ = 0.388 (RUN 16)

Since only imaginary values of ν satisfy Equation (2-36) when the inertia ratio J/I is greater than 1, we conclude that roll resonance is no problem for the Ames probe.

Figure 3-8 exhibits another striking feature; θ is damped to a trim angle of 1.25 degrees and no farther. The damping of θ to a small trim angle is characteristic of the damper performance on a spinning entry body. When the trim angle is reached, the precession rate $\dot{\phi}$ is rapidly reduced in magnitude. This is illustrated in Figure 3-10 where the envelope of $\dot{\phi}$ is plotted as a function of altitude for Run 13. Meanwhile, the spin rate ω_z remains nearly constant during entry.

3.2.2 EFFECT OF DAMPER CURVATURE

The mean path radius R for the nominal "tuned" damper is 7.05 inches. The effects of doubling and halving R are examined in the following. A long radius tube with R = 14.1 inches and a short radius tube with R = 3.525 inches are shown (in slightly reduced scale) in Figure 3-11. The angle limits, α_L = 12.4 degrees for the long radius tube and 59.3 degrees for the short radius tube, were specified so that the maximum ball excursion R sin α_L from the symmetry axis is the same as for the nominal design. All other parameters were held fixed with respect to Run 13.

The angle of attack profiles for the long (Run 31), tuned (Run 13) and short (Run 32) radii tubes are plotted in Figure 3-12. The corresponding values for k, b^2, λ, and α_L are listed above the figure. The importance of tuning is dramatically illustrated in this figure.

The ball motions for Runs 31 and 32 are shown in Figures 3-13 (a and b).

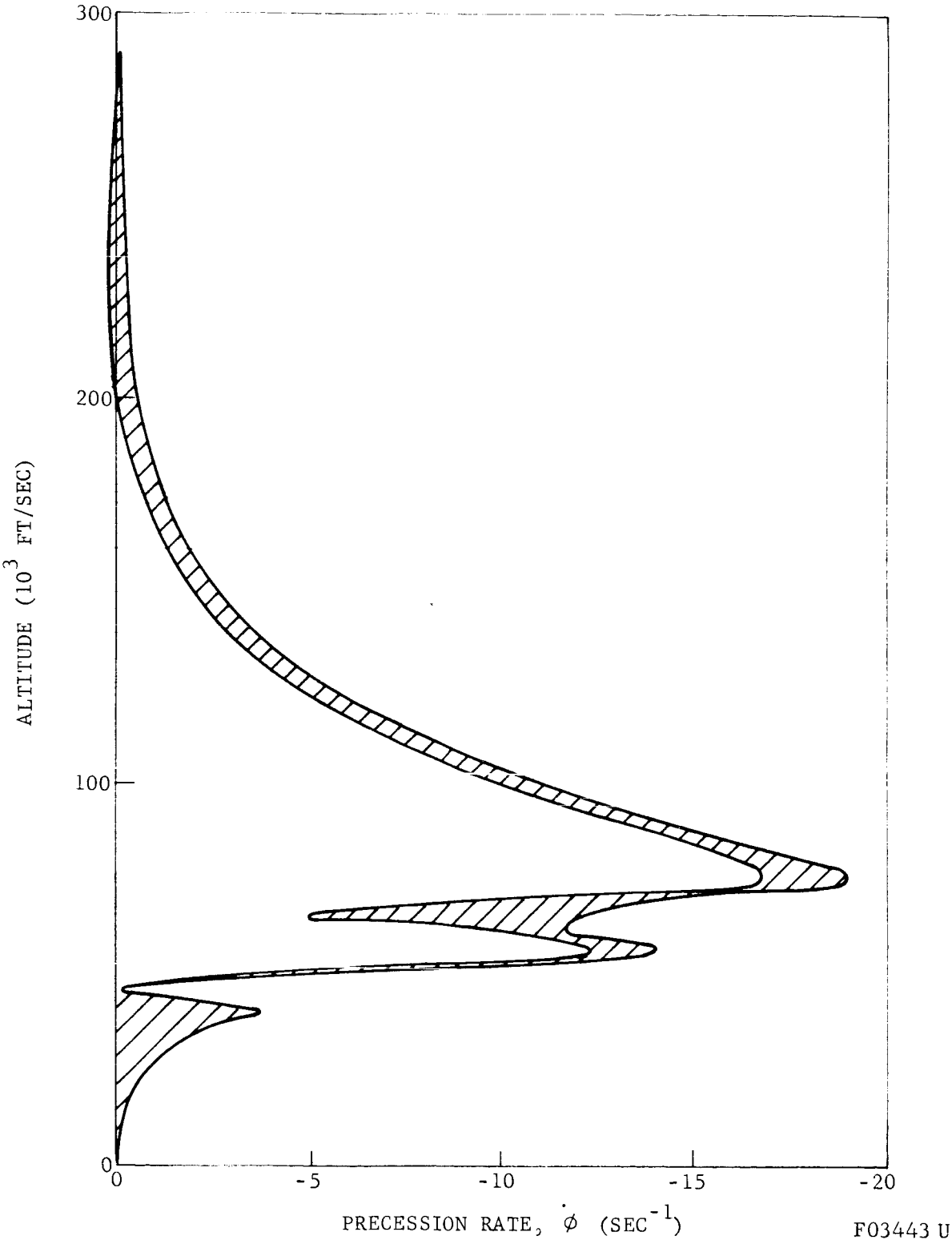

FIGURE 3-10. PRECESSION RATE ENVELOPE (RUN 13)

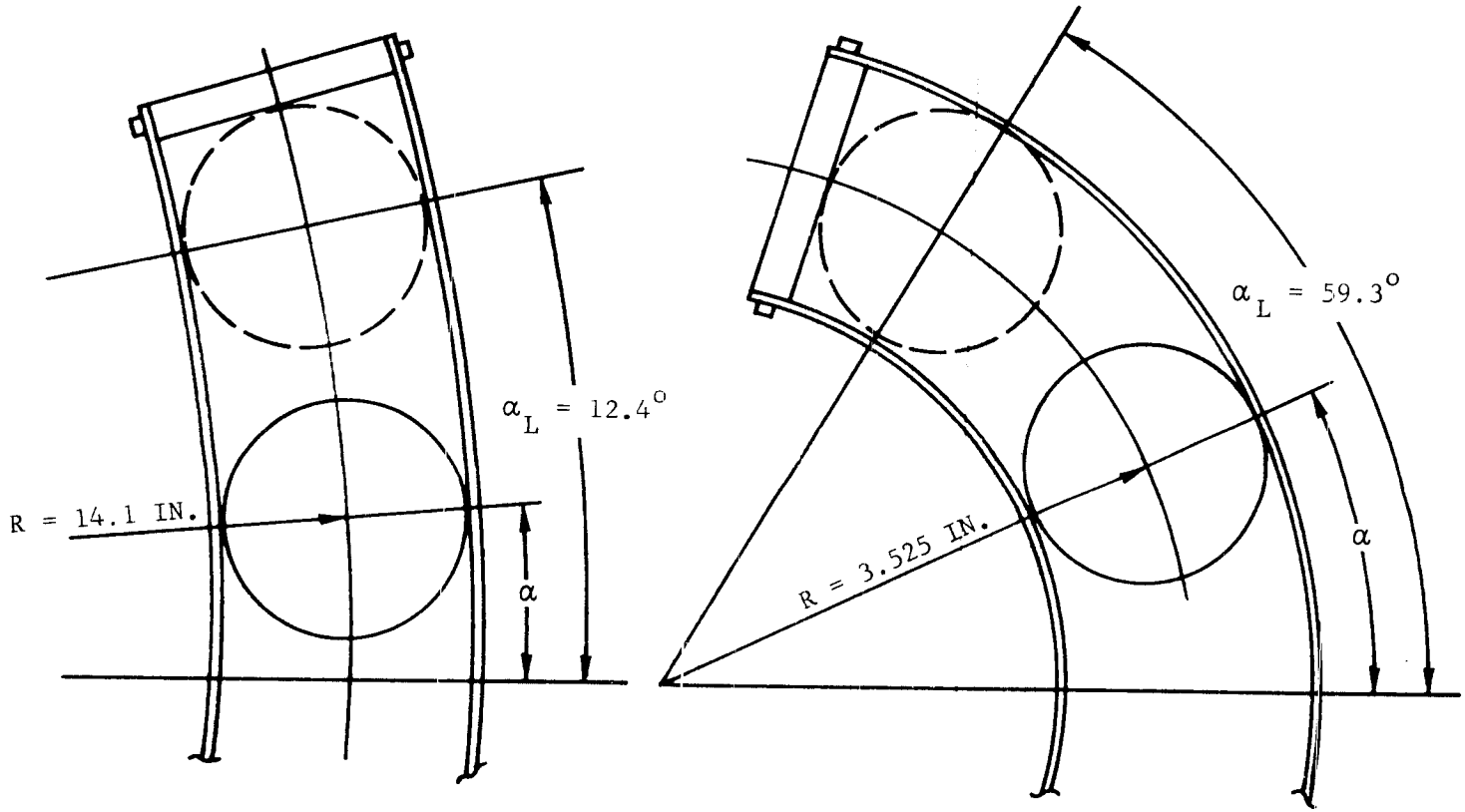

a) LONG RADIUS TUBE

b) SHORT RADIUS TUBE

F03350 U

FIGURE 3-11. LONG AND SHORT RADII CURVATURE TUBES

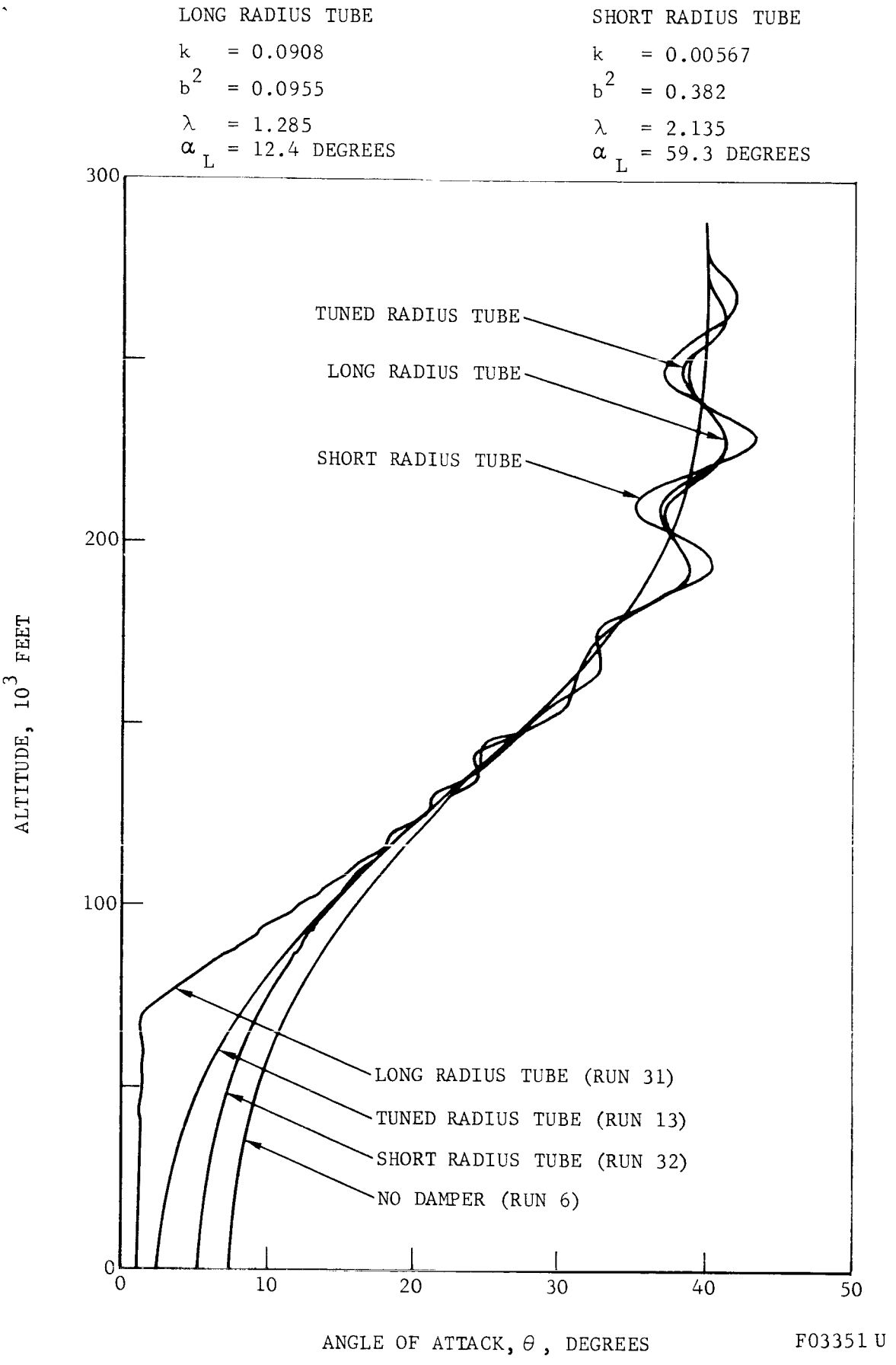

FIGURE 3-12. EFFECT OF TUBE RADIUS OF CURVATURE

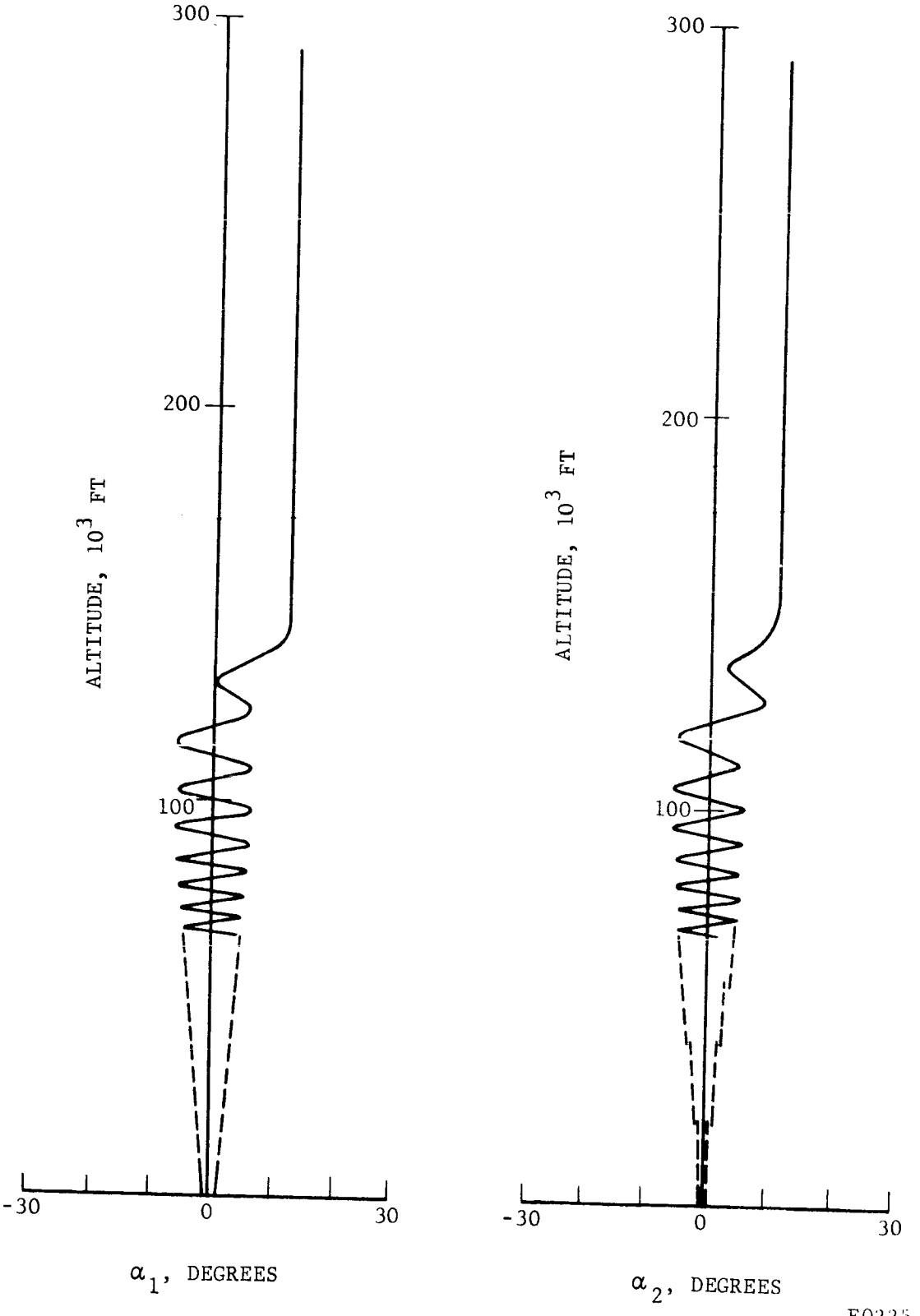

FIGURE 3-13a. BALL MOTIONS FOR LONG RADIUS TUBE (RUN 31)

F033524

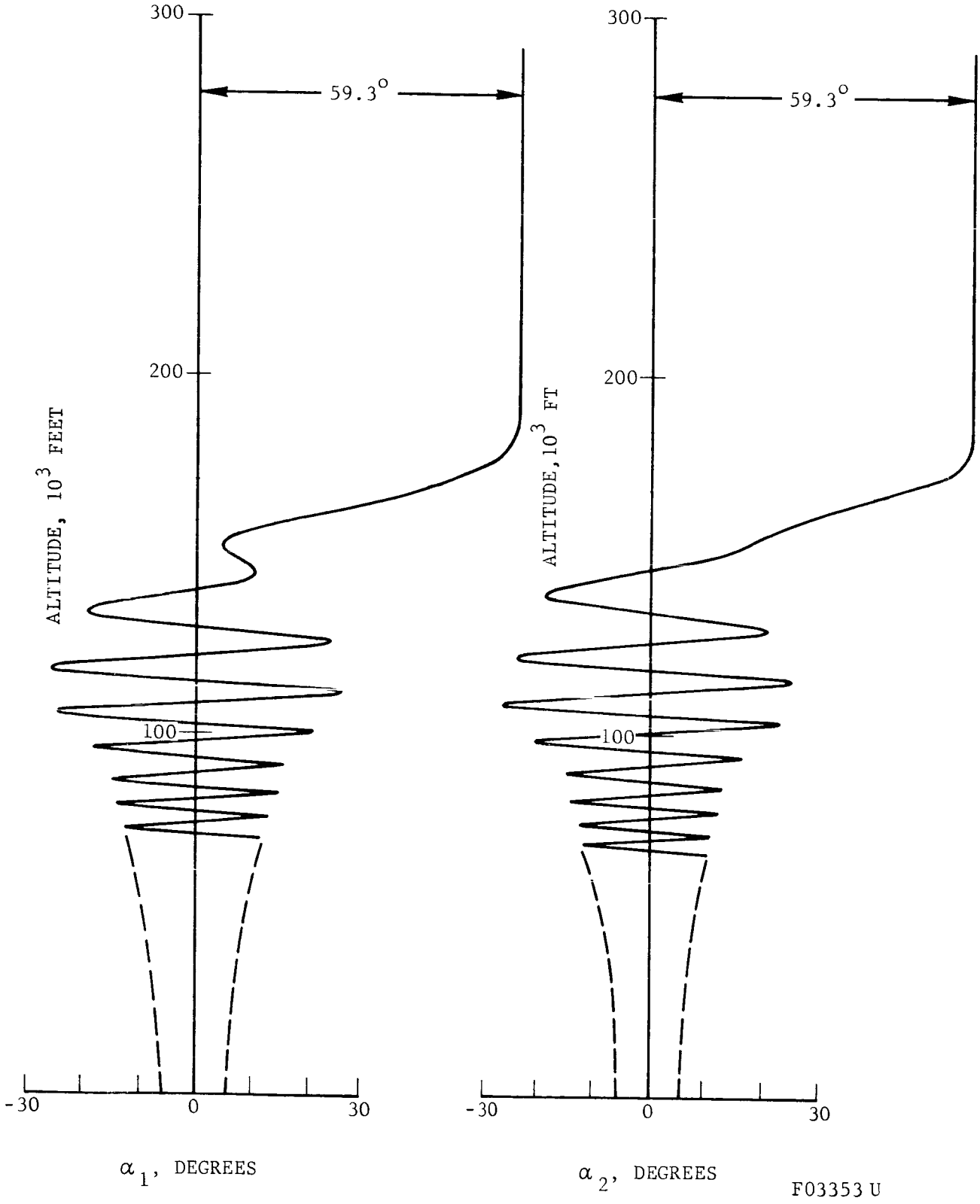

FIGURE 3-13b. BALL MOTIONS FOR SHORT RADIUS TUBE (RUN 32)

3.2.3 FLUID DRAG PERTURBATIONS

The effect of varying the linear damping coefficient μ_1 is illustrated in Figure 3-14. With the nominal value, $\mu_1 = 2\ \text{sec}^{-1}$, θ reaches a trim angle of 1.25 degrees at 68,000 feet. When μ_1 is doubled, θ reaches a slightly smaller trim angle of 1.10 degrees but at a lower altitude, 57,000 feet. The only effect of halving μ_1 is to increase the trim angle to 2 degrees. While these perturbations about the nominal are noticable, they are nonetheless small when compared to the θ solution without a damper. The ball motions for $\mu_1 = 1\ \text{sec}^{-1}$ and $\mu_1 = 4\ \text{sec}^{-1}$ are shown in Figures 3-15a and b, respectively. As would be expected, the amplitudes of the ball oscillations vary inversely with μ_1.

With the nominal μ_1, the ball reaches a maximum speed U of 3.67 ft/sec. In Figure 3-16 we have plotted:

(1) The nominal linear fluid drag law
$D_\alpha = C_1\ U$, where $C_1 = 0.174$ lb sec/ft
for ball speeds up to 4 ft/sec.

(2) The nonlinear fluid drag law for air and a gap ratio $\lambda_g = 0.0195$. The method for obtaining this curve is described in Paragraph 2.2.3.

(3) A cubic approximation to the nonlinear drag law based on the equation

$$D_\alpha = C_1\ U + C_2\ U|U| + C_3\ U^3$$

where $C_1 = 0.06591$ lb sec/ft, $C_2 = 0.04624$ lb sec^2/ft^2 and $C_3 = -5.42 \times 10^{-5}$ lb sec^3/ft^3.
The corresponding computer parameters are
$\mu_1 = 0.754\ \text{sec}^{-1}$, $\mu_2 = 0.311$ and
$\mu_3 = -2.14 \times 10^{-4}$ sec.

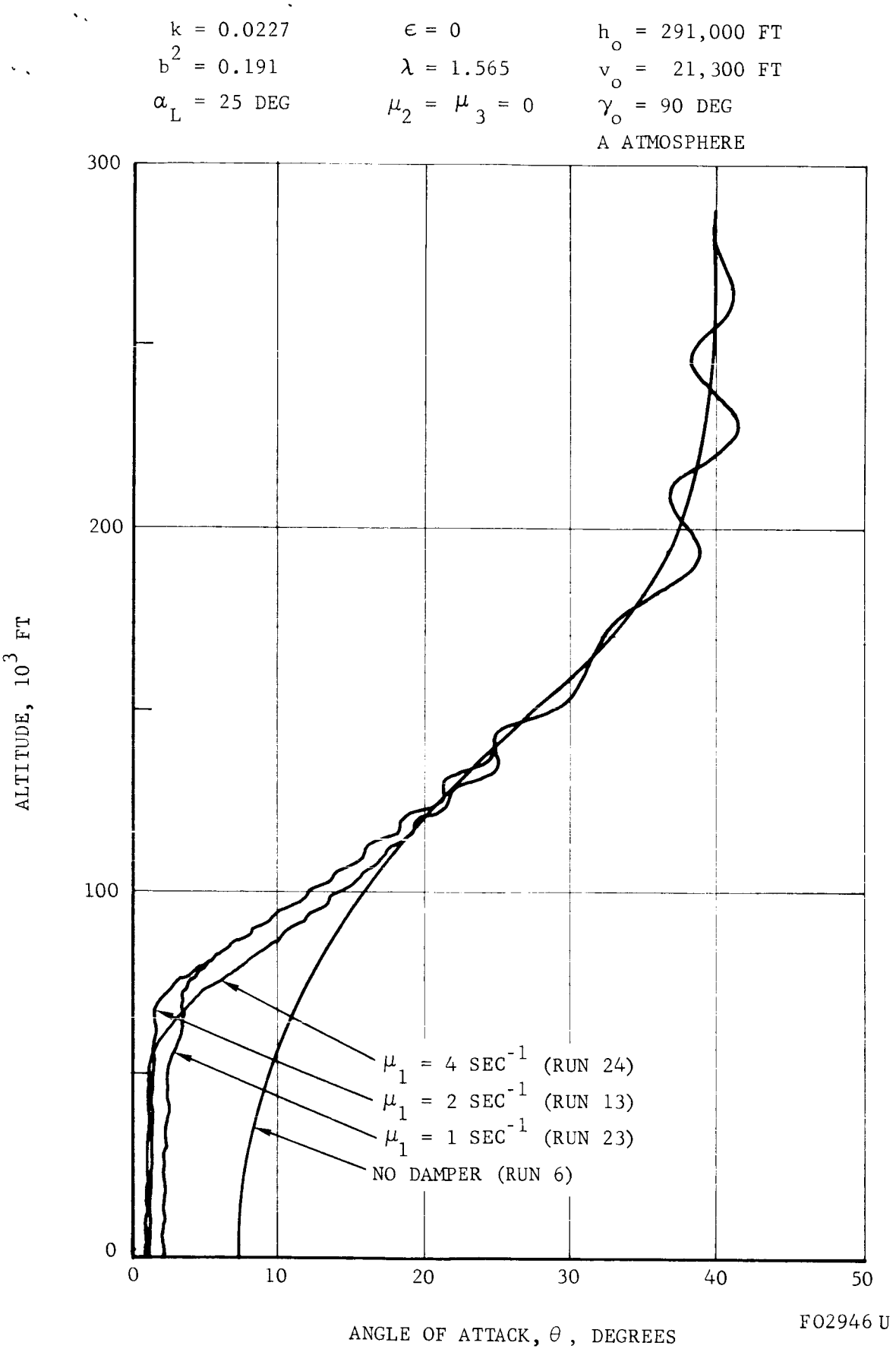

FIGURE 3-14. EFFECT OF VARYING THE LINEAR DAMPING COEFFICIENT

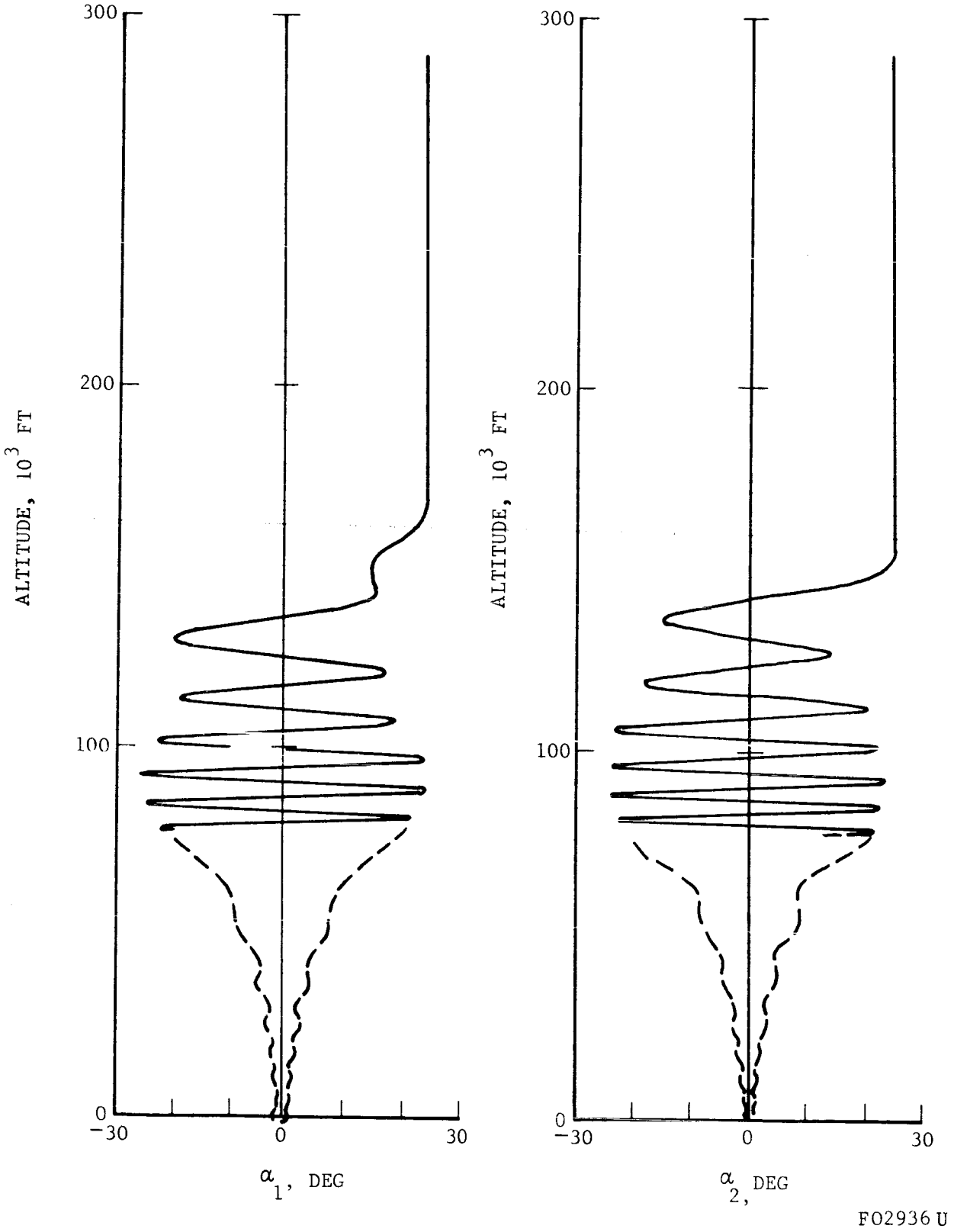

FIGURE 3-15a. BALL MOTIONS FOR μ_1 = 1 SEC^{-1} (RUN 23)

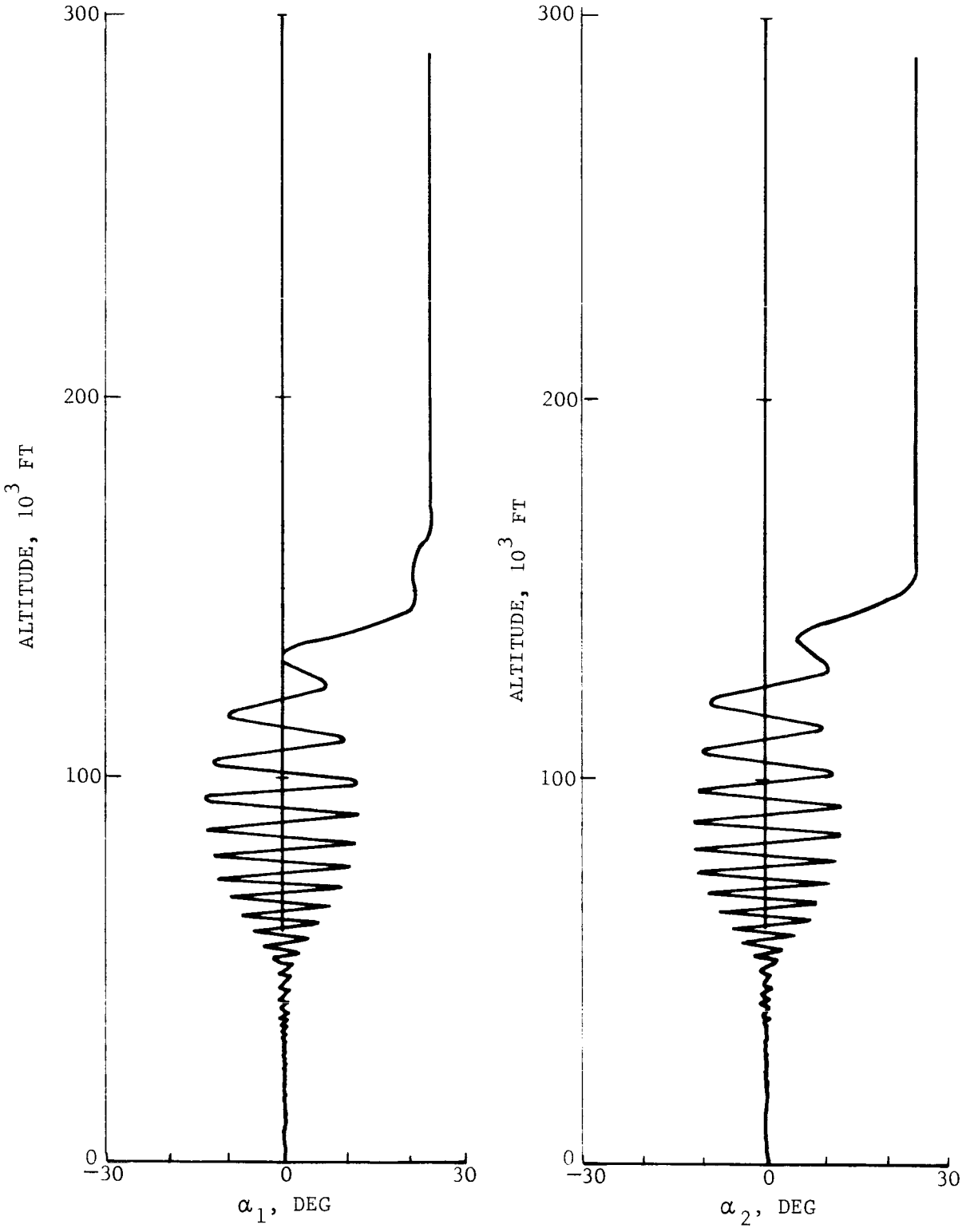

F02934 U

FIGURE 3-15b. BALL MOTIONS FOR μ_1 = 4 SEC^{-1} (RUN 24)

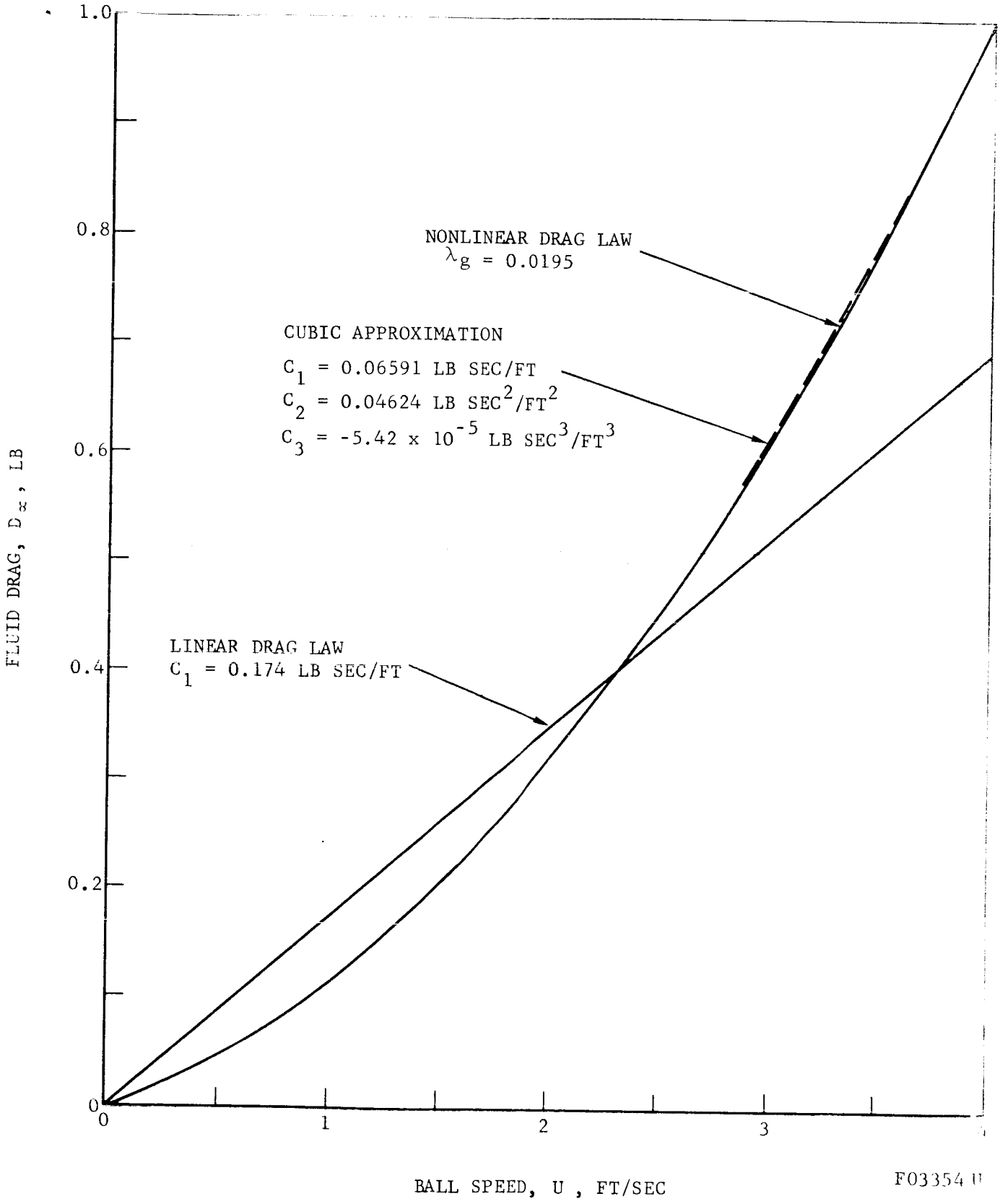

FIGURE 3-16. LINEAR AND NONLINEAR DRAG LAWS

We compared the damper performance using the above μ_i (Run 34) with the damper performance using $\mu_1 = 2\ \text{sec}^{-1}$ (Run 13). The results are practically the same except that the trim angle is slightly larger using the non-linear damping law (1.93 degrees compared to 1.25 degrees).

3.2.4 TUBE LENGTH AND IMPACT COEFFICIENT

The effects of reducing α_L while holding R fixed are illustrated in Figure 3-17. At high altitude when the balls are caged against their stops, the coning amplitude varies in almost direct proportion to α_L. In this respect, it is beneficial to reduce α_L. However, the altitude at which θ reaches the trim angle decreases as α_L decreases below some critical value near 20 degrees. The trim angle itself is unaffected by the reduction in α_L.

The ball motions for α_L = 18.8, 12.5 and 6.25 degrees are plotted in Figures 3-18a, b, and c, respectively. The slower decay to the trim angle is explained by the fact that the balls impact the stops earlier in their oscillations as α_L is reduced. For α_L = 18.8 degrees, the balls barely touch the stops, which is why the θ traces for α_L = 25 and 18.8 degrees are almost identical at low altitudes.

The impact parameter ϵ is unimportant if the balls do not hit the stops. The effect of varying ϵ between 0 and 1 is illustrated in Figure 3-19 for a case (α_L = 12.5 degrees) when the balls do hit the stops. The rate at which θ approaches its trim value is seen to decrease as ϵ increases, which supports our earlier contention that the impact should be as inelastic as possible.

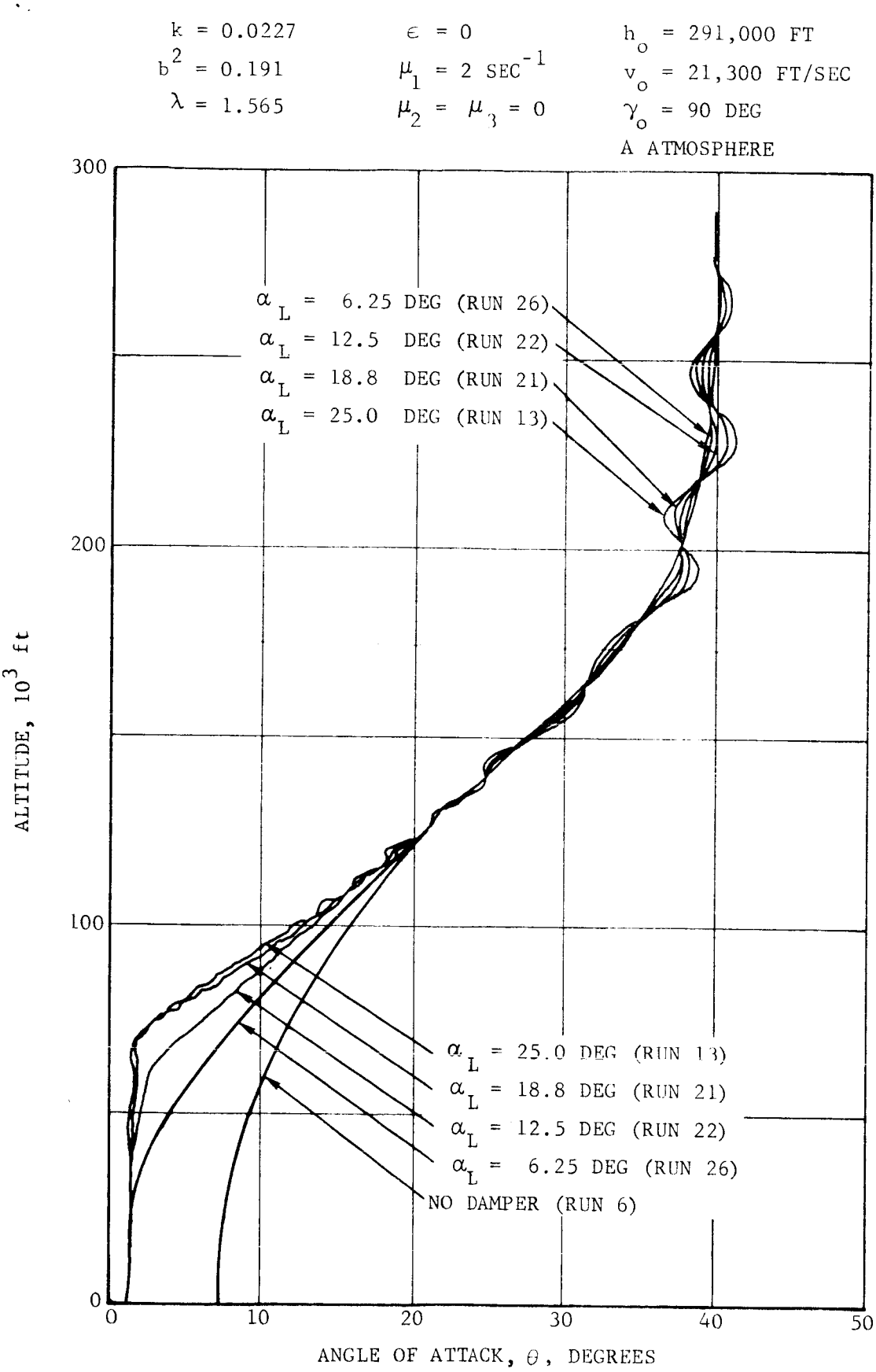

F02944 U

FIGURE 3-17. EFFECT OF VARYING THE TUBE LENGTH

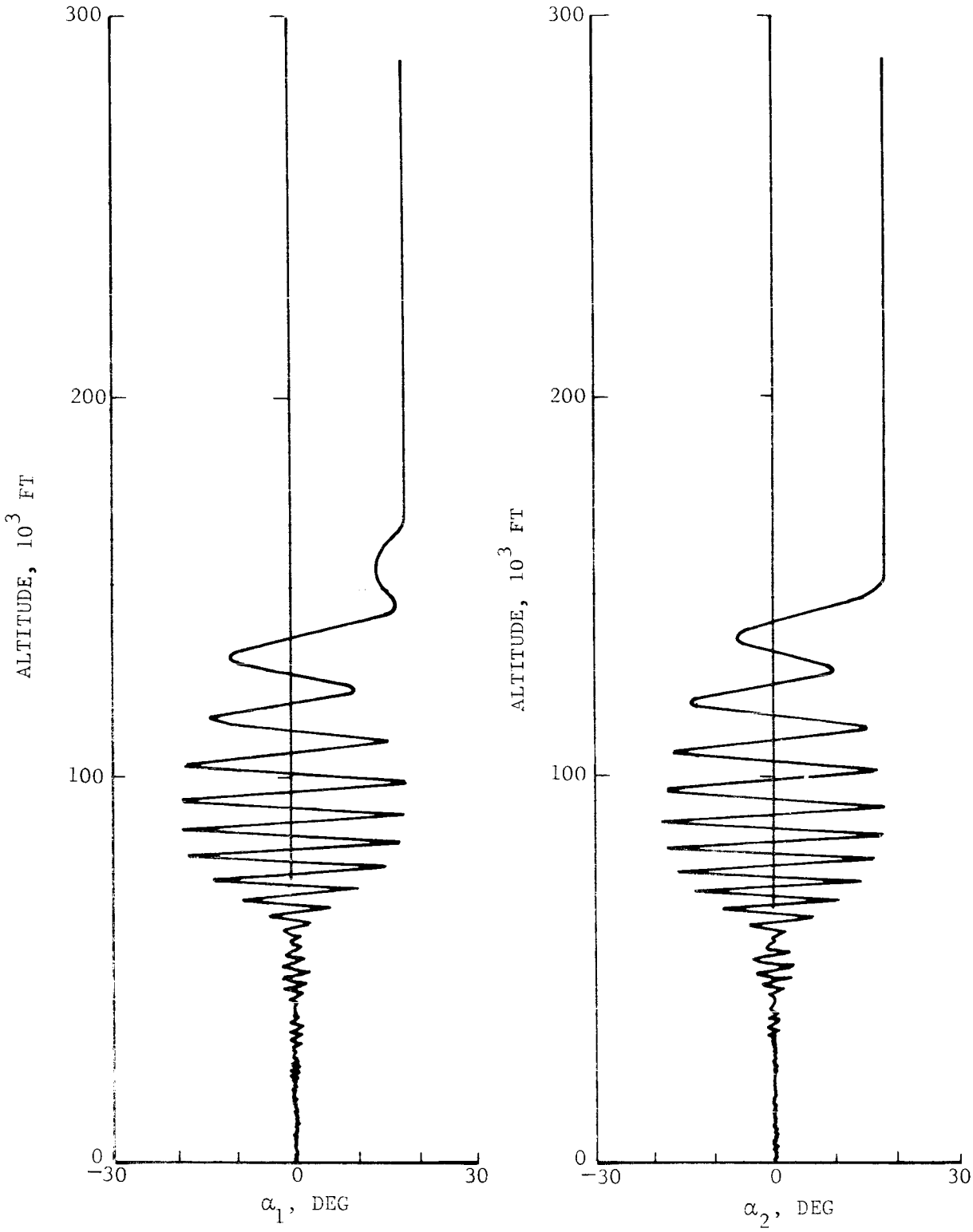

F02943 U

FIGURE 3-18a. BALL MOTIONS FOR α_L = 18.8 DEG (RUN 21)

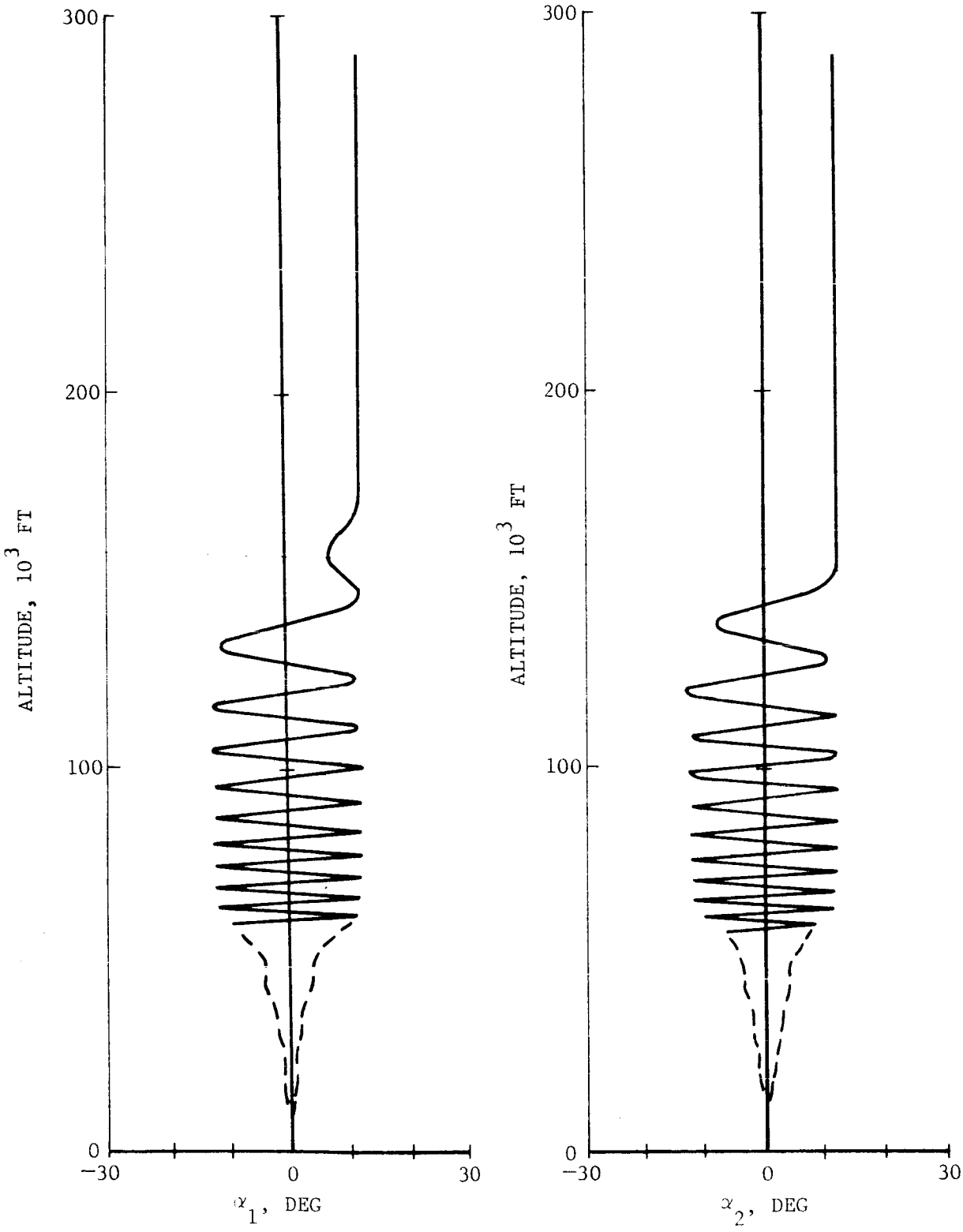

F02940 U

FIGURE 3-18b. BALL MOTIONS FOR α_L = 12.5 DEG (RUN 22)

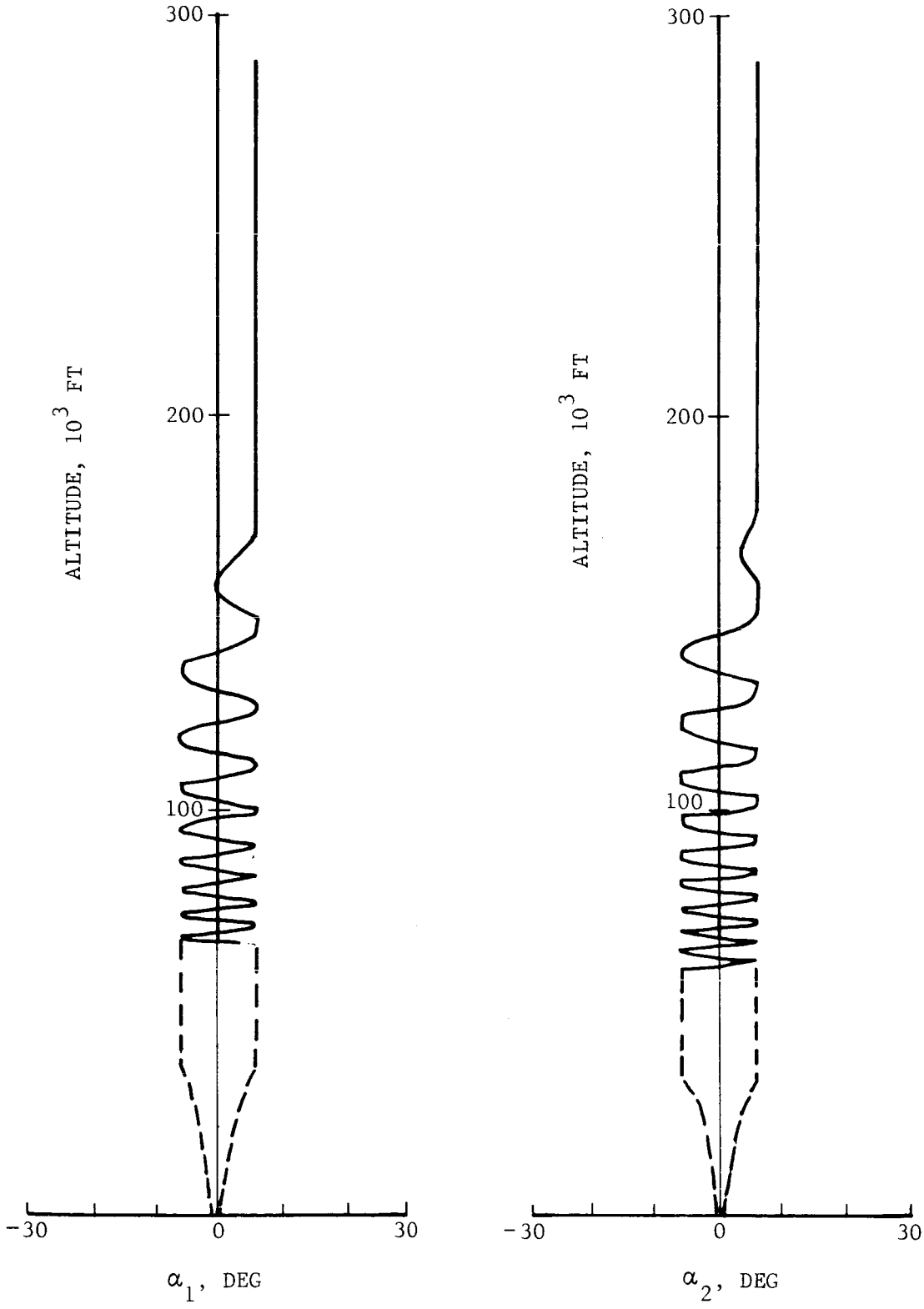

F02942 U

FIGURE 3-18c. BALL MOTIONS FOR α_L = 6.25 DEG (RUN 26)

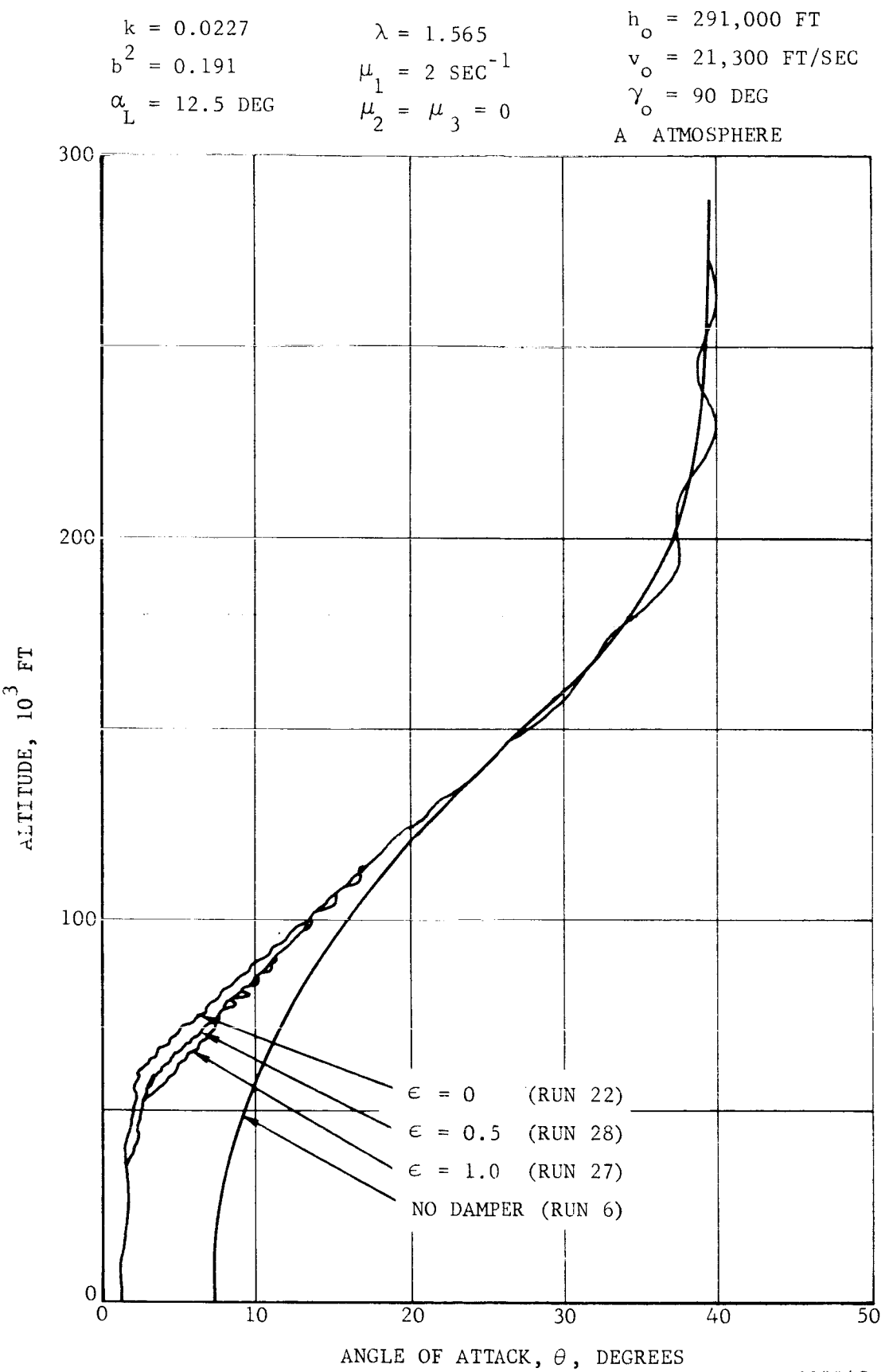

F02945 U

FIGURE 3-19. EFFECT OF VARYING IMPACT COEFFICIENT

3.2.5 OTHER ENTRY CONDITIONS

The previous results were for a direct entry into the A atmosphere. There is every reason to believe that the nominal damper design will perform equally well under other entry conditions.

In Figure 3-20, we compare the angle of attack profiles with and without a damper for an indirect entry into the B atmosphere. The corresponding velocity and dynamic pressure profiles were presented earlier in Figure 3-5. The damper trims the angle of attack to less than 2 degrees well before peak dynamic pressure and holds it at the trim angle until impact. The ball motions are shown in Figure 3-21. All the activity occurs between 400,000 and 220,000 feet.

A similar angle of attack comparison is made in Figure 3-22 for an orbital entry into the A atmosphere. The velocity and dynamic pressure profiles were presented in Figure 3-6. The ball motions are shown in Figure 3-23.

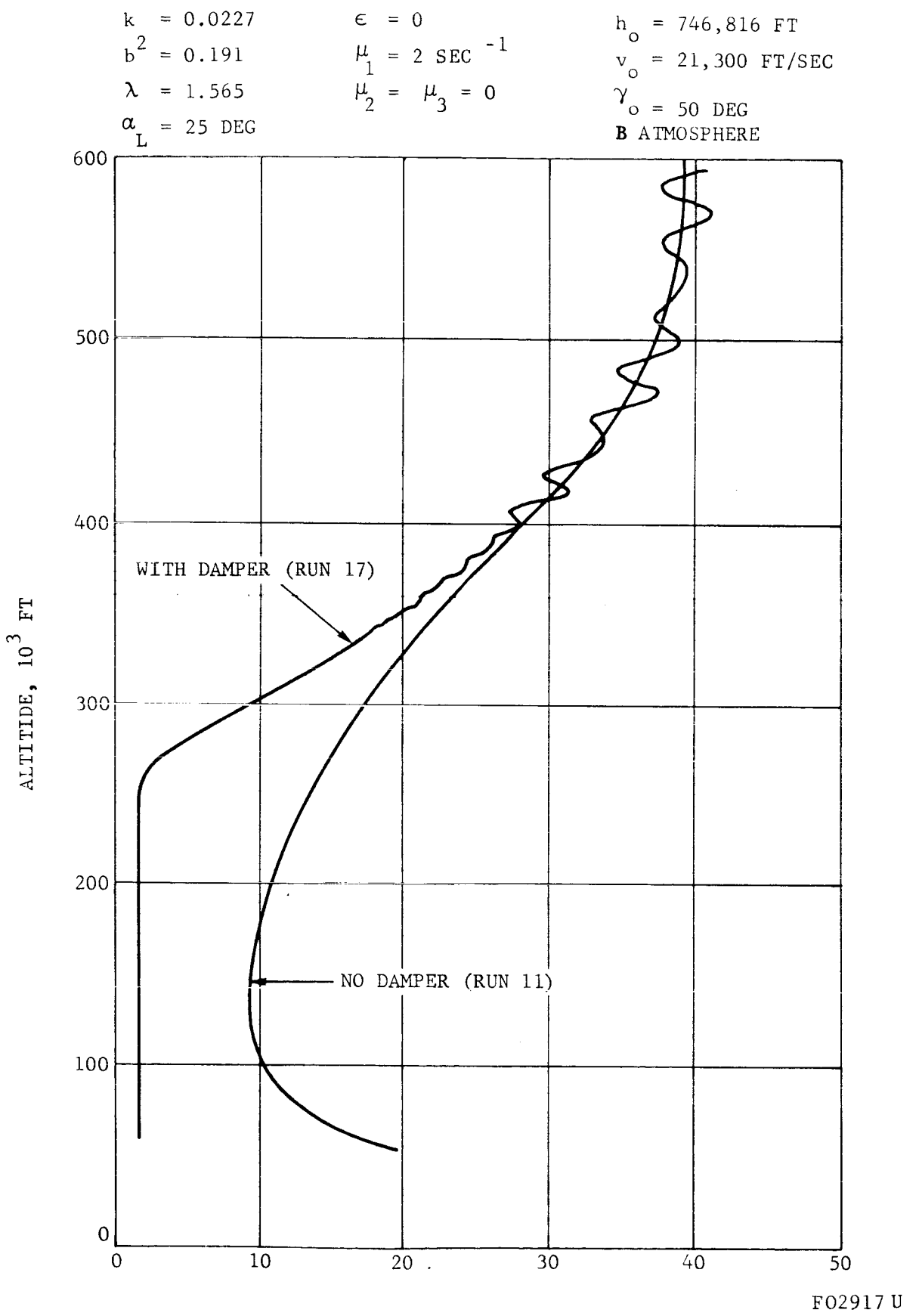

FIGURE 3-20. ANGLE OF ATTACK PROFILE FOR INDIRECT ENTRY INTO THE B ATMOSPHERE

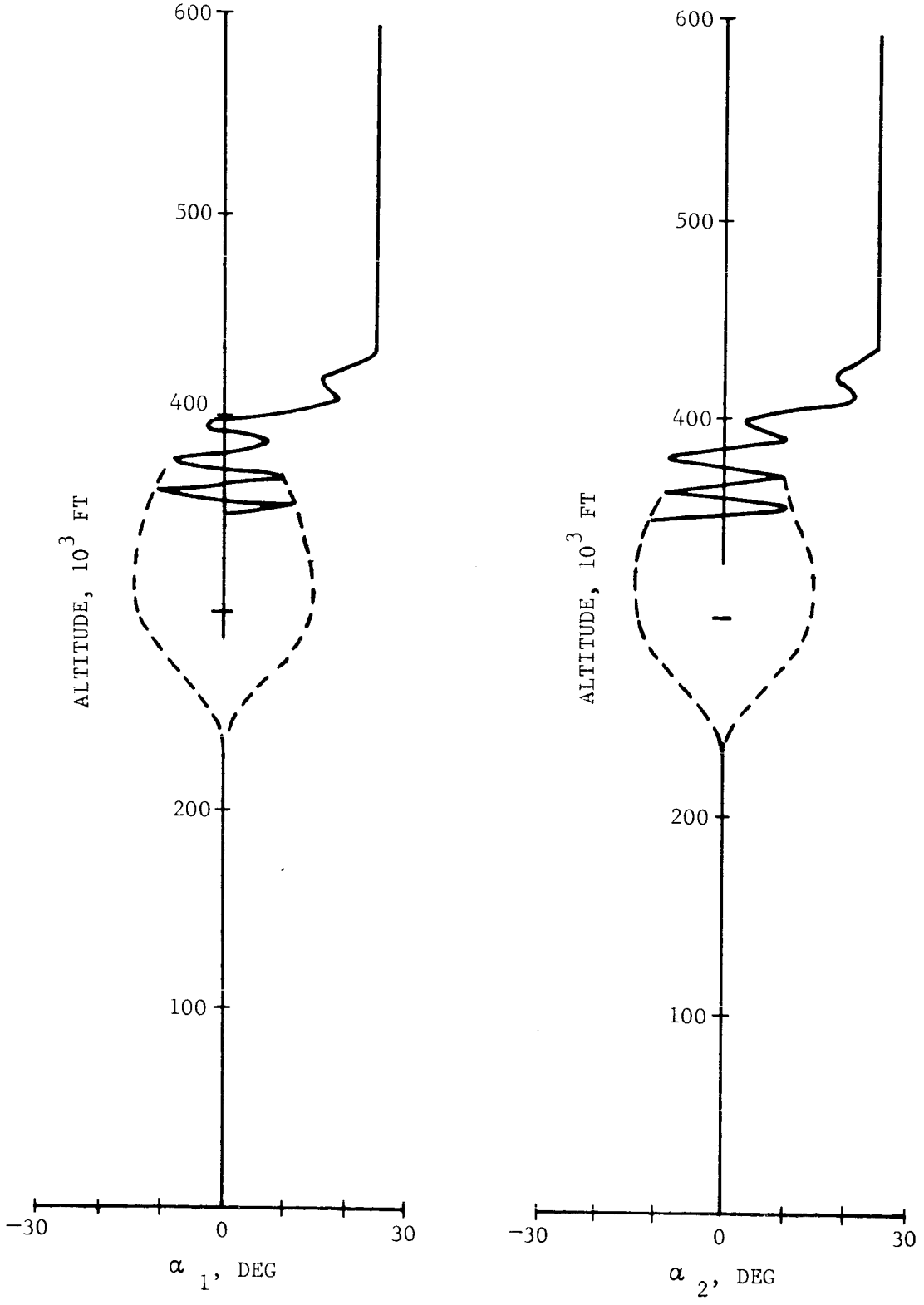

F02931U

FIGURE 3-21. BALL MOTIONS (RUN 17)

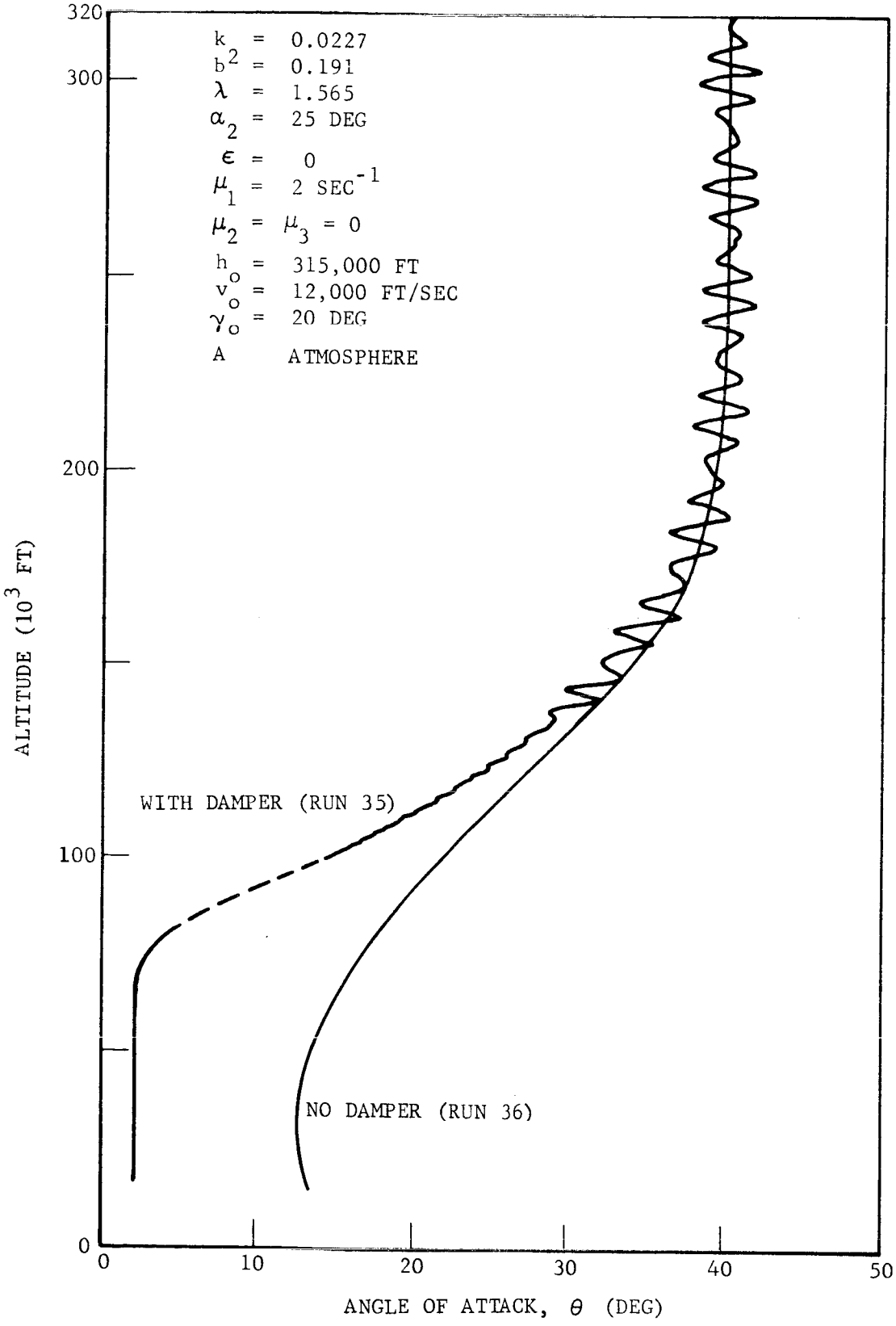

F03444 U

FIGURE 3-22. ANGLE OF ATTACK PROFILE FOR ORBITAL ENTRY INTO THE A ATMOSPHERE

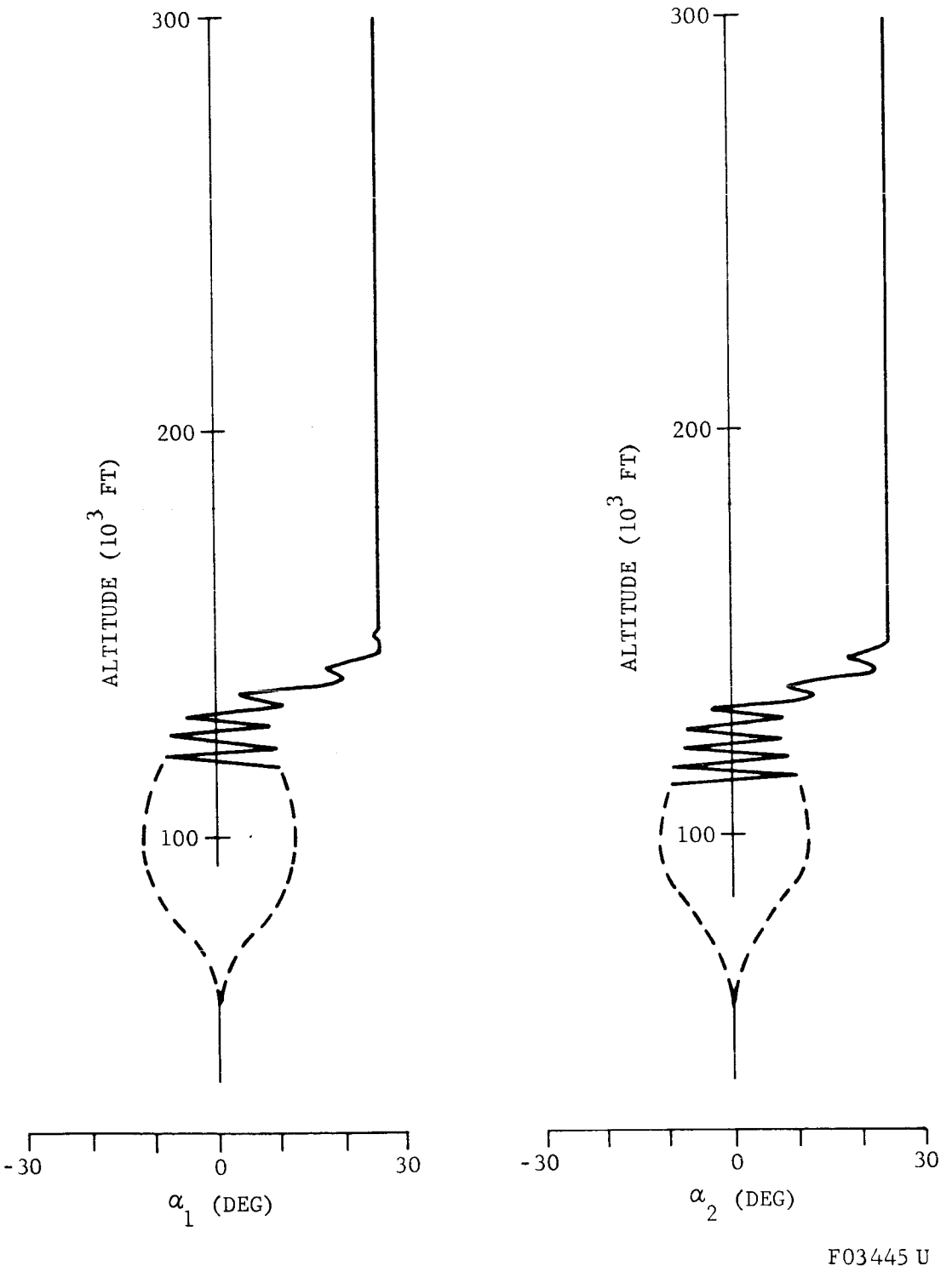

FIGURE 3-23. BALL MOTIONS (RUN 35)

SECTION 4

THE GODDARD MARS ATMOSPHERIC PROBE

4.1 VEHICLE DESCRIPTION AND DYNAMICS

The Goddard Needle-Nosed Probe (also designed for the penetration of the Mars atmosphere) is shown in Figure 4-1. The vehicle mass M is 1.88 slugs, the roll inertia J is 0.030 slug ft^2, and the pitch (and yaw) inertia I is 1.470 slug ft^2.

The aerodynamic coefficients C_A, C_N, and C_m along with the trigonometric approximations

$$C_A = -0.3184 + 0.454 \sin\theta + 0.104 \sin 2\theta - 0.086 \sin 3\theta - 0.03 \sin 4\theta + 0.442 \cos\theta$$

$$C_N = 3.75 \sin\theta + 0.053 \sin 2\theta - 0.53 \sin 3\theta$$

$$C_m = -1.83 \sin\theta + 0.239 \sin 2\theta + 0.092 \sin 3\theta$$

are plotted as functions of the angle of attack θ in Figures 4-2a, b, and c, respectively. The reference area S is 0.56745 ft^2, and the reference length ℓ is 0.850 foot.

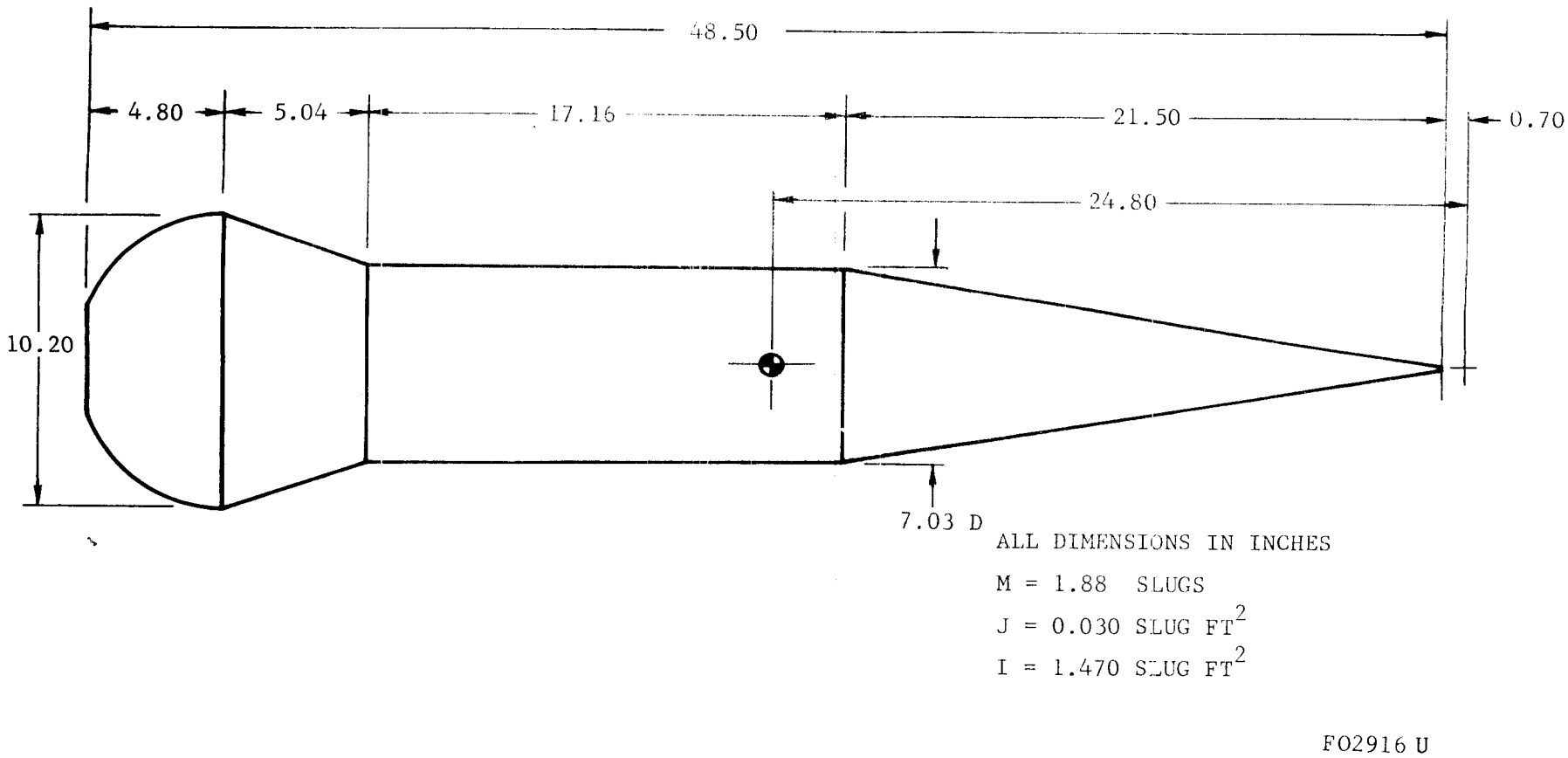

FIGURE 4-1. GODDARD NEEDLE-NOSED PROBE

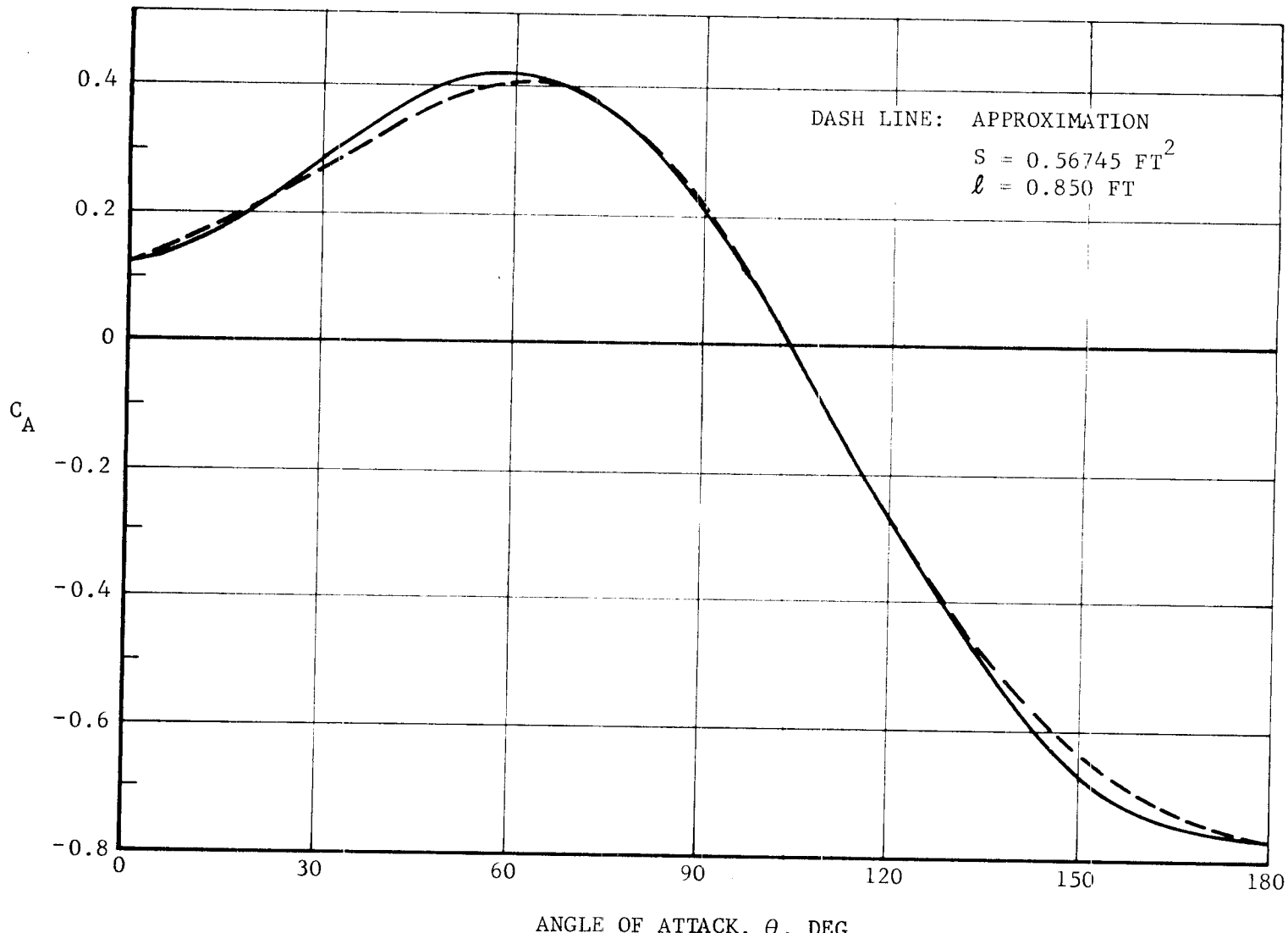

F02947 U

FIGURE 4-2a. AXIAL FORCE COEFFICIENT (GODDARD PROBE)

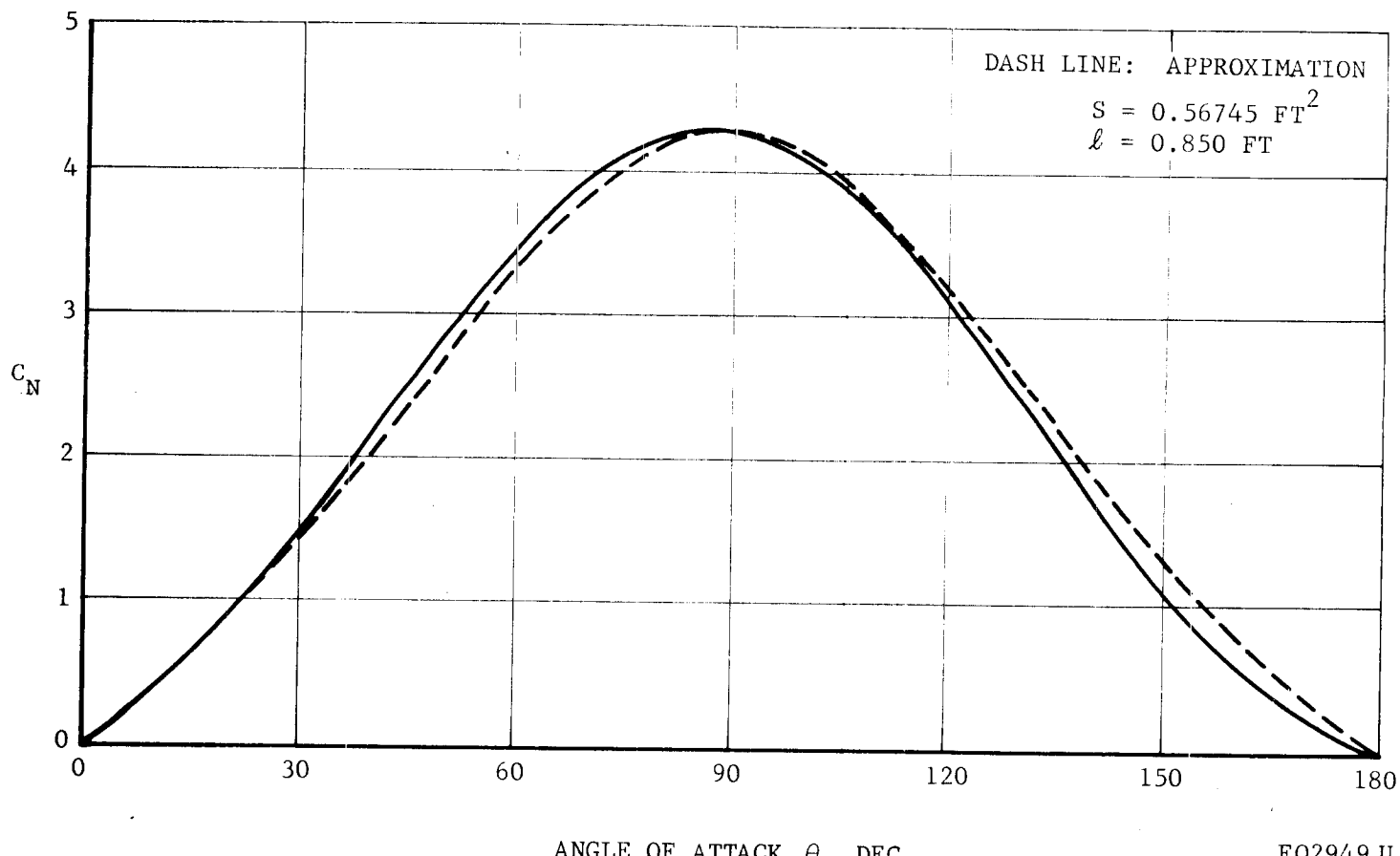

FIGURE 4-2b. NORMAL FORCE COEFFICIENT (GODDARD PROBE)

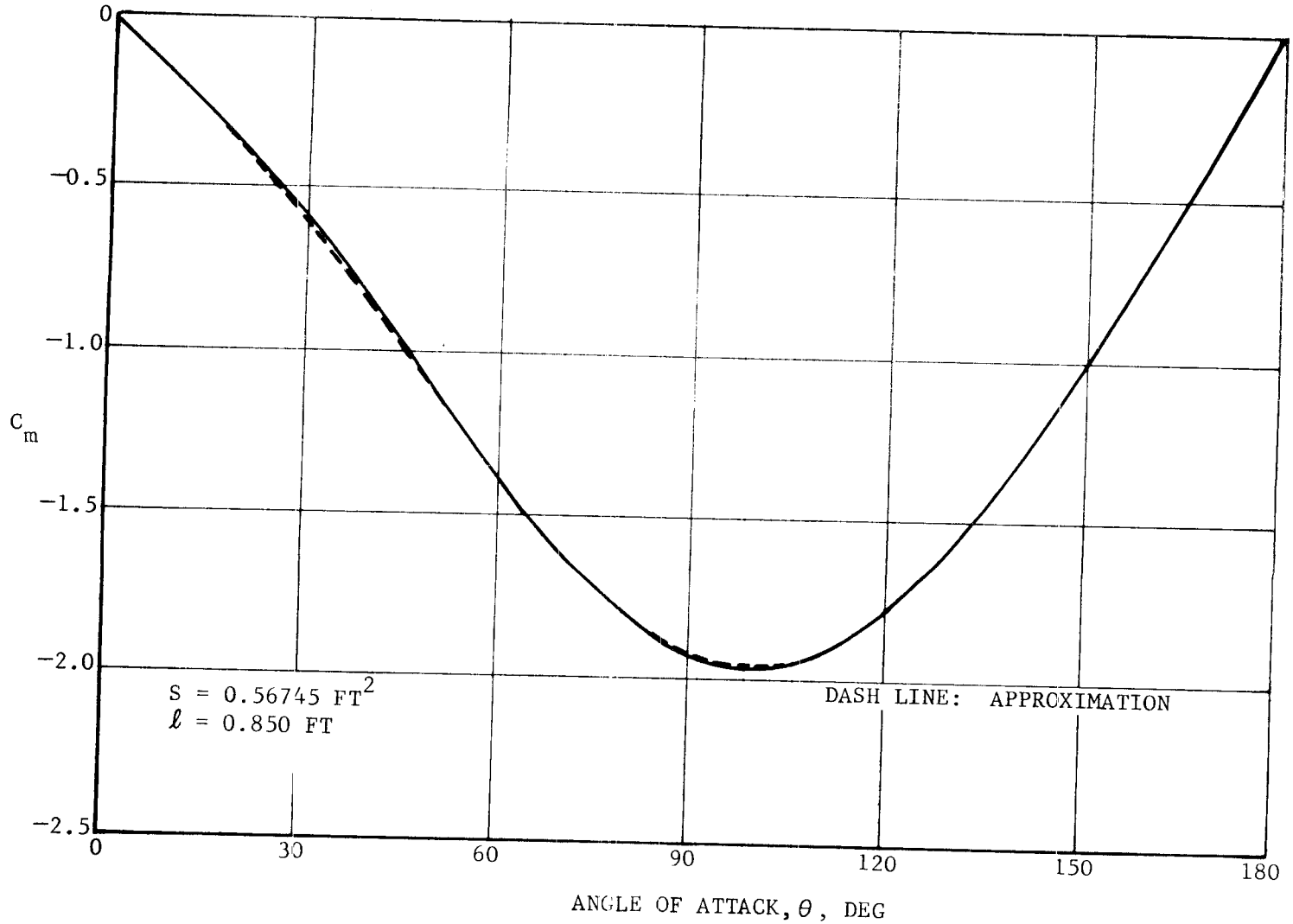

F02948 U

FIGURE 4-2c. MOMENT COEFFICIENT (GODDARD PROBE)

The ballistic coefficient $M/(C_D S)$ for the Goddard probe is 27.2 slug/ft^2 compared to 0.18 slug/ft^2 for the Ames probe. Because the ballistic coefficient is relatively large, the vehicle velocity can be treated as a constant even for entry into the B atmosphere. This is easily verified. The velocity ratio is given by

$$\frac{v}{v_o} = e^{-L\rho}$$

where

$$L = \frac{C_D S/M}{2\beta \sin\gamma}$$

For a 90 degree entry in the B atmosphere, L = 850 ft^3/slug, and at the surface $L\rho = 0.051$, which indicates that the impact velocity is 95 percent of the entry velocity. The percentages are even larger for entries into the A and the NASA Model 3 atmospheres.

For a constant velocity entry into an exponential atmosphere we have

$$\Omega^2 = \Omega_o^2 e^{ct}, \quad \dot{\Omega} = \frac{c}{2}\Omega \tag{4-1}$$

where $c = \beta\, v \sin\gamma$. With $\tau = 2\Omega/c$ as the independent variable, Equations (2-1) and (2-2) can be expressed as

$$\begin{aligned}\frac{d^2\theta}{d\tau^2} + \frac{1}{\tau}\frac{d\theta}{d\tau} - C_m = -k\Bigg[&\left(1-2\lambda\cos\alpha + \lambda^2\right)\left(\frac{d^2\theta}{d\tau^2} + \frac{1}{\tau}\frac{d\theta}{d\tau}\right)\\ &+\zeta\left(\frac{d^2\alpha}{d\tau^2} + \frac{1}{\tau}\frac{d\alpha}{d\tau}\right) + \lambda\left(2\frac{d\theta}{d\tau} + \frac{d\alpha}{d\tau}\right)\frac{d\alpha}{d\tau}\sin\alpha\\ &+\frac{7}{5}b^2\left(C_A\sin\alpha + C_N\eta\right)\Bigg]\end{aligned} \tag{4-2}$$

$$\begin{aligned}\frac{d^2\alpha}{d\tau^2} + \frac{1}{\tau}\left(1 + \frac{4\mu_1}{c}\right)\frac{d\alpha}{d\tau} + 2\mu_2\frac{d\alpha}{d\tau}\left|\frac{d\alpha}{d\tau}\right| + \mu_3 c\tau\left(\frac{d\alpha}{d\tau}\right)^3\\ = -\frac{5}{7}\zeta\left(\frac{d^2\theta}{d\tau^2} = \frac{1}{\tau}\frac{d\theta}{d\tau}\right) + \frac{5}{7}\left(\frac{d\theta}{d\tau}\right)^2\sin\alpha - b^2\left(C_A\sin\alpha + C_N\cos\alpha\right)\end{aligned} \tag{4-3}$$

Equations (4-2) and (4-3) indicate that a single solution applies to all values of c, provided that the nondimensional damping coefficients μ_1/c, μ_2, and $\mu_3 c$, rather than the μ_i, are treated as basic parameters.

The atmospheric density ρ is related to τ by the equation

$$\rho = \frac{I \beta^2 \sin^2 \gamma}{2S\ell} \tau^2 \tag{4-4}$$

For a 90 degree entry into the A atmosphere, Equation (4-4) provides

$$\rho\left(\text{slug/ft}^3\right) = \left(3.36 \times 10^{-9} \text{ slug/ft}^3\right) \tau^2 \tag{4-5}$$

This relation also applies to the NASA Model 3 atmosphere above 80,000 feet, since its scale height is the same as for the A atmosphere. Equation (4-5) and the density-altitude profiles in Figure 3-3 were used to obtain the altitude-τ curves in Figure 4-3. Figure 4-3 shows that impact for a direct entry through the A atmosphere occurs at $\tau = 62.5$.

The design entry condition for the probe is $\theta = 155$ degrees at $\tau = 1$ with no initial rates, including spin. The angle-of-attack profile is shown in Figure 4-4 as a function τ. By $\tau = 62.5$, the vehicle has gone through 10.5 cycles and the θ envelope has decayed to 23.7 degrees.

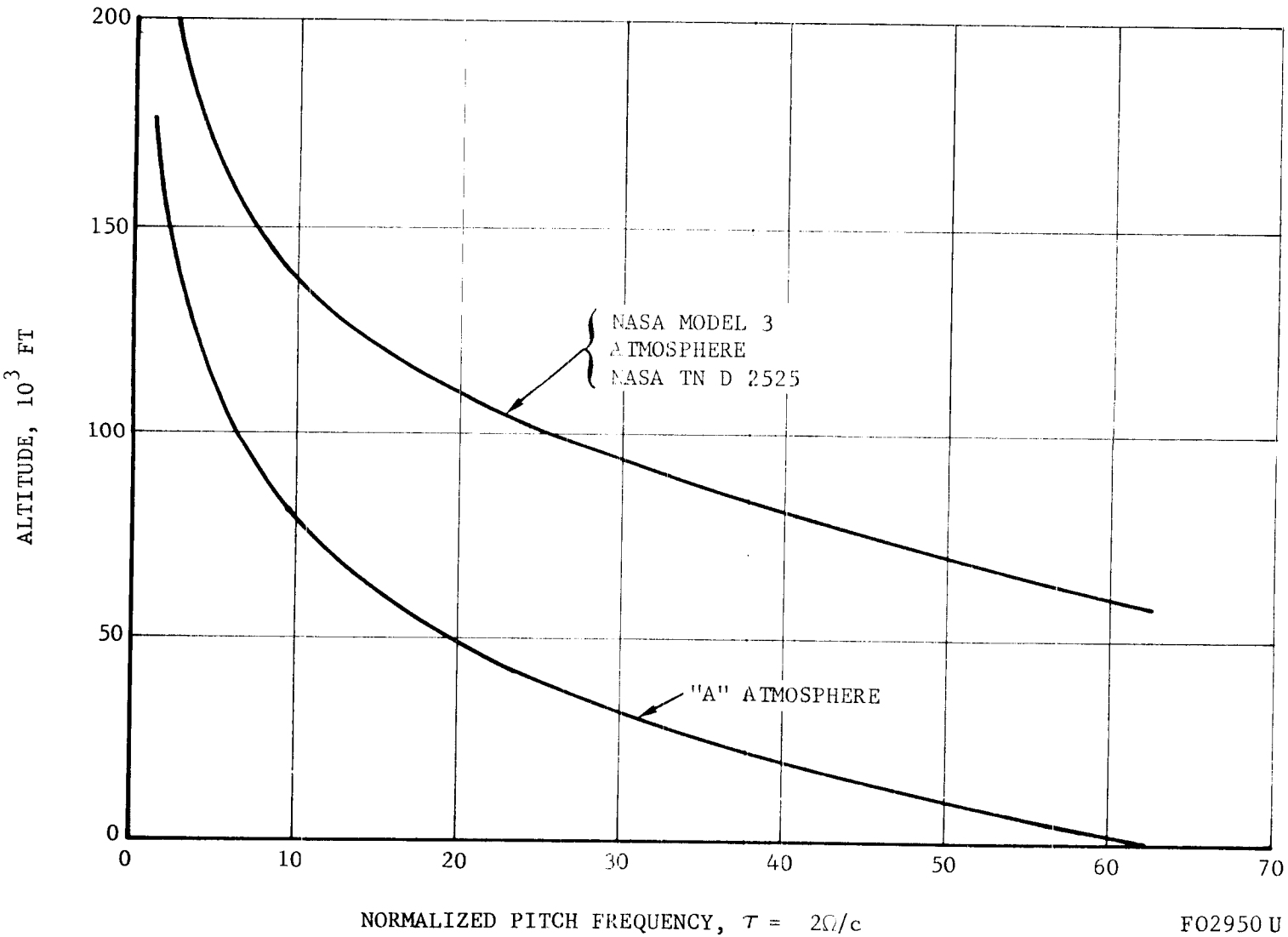

FIGURE 4-3. ALTITUDE AS A FUNCTION OF PITCH FREQUENCY FOR THE GODDARD PROBE USING TWO ATMOSPHERIC MODELS

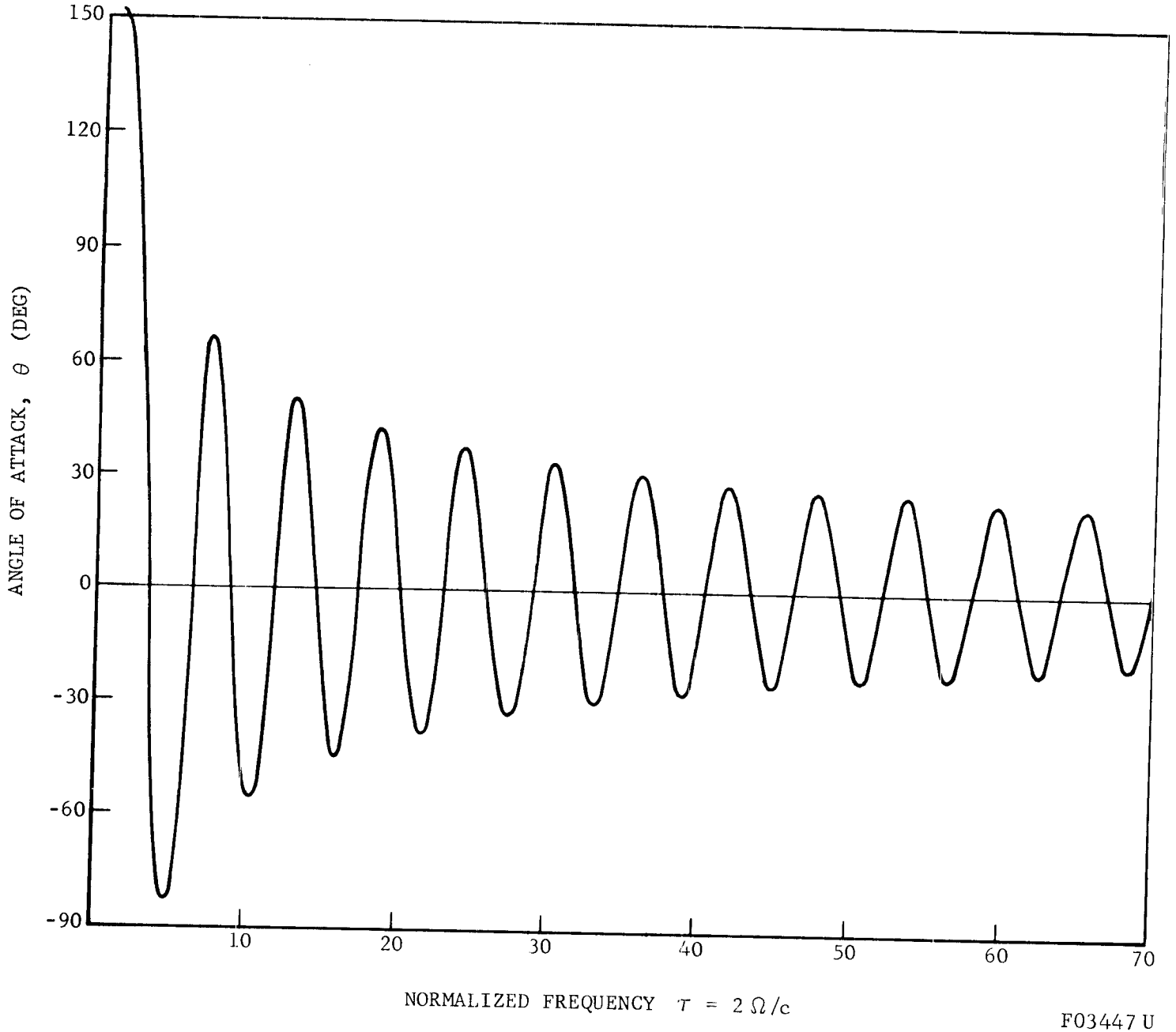

F03447 U

FIGURE 4-4. ANGLE OF ATTACK AS A FUNCTION OF τ (RUN 1)

4.2 DAMPER DESIGN

4.2.1 INTRODUCTION

Six pounds are allotted for a damper in the Goddard probe. This allows for two 2.1-inch diameter tungsten-carbide balls, each weighing 2.65 pounds and 0.35 pound for each tube. Presumably, the fluid would be a gas. The design of such a damper is detailed in Paragraph 4.2.3.

Since the vehicle has zero-spin rate, the angle-of-attack oscillations are nearly planar. Deviations from planar motion are due to pitch and yaw rates at entry. However, these effects diminish during entry as the dynamic pressure increases. All this suggests that a single ball which is free to move on a spherical surface would tend to oscillate in the vehicle plane of oscillation. Such an "omnidirectional" damper makes the most efficient use of the damper mass.

The main problem is to develop the required fluid drag without incurring a large weight penalty. Since a gas cannot be used in an omnidirectional damper, the volume of fluid must be minimized.

4.2.2 OMNIDIRECTIONAL DAMPER

Three damper designs were tried before a suitable one was found. Design 1 is a tuned damper with R = 0.905 inch. A 2.5-inch diameter tungsten-carbide ball weighing 4.46 pounds rolls in a liquid bath inside a 2.155-inch radius spherical shell. The estimated weight of the fluid and shell are 1.22 pounds and 0.18 pound, respectively. The CC is located a distance D = 19.6 inch aft of the CM. For this design, $k = 0.00054$, $b^2 = 8.7$, and $\lambda = 21.6$.

The planar computer program was used to evaluate the damper performance for various combinations of α_L, ϵ, and μ_1/c. The best results were obtained with $\alpha_L = 60$ degrees, $\epsilon = 0$, and μ_1/c between 0.5 and 2. With this design, the θ envelope is damped to 12.5 degrees (compared to 23.7 degrees without a damper) by $\tau = 62.5$. The reason for the only average

performance of the tuned damper is that the ball path length is only 2 inches between stops. With large vehicle oscillations, the ball hits the stops almost before it gets started.

Designs 2 and 3 use the same ball as Design 1, but the path radius R is doubled in Design 2 and doubled again in Design 3. The problem of providing the necessary fluid drag for less than 1.5 pounds is considered later. For Design 2, $k = 0.00216$, $b^2 = 4.35$, $\lambda = 10.8$, $\epsilon = 0$, and $\alpha_L = 60$ degrees. The damper performance is illustrated in Figure 4-5 for the case when θ_o is only 1 degree. The θ envelope is completely damped in three cycles. We considered this case first, to show just how effective the damper is when the amplitudes are small and the ball does not hit the stops. The damper performance with $\theta_o = 155$ degrees is illustrated in Figure 4-6. A comparison between Figures 4-5 and 4-6 indicates the detrimental effect of hitting the stops. Still, the θ envelope is reduced to 5.9 degrees by $\tau = 62.5$, which is twice as good as Design 1.

Even better results were obtained with Design 3 for which $k = 0.00864$, $b^2 = 2.175$, $\lambda = 5.7$, $\epsilon = 0$, and $\alpha_L = 60$ degrees. The results shown in Figure 4-7 were obtained with $\mu_1/c = 2$. The θ envelope is essentially eliminated in six cycles or by $\tau = 52$.

Having established a suitable set of damper parameters, the problem of providing the required fluid drag within 1.5 pounds remains. If the ball were placed in a sphere (or portion of a sphere) the volume and weight of fluid would be prohibitive because R is large.

One solution is to place the ball on an arm, pivot the arm about the CC, and provide damping on the arm rather than directly on the ball. An arrangement of this type is shown in Figures 4-8 and 4-9. The pivot has two orthogonal bearings (as in a Hooke's joint) with a dash pot about each degree of freedom.

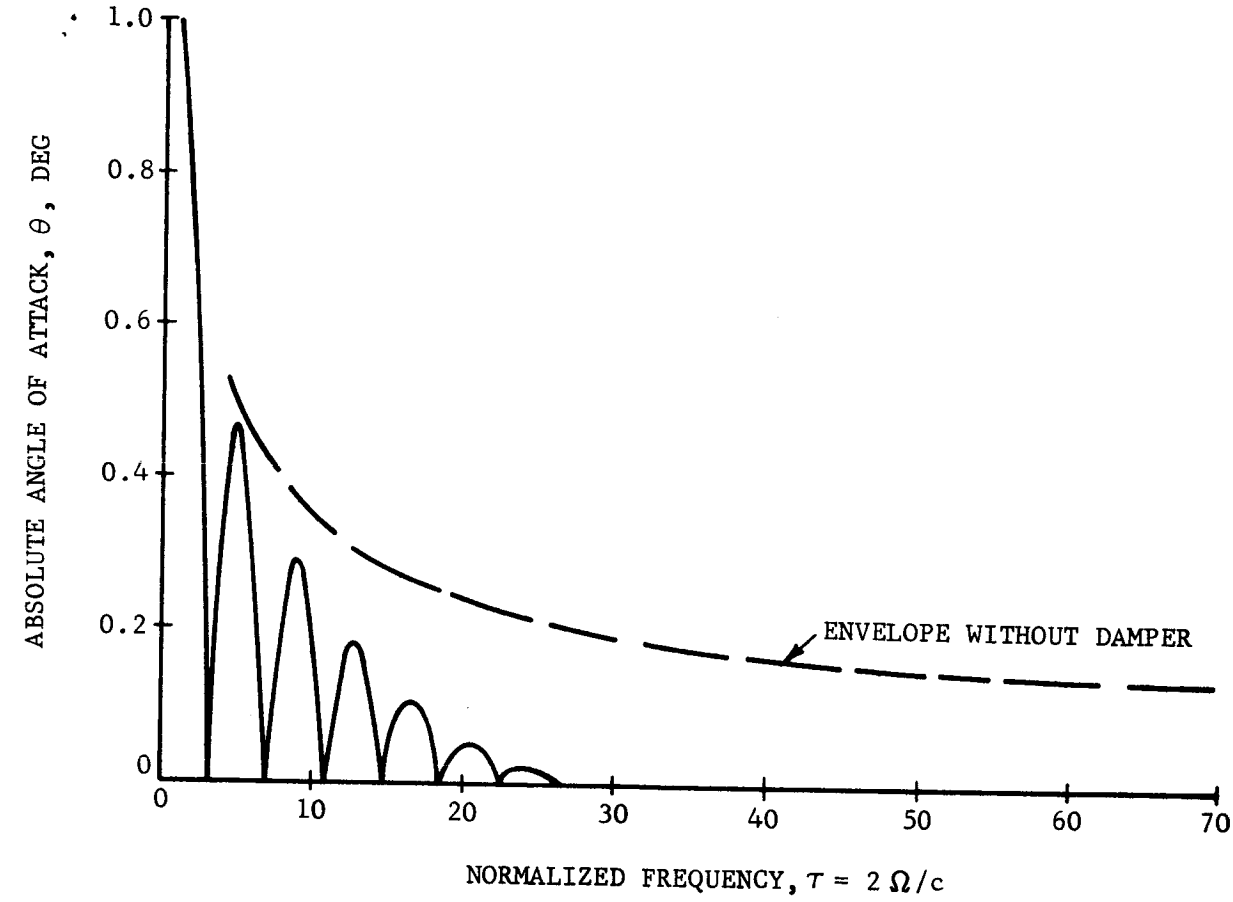

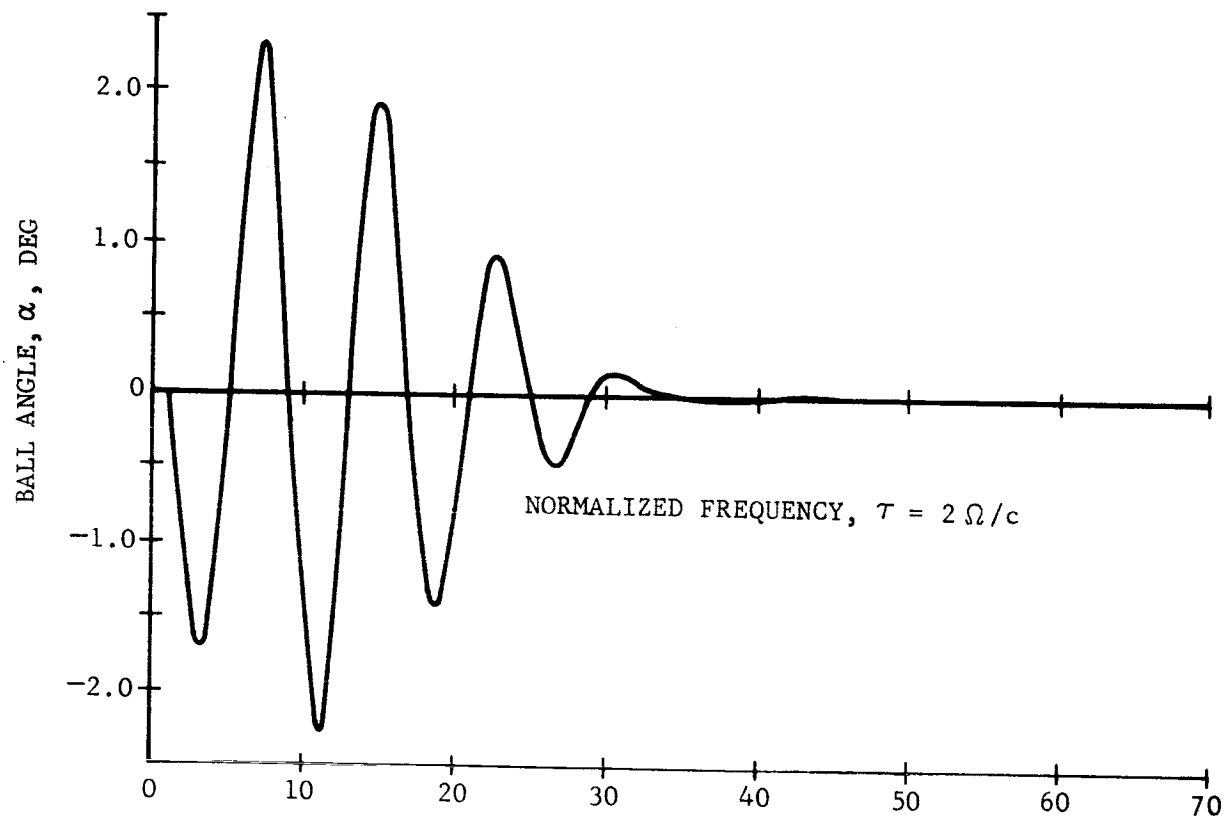

FO2935 U

FIGURE 4-5. SMALL ANGLE RESPONSE OF DAMPER DESIGN 2, WITH μ_1 = 5 SEC^{-1} (RUN 35)

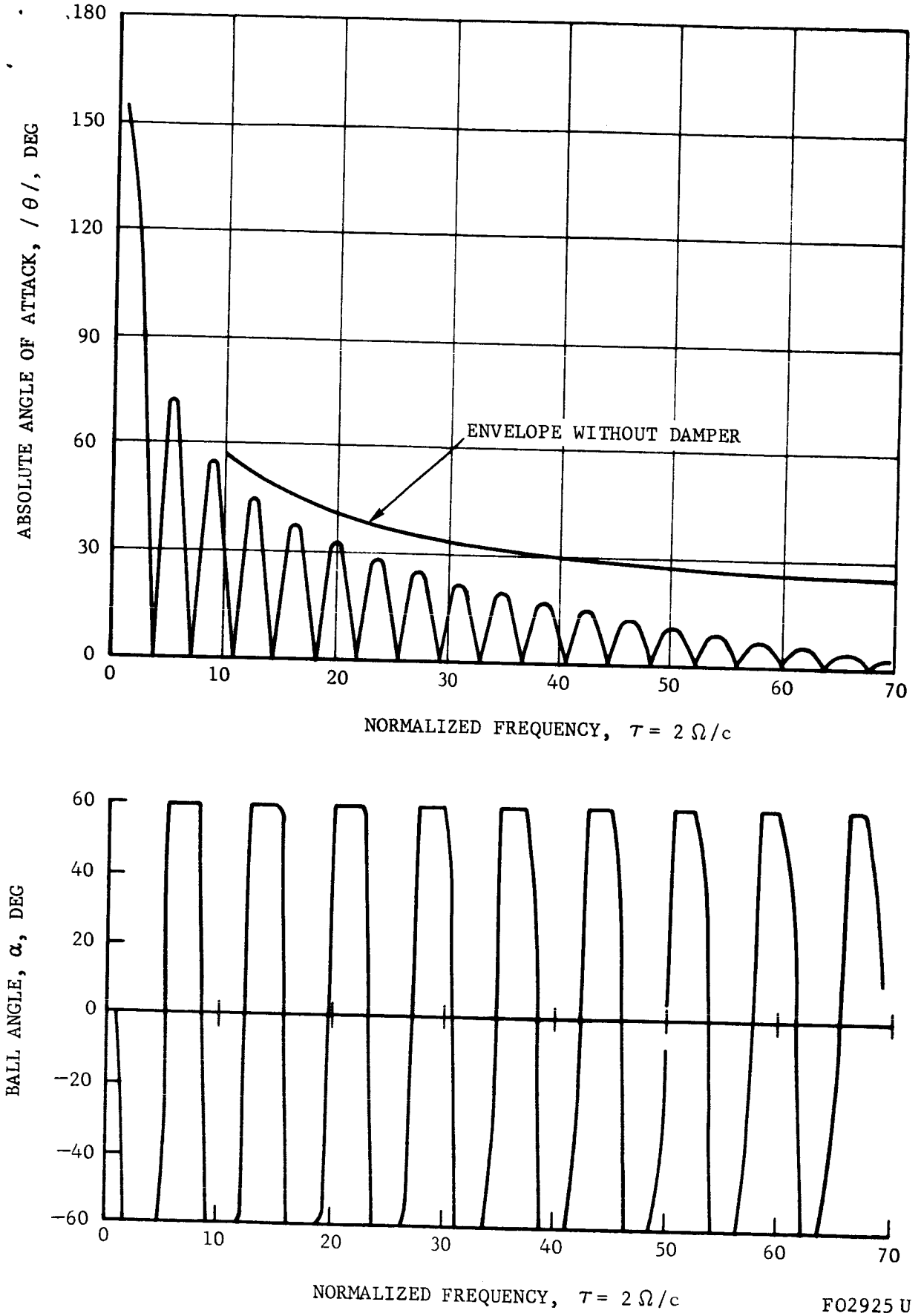

F02925 U

FIGURE 4-6. DAMPER DESIGN 2 WITH $\mu_1 / c = 2$ (RUN 45)

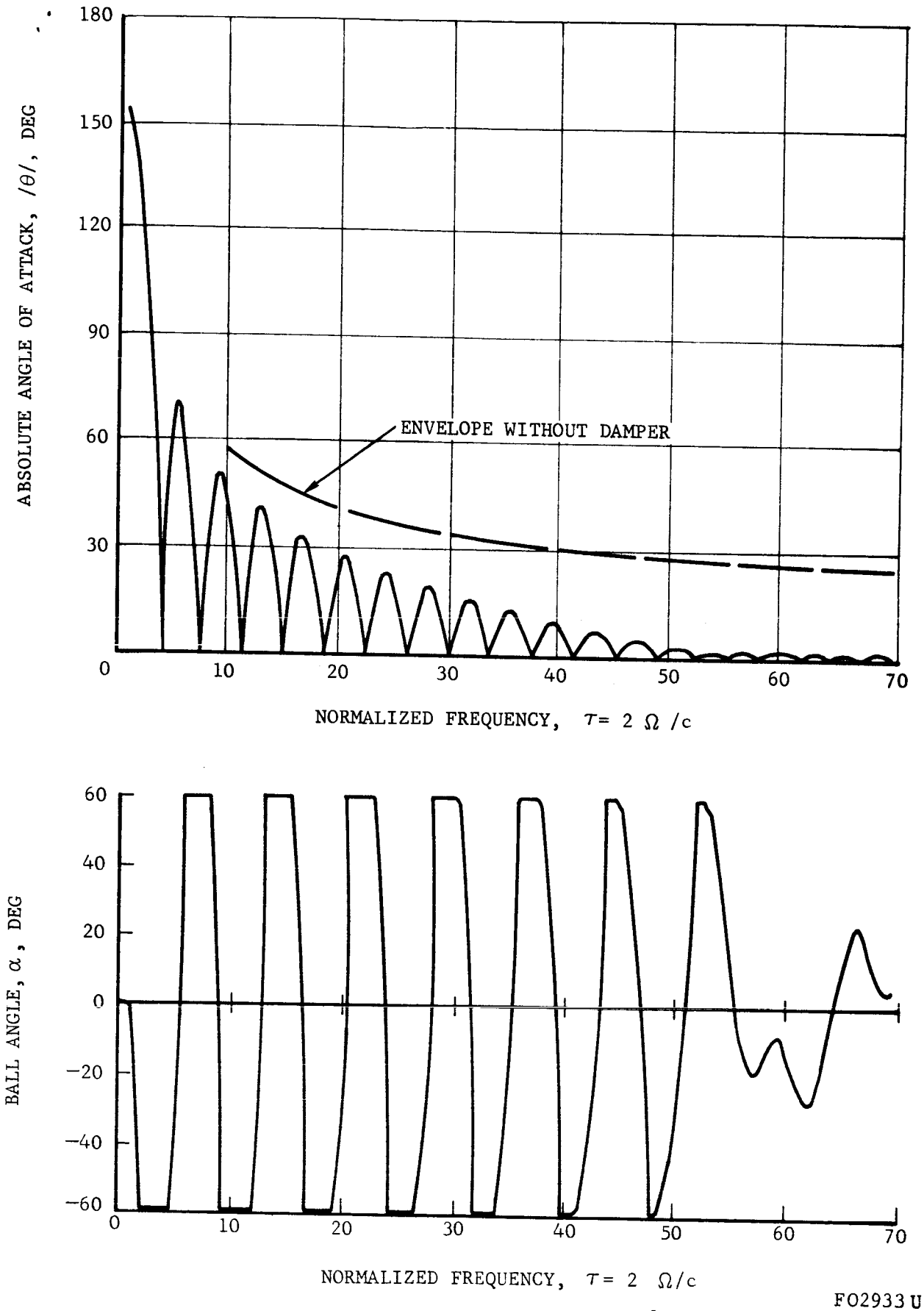

FO2933 U

FIGURE 4-7. DAMPER DESIGN 3 WITH $\mu_1 = 2\ \mathrm{SEC}^{-1}$ (RUN 42)

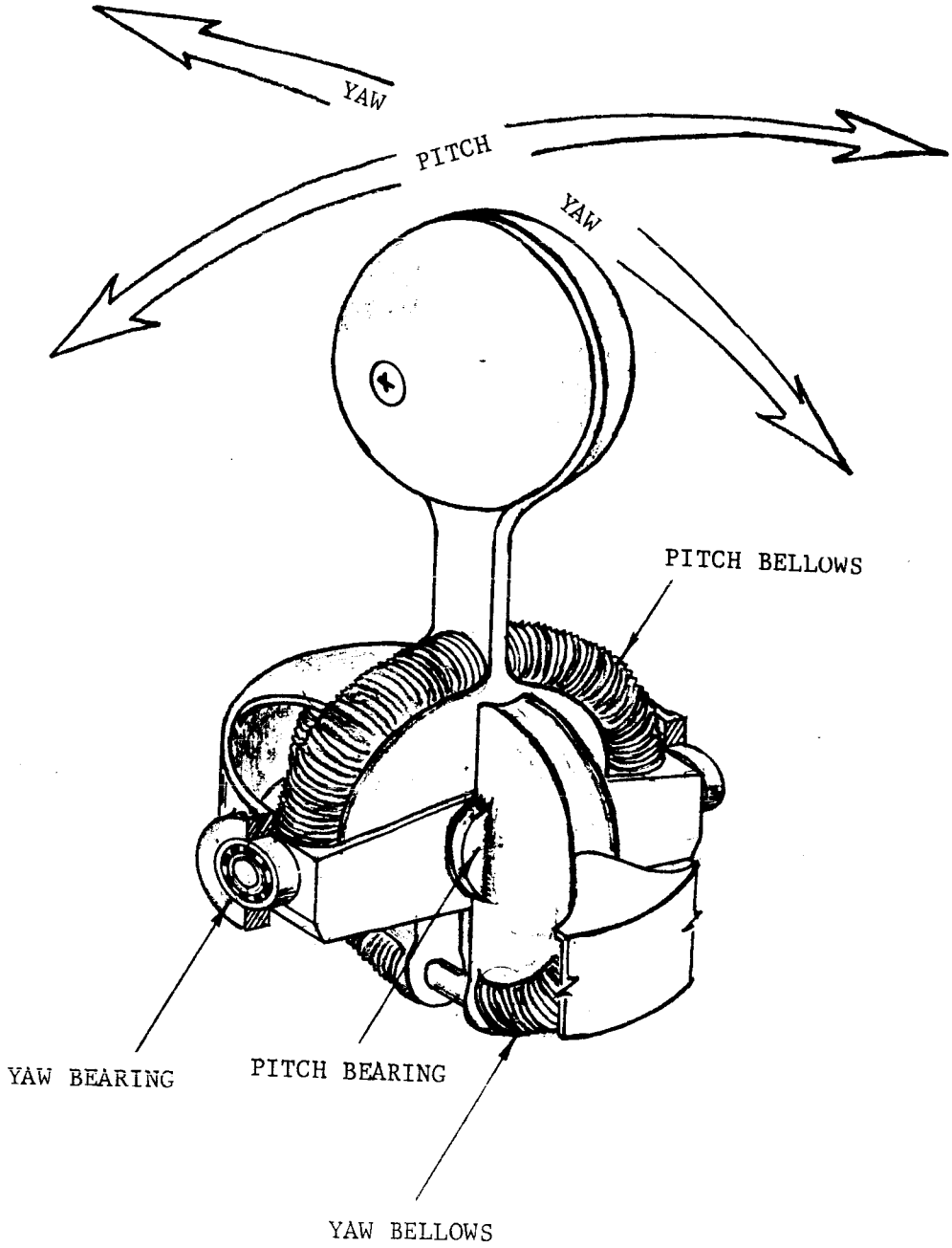

F03355U

FIGURE 4-8. PIVOT-DASH POT MECHANISM FOR OMNIDIRECTIONAL DAMPER

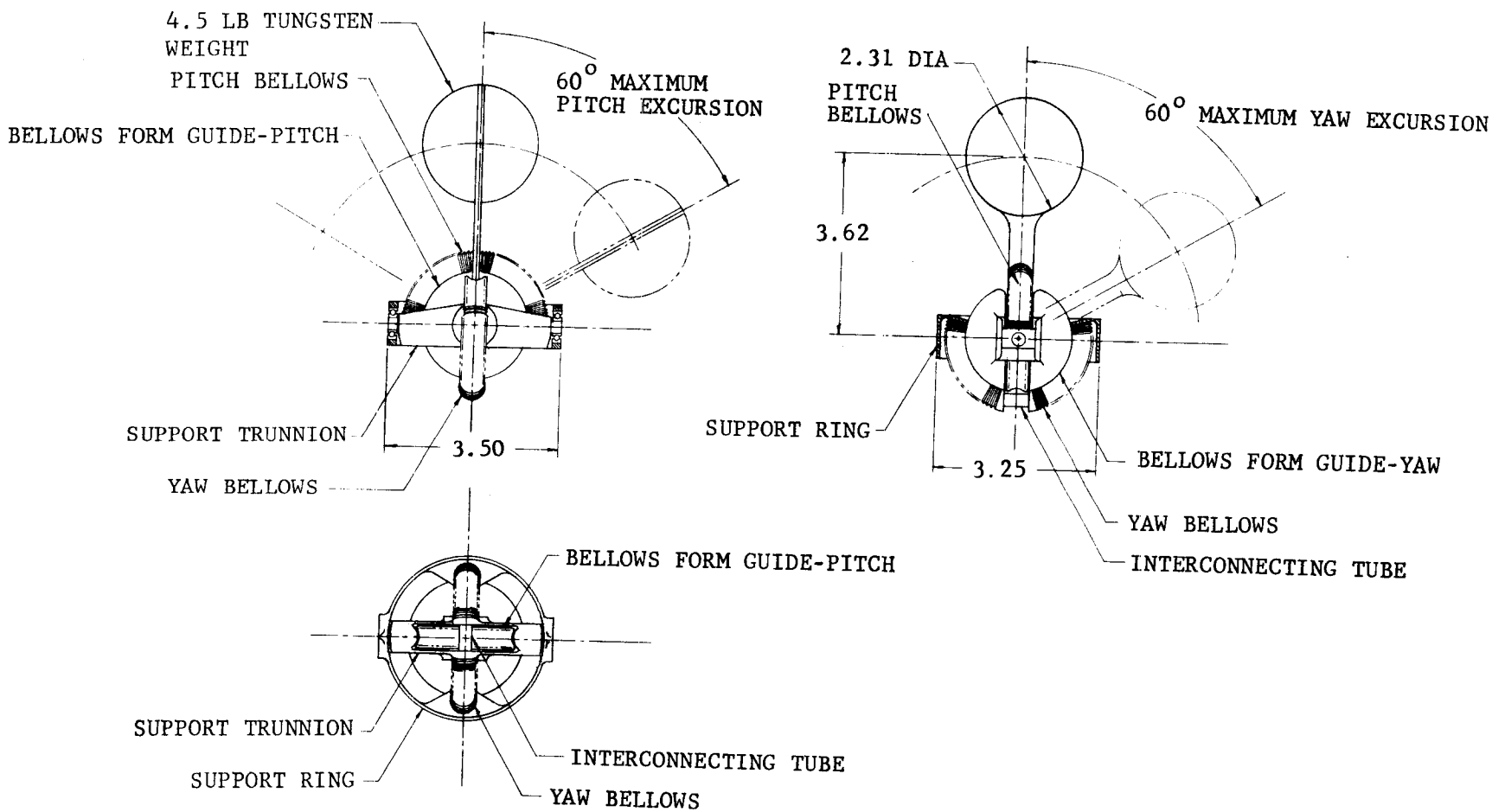

F03356 U

FIGURE 4-9. DETAIL DRAWINGS OF PIVOT-DASH POT MECHANISM

The dash pot consists of a bellows with a center orifice and a viscous fluid.* As the ball pitches (or yaws) the pitch (or yaw) bellows expands and contracts forcing the fluid back and forth through the orifice. The amount of damping is controlled by the viscosity of the fluid and the size of the orifice. The bellows design has no inherent sealing problems. Finally, there is little question that the pivot-dashpot mechanism could be built to weigh less than 1.5 pounds.

The pivot arrangement shown in Figures 4-8 and 4-9 does not permit the damper ball to roll. The effect of rolling appears as the factor 7/5 in the equations of motion. For the run shown in Figure 4-10, the effect of the ball rolling was removed. A comparison between Figures 4-10 and 4-7 indicates some but not decisive changes in the damper performance.

4.2.3 TWO-TUBE DAMPER DESIGN

Damper Design 4, shown in Figure 4-11, has two orthogonally mounted ball-in-tube dampers. Each tube contains a 2.1-inch diameter tungsten-carbide ball, which weighs 2.65 pounds and a gas. The forward tube lies in the yz plane. and the rearward tube lies in the xz plane. The path radius R is 4 inches and the mean value for D is 22.3 inches. For this design, $k = 0.00622$, $b^2 = 1.972$, $\lambda = 5.575$, $\alpha_L = 55$ deg, $\epsilon = 0$, and $\mu_1/c = 1$.

The damper performance is illustrated in Figure 4-12. The θ envelope is reduced to 5.1 degrees by $\tau = 62.5$.

Two nonlinear fluid drag laws, which approximate the linear law used in Run 47, are shown in Figure 4-13. The fluid is air in both nonlinear laws. However, the gap ratios are different; $\lambda_g = 0.036$ and 0.05. The corresponding nonlinear damping coefficients are:

$$\mu_1/c = 0.114, \qquad \mu_2 = 0.0303, \qquad \mu_3 c = -9.7\times10^{-6} \text{ for } \lambda_g = 0.036$$

$$\mu_1/c = 0.0593, \qquad \mu_2 = 0.0187, \qquad \mu_3 c = 2.55\times10^{-6} \text{ for } \lambda_g = 0.05$$

The θ envelopes obtained using the two nonlinear drag laws are almost identical to the θ envelope shown in Figure 4-12.

---

*The bellows arrangement was conceived by W. Bachle of Aeronutronic.

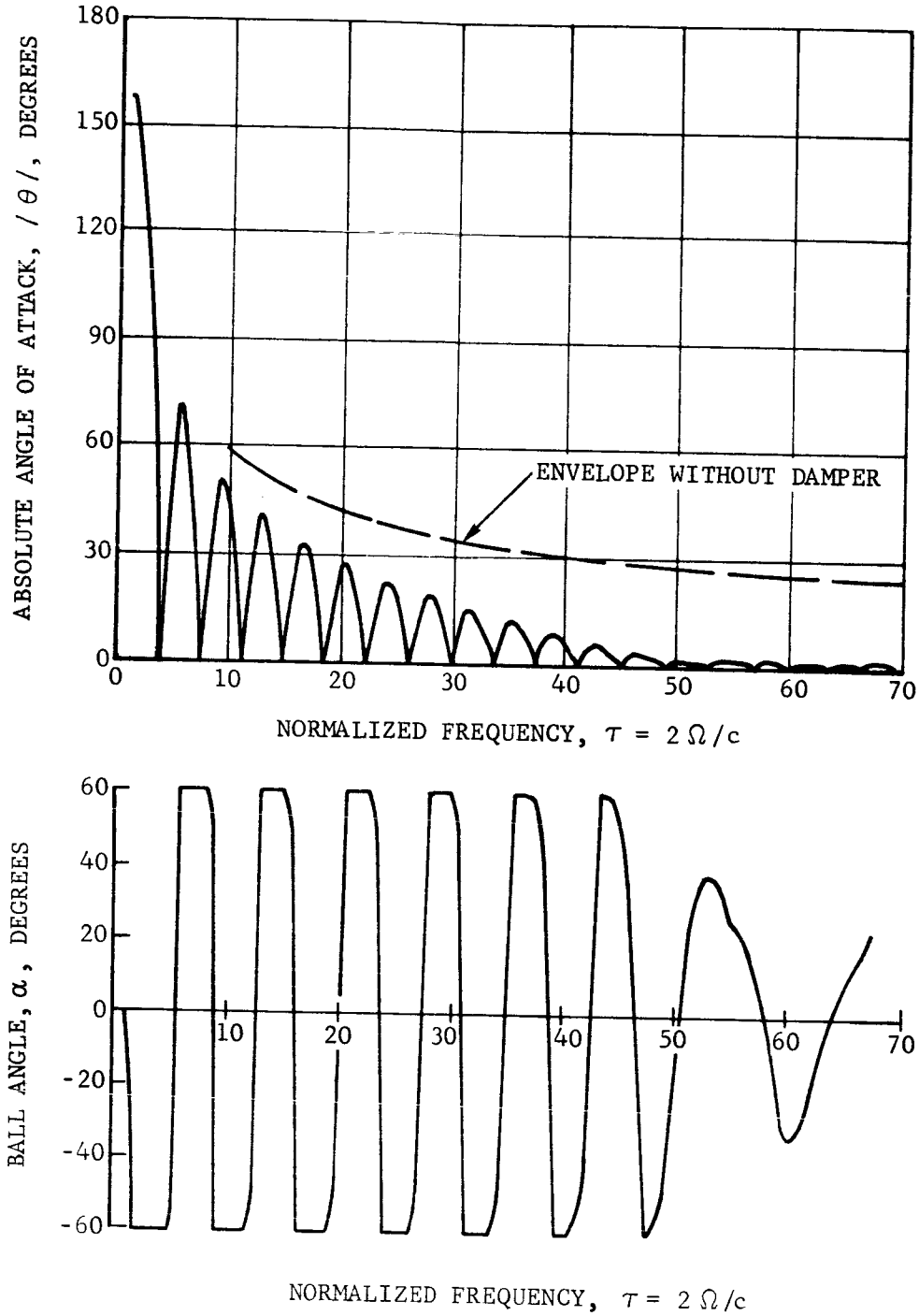

F03357 U

FIGURE 4-10. DAMPER DESIGN 3 WITH μ_1 = 2 SEC^{-1} BUT WITHOUT ROLLING (RUN 51)

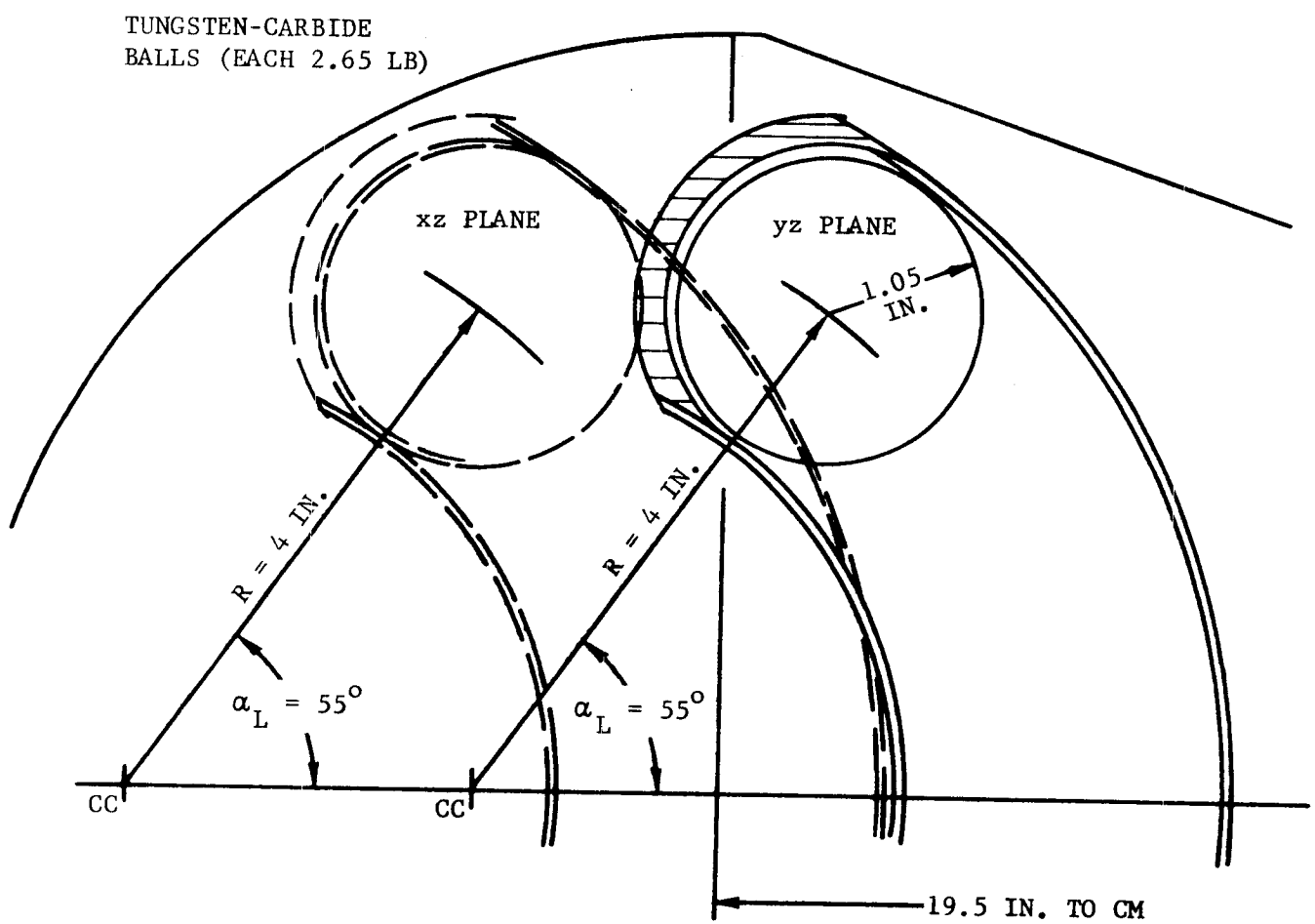

FIGURE 4-11. DAMPER DESIGN 4 (TWO ORTHOGONAL TUBES)

F03358 U

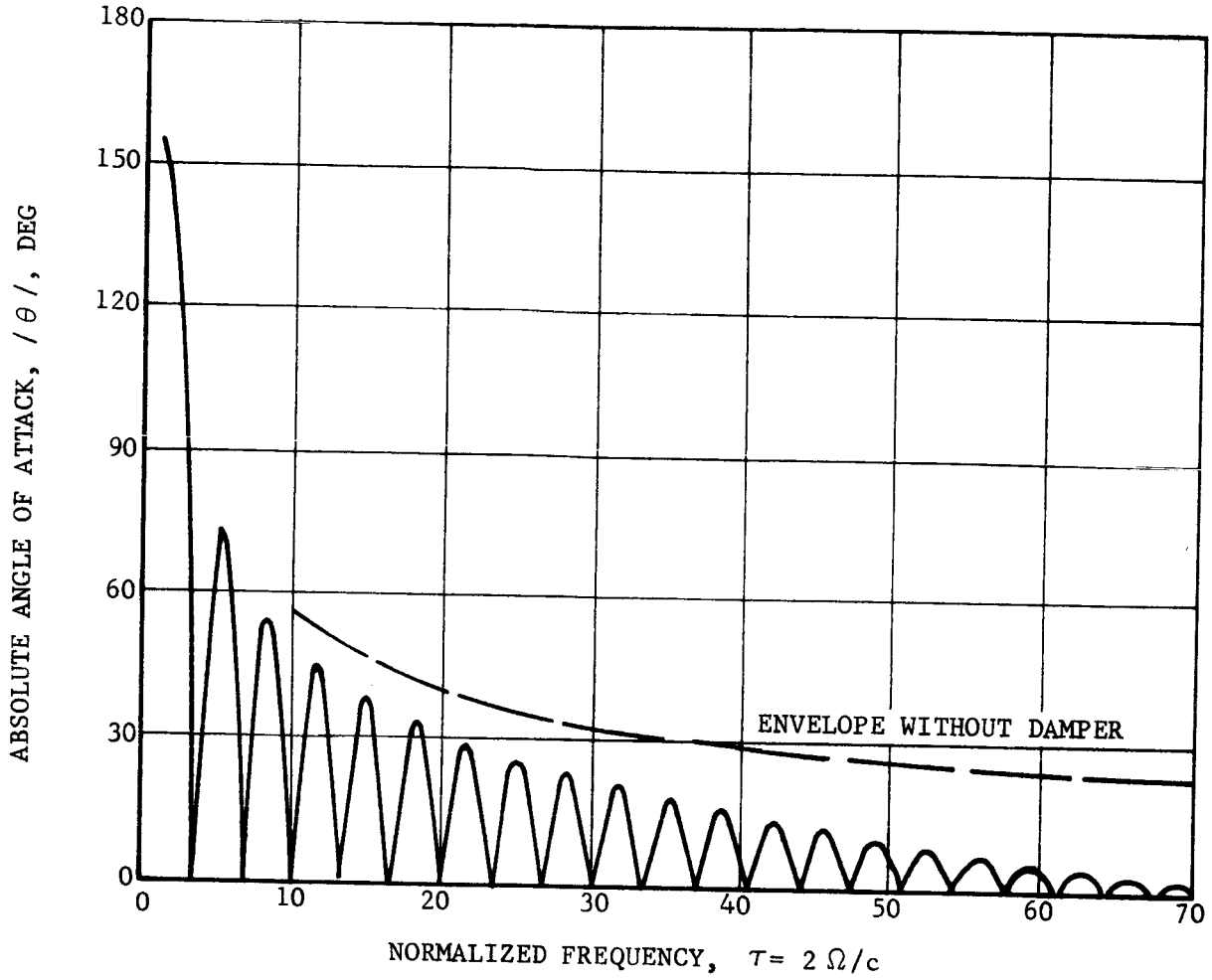

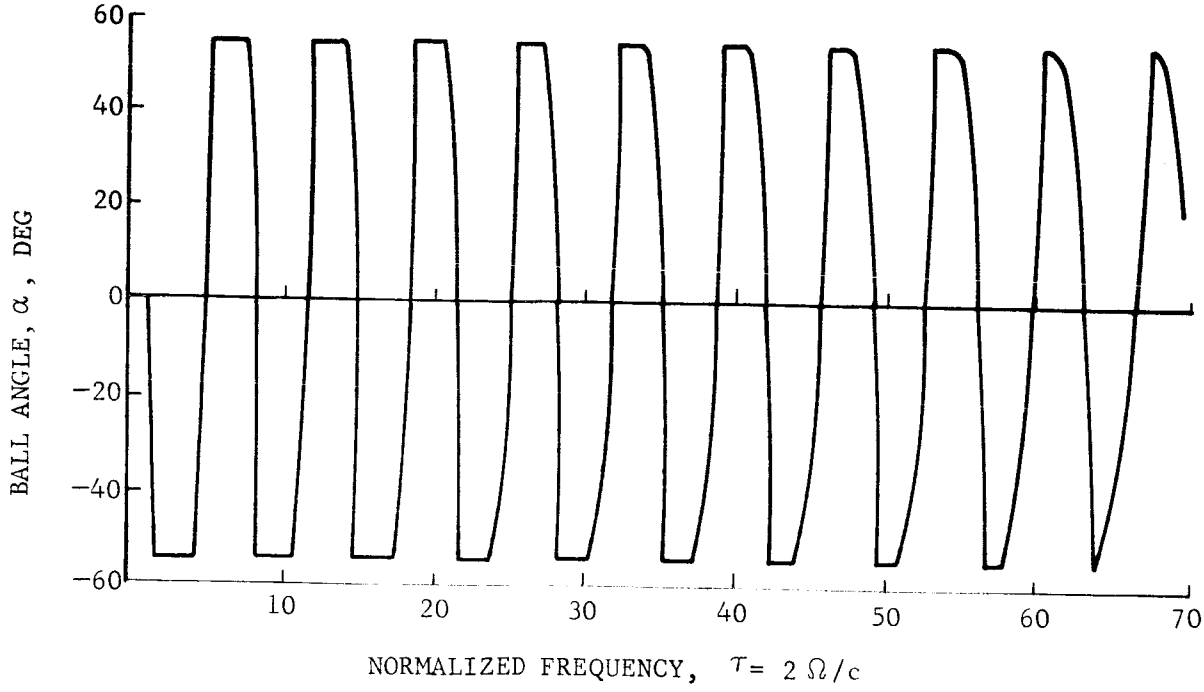

FIGURE 4-12. TWO TUBE DAMPER DESIGN 4 WITH μ_1 = 1 SEC^{-1} (RUN 47)

F02939 U

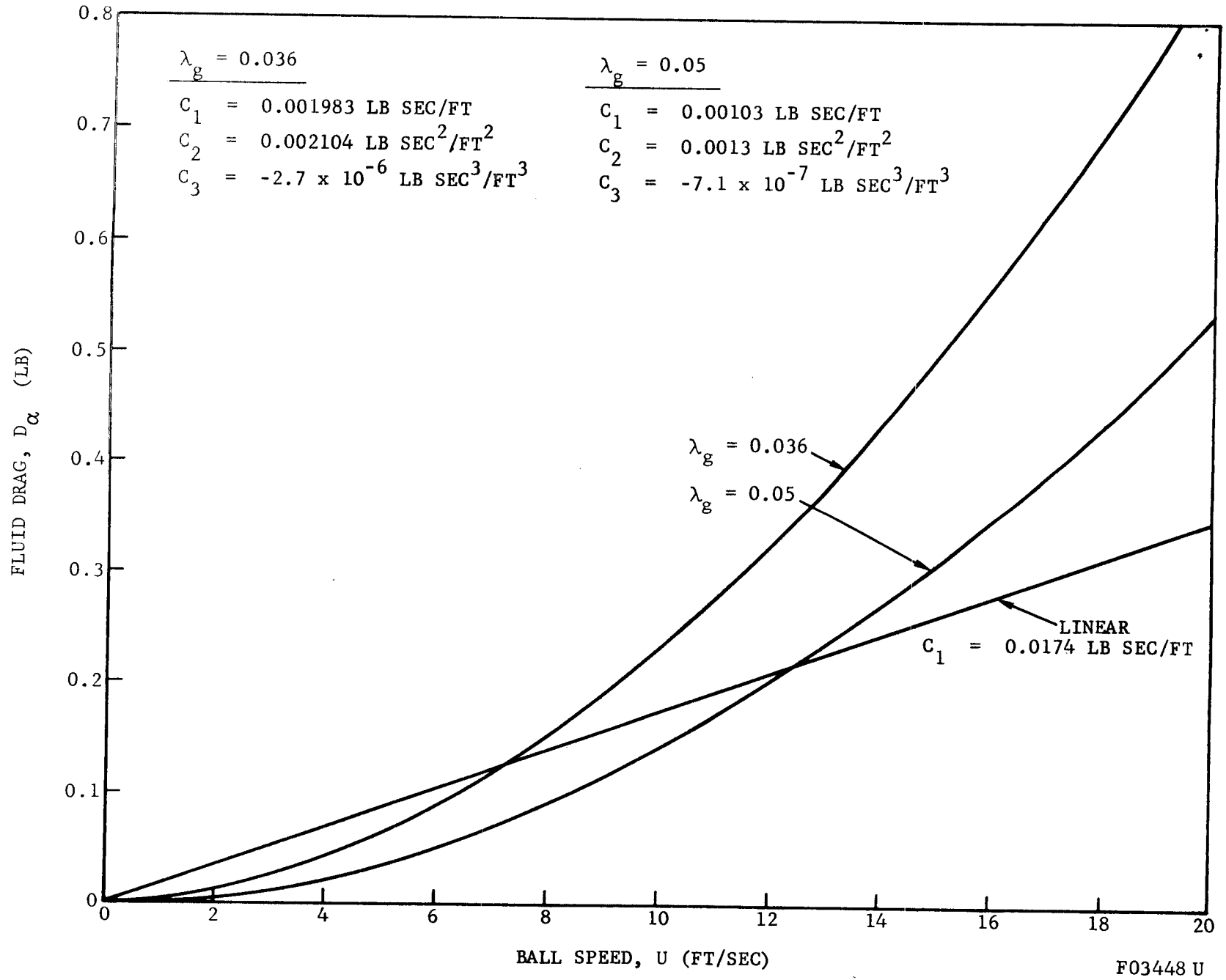

FIGURE 4-3. LINEAR AND NONLINEAR DRAG LAWS

SECTION 5

SMALL EARTH RE-ENTRY CONE

5.1 VEHICLE DESCRIPTION AND DYNAMICS

The dynamics of a small spinning Earth re-entry body with a pair of orthogonal dampers is examined. The vehicle, which weighs about the same as the Ames probe, is fictitious. It is a slender cone, 2.5 ft long, with a half cone angle of 10 degrees and a base area of 0.61 ft^2. The CP is located 1.72 ft aft of the cone apex and the CM is 0.15 ft (or 6 percent of the cone length) forward of the CP. The vehicle mass M is 1.14 slug, the pitch (and yaw) inertia I is 0.561 slug ft^2 and the roll inertia J is 0.0561 slug ft^2.

The reference area S is 0.61 ft^2 and the reference length ℓ is 2.5 ft. The axial force coefficient C_A and the normal force coefficient C_N, based on Newtonian theory*, are plotted in Figure 5-1. The moment coefficient C_m, about the CM, is -0.06 C_N. The dashed line curves in Figure 5-1 are given by

$$C_A = 0.0605 + 0.518 \sin\theta - 0.128 \sin 2\theta + 0.092 \sin 3\theta - 0.1006 \sin 4\theta$$

$$C_N = 2.33 \sin\theta + 0.1099 \sin 2\theta - 0.15344 \sin 4\theta$$

which expressions were used in the computer runs.

*White, C. O., "Generalized Representation of Cone Force Coefficients by Newtonian Theory," EATN-1, Internal Aeronutronic Document, August 1963.

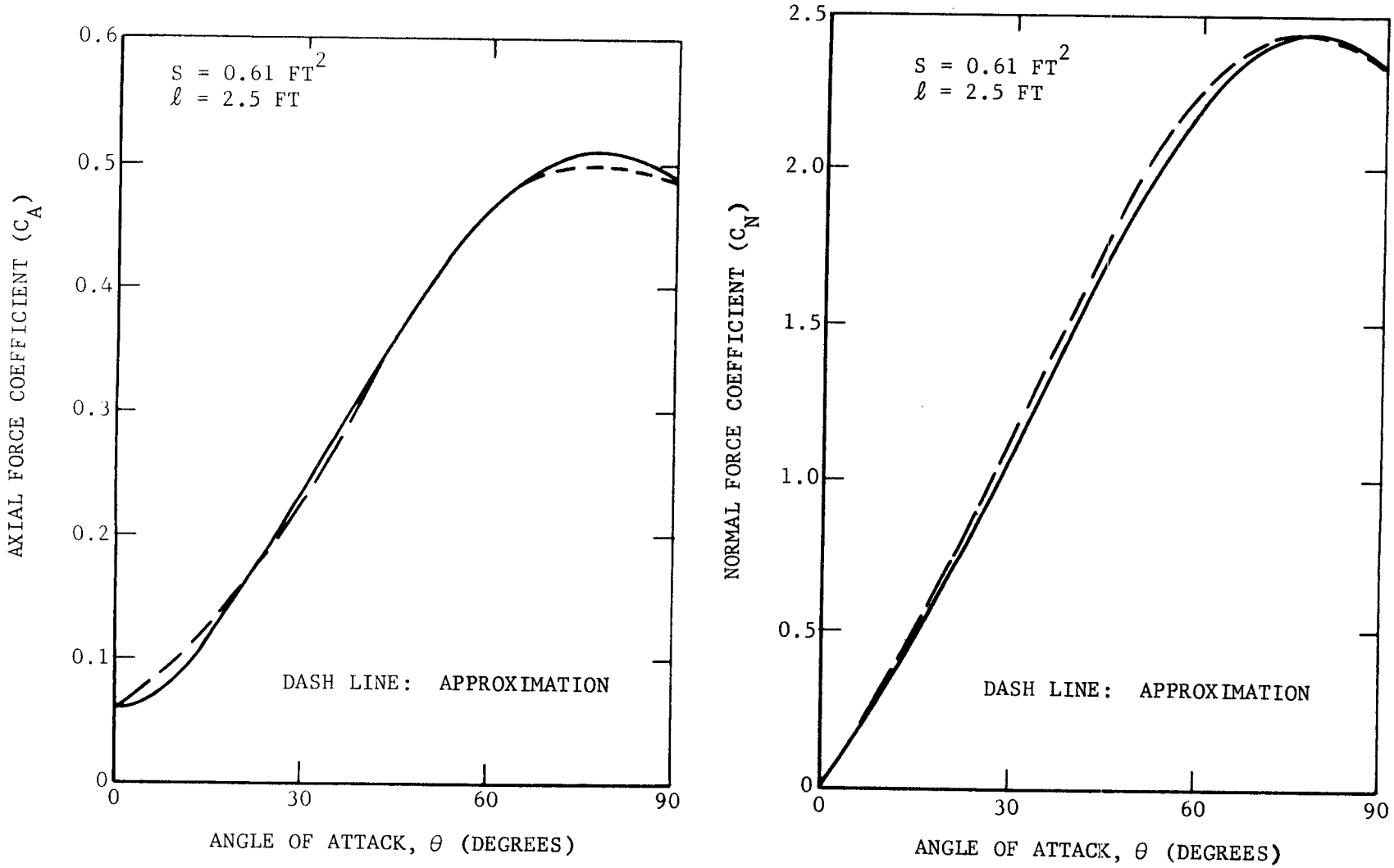

F03449 U

FIGURE 5-1. AXIAL AND NORMAL FORCE COEFFICIENTS
(SMALL EARTH RE-ENTRY CONE)

The atmospheric density profile is approximated by the exponential function $\rho = \rho_* e^{-\beta h}$ where $\rho_* = 2.378 \times 10^{-3}$ slug/ft^3 and $\beta^{-1} =$ 22,000 ft. The entry conditions are $v_o = 22{,}000$ ft/sec, $\gamma_o = 22$ deg and $h_o = 381{,}000$ ft. The vehicle spins at 60 rpm and enters the atmosphere with $\theta_o = 40$ degrees. The velocity v, the dynamic pressure q and the angle of attack θ are plotted in Figure 5-2 as functions of altitude for the above entry conditions.

5.2 DAMPER DESIGN AND PERFORMANCE

5.2.1 NOMINAL DESIGN

The nominal damper design has two orthogonal damper tubes each containing a 1 pound tungsten-carbide ball and a gas. The ball diameter is 1.52 inches and the mean path radius R is 2 inches. This is not a tuned damper. The angle limit α_L is set at 39 degrees to reduce the wobble amplitude when the balls are at the stops. The limits are represented as inelastic. The vehicle damper-geometry is shown in Figure 5-3. The rearward damper lies in the yz plane with its CC 10.8 inches aft of the CM, and the forward damper lies in the xz plane with its CC 9.05 inches aft of the CM. For these specifications, $k = 0.001546$, $b^2 = 0.84$, $\lambda_1 = 5.4$, $\lambda_2 = 4.525$, $\alpha_L = 39$ degrees, and $\epsilon = 0$.

5.2.2 DAMPER PERFORMANCE

The angle of attack profiles for the linear damping coefficient $\mu_1 =$ 2, 5, and 20 sec^{-1} are illustrated in Figures 5-4a, b, and c, respectively. The main differences in these plots are the θ trim angles; 1.98 degrees for $\mu_1 = 2$ sec^{-1}, 0.84 degrees for $\mu_1 = 5$ sec^{-1} and 0.38 degrees for $\mu_1 = 20$ sec^{-1}. Examination of the corresponding plots (Figures 5-5a, b, and c) for α_1 and α_2 show that the balls oscillate about and converge to the centers of their respective tubes. This is the same behavior observed in the study of the blunt Ames probe.

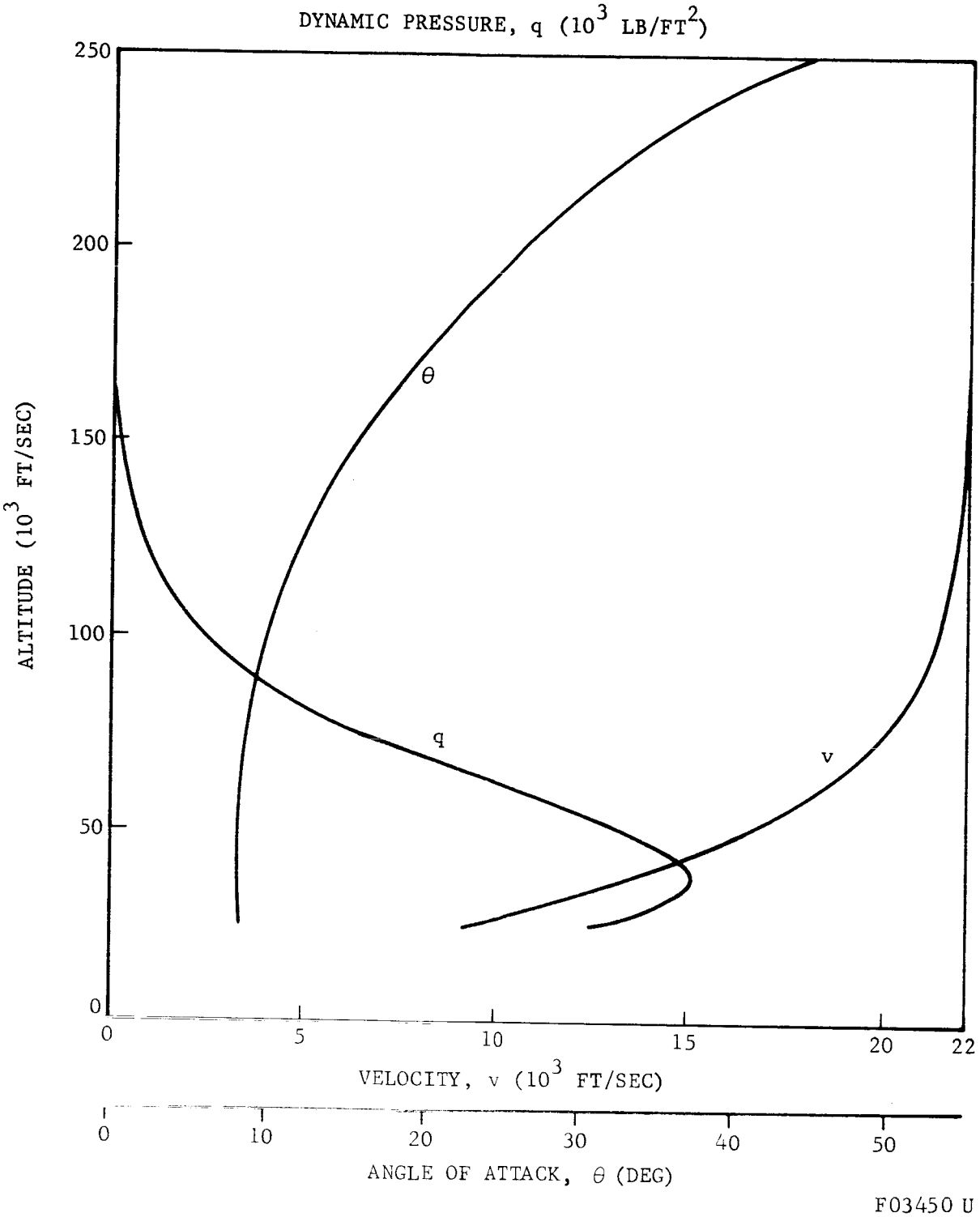

FIGURE 5-2. VELOCITY, DYNAMIC PRESSURE, AND ANGLE OF ATTACK PROFILES FOR THE NOMINAL ENTRY CONDITIONS (RUN 1)

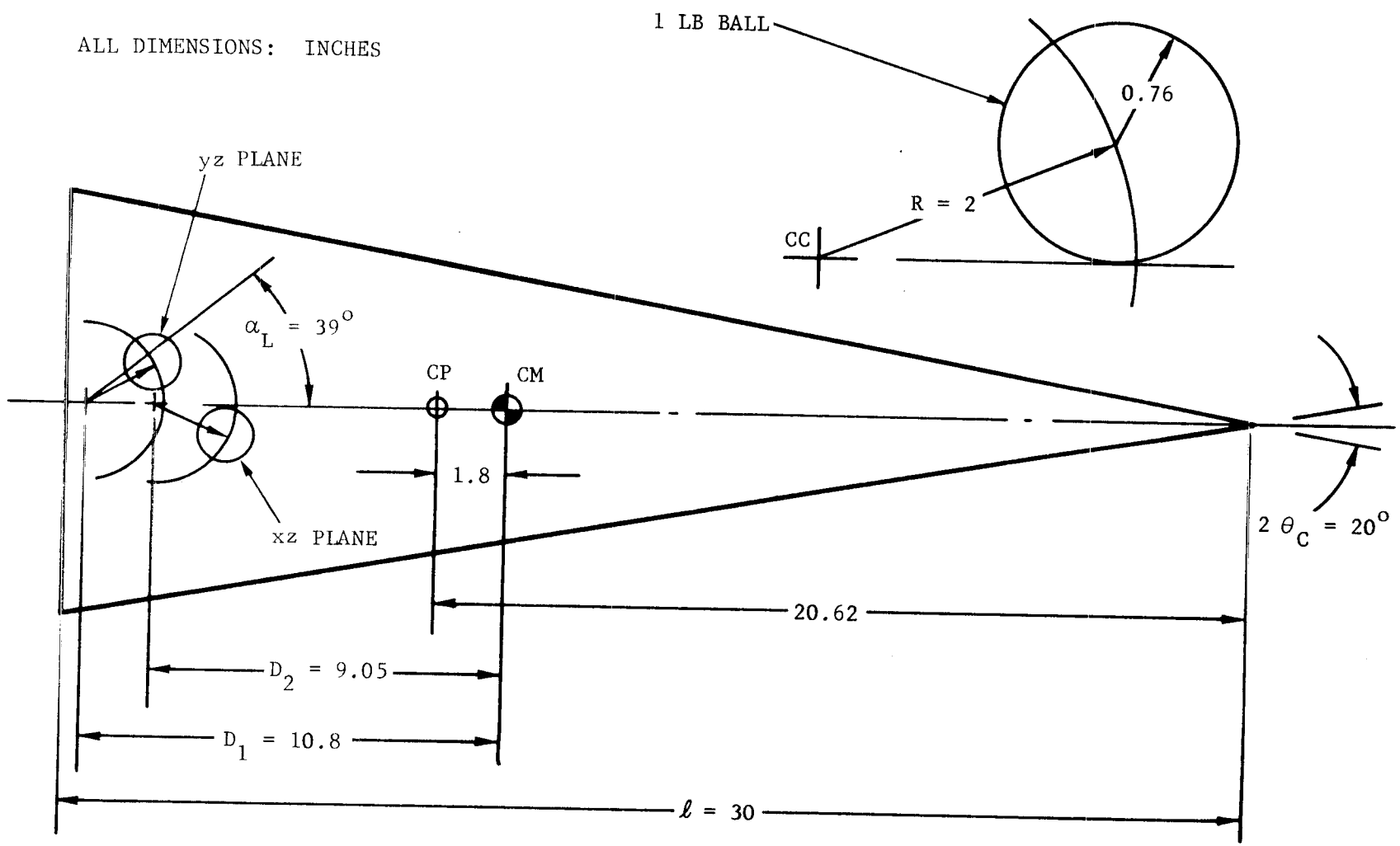

FIGURE 5-3. VEHICLE-DAMPER GEOMETRY

F03452 U

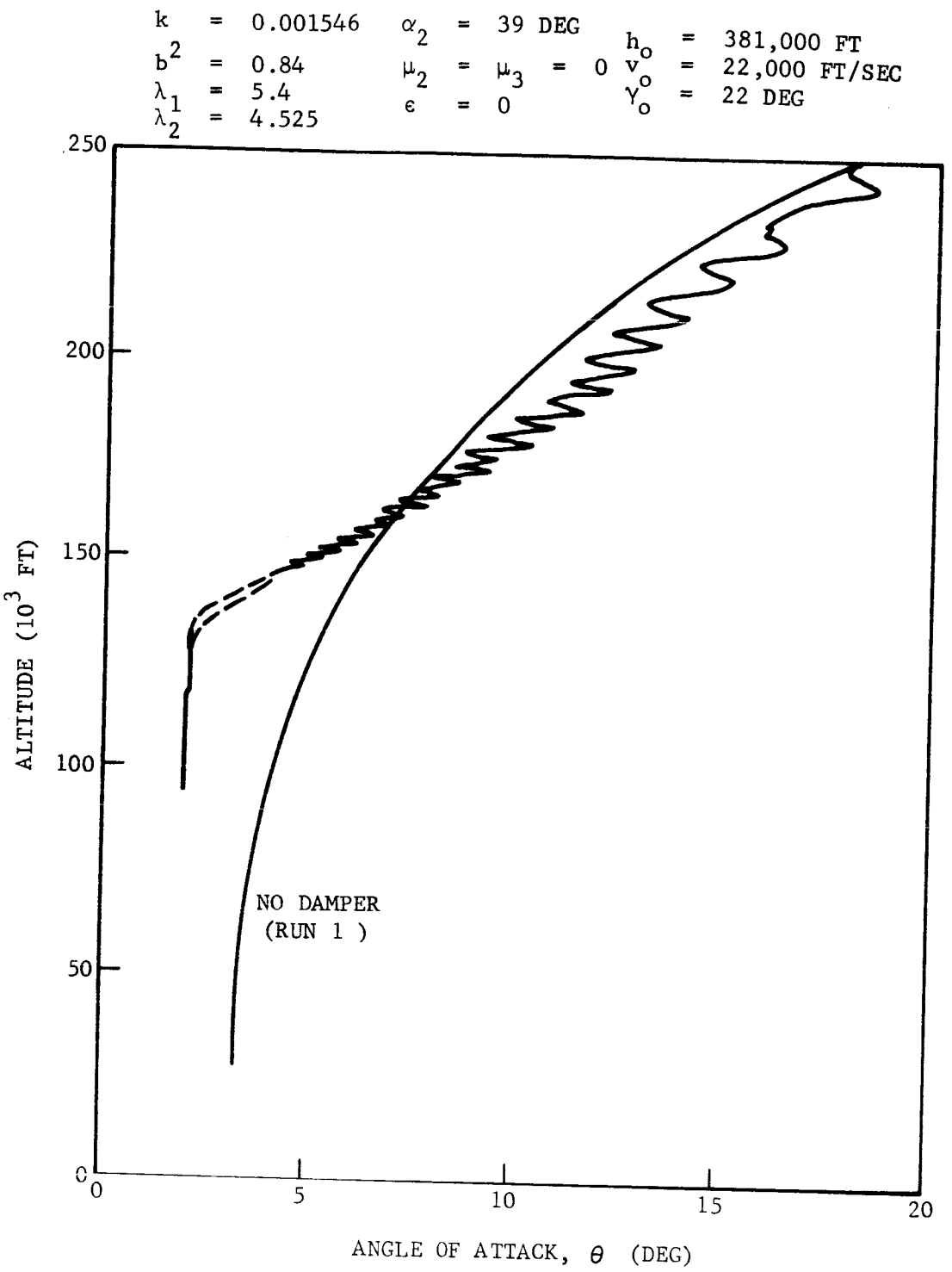

F03451 U

FIGURE 5-4a. NOMINAL DAMPER DESIGN WITH μ_1 = 2 SEC^{-1} (RUN 9)

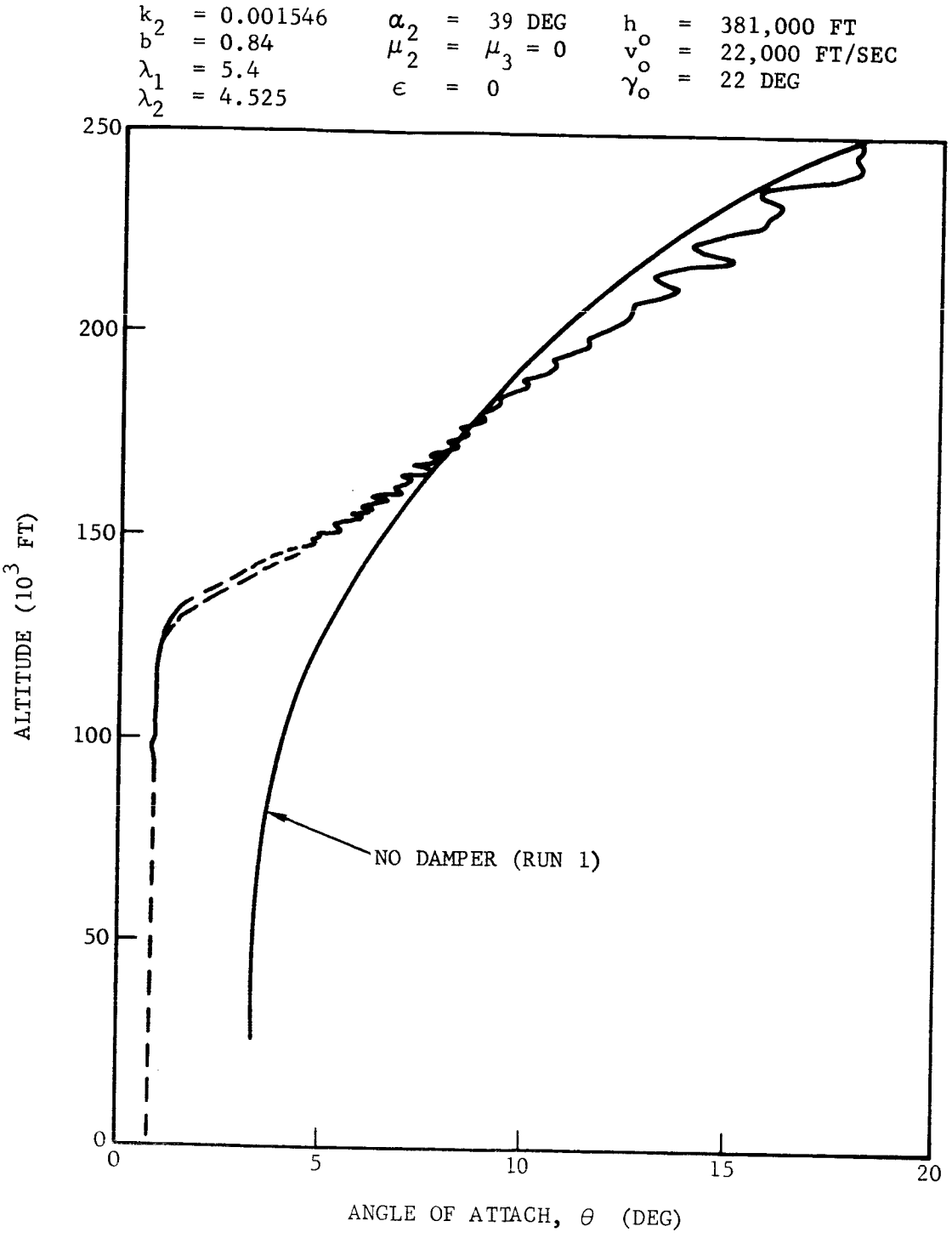

F03453 U

FIGURE 5-4b. NOMINAL DAMPER DESIGN WITH μ_1 = 5 SEC^{-1} (RUN 10)

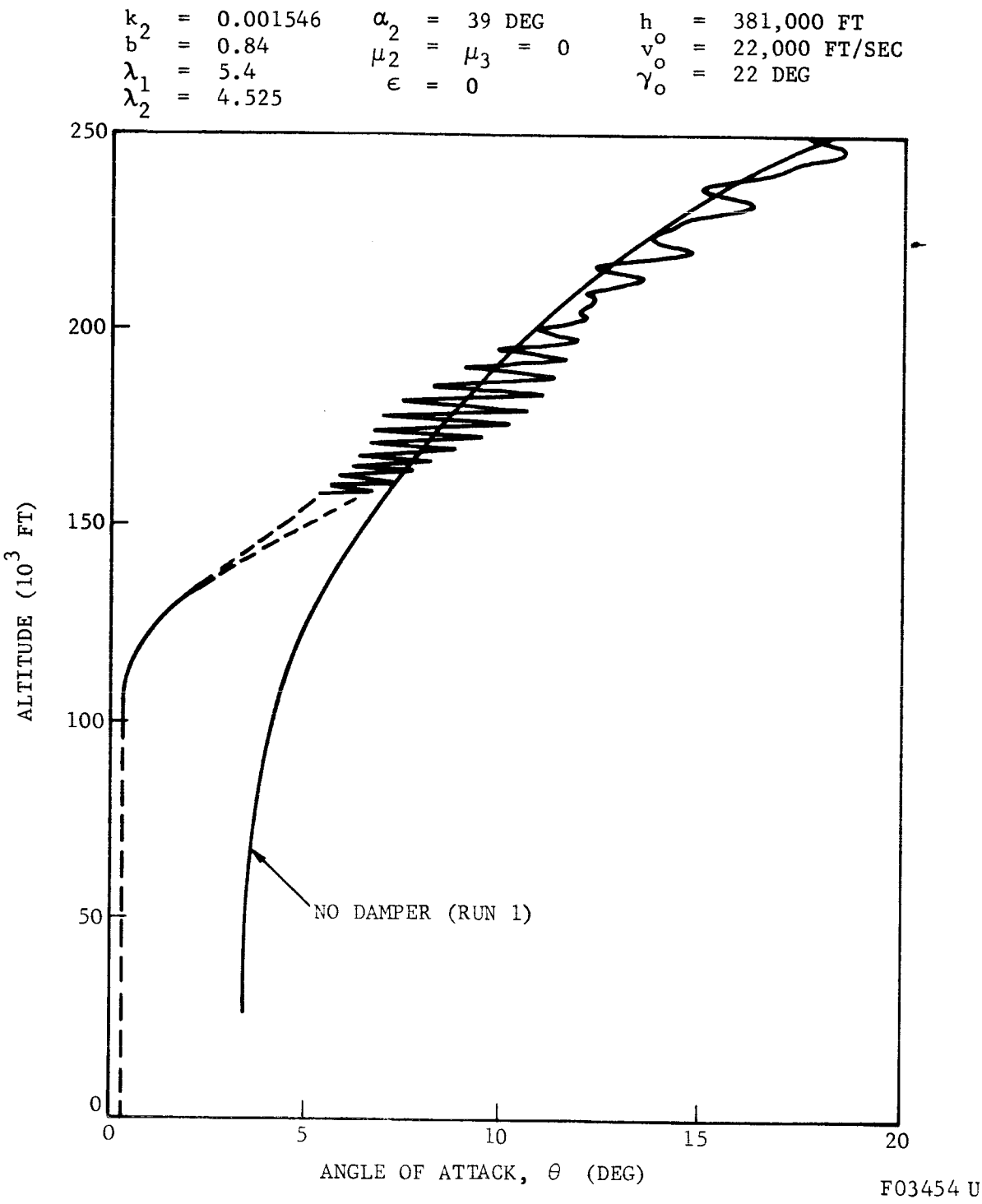

FIGURE 5-4c. NOMINAL DAMPER DESIGN WITH μ_1 = 20 SEC^{-1} (RUN 13)

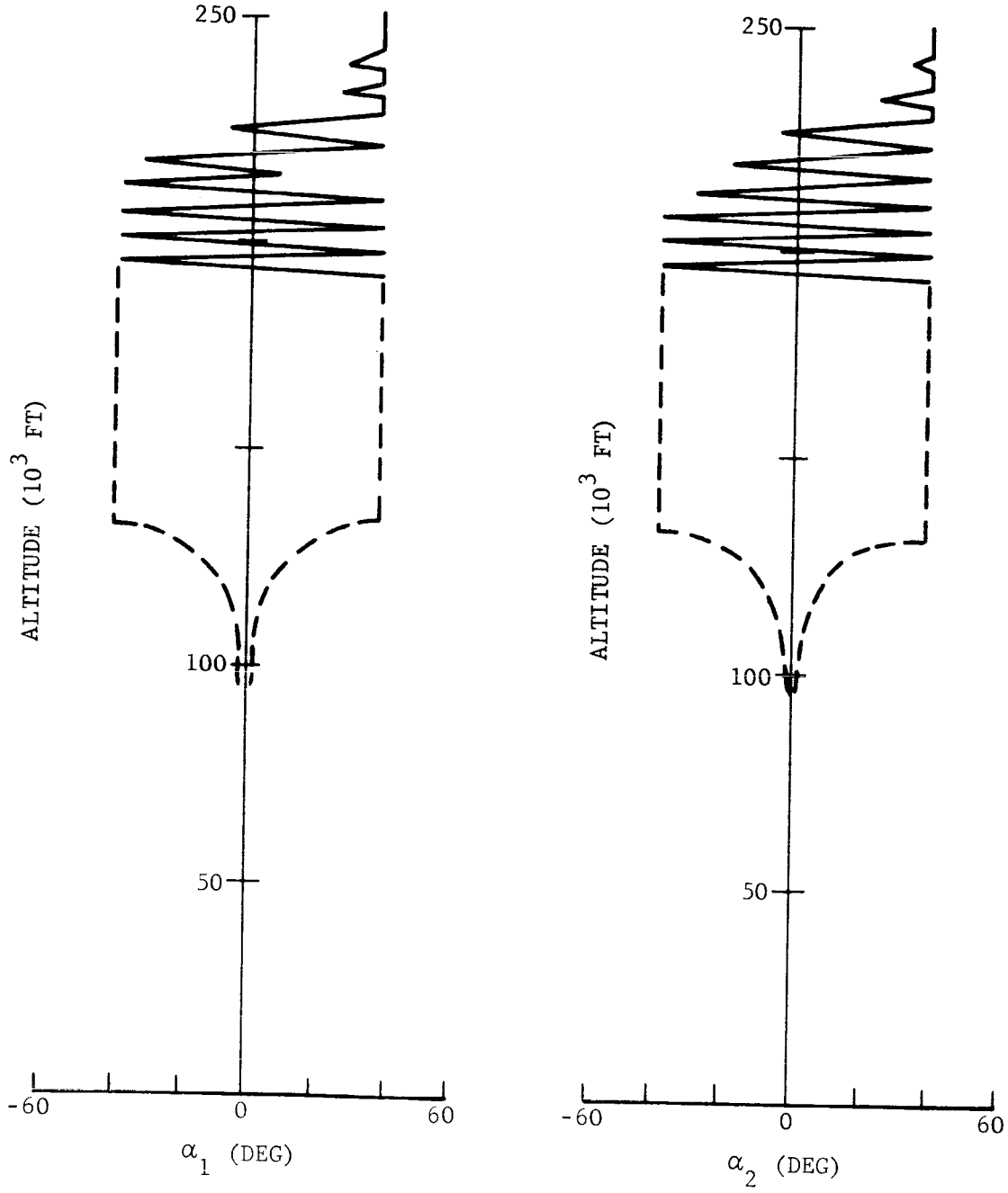

F03455 U

FIGURE 5-5a. BALL MOTIONS FOR μ_1 = 2 SEC^{-1} (RUN 9)

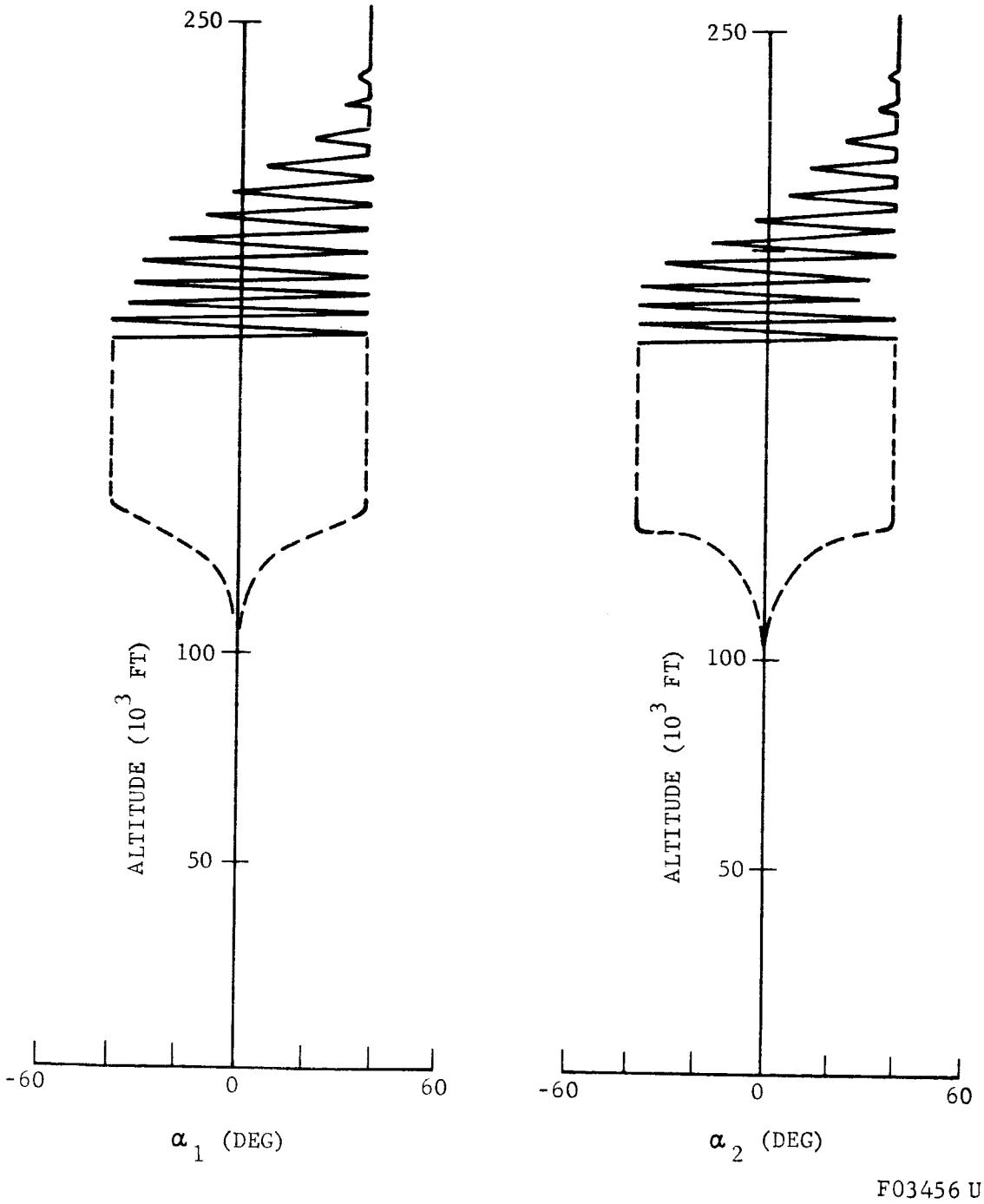

FIGURE 5-5b. BALL MOTIONS FOR μ_1 = 5 SEC^{-1} (RUN 10)

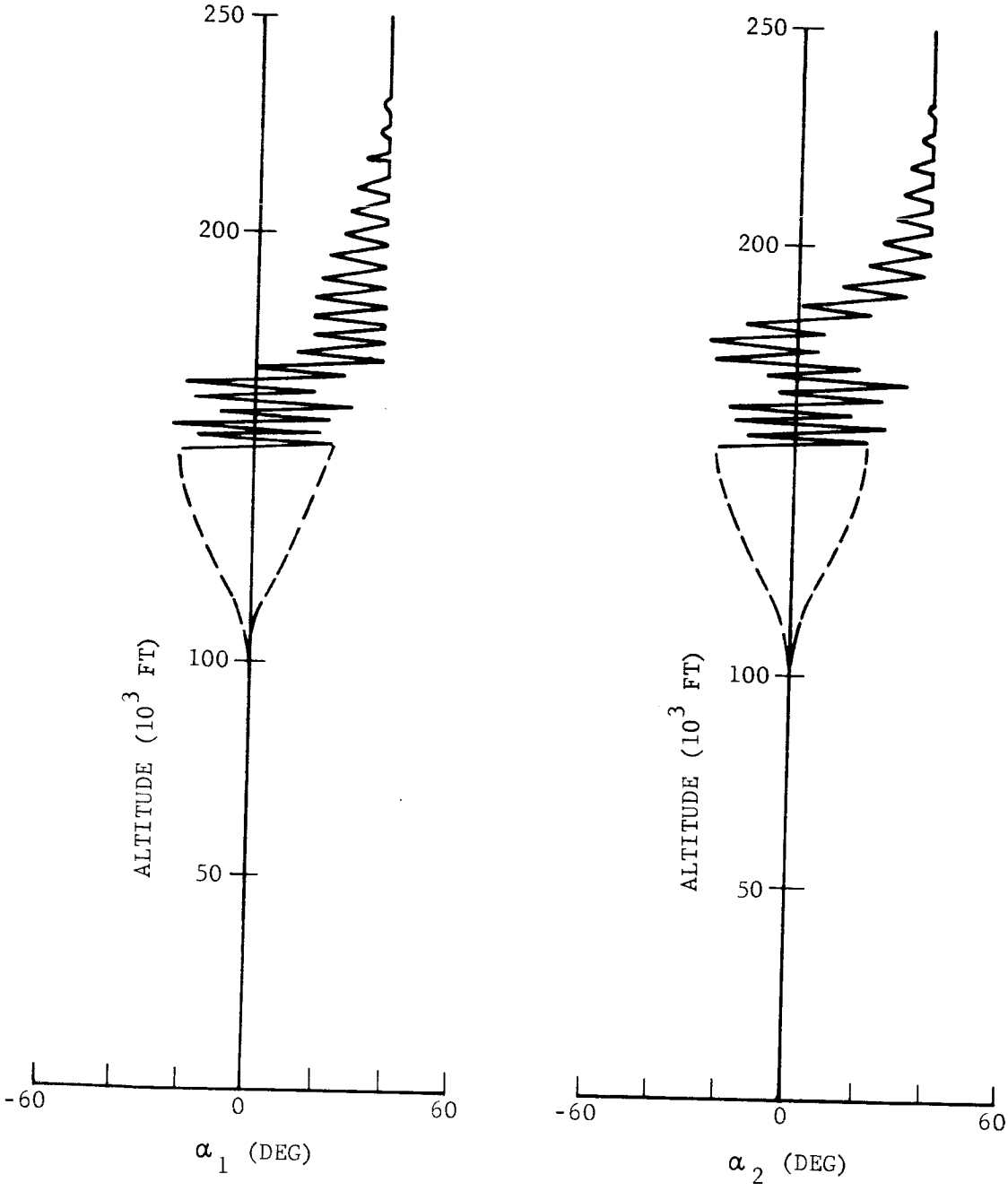

F03457 U

FIGURE 5-5c. BALL MOTIONS FOR μ_1 = 20 SEC^{-1} (RUN 13)

The spin rate ω_z is the z component of the total angular velocity $\overline{\omega}$. Using the nominal damper design, the spin rate decreases to a steady value which depends on μ_1. This effect is shown in Figure 5-6. The point at which the steady-state value for ω_z is reached corresponds closely to the altitude at which θ reaches its trim value. The spin-reduction can be quite significant. A similar phenomena was observed for the Ames probe but in that case ω_z went from 30 to 28 RPM, a relatively small change.

The precession rate $\dot{\varphi}$ is the rate at which the z axis cones about the velocity vector $\overline{v}$. For positive ω_z and a statically stable body $\dot{\varphi}$ is negative and decreases as dynamic pressure increases. The effect of the damper is to drive $\dot{\varphi}$ to zero at approximately the same altitude at which θ reaches its trim value. This is shown by the precession rate envelope plots in Figure 5-7.

We now have a clear picture of the steady state trim conditions; the vehicle spins at a reduced rate without coning at a fixed value of θ. The trim values and the altitude at which they are reached depend on the damping coefficient.

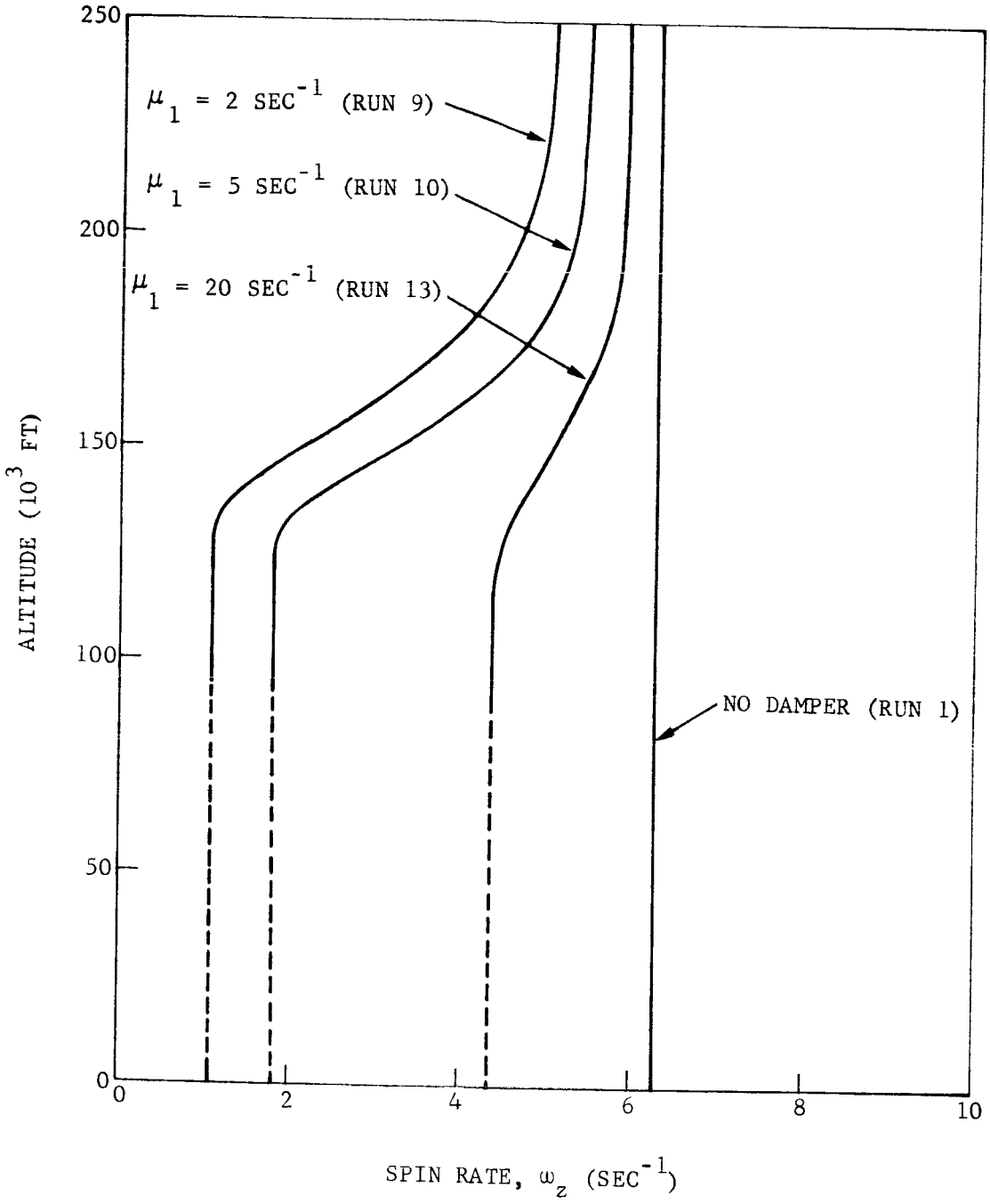

F03458 U

FIGURE 5-6. EFFECT OF DAMPING COEFFICIENT ON SPIN RATE

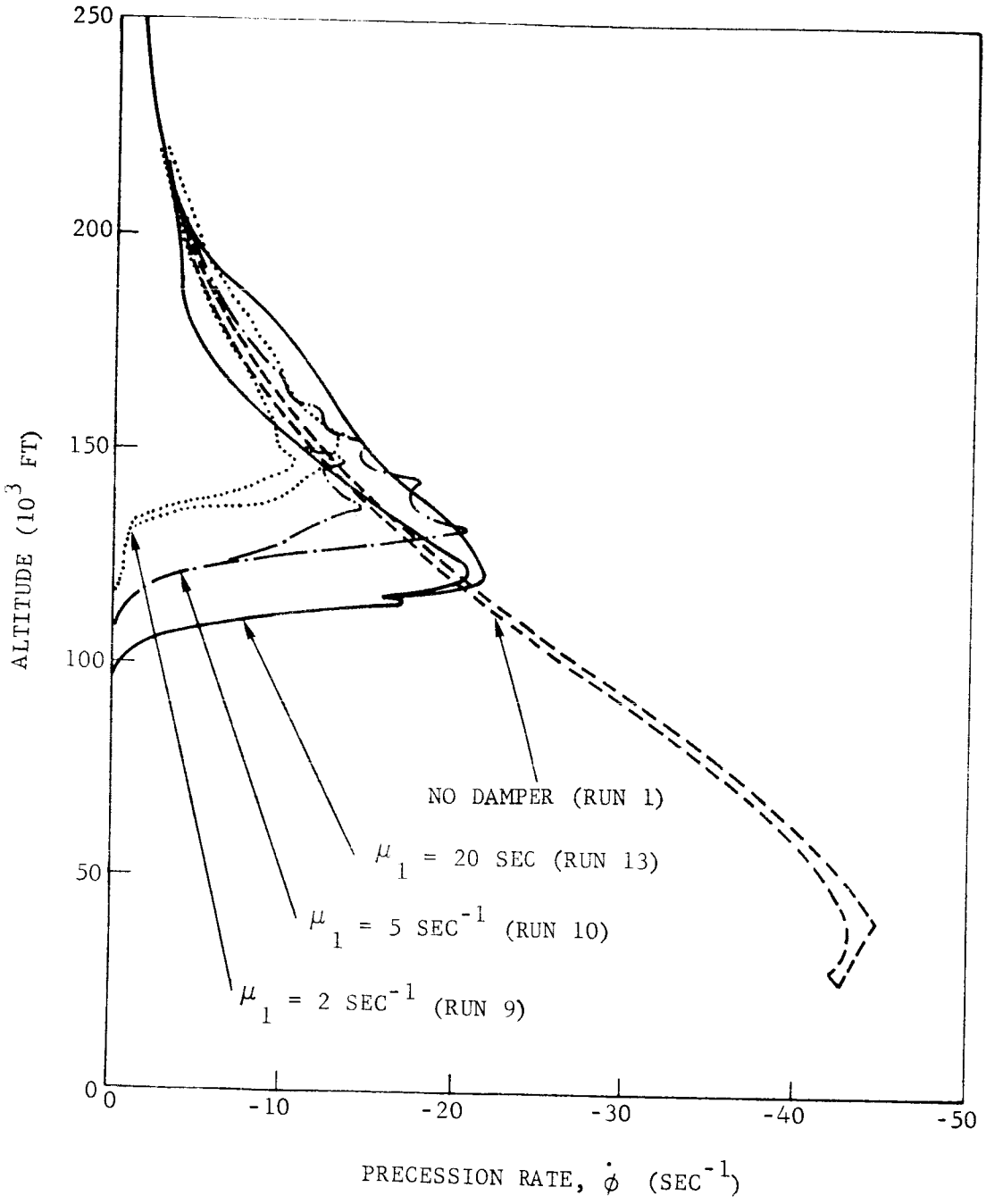

F03459 U

FIGURE 5-7. EFFECT OF DAMPING COEFFICIENT ON THE PRECESSION RATE ENVELOPE

SECTION 6

MODEL FOR THE VEHICLE-DAMPER DYNAMICS

6.1 INTRODUCTION

The mathematical model for the vehicle-damper dynamics is developed in this section. The mechanization of the model for solution on a digital computer is described in Section 7.

Because of the complexity of the forces of constraint between the damper balls and the vehicle, the problem of deriving the equations of motion, including the effects of spin and out-of-plane oscillations, is more than routine. In a strictly Newtonian formulation each of the bodies is isolated and all the forces acting on the body, including the constraint forces, must be expressed explicitly. Thus, for the vehicle one would write Euler's equations with external forces caused by aerodynamics and the damper balls. The forces caused by the damper balls are constraint forces and their correct formulation is of such difficulty as to render the Newtonian approach impractical.

In theory, the difficulties (of the Newtonian formulation) arising from the forces of constraint are overcome by using Lagrange's equations. In the Lagrangian formulation, the forces of constraint are automatically taken into account by employing a set of generalized coordinates, a set of dependent variables which are compatible with the forces of constraint and

yet completely define the motion of the system. A set of generalized coordinates for the system would include three Cartesian coordinates for the center of mass of the system, three Euler angles to orient the vehicle and an angle to locate each damper mass with respect to the vehicle centerline. The Lagrangian formulation would be ideal if it were not that the resulting equations are overwhelmingly complex. This complexity can be traced to the fact that the Euler angles are rotations about non-orthogonal axes.

The main difficulties of the Newtonian and Lagrangian formulations may be circumvented by using what might be best described as a "quasi-Lagrangian" formulation. The forces of constraint between the damper balls and the vehicle arise from two sources; the angular motion of the vehicle about the mass center and the acceleration of the mass center. Using a two-dimensional Lagrangian formation (Section 6.3), in which one damper mass and the vehicle oscillate in a fixed plane, rather simple expressions for the constraint forces caused by acceleration of the mass center were deduced.

This fact is used in the development of the three dimensional model in Section 6.4. Specifically, the forces of constraint caused by the acceleration of the mass center are treated as applied forces similar to the aerodynamic forces. This allows use to describe the motion about the mass center directly. To handle the forces of constraint caused by the angular motion of the vehicle about the mass center, we employ a Lagrangian-type formulation but use body-fixed angular rates rather than the Euler angle rates. The body-fixed angular rates are derivatives of quasi-variables, that is, they are not exact differentials. Their use is described by Whittaker.* However, we go beyond Whittaker's discussion in that true generalized coordinates and quasi-variables are mixed in the formulation. The validity of this approach is easy to establish. The resulting equations while admittedly complex, are nevertheless manageable.

---

*Whittaker, E. T., Analytical Dynamics, 4th Edition, Cambridge University Press, 1937, pp 41-44.

The model developed in Section 6.4 was used to obtain most of the results in the study. It is based on the following assumptions:

(1) The vehicle has mass and aerodynamic symmetry.

(2) The aerodynamic coefficients vary only with angle of attack, that is, they are independent of changes in Mach number and Reynold's number.

(3) Aerodynamic damping caused by pitch and yaw rate damping derivatives can be ignored.

(4) Aerodynamic damping caused by the lift force can be ignored.

(5) Gravitational acceleration of the vehicle mass center can be ignored.

(6) The radius of curvature of the target planet surface is infinite.

(7) The damper masses are small compared to the vehicle mass.

(8) The ball radius is small compared to the mean path radius of the ball.

(9) The damper balls roll without slipping.

(10) Energy dissipation caused by rolling friction can be ignored.

An extended model, in which assumptions (1), (3), and (4) are removed, is developed in Section 6.5. This latter model was used to evaluate certain special effects.

6.2 GEOMETRY AND FORCES

6.2.1 VEHICLE GEOMETRY

The vehicle geometry is shown in Figure 6-1. The x*y*z* axis system is nonrotating with origin at the vehicle center of mass (CM). The z* axis

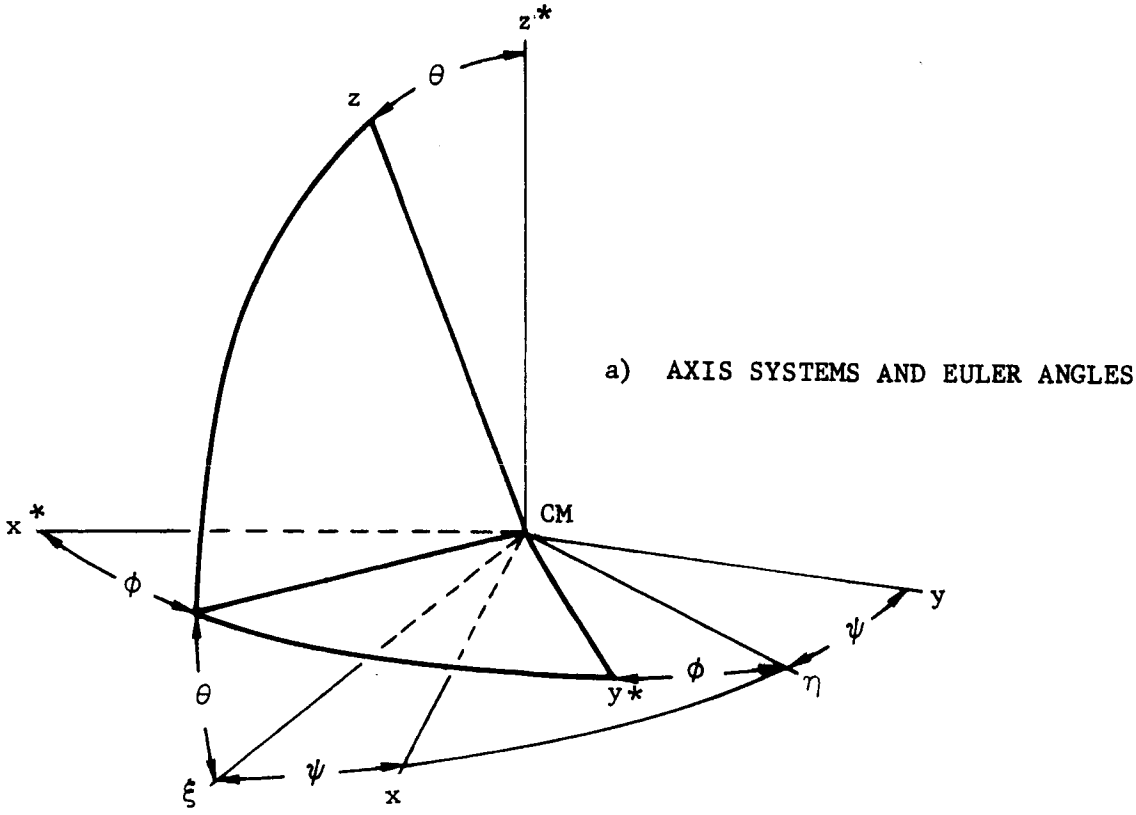

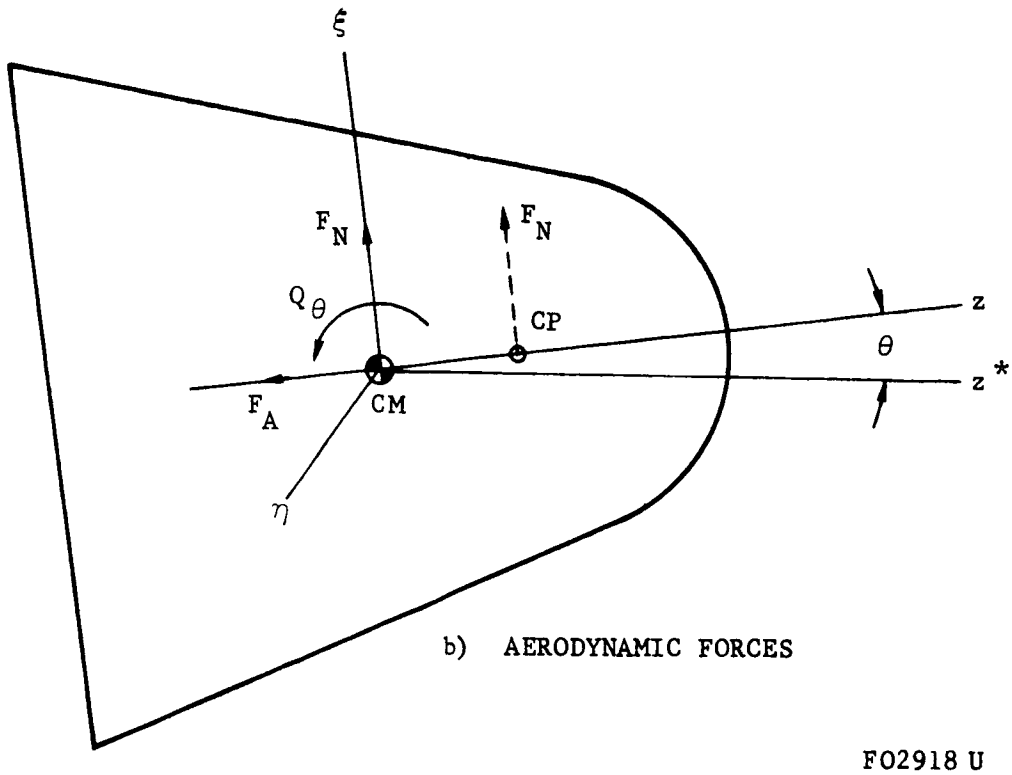

F02918 U

FIGURE 6-1. VEHICLE GEOMETRY AND FORCES

points in the direction of the vehicle velocity vector $\bar{v}$. The xyz axis system also with origin at the CM is fixed to the vehicle with z along the vehicle symmetry axis. The Euler angles ϕ about z*, θ about the nodal axis η and ψ about z define the orientation of xyz relative to x*y*z*. The transformation equations are

$$\begin{pmatrix} x \\ y \\ z \end{pmatrix} = \begin{pmatrix} \cos\psi & \sin\psi & 0 \\ -\sin\psi & \cos\psi & 0 \\ 0 & 0 & 1 \end{pmatrix} \begin{pmatrix} \cos\theta & 0 & -\sin\theta \\ 0 & 1 & 0 \\ \sin\theta & 0 & \cos\theta \end{pmatrix} \begin{pmatrix} \cos\phi & \sin\phi & 0 \\ -\sin\phi & \cos\phi & 0 \\ 0 & 0 & 1 \end{pmatrix} \begin{pmatrix} x^* \\ y^* \\ z^* \end{pmatrix} \quad (6\text{-}1)$$

Let $\bar{k}$ be a unit vector along $\bar{v}$. The xyz components of $\bar{k}$

$$k_x = -\cos\psi \sin\theta, \quad k_y = \sin\psi \sin\theta, \qquad k_z = \cos\theta \qquad (6\text{-}2)$$

are obtained from Equation (6-1). They correspond to direction cosines. The angle θ is the total angle of attack.

6.2.2 AERODYNAMIC FORCES

The aerodynamic forces are the only applied forces on the system. Let F_A denote the axial component of force in the -z direction and F_N denote the normal component force in the ξ direction where ξ is orthogonal to η and z. The functional forms for F_A and F_N are

$$F_A = qSC_A, \qquad F_N = qSC_N \qquad (6\text{-}3)$$

where q is the dynamic pressure, S is the vehicle reference area, C_A is the axial force coefficient and C_N is the normal force coefficient. C_A and C_N are functions of θ, and q is a function of time.

The normal force F_N acts through the center of pressure (CP) which in Figure 6-1 is shown forward of the CM. An equivalent force system is obtained by shifting F_N to the CM and introducing a torque

$$Q_\theta = qS\ell C_m \qquad (6\text{-}4)$$

about η where ℓ is the vehicle reference length and C_m is the moment coefficient. Q_θ is equal to the product of F_N and the distance between the

CM and CP, which distance may be a function of θ. For the cases considered in this report the CP is behind the CM in which case C_m is negative. Resolving Q_θ along x and y body axes we obtain

$$\left.\begin{aligned} G_x &= Q_\theta \sin\psi = Q_\theta k_y \left(1-k_z^2\right)^{-1/2} \\ G_y &= Q_\theta \cos\psi = -Q_\theta k_x \left(1-k_z^2\right)^{-1/2} \end{aligned}\right\} \quad (6\text{-}5)$$

6.2.3 DAMPER GEOMETRY

One damper is mounted in the yz plane and the other damper is mounted in the xz plane (Figure 6-2). Both dampers are identical with the same ball mass m and same ball path radius R. The subscripts 1 and 2 will refer to the dampers in the yz and xz planes, respectively. The angles α_1 and α_2 locate the two damper masses with respect to z. The center of curvatures (CC) for the tubes are located the distances D_1 and D_2 behind the CM. Since the tubes cannot intersect on the z axis D_1 and D_2 cannot strictly be equal, though the differences may be small. The coordinates of the damper masses are

$$\left.\begin{aligned} x_1 &= 0, & y_1 &= -R\sin\alpha_1, & z_1 &= R\cos\alpha_1 - D_1 \\ x_2 &= R\sin\alpha_2, & y_2 &= 0 & z_2 &= R\cos\alpha_2 - D_2 \end{aligned}\right\} \quad (6\text{-}6)$$

Let r_b be the ball radius and θ_b be the relative angle of rotation of the ball about its mass center with respect to z. The balls are assumed to roll without slipping. When the ball rolls on the forward wall of the tube the constraint equation is

$$-r_b\dot{\theta}_b = (R + r_b)\,\dot{\alpha}$$

and when the ball rolls on the back wall of the tube the constraint equation is

$$r_b\dot{\theta}_b = (R - r_b)\,\dot{\alpha}$$

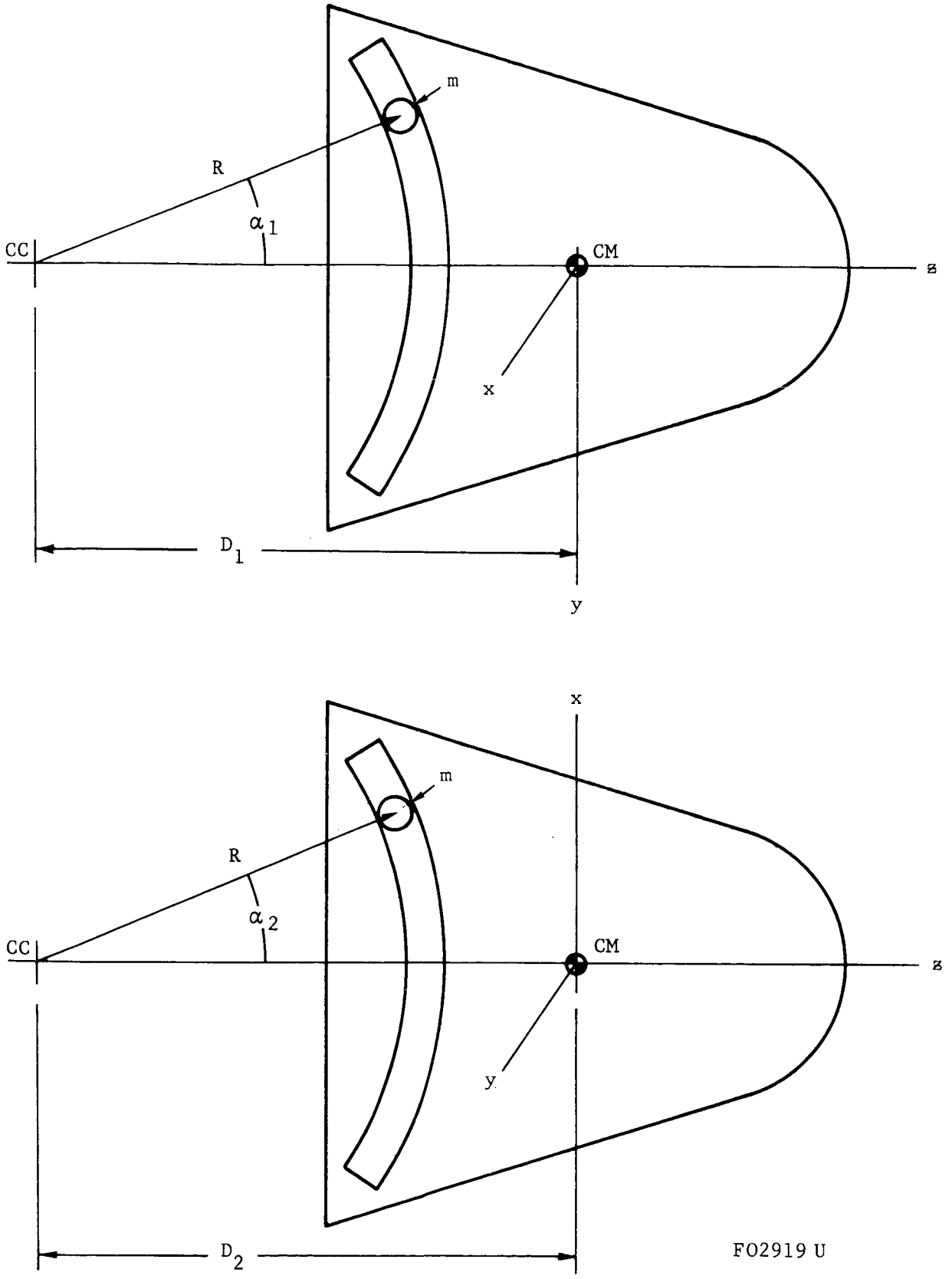

FIGURE 6-2. DAMPER GEOMETRY

For $r_b << R$ both constraint equations provide

$$\dot{\theta}_b^2 = \left(\frac{R}{r_b}\right)^2 \dot{\alpha}^2 \tag{6-7}$$

6.3 PLANAR MODEL

6.3.1 PLANAR GEOMETRY

Before considering the full-blown three-dimensional model, it is well to treat a special case in which the vehicle and one of the damper masses move in a single fixed plane. The geometry for the planar model is shown in Figure 6-3. The X and Z axes with origin at 0 define an inertial frame, that that is, 0 is unaccelerated and X and Z are nonrotating. The velocity $\bar{v}$ of the CM is assumed to be constant in direction and in the Z direction. By previous notation, Z is parallel to z*. The radius vector $\bar{\rho}$ locates the CM with respect to 0 and the radius vector $\bar{r}$ locates the ball with respect to the CM.

6.3.2 KINETIC ENERGY

The generalized coordinates for the system are ρ_X, ρ_Z, θ and α. Let M be the mass of the vehicle, m be damper mass and I be the moment of inertia of the vehicle about the CM. The kinetic energy of the vehicle is

$$T_a = \frac{1}{2} M\left(\dot{\rho}_X^2 + \dot{\rho}_Z^2\right) + \frac{1}{2} I \dot{\theta}^2 \tag{6-8}$$

The kinetic energy of translation for the damper mass is

$$T_b = \frac{1}{2} m \left[\left(\dot{\rho}_X + \dot{r}_X\right)^2 + \left(\dot{\rho}_Z + \dot{r}_Z\right)^2\right]$$

With

$$r_X = R\sin(\alpha+\theta) - D\sin\theta$$

$$r_Z = R\cos(\alpha+\theta) - D\cos\theta$$

$$\dot{r}_X = R(\dot{\alpha} + \dot{\theta})\cos(\alpha+\theta) - D\dot{\theta}\cos\theta$$

$$\dot{r}_Z = -R(\dot{\alpha} + \dot{\theta})\sin(\alpha+\theta) + D\dot{\theta}\sin\theta$$

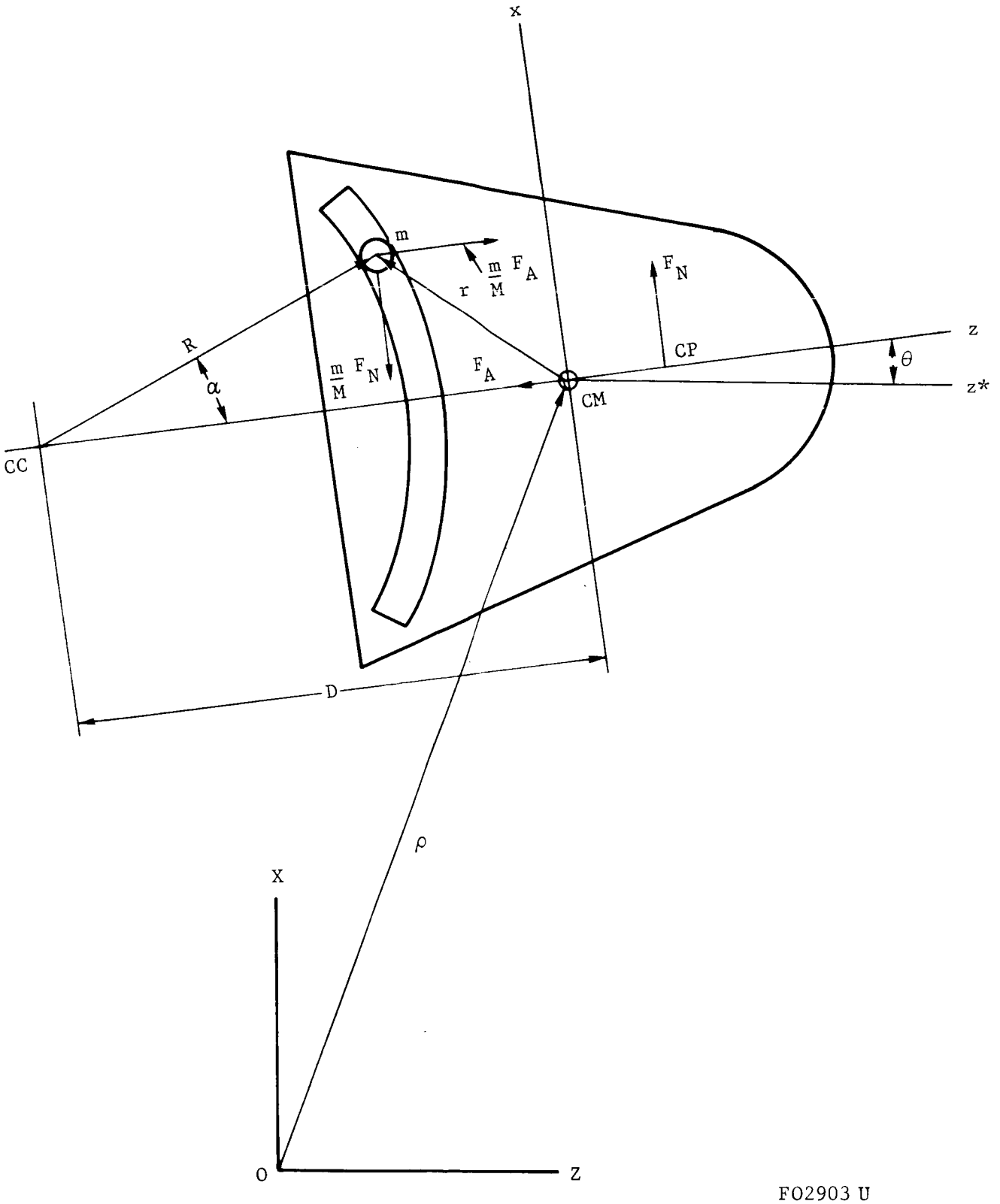

F02903 U

FIGURE 6-3. PLANAR MODEL GEOMETRY

the expression for T_b becomes

$$T_b = \frac{1}{2} m \left[\dot{\rho}_X + R(\dot{\alpha} + \dot{\theta})\cos(\alpha + \theta) - D\dot{\theta}\cos\theta \right]^2 + \frac{1}{2} m \left[\dot{\rho}_Z - R(\dot{\alpha} + \dot{\theta})\sin(\alpha+\theta) + D\dot{\theta}\sin\theta \right]^2 \tag{6-9}$$

In view of the constraint Equation (6-7), the kinetic energy of rotation of the ball about its mass center is

$$T_c = \frac{1}{2}\left(\frac{2}{5} m r_b^{\,2}\right)\left(\dot{\theta} + \dot{\theta}_b\right)^2 = \frac{1}{5} mR^2 \left(\dot{\alpha} + \frac{r_b}{R}\dot{\theta}\right)^2$$

Again invoking the condition $r_b << R$, the form for T_c reduces to

$$T_c = \frac{1}{5} m R^2 \dot{\alpha}^2 \tag{6-10}$$

The total kinetic energy of the system is thus given by

$$T = \frac{1}{2} M\left(\dot{\rho}_X^2 + \dot{\rho}_Z^2\right) + \frac{1}{2} I\dot{\theta}^2 + \frac{1}{5} mR^2\dot{\alpha}^2 + \frac{1}{2} m \left[\dot{\rho}_X + R(\dot{\alpha} + \dot{\theta})\cos(\alpha + \theta) - D\dot{\theta}\cos\theta\right]^2 + \frac{1}{2} m \left[\dot{\rho}_Z - R(\dot{\alpha} + \dot{\theta})\sin(\alpha + \theta) + D\dot{\theta}\sin\theta\right]^2 \tag{6-11}$$

6.3.3 LAGRANGE'S EQUATIONS

Langrange's equations for the four generalized coordinates ρ_X, ρ_Z, θ and α are

$$\left.\begin{aligned} &\frac{d}{dt}\frac{\partial T}{\partial \dot{\rho}_X} = F_X, \qquad \frac{d}{dt}\frac{\partial T}{\partial \dot{\rho}_Z} = F_Z \\ &\frac{d}{dt}\frac{\partial T}{\partial \dot{\theta}} - \frac{\partial T}{\partial \theta} = Q_\theta \qquad \frac{d}{dt}\frac{\partial T}{\partial \dot{\alpha}} - \frac{\partial T}{\partial \alpha} = -RD_\alpha \end{aligned}\right\} \tag{6-12}$$

where

$$\left.\begin{aligned} F_X &= -F_A\sin\theta + F_N\cos\theta \\ F_Z &= -F_A\cos\theta - F_N\sin\theta \end{aligned}\right\} \quad (6\text{-}13)$$

are the applied aerodynamic forces,

$$Q_\theta = qS\ell C_m \quad (6\text{-}14)$$

is the aerodynamic torque about the CM, and D_α is the fluid drag on the ball which we assume depends only on $\dot{\alpha}$.

With the assumption that $m \ll M$, the equations for ρ_X and ρ_Z can be approximated by

$$\left.\begin{aligned} M\ddot{\rho}_X &= -F_A\sin\theta + F_N\cos\theta \\ M\ddot{\rho}_Z &= -F_A\cos\theta - F_N\sin\theta \end{aligned}\right\} \quad (6\text{-}15)$$

Lagrange's equations for θ and α are

$$\begin{aligned} &I\ddot{\theta} + mR^2\left[(1-2\lambda\cos\theta+\lambda^2)\,\ddot{\theta} + (1-\lambda\cos\alpha)\,\ddot{\alpha} + \lambda(2\dot{\theta}+\dot{\alpha})\,\dot{\alpha}\sin\alpha\right] \\ &= qS\ell C_m - mR\left\{\ddot{\rho}_X\left[\cos(\alpha+\theta) - \lambda\cos\theta\right] + \ddot{\rho}_Z\left[-\sin(\alpha+\theta) + \lambda\sin\theta\right]\right\} \end{aligned} \quad (6\text{-}16)$$

$$\begin{aligned} &mR^2\left[\ddot{\alpha} + (1-\lambda\cos\alpha)\,\ddot{\theta} - \lambda\dot{\theta}^2\sin\alpha\right] + RD_\alpha \\ &= -mR\left[\ddot{\rho}_X\cos(\alpha+\theta) - \ddot{\rho}_Z\sin(\alpha+\theta)\right] \end{aligned} \quad (6\text{-}17)$$

where $\lambda = D/R$. Using Equation (6-15) to eliminate $\ddot{\rho}_X$ and $\ddot{\rho}_Z$, Equations (6-16) and (6-17) become

$$\begin{aligned} &I\ddot{\theta} + mR^2\left[\left(1-2\lambda\cos\alpha+\lambda^2\right)\ddot{\theta} + (1-\lambda\cos\alpha)\,\ddot{\alpha} + \lambda\,(2\dot{\theta}+\dot{\alpha})\dot{\alpha}\sin\alpha\right] \\ &= qS\ell C_m - \frac{m}{M}R\left[F_A\sin\alpha + F_N\,(\cos\alpha - \lambda)\right] \end{aligned} \quad (6\text{-}18)$$

$$mR^2\left[\ddot{\alpha} + (1-\lambda\cos\alpha)\,\ddot{\theta} - \lambda\dot{\theta}^2\sin\alpha\right] + RD_\alpha = -\frac{m}{M}R\left(F_A\sin\alpha + F_N\cos\alpha\right) \quad (6\text{-}19)$$

Setting

$$k = \frac{mR^2}{I}, \quad \Omega^2 = \frac{qS\ell}{I}, \quad b^2 = \frac{5I}{7MR\ell}, \quad \delta = \frac{5D_\alpha}{7mR^2}$$

$$\eta = \cos\alpha - \lambda, \quad \zeta = 1 - \lambda\cos\alpha$$

Equations (6-18) and (6-19) can be written as

$$\ddot{\theta} + k\left[\left(1-2\lambda\cos\alpha + \lambda^2\right)\ddot{\theta} + \zeta\ddot{\alpha} + \lambda\,(2\dot{\theta}+\dot{\alpha})\dot{\alpha}\sin\alpha\right]$$
$$= \Omega^2 C_m - \frac{7}{5}\,kb^2\Omega^2\left(C_A\sin\alpha + C_N\eta\right) \tag{6-20}$$

$$\ddot{\alpha} + \frac{5}{7}\left(\zeta\ddot{\theta} - \lambda\dot{\theta}^2\sin\alpha\right) + 2\delta = -b^2\Omega^2\left(C_A\sin\alpha + C_N\cos\alpha\right) \tag{6-21}$$

In these equations, Ω^2 is a function of time determined by the motion of the mass center, δ is a function of $\dot{\alpha}$, and C_A, C_N and C_m are functions of the angle of attack θ.

6.3.4 CONSTRAINT FORCES CAUSED BY THE ACCELERATION OF THE CM

The terms

$$Q'_\theta = -\frac{m}{M}R\left(F_A\sin\alpha + F_N\eta\right) \tag{6-22}$$

$$Q'_\alpha = -\frac{m}{M}R\left(F_A\sin\alpha + F_N\cos\alpha\right) \tag{6-23}$$

appearing on the right-hand sides of Equations (6-18) and (6-19), respectively, can be identified as the forces (or more correctly the torques) of constraint due to the acceleration of the CM.

In Figure 6-3, we show the inertial forces $(m/M)F_A$ in the z direction and $(m/M)F_N$ in the -x direction acting on the ball. One can easily identify Q'_θ as the torque about the CM and Q'_α as the torque about the CC caused by the above inertial forces. This observation is used the development of the three dimensional model in Section 6.4.

6.4 THREE DIMENSIONAL MODEL

6.4.1 THE QUASI-LAGRANGIAN FORMULATION

In the three dimensional model we formulate the motion about the CM and treat the inertial forces caused by the acceleration of the CM as additional applied forces. The kinetic energy of the system about the CM is of the form

$$T = T(\omega_x, \omega_y, \omega_z, \alpha_1, \alpha_2, \dot{\alpha}_1, \dot{\alpha}_2) \tag{6-24}$$

where ω_x, ω_y and ω_z are components of the vehicle angular velocity $\bar{\omega}$, the α_i are the ball angles, and the $\dot{\alpha}_i$ are their derivatives. It is significant that T does not depend on the orientation of the vehicle.

The equations of motion for ω_x, ω_y and ω_z are generated using the quasi-Lagrangian equations

$$\left.\begin{aligned}
\frac{d}{dt}\frac{\partial T}{\partial \omega_x} - \omega_z \frac{\partial T}{\partial \omega_y} + \omega_y \frac{\partial T}{\partial \omega_z} &= G_x + G'_x \\
\frac{d}{dt}\frac{\partial T}{\partial \omega_y} - \omega_x \frac{\partial T}{\partial \omega_z} + \omega_z \frac{\partial T}{\partial \omega_x} &= G_y + G'_y \\
\frac{d}{dt}\frac{\partial T}{\partial \omega_z} - \omega_y \frac{\partial T}{\partial \omega_x} + \omega_x \frac{\partial T}{\partial \omega_y} &= 0
\end{aligned}\right\} \tag{6-25}$$

where

$$G_x = qS\ell C_m k_y \left(1-k_z^2\right)^{-1/2}, \quad G_y = -qS\ell C_m k_x \left(1-k_z^2\right)^{-1/2} \tag{6-26}$$

are the body fixed components of the aerodyanmic torque Q_θ and

$$\left.\begin{aligned} G'_x &= -\frac{m}{M} RqS\left[C_A \sin\alpha_1 + \frac{C_N k_y}{\sqrt{1-k_z^2}}\left(\cos\alpha_1 - \lambda_1\right)\right] \\ G'_y &= -\frac{m}{M} RqS\left[C_A \sin\alpha_2 - \frac{C_N k_x}{\sqrt{1-k_z^2}}\left(\cos\alpha_2 - \lambda_2\right)\right] \end{aligned}\right\} \tag{6-27}$$

are the body fixed components of the constraint torque Q'_θ given by Equation (6-22).

The above torque components depend on the instantaneous values of the direction cosines k_x, k_y and k_z between the xyz axes and the velocity vector $\overline{v}$. Since the direction of $\overline{v}$ is assumed fixed, the direction cosines satisfy Poisson's equations

$$\begin{pmatrix} \dot{k}_x \\ \dot{k}_y \\ \dot{k}_z \end{pmatrix} + \begin{pmatrix} 0 & -\omega_z & \omega_y \\ \omega_z & 0 & -\omega_x \\ -\omega_y & \omega_x & 0 \end{pmatrix}\begin{pmatrix} k_x \\ k_y \\ k_z \end{pmatrix} = 0 \tag{6-28}$$

The equations for the two damper masses are obtained from

$$\frac{d}{dt}\frac{\partial T}{\partial \dot{\alpha}_i} - \frac{\partial T}{\partial \alpha_i} = -RD_{\alpha_i} + Q'_{\alpha_i} \qquad i = 1,2 \tag{6-29}$$

where the D_{α_i} are the fluid damping forces and

$$\left.\begin{aligned} Q'_{\alpha_1} &= -\frac{m}{M} RqS\left(C_A \sin\alpha_1 + \frac{C_N k_y}{\sqrt{1-k_z^2}} \cos\alpha_1\right) \\ Q'_{\alpha_2} &= -\frac{m}{M} RqS\left(C_A \sin\alpha_2 - \frac{C_N k_x}{\sqrt{1-k_z^2}} \cos\alpha_2\right) \end{aligned}\right\} \tag{6-30}$$

are the constraint torques corresponding to Equation (6-23).

6.4.2 KINETIC ENERGY

The kinetic energy of the vehicle about the CM is

$$T_a = \frac{1}{2} I \left(\omega_x^2 + \omega_y^2\right) + \frac{1}{2} J \omega_z^2 \tag{6-31}$$

where I is the moment of inertia about x and y and J is the moment of inertia about z. Later n will be used to denote the inertia ratio J/I.

The kinetic energy of translation of the two balls is

$$T_b = \frac{1}{2} \sum_{i=1}^{2} m \left(U_{x_i}^2 + U_{y_i}^2 + U_{z_i}^2\right)$$

where

$$\begin{pmatrix} U_{x_1} \\ U_{y_1} \\ U_{z_1} \end{pmatrix} = \begin{pmatrix} 0 \\ \dot{y}_1 \\ \dot{z}_1 \end{pmatrix} + \begin{pmatrix} 0 & -\omega_z & \omega_y \\ \omega_z & 0 & -\omega_x \\ -\omega_y & \omega_x & 0 \end{pmatrix} \begin{pmatrix} 0 \\ y_1 \\ z_1 \end{pmatrix}$$

$$\begin{pmatrix} U_{x_2} \\ U_{y_2} \\ U_{z_2} \end{pmatrix} = \begin{pmatrix} \dot{x}_2 \\ 0 \\ \dot{z}_2 \end{pmatrix} + \begin{pmatrix} 0 & -\omega_z & \omega_y \\ \omega_z & 0 & -\omega_x \\ -\omega_y & \omega_x & 0 \end{pmatrix} \begin{pmatrix} x_2 \\ 0 \\ z_2 \end{pmatrix}$$

Introducing these velocity components into T_b we obtain

$$\begin{aligned} T_b = {} & \frac{1}{2} m_1 \Big[\omega_x^2 \left(y_1^2 + z_1^2\right) + \omega_y^2 z_1^2 + \omega_z^2 y_1^2 - 2\omega_z \omega_y y_1 z_1 \\ & + 2\omega_x \left(y_1 \dot{z}_1 - z_1 \dot{y}_1\right) + \dot{y}_1^2 + \dot{z}_1^2 \Big] \\ & + \frac{1}{2} m_2 \Big[\omega_x^2 z_2^2 + \omega_y^2 \left(x_2^2 + z_2^2\right) + \omega_z^2 x_2^2 - 2\omega_z \omega_x x_2 z_2 \\ & + 2\omega_y \left(z_2 \dot{x}_2 - x_2 \dot{z}_2\right) + \dot{x}_2^2 + \dot{z}_2^2 \Big] \end{aligned} \tag{6-32}$$

Using the transformation equations

$$y_1 = -R \sin\alpha_1 \qquad z_1 = R\left(\cos\alpha_1 - \lambda_1\right)$$

$$x_2 = R \sin\alpha_2 \qquad z_2 = R\left(\cos\alpha_2 - \lambda_2\right)$$

where $\lambda_i = D_i/R$, Equation (6-32) becomes

$$\begin{aligned} T_b = \frac{1}{2} mR^2 \Big\{ & \omega_x^2 \left[\sin^2\alpha_1 + \left(\cos\alpha_1 - \lambda_1\right)^2 + \left(\cos\alpha_2 - \lambda\right)^2\right] \\ & + \omega_y^2 \left[\sin^2\alpha_2 + \left(\cos\alpha_2 - \lambda_2\right)^2 + \left(\cos\alpha_1 - \lambda\right)^2\right] \\ & + \omega_z^2 \left(\sin^2\alpha_1 + \sin^2\alpha_2\right) + 2\omega_z \omega_y \sin\alpha_1 \left(\cos\alpha_1 - \lambda_1\right) \\ & - 2\omega_z \omega_x \sin\alpha_2 \left(\cos\alpha_2 - \lambda_2\right) + \dot{\alpha}_1^2 + \dot{\alpha}_2^2 \\ & + 2\omega_x \dot{\alpha}_1 \left(1 - \lambda_1 \cos\alpha_1\right) + 2\omega_y \dot{\alpha}_2 \left(1 - \lambda_2 \cos\alpha_2\right) \end{aligned} \tag{6-33}$$

The kinetic energy of rotation of the two balls is

$$T_c = \frac{1}{5} mR^2 \left(\dot{\alpha}_1^2 + \dot{\alpha}_2^2\right) \tag{6-34}$$

where we again assume that the ball radius is small compared to the tube radius of curvature.

The total kinetic energy about the CM is given by

$$T = T_a + T_b + T_c \tag{6-35}$$

6.4.3 EXPLICIT FORMS OF THE EQUATIONS OF MOTION

In forming the equations of motion it is expedient to introduce

$$\eta_i = \cos\alpha_i - \lambda_i \qquad \zeta_i = 1 - \lambda_i \cos\alpha_i \qquad i = 1,2$$

To obtain the explicit forms for Equations (6-25) and (6-29) we first form

$$\frac{\partial T}{\partial \omega_x} = I\,\omega_x + mR^2\left[\omega_x\left(\sin^2\alpha_1 + \eta_1^2 + \eta_2^2\right) - \omega_z\,\eta_2\,\sin\alpha_2 + \dot{\alpha}_1\,\zeta_1\right]$$

$$\frac{\partial T}{\partial \omega_y} = I\,\omega_y + mR^2\left[\omega_y\left(\sin^2\alpha_2 + \eta_2^2 + \eta_1^2\right) + \omega_z\,\eta_1\,\sin\alpha_1 + \dot{\alpha}_2\,\zeta_2\right]$$

$$\frac{\partial T}{\partial \omega_z} = J\,\omega_z + mR^2\left[\omega_z\left(\sin^2\alpha_1 + \sin^2\alpha_2\right) + \omega_y\,\eta_1\,\sin\alpha_1 - \omega_x\eta_2\,\sin\alpha_2\right]$$

$$\begin{aligned}\frac{d}{dt}\frac{\partial T}{\partial \omega_x} = {} & I\,\dot{\omega}_x + mR^2\Big[\dot{\omega}_x\left(\sin^2\alpha_1 + \eta_1^2 + \eta_2^2\right) - \dot{\omega}_z\,\eta_2\,\sin\alpha_2 \\ & + 2\,\omega_x\left(\dot{\alpha}_1\,\sin\alpha_1\,\cos\alpha_1 - \dot{\alpha}_1\,\eta_1\,\sin\alpha_1 - \dot{\alpha}_2\,\eta_2\,\sin\alpha_2\right) \\ & + \omega_z\,\dot{\alpha}_2\,\sin^2\alpha_2 - \omega_z\,\dot{\alpha}_2\eta_2\,\cos\alpha_2 + \ddot{\alpha}_1\,\zeta_1 + \lambda_1\,\dot{\alpha}_1^2\,\sin\alpha_1\Big]\end{aligned}$$

$$\begin{aligned}\frac{d}{dt}\frac{\partial T}{\partial \omega_y} = {} & I\,\dot{\omega}_y + mR^2\Big[\dot{\omega}_y\left(\sin^2\alpha_2 + \eta_2^2 + \eta_1^2\right) + \dot{\omega}_z\,\eta_1\,\sin\alpha_1 \\ & + 2\omega_y\left(\dot{\alpha}_2\sin\alpha_2\,\cos\alpha_2 - \dot{\alpha}_2\,\eta_2\,\sin\alpha_2 - \dot{\alpha}_1\,\eta_1\,\sin\alpha_1\right) \\ & - \omega_z\,\dot{\alpha}_1\,\sin^2\alpha_1 + \omega_z\dot{\alpha}_1\eta_1\,\cos\alpha_1 + \ddot{\alpha}_2\zeta_2 + \lambda_2\,\dot{\alpha}_2^2\,\sin\alpha_2\Big]\end{aligned}$$

$$\begin{aligned}\frac{d}{dt}\frac{\partial T}{\partial \omega_z} = {} & J\dot{\omega}_z + mR^2\Big[\dot{\omega}_z\left(\sin^2\alpha_1 + \sin^2\alpha_2\right) + \dot{\omega}_y\,\eta_1\,\sin\alpha_1 - \dot{\omega}_x\eta_2\,\sin\alpha_2 \\ & + 2\omega_z\left(\dot{\alpha}_1\,\sin\alpha_1\,\cos\alpha_1 + \dot{\alpha}_2\,\sin\alpha_2\,\cos\alpha_2\right) \\ & - \omega_y\,\dot{\alpha}_1\,\sin^2\alpha_1 + \omega_y\,\dot{\alpha}_1\eta_1\,\cos\alpha_1 + \omega_x\,\dot{\alpha}_2\,\sin^2\alpha_2 - \omega_x\dot{\alpha}_2\eta_2\,\cos\alpha_2\Big]\end{aligned}$$

$$\frac{\partial T}{\partial \dot{\alpha}_1} = mR^2 \left(\omega_x \zeta_1 + \frac{7}{5} \dot{\alpha}_1\right)$$

$$\frac{\partial T}{\partial \dot{\alpha}_2} = mR^2 \left(\omega_y \zeta_2 + \frac{7}{5} \dot{\alpha}_2\right)$$

$$\frac{d}{dt} \frac{\partial T}{\partial \dot{\alpha}_1} = mR^2 \left(\frac{7}{5} \ddot{\alpha}_1 + \dot{\omega}_x \zeta_1 + \lambda_1 \omega_x \dot{\alpha}_1 \sin\alpha_1\right)$$

$$\frac{d}{dt} \frac{\partial T}{\partial \dot{\alpha}_2} = mR^2 \left(\frac{7}{5} \ddot{\alpha}_2 + \dot{\omega}_y \zeta_2 + \lambda_2 \omega_y \dot{\alpha}_2 \sin\alpha_2\right)$$

$$\frac{\partial T}{\partial \alpha_1} = mR^2 \Big[\omega_z^2 \sin\alpha_1 \cos\alpha_1 + \omega_x^2 \left(\cos\alpha_1 - \eta_1\right) \sin\alpha_1$$

$$-\omega_y^2 \eta_1 \sin\alpha_1 - \omega_z \left(\omega_y \sin^2\alpha_1 - \omega_y \eta_1 \cos\alpha_1\right) + \lambda_1 \omega_x \dot{\alpha}_1 \sin\alpha_1\Big]$$

$$\frac{\partial T}{\partial \alpha_2} = mR^2 \Big[\omega_z^2 \sin\alpha_2 \cos\alpha_2 + \omega_y^2 \left(\cos\alpha_2 - \eta_2\right) \sin\alpha_2$$

$$-\omega_x^2 \eta_2 \sin\alpha_2 + \omega_z \left(\omega_x \sin^2\alpha_2 - \omega_x \eta_2 \cos\alpha_2\right) + \lambda_2 \omega_y \dot{\alpha}_2 \sin\alpha_2\Big]$$

When the above expressions along with the torque defined in Equations (6-26), (6-27) and (6-30) are introduced into Equations (6-25) and (6-26) we obtain the following set of equations.

$$\dot{\omega}_x - (1-n)\omega_z\omega_y + k\Big[\dot{\omega}_x\left(\sin^2\alpha_1 + \eta_1^2 + \eta_2^2\right) - \dot{\omega}_z\eta_2 \sin\alpha_2 + 2\omega_x\left(\lambda_1 \dot{\alpha}_1 \sin\alpha_1 - \dot{\alpha}_2\eta_2 \sin\alpha_2\right)$$

$$-2\omega_z \dot{\alpha}_2\eta_2 \cos\alpha_2 + \ddot{\alpha}_1\zeta_1 + \lambda_1 \dot{\alpha}_1^2 \sin\alpha_1 + \omega_z\omega_y\left(\sin^2\alpha_1 - \eta_1^2 - \eta_2^2\right) + \left(\omega_y^2 - \omega_z^2\right)\eta_1 \sin\alpha_1 - \omega_x\omega_y\eta_2 \sin\alpha_2\Big]$$

$$= \Omega^2\left[\frac{C_m k_y}{\sqrt{1-k_z^2}} - \frac{7}{5} kb^2\left(C_A \sin\alpha_1 + \frac{C_N k_y}{\sqrt{1-k_z^2}} \eta_1\right)\right] \tag{6-36}$$

$$\dot{\omega}_y + (1-n)\,\omega_z\omega_x + k\Big[\dot{\omega}_y\left(\sin^2\alpha_2 + \eta_2^2 + \eta_1^2\right) + \dot{\omega}_z\eta_1 \sin\alpha_1 + 2\omega_y\left(\lambda_2\dot{\alpha}_2 \sin\alpha_2 - \dot{\alpha}_1\eta_1 \sin\alpha_1\right)$$

$$+ 2\omega_z \dot{\alpha}_1\eta_1 \cos\alpha_1 + \ddot{\alpha}_2\zeta_2 + \lambda_2\dot{\alpha}_2^2 \sin\alpha_2 - \omega_z\omega_x\left(\sin^2\alpha_2 - \eta_2^2 - \eta_1^2\right) + \left(\omega_x^2 - \omega_z^2\right)\eta_2 \sin\alpha_2 - \omega_x\omega_y\eta_1 \sin\alpha_1\Big]$$

$$= \Omega^2\left[-\frac{C_m k_x}{\sqrt{1-k_z^2}} - \frac{7}{5} kb^2\left(C_A \sin\alpha_2 - \frac{C_N k_x}{\sqrt{1-k_z^2}} \eta_2\right)\right] \tag{6-37}$$

$$\dot{\omega}_z + \frac{k}{n}\Big[\dot{\omega}_z\left(\sin^2\alpha_1 + \sin^2\alpha_2\right) + \left(\dot{\omega}_y + \omega_z\,\omega_x\right)\eta_1 \sin\alpha_1 - \left(\dot{\omega}_x - \omega_z\omega_y\right)\eta_2 \sin\alpha_2 + \omega_x\omega_y\left(\sin^2\alpha_2 - \sin^2\alpha_1\right)$$

$$-2\omega_y \dot{\alpha}_1 \sin^2\alpha_1 + 2\omega_x\dot{\alpha}_2 \sin^2\alpha_2 + 2\omega_z\left(\dot{\alpha}_1 \sin\alpha_1 \cos\alpha_1 + \dot{\alpha}_2 \sin\alpha_2 \cos\alpha_2\right)\Big] = 0 \tag{6-38}$$

$$\ddot{\alpha}_1 + \frac{5}{7}\Big[\dot{\omega}_x\zeta_1 + \left(\omega_y^2 - \omega_z^2\right) \sin\alpha_1 \cos\alpha_1 - \lambda_1\left(\omega_x^2 + \omega_y^2\right) \sin\alpha_1 + \omega_z\omega_y\left(\sin^2\alpha_1 - \eta_1 \cos\alpha_1\right)\Big]$$

$$= -2\delta_1 - b^2\,\Omega^2\left(C_A \sin\alpha_1 + \frac{C_N k_y}{\sqrt{1-k_z^2}} \cos\alpha_1\right) \tag{6-39}$$

$$\ddot{\alpha}_2 + \frac{5}{7}\left[\dot{\omega}_y \zeta_2 + \left(\omega_x^2 - \omega_z^2\right) \sin\alpha_2 \cos\alpha_2 - \lambda_2\left(\omega_x^2 + \omega_y^2\right) \sin\alpha_2 - \omega_z\omega_x\left(\sin^2\alpha_2 - \eta_2 \cos\alpha_2\right)\right]$$

$$= -2\delta_2 - b^2 \Omega^2 \left(C_A \sin\alpha_2 - \frac{C_N k_x}{\sqrt{1-k_z^2}} \cos\alpha_2\right) \tag{6-40}$$

6.4.4 MOTION OF THE CM

The function Ω^2 is a function of time depending on the dynamic pressure q by the equation

$$\Omega^2 = qS\ell/I \tag{6-41}$$

where S is the vehicle reference area and ℓ is the vehicle reference length. Dynamic pressure is defined by

$$q = \frac{1}{2}\rho v^2 \tag{6-42}$$

where ρ is the atmospheric density and v is the vehicle speed. We assume that ρ is an exponential function of altitude h. Then if ρ^* denotes the density at some reference altitude h* (note: h* may or may not be zero) and if β denotes the reciprocal of the atmospheric scale height, ρ is given by

$$\rho = \rho^* e^{-\beta (h-h^*)} \tag{6-43}$$

The drag on the vehicle can be expressed as

$$F_D = q\, S \left(C_A \cos\theta + C_N \sin\theta\right) \tag{6-44}$$

With $k_z = \cos\theta$, the acceleration $\dot{v}$ becomes

$$\dot{v} = \frac{qS}{M}\left(C_A k_z + C_N\sqrt{1-k_z^2}\right) \tag{6-45}$$

The change in h is given by

$$\dot{h} = -v \sin\gamma \tag{6-46}$$

where γ is the angle between the velocity vector and the local horizontal (positive down). Equations (6-45) and (6-46) presuppose that the gravity acceleration is zero and that γ is a constant.

In certain cases, only the motion above the point of peak dynamic pressure is of interest. Above peak q, the speed v is nearly constant. If v is indeed treated as a constant, Ω^2 can be represented as a simple exponential function of time. Specifically we have

$$\Omega^2 = \Omega_o^2 e^{ct} \tag{6-47}$$

where Ω_o is the value of Ω at t = 0 and c is a constant defined by

$$c = \beta v \sin\gamma \tag{6-48}$$

with dimensions of $(\text{time})^{-1}$.

6.5 MODEL EXTENSIONS

6.5.1 DAMPING CAUSED BY LIFT

To this point, the direction of $\bar{v}$ has been assumed fixed. Now we remove this restriction and include the effects of directional changes in $\bar{v}$ caused by lift. For a statically stable vehicle with a positive lift coefficient, the effect is to damp the oscillations; while for a statically stable vehicle with a negative lift coefficient, the effect is destabilizing.

Directional changes in $\bar{v}$ are reflected by the differential equations for the unit vector $\bar{k}$ along $\bar{v}$. With $\bar{k}$ fixed the righthand side of Equation (6-28) is correctly zero. When the lift force

$$F_L = qS\left(C_N \cos\theta - C_A \sin\theta\right) \tag{6-49}$$

is included, Equation (6-28) must be replaced by

$$\begin{pmatrix} \dot{k}_x \\ \dot{k}_y \\ \dot{k}_z \end{pmatrix} + \begin{pmatrix} 0 & -\omega_z & \omega_y \\ \omega_z & 0 & -\omega_x \\ -\omega_y & \omega_x & 0 \end{pmatrix} \begin{pmatrix} k_x \\ k_y \\ k_z \end{pmatrix} = -\frac{F_L}{Mv \sin\theta} \begin{pmatrix} k_x \\ ky \\ k_z \end{pmatrix} \tag{6-50}$$

6.5.2 AERODYNAMIC PITCH AND YAW RATE DERIVATIVES

The applied aerodynamic torque components caused by the vehicle pitch and yaw rates are given by

$$G_x = qS\ell\, C_{mq}\left(\frac{\ell}{2v}\right)\omega_x\,, \quad G_y = qS\ell\, C_{mq}\left(\frac{\ell}{2v}\right)\omega_y \tag{6-51}$$

where C_{mq} is the rate damping coefficient. To include the effects of these terms it is necessary to add

$$\Omega^2\, C_{mq}\left(\frac{\ell}{2v}\right)\omega_x \quad \text{and} \quad \Omega^2\, C_{mq}\left(\frac{\ell}{2v}\right)\omega_y$$

to the righthand sides of Equations (6-36) and (6-37), respectively.

For a nonspinning body, the effects of the lift force and the above rate damping terms are qualitatively the same. This is not the case when the body spins.

6.5.3 VEHICLE ASYMMETRIES

In developing the equations of motion we assumed that the vehicle has mass and aerodynamic symmetry. Certain asymmetries are now included in the model.

To handle the case when the moments of inertia I_1 about x and I_2 about y are unequal, the following changes must be made:

(1) Define

$$k_1 = \frac{mR^2}{I_1}, \quad k_2 = \frac{mR^2}{I_2}, \quad k_3 = \frac{mR^2}{J}$$

$$b_1^2 = \frac{5I_1}{7MR\ell}, \quad b_2^2 = \frac{5I_2}{7MR\ell}, \quad \Omega_1^2 = \frac{qS\ell}{I_1}, \quad \Omega_2^2 = \frac{qS\ell}{I_2}$$

(2) In Equation (6-36), replace $1 - n$ by $(I_2 - J)/I_1$, Ω^2 by Ω_1^2, b^2 by b_1^2 and k by k_1

(3) In Equation (6-37), replace $1 - n$ by $(I_1 - J)/I_2$, Ω^2 by Ω_2^2, b^2 by b_2^2 and k by k_2.

(4) In Equation (6-38), replace k by k_3 and add $(I_2 - I_1)/J\ \omega_x\ \omega_y$ to the left-hand side.

(5) In Equation (6-39), replace $b^2\ \Omega^2$ by $b_1^2\ \Omega_1^2$.

(6) In Equation (6-40), replace $b^2\ \Omega^2$ by $b_2^2\ \Omega_2^2$.

Next, consider the case when the CM is displaced a distance Δ in the -x direction from the geometric centerline. The first order effects of Δ can be examined by adding

$$\Omega_2^2 \left(a_o + \sqrt{1 - k_z^2}\ K_a\right) \frac{\Delta}{\ell}$$

to the right-hand side of Equation (6-37) and adding

$$-\frac{qS}{J}\ \Delta K_n\ k_y$$

to the right-hand side of Equation (6-38).

Last, we include moments caused by nonzero trim about the x and y axis. Somewhat unconventionally we define C_{m_o} as the trim moment coefficient about x and C_{n_o} as the trim moment about y. These effects are treated by adding $\Omega_1^2 C_{m_o}$ to the right-hand side of Equation (6-36) and $\Omega_2^2 C_{n_o}$ to the right-hand side of Equation (6-37).

SECTION 7

DIGITAL COMPUTER PROGRAMS

7.1 THREE DIMENSIONAL PROGRAM

7.1.1 PROGRAM MODEL

The three dimensional computer program, which is documented in this section, was used to obtain the results for the Ames probe in Section 3 and the small Earth re-entry cone in Section 5.

The basic equations for the three dimensional model were derived in Paragraph 6.4. Because the derivatives are coupled, Equations (6-36) through (6-40) are not suitable for numerical integration. The equations which were actually programmed for numerical solution are listed in Table 7.1. They are only partially coupled. The procedure for evaluating the derivatives (the crux of the problem when there is any coupling) is as follows:

(1) Solve Equations (7-1) and (7-2) for $\dot{\omega}_x$ and $\dot{\omega}_y$ with $\dot{\omega}_z = 0$.

(2) Solve Equation (7-3) for $\dot{\omega}_z$ using above values of $\dot{\omega}_x$ and $\dot{\omega}_y$.

TABLE 7 1

EQUATIONS FOR THE THREE DIMENSIONAL COMPUTER PROGRAM

Attitude Differential Equations:

$$\left[1 + k_1\left(\sin^2\alpha_1 + \eta_1^2 + \eta_2^2 - \frac{5}{7}\zeta_1^2\right)\right]\dot{\omega}_x = \left(\frac{I_2 - J}{I_1}\right)\omega_z\,\omega_y + \Omega_1^2 K_m k_y - k_1\Big\{2\omega_x\left(\lambda_1 p_1 \sin\alpha_1 - p_2\eta_2\sin\alpha_2\right) - 2\zeta_2 p_2\eta_2\cos\alpha_2 + \lambda_1 p_1^2\sin\alpha_1 + \omega_z\omega_y\left(\sin^2\alpha_1 - \eta_1^2 - \eta_2^2\right)$$
$$+\left(\omega_y^2 - \omega_z^2\right)\eta_1\sin\alpha_1 - \omega_z\omega_y\eta_2\sin\alpha_2 - \frac{5}{7}\zeta_1\left[\left(\omega_y^2 - \omega_z^2\right)\sin\alpha_1\cos\alpha_1 - \lambda_1\left(\omega_x^2 + \omega_y^2\right)\sin\alpha_1 + \omega_z\omega_y\left(\sin^2\alpha_1 - \eta_1\cos\alpha_1\right)\right] \tag{7-1}$$
$$- 2\zeta_1\dot{\zeta}_1 + b_1^2\Omega_1^2\left[\left(\frac{7}{5} - \zeta_1\right)\left(a_o + \sqrt{1 - k_z^2}\,K_a\right)\sin\alpha_1 + \left(\frac{7}{5}\eta_1 - \zeta_1\cos\alpha_1\right)K_n k_y\right]\Big\} + k_1\dot{\omega}_z\eta_2\sin\alpha_2 + \Omega_1^2 C_{m_o} + \Omega_1^2\left(\frac{\ell}{2v}\right)C_{m_q}\omega_x$$

$$\left[1 + k_2\left(\sin^2\alpha_2 + \eta_2^2 + \eta_1^2 - \frac{5}{7}\zeta_2^2\right)\right]\dot{\omega}_y = -\left(\frac{I_1 - J}{I_2}\right)\omega_z\,\omega_x - \Omega_2^2 K_m k_x - k_2\Big\{2\omega_y\left(\lambda_2 p_2\sin\alpha_2 - p_1\eta_1\sin\alpha_1\right) + 2\omega_z p_1\eta_1\cos\alpha_1 + \lambda_2 p_2^2\sin\alpha_2 - \omega_z\omega_x\left(\sin^2\alpha_2 - \eta_2^2 - \eta_1^2\right)$$
$$+\left(\omega_x^2 - \omega_z^2\right)\eta_2\sin\alpha_2 - \omega_z\omega_y\eta_1\sin\alpha_1 - \frac{5}{7}\zeta_2\left[\left(\omega_x^2 - \omega_z^2\right)\sin\alpha_2\cos\alpha_2 - \lambda_2\left(\omega_x^2 + \omega_y^2\right)\sin\alpha_2 - \omega_z\omega_x\left(\sin^2\alpha_2 - \eta_2\cos\alpha_2\right)\right] \tag{7-2}$$
$$- 2\zeta_2\dot{\zeta}_2 + b_2^2\Omega_2^2\left[\left(\frac{7}{5} - \zeta_2\right)\left(a_o + \sqrt{1 - k_z^2}\,K_a\right)\sin\alpha_2 - \left(\frac{7}{5}\eta_2 - \zeta_2\cos\alpha_2\right)K_n k_x\right]\Big\} - k_2\dot{\omega}_z\eta_1\sin\alpha_1 + \Omega_2^2 C_{n_o} + \Omega_2^2\left(\frac{\ell}{2v}\right)C_{n_q}\omega_y + \Omega_2^2\left(a_o + \sqrt{1 - k_z^2}\,K_a\right)\frac{\ell}{v}$$

$$\left[1 + k_3\left(\sin^2\alpha_1 + \sin^2\alpha_2\right)\right]\dot{\omega}_z = -k_3\Big[\left(\dot{\omega}_y + \omega_z\omega_x\right)\eta_1\sin\alpha_1 - \left(\dot{\omega}_x - \omega_z\omega_y\right)\eta_2\sin\alpha_2 - 2\omega_y p_1\sin^2\alpha_1 + 2\omega_x p_2\sin^2\alpha_2 + \omega_x\omega_y\left(\sin^2\alpha_2 - \sin^2\alpha_1\right)$$
$$+ 2\omega_z\left(p_1\sin\alpha_1\cos\alpha_1 + p_2\sin\alpha_2\cos\alpha_2\right)\Big] + \left(\frac{I_1 - I_2}{J}\right)\omega_x\,\omega_y - \frac{qS}{J}\,\ell K_n k_y \tag{7-3}$$

$$\dot{p}_1 = -\frac{5}{7}\Omega_1\Big[\zeta_1\dot{\zeta}_1 + \left(\omega_y^2 - \omega_z^2\right)\sin\alpha_1\cos\alpha_1 - \lambda_1\left(\omega_x^2 + \omega_y^2\right)\sin\alpha_1 + \omega_z\omega_y\left(\sin^2\alpha_1 - \eta_1\cos\alpha_1\right)\Big] - 2\zeta_1 - b_1^2\Omega_1^2\left[\left(a_o + \sqrt{1 - k_z^2}\,K_a\right)\sin\alpha_1 + K_n k_y\cos\alpha_1\right] \tag{7-4}$$

$$\dot{p}_2 = -\frac{5}{7}\Omega_2\Big[\zeta_2\dot{\zeta}_2 + \left(\omega_x^2 - \omega_z^2\right)\sin\alpha_2\cos\alpha_2 - \lambda_2\left(\omega_x^2 + \omega_y^2\right)\sin\alpha_2 - \omega_z\omega_y\left(\sin^2\alpha_2 - \eta_2\cos\alpha_2\right)\Big] - 2\zeta_2 - b_2^2\Omega_2^2\left[\left(a_o + \sqrt{1 - k_z^2}\,K_a\right)\sin\alpha_2 - K_n k_x\cos\alpha_2\right] \tag{7-5}$$

$$\dot{k}_x = \omega_z k_y - \omega_y k_z - \frac{E_3\,qS}{Mv}\left[K_n k_z - \left(a_o + \sqrt{1 - k_z^2}\,K_a\right)\right]k \tag{7-6}$$

$$\dot{k}_y = \omega_x k_z - \omega_z k_x - \frac{E_3\,qS}{Mv}\left[K_n k_z - \left(a_o + \sqrt{1 - k_z^2}\,K_a\right)\right]k_y \tag{7-7}$$

$$\dot{k}_z = \omega_y k_x - \omega_x k_y \tag{7-8}$$

$$\dot{\eta}_1 = p_1 \tag{7-9}$$

$$\dot{\eta}_2 = p_2 \tag{7-10}$$

$$\dot{\zeta} = \frac{\omega_x k_x + \omega_y k_y}{1 - k_z^2} \tag{7-11}$$

TABLE 7.1 (Continued)

Side Conditions:

$$\left.\begin{array}{ll} \text{If } \alpha_i > \alpha_L & \text{set } p_1 = -\varepsilon p_1 \\ & \alpha_1 = \alpha_M \\ \text{If } \alpha_i < -\alpha_L & \text{set } p_1 = -\varepsilon p_1 \\ & \alpha_1 = -\alpha_M \end{array}\right\} \quad (7\text{-}12)$$

Calculation of Ω_i^2:

$$\text{For constant velocity} \quad \Omega_i^2 = \Omega_{i_o}^2 e^{ct} \quad (7\text{-}13)$$

$$\text{For variable velocity} \quad \Omega_i^2 = q\, S\ell / I_i \quad (7\text{-}14)$$

$$q = \frac{1}{2} \rho_* e^{-\beta(h-h_*)} v^2 \quad (7\text{-}15)$$

$$\dot{v} = -\frac{qS}{M}\left[\left(a_o + \sqrt{1-k_z^2}\, K_a\right) k_z + K_n \left(1 - k_z^2\right)\right] \quad (7\text{-}16)$$

$$\dot{h} = -v \sin\gamma \quad (7\text{-}17)$$

Algebraic Equations:

$$\eta_i = \cos\alpha_i - \lambda \quad (7\text{-}18)$$

$$\zeta_i = 1 - \lambda\cos\alpha_i \quad (7\text{-}19)$$

$$\delta_i = \mu_1 p_i - \mu_2 p_i |p_i| + \mu_3 p_i^3 \quad (7\text{-}20)$$

$$K_a = a_1 + 2a_2 k_z + a_3\left(4 k_z^2 - 1\right) + 4 a_4 K_z \left(2 k_z^2 - 1\right) \quad (7\text{-}21)$$

$$K_n = n_1 + 2n_2 k_z + n_3\left(4 k_z^2 - 1\right) + 4 n_4 k_z \left(2 k_z^2 - 1\right) \quad (7\text{-}22)$$

$$K_m = m_1 + 2m_2 k_z + m_3\left(4 k_z^2 - 1\right) + 4 m_4 k_z \left(2 k_z^2 - 1\right) \quad (7\text{-}23)$$

$$\theta = \frac{180}{\pi} \cos^{-1} k_z \quad (7\text{-}24)$$

$$\omega_T = \sqrt{\omega_x^2 + \omega_y^2} \quad (7\text{-}25)$$

$$\tau/\tau_o = e^{ct/2} \quad (7\text{-}26)$$

(3) Re-evaluate $\dot{\omega}_x$ and $\dot{\omega}_y$ using the above value of $\dot{\omega}_z$.

(4) Solve Equations (7-4) and (7-5) for $\dot{p}_1$ and $\dot{p}_2$ using the new values for $\dot{\omega}_x$ and $\dot{\omega}_y$.

The aerodynamic coefficients C_A, C_N, and C_m are approximated by the truncated trigonometric series

$$C_A = a_o + \sum_{p=1}^{4} a_p \sin p\theta \tag{7-27}$$

$$C_N = \sum_{p=1}^{4} n_p \sin p\theta \tag{7-28}$$

$$C_m = \sum_{p=1}^{4} m_p \sin p\theta \tag{7-29}$$

where the a_p, n_p, and m_p are selected to obtain best fit curves to the actual data. The program computes C_A, C_N, and C_m by the formulas

$$C_A = a_o + \sqrt{1 - k_z^2} \quad K_a \tag{7-30}$$

$$C_N = \sqrt{1 - k_z^2} \quad K_n \tag{7-31}$$

$$C_m = \sqrt{1 - k_z^2} \quad K_m \tag{7-32}$$

where K_a, K_n, and K_m are given by Equations (7-21), (7-22), and (7-23), respectively.

The fluid drag D_{α_i} is approximated by the cubic equation

$$D_{\alpha_i} = C_1 R\dot{\alpha}_i + C_2 R^2 \dot{\alpha}_i |\dot{\alpha}_i| + C_3 R^3 \dot{\alpha}_i^3 \tag{7-33}$$

The computer program uses Equation (7-20) where

$$\mu_1 = \frac{5C_1}{14m}, \quad \mu_2 = \frac{5C_2 R}{14m}, \quad \mu_3 = \frac{5C_3 R^2}{14m}$$

The artificial parameters E_1 and E_2, which appear in Equations (7-4) and (7-5), should be set equal to 1 unless:

(1) The damper in the yz plane is removed (set $E_1 = 0$, $E_2 = 1$).

(2) The damper in the xz plane is removed (set $E_1 = 1$, $E_2 = 0$), or

(3) Both dampers are removed (set $E_1 = E_2 = 0$).

Condition (3) is optional since the k_i can also be set to 0. However, the integration proceeds faster when E_1 and E_2 are zero.

The artificial parameter E_3, which appears in Equations (7-6) and (7-7), is either 1 or 0. With $E_3 = 1$, the changes in the velocity direction caused by lift are included, while with $E_3 = 0$ these changes are not included. All the runs in this report have $E_3 = 0$.

7.1.2 FLOW DIAGRAMS

PEND 3D (Figure 7-1) is the main routine performing the reading of the input data, the initialization, and the call of the Runge-Kutta integration subroutine.

Data are read according to Figure 7-2. This method permits the processing of several cases by only inputing changed quantities. It is accomplished through the assignment of a card number (KARD) and a field number (IELD) to each variable.

Integration is performed in a variable interval mode. Every integration step is performed in two half-steps using conventional Runge-Kutta to obtain the midpoint values of the derivative. The derivatives at the initial and end points are used to form a Simpson's Rule evaluation for the full step. The magnitude of the difference between Runge-Kutta integration over the two half-steps and the Simpson's Rule integration over the full step is taken as an indication of the error. This magnitude is computed by the following ratio

$$\epsilon_i = \frac{d_i}{a_i + r_i |y_i|}$$

where

d_i = the difference between the two integrations,

a_i = absolute error factor,

r_i = relative error factor,

y_i = value computed by Runge-Kutta

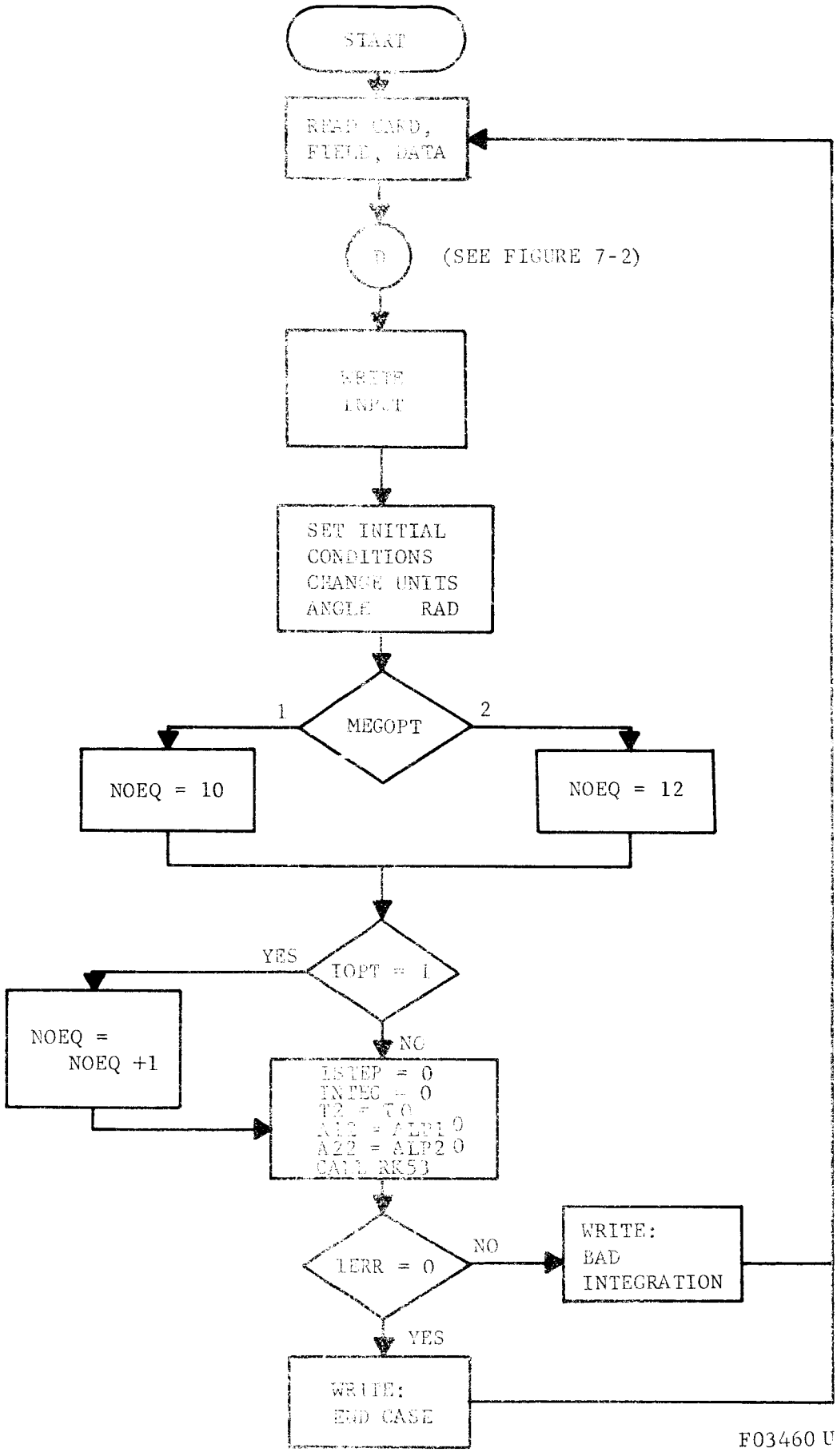

FIGURE 7-1. PEND 3D

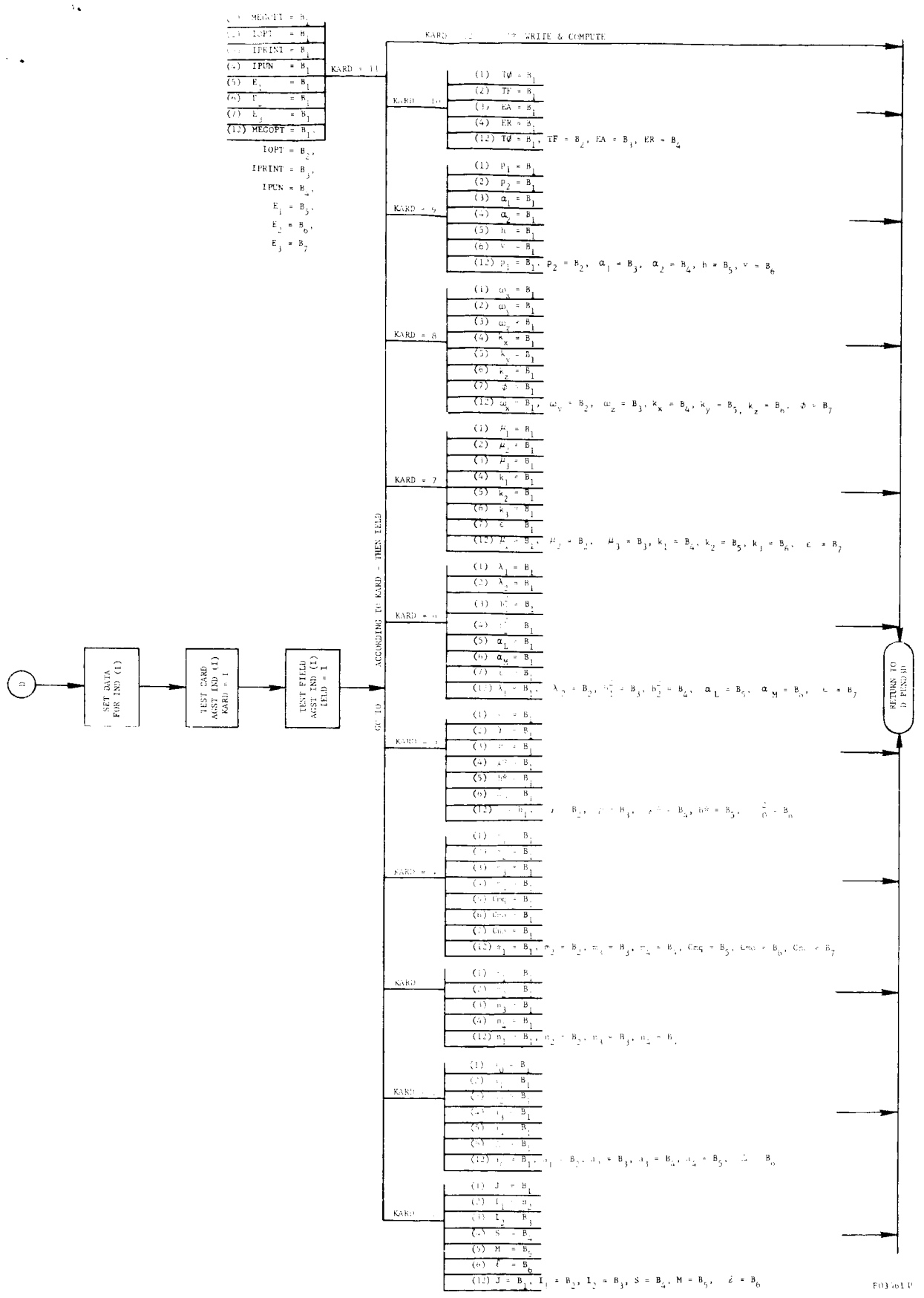

D
SET DATA FOR IND (I)
TEST CARD AGST IND (I) KARD = I
TEST FIELD AGST IND (I) IELD = I
GO TO ACCORDING TO KARD - THEN IELD
KARD = 11
KARD = 10
KARD = 9
KARD = 8
KARD = 7
KARD = 6
KARD = 5
KARD = 4
KARD = 3
KARD = 2
KARD = 1
WRITE & COMPUTE
RETURN TO D PENDING

FIGURE 7-2.

The maximum, m, of ϵ_i is determined. If $m > 1$, dt is divided by $\sqrt[5]{10}$ and integration is repeated using the reduced dt until the error term is acceptable. If $0.75 < m \leq 1$, dt is divided by $\sqrt[5]{10}$. When $0.075 \leq m \leq 0.75$, dt is unchanged. For $m < 0.075$, dt is multiplied by $\sqrt[5]{10}$.

The integration routine begins with a single entry to DERIV, immediately followed by an entry to CNTRL to allow printing of initial values of the system. DERIV (Figure 7-3) is entered eight times for each full integration step. It computes the value of the derivatives. If MEGOPT is equal to 2.0, the derivatives of velocity and altitude are computed; MEGOPT equal to 1.0 causes the omission of this computation. The derivative of ϕ is computed when IOPT is equal to 1.0.

The CNTRL subroutine (Figure 7-4) computes auxiliary equations and prints results. The angles α_1 and α_2 are restricted to a user-set limit in this routine. If either exceeds the limit, a new dt is computed and the integration step is repeated. The next entrance to CNTRL sets the angles equal to α_M, a value slightly below the limit. P_1 and P_2 are multiplied by ϵ, thus changing the slope of the angles, and the integration is restarted.

7.1.3 INPUT DATA AND FORMAT

All cards are given a card number which must be entered in Columns 1 and 2. Each variable is given a field number specified in Column 3. The field number is left blank in the first case and at all other times when the program is to read all data on that card. Thus, the input format is as follows:

(Columns 1 and 2) Card No.	(Column 3) Field	Columns	Program Name	Description
		1-72	Title	Identification
01	1	4-13	XJ	J
	2	14-23	XI1	I_1
	3	24-33	XI2	I_2
	4	34-43	S	S
	5	44-53	XM	M
	6	54-63	XL	ℓ

Columns 1 and 2) Card No.	(Column 3) Field	Columns	Program Name	Description
02	1	4-13	AO	a_o
	2	14-23	A1	a_1
	3	24-33	A2	a_2
	4	34-43	A3	a_3
	5	44-53	A4	a_4
	6	54-63	DELTA	Δ
03	1	4-13	XN1	n_1
	2	14-23	XN2	n_2
	3	24-33	XN3	n_3
	4	34-43	XN4	n_4
04	1	4-13	XM1	m_1
	2	14-23	XM2	m_2
	3	24-33	XM3	m_3
	4	34-43	XM4	m_4
	5	44-53	CMQ	C_{m_q}
	6	54-63	CMO	C_{m_o}
	7	64-73	CNO	C_{n_o}
05	1	4-13	C	C
	2	14-23	GAMMA	γ
	3	24-33	BETA	β
	4	34-43	RHOS	ρ^*
	5	44-53	HS	h^*
	6	54-63	OMEG1O	$\Omega^2_{1_o}$
	7	64-73	OMEG2O	$\Omega^2_{1_o}$
06	1	4-13	XLAMB1	λ_1
	2	14-23	XLAMB2	λ_2
	3	24-33	BSQ1	b_2^1
	4	34-43	BSQ2	b_2^2
	5	44-53	ALPHAL	α_L
	6	54-63	ALPHAM	α_m
	7	64-73	E	ϵ
07	1	4-13	XMU1	μ_1
	2	14-23	XMU2	μ_2
	3	24-33	XMU3	μ_3
	4	34-43	XK1	k_1
	5	44-53	XK2	k_2
	6	54-63	XK3	k_3

Columns 1 and 2) Card No.	(Column 3) Field	Columns	Program Name	Description
08	1	4-13	WXO	ω_x
	2	14-23	WYO	ω_y
	3	24-33	WZO	ω_z
	4	34-43	XKXO	k_x
	5	44-53	XKYO	k_y
	6	54-63	XKZO	k_z
	7	64-73	PHIO	ϕ
09	1	4-13	P1O	p_1
	2	14-23	P2O	p_2
	3	24-33	ALP1O	α_1
	4	34-43	ALP2O	α_2
	5	44-53	HO	h
	6	54-63	VO	v
10	1	4-13	TO	t_o
	2	14-23	TF	t_f
	3	24-33	EA	absolute error
	4	34-43	ER	relative error
	5	44-53	DT	dt
11	1	4-13	MEGOPT	omega option
	2	14-23	IOPT	phi option
	3	24-33	IPRINT	print option
	4	34-43	IPUN	punch option
	5	44-53	CAPE1	E_1
	6	54-63	CAPE2	E_2
	7	64-73	CAPE3	E_3
**				

The last card for each case must consist of asterisks in Columns 1 and 2.

The input format allows for the stacking of cases, that is, the first case must contain all input data. If only a few quantities are to be changed in the next case, it is necessary to specify only those values. This is done with a change of variable card whose format is as follows:

Columns	Description
1 and 2	Card number from which the variable is read
3	Field number of the variable
4 - 13	New value of the variable

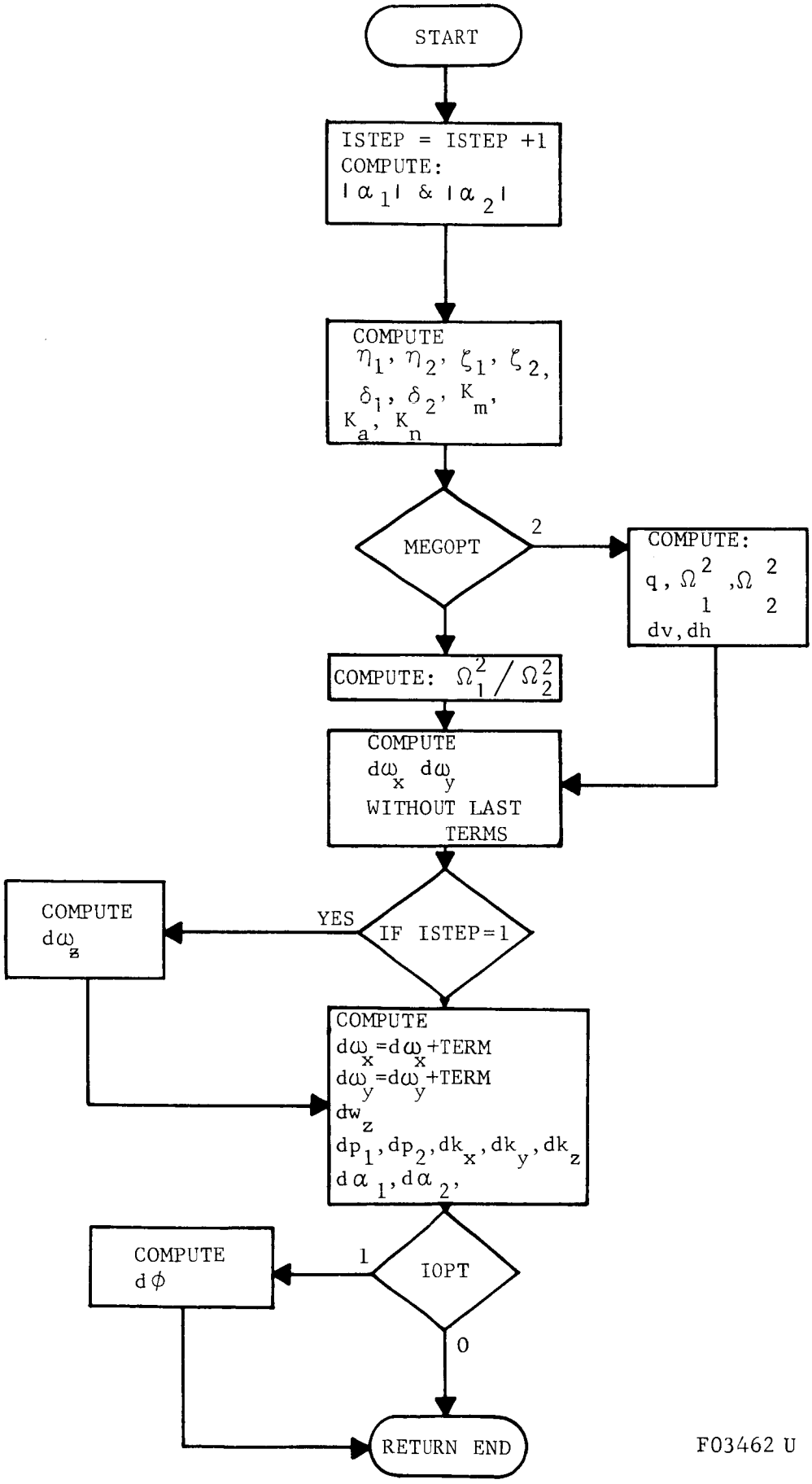

FIGURE 7-3. DERIV

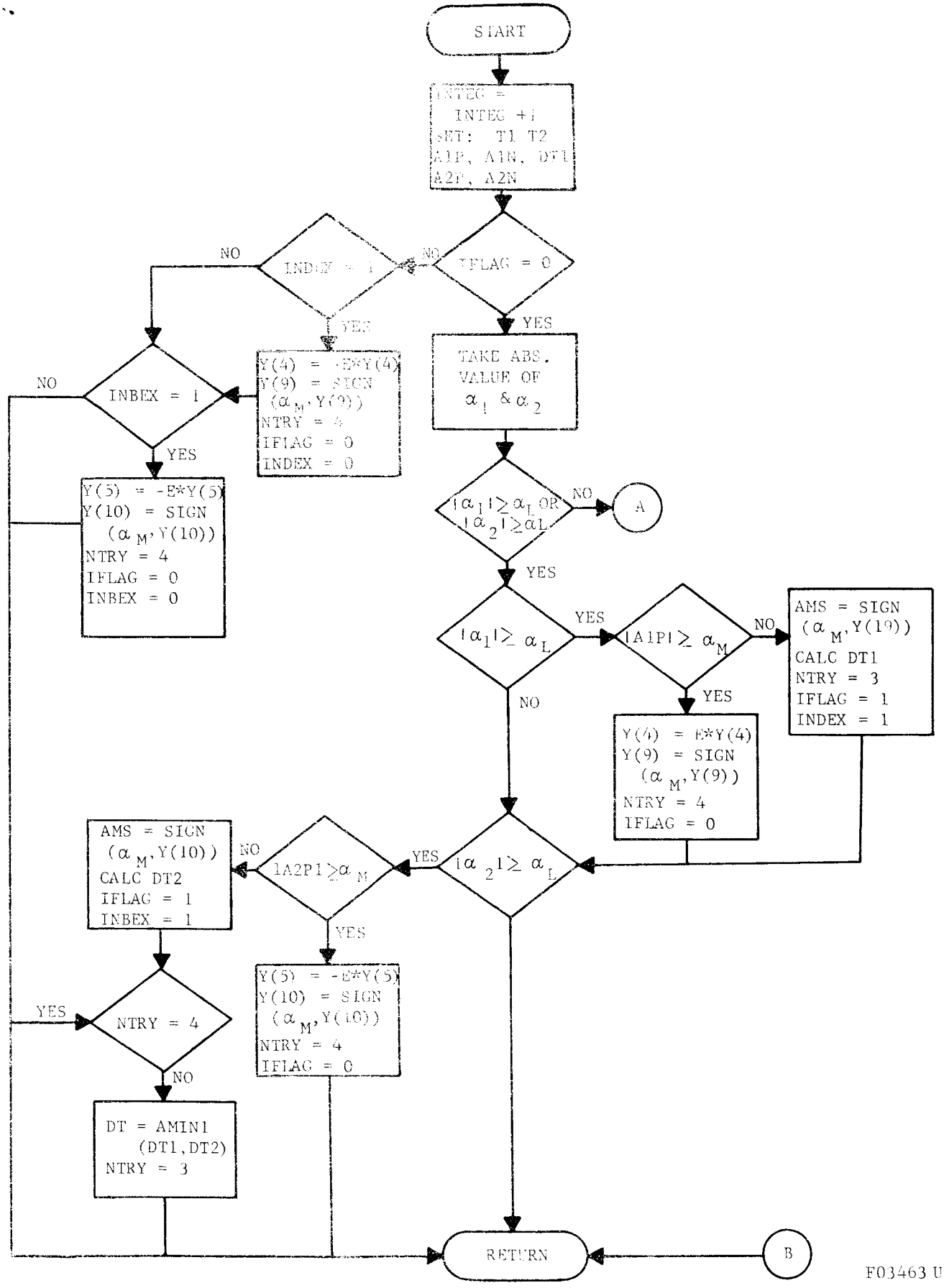

F03463 U

FIGURE 7-4. CNTRL

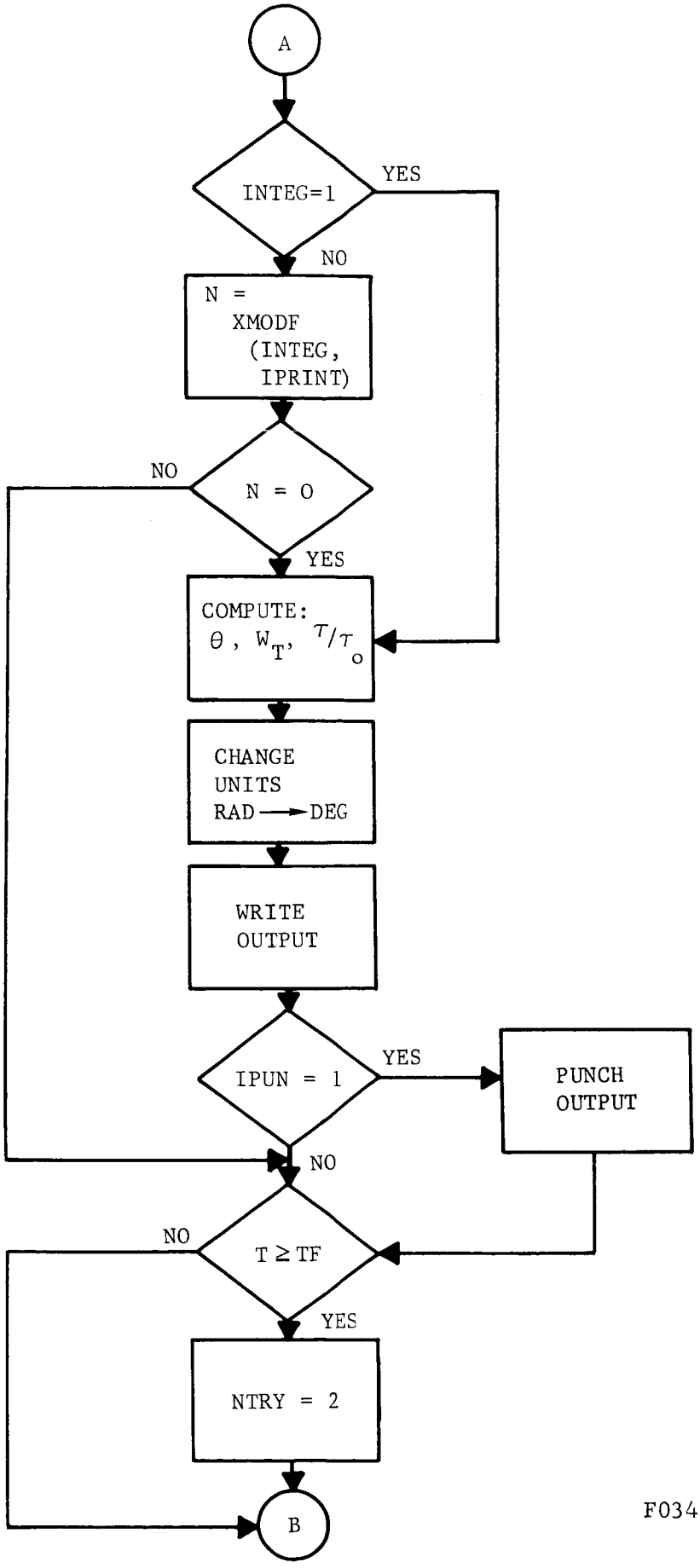

F03464 U

FIGURE 7-4. CNTRL (Continued)

When a field number is specified, as above, the program will change the variable according to the card and field numbers. As many variables as desired per case may be changed; however, each change requires a change of variable card. When using change of variable cards, a title card and a double asterisk card are still necessary.

The variable IPRINT controls the number of integration steps between each printout. It is recommended, because of a variable interval mode, that results be printed at each step, that is, IPRINT should be set equal to 1.0. The following absolute and relative error controls proved to be the most successful in dictating interval control:

$$EA = 0.0001$$

$$ER = 0.001$$

IPUN controls the punching of output data. When IPUN is equal to 0.0, data will not be punched.

The desk "set-up" is shown in Figure 7-5.

7.1.4 OUTPUT

The output will include all input data. The following calculated quantities are also output:

t	τ/τ_o	q	h	θ	ω_z	α_1	α_2
		v	ω_x	ω_y	ϕ	P_1	P_2
		k_x	k_y	k_z	$\dot{\phi}$		

Figure 7-6 is a sample of the print-out.

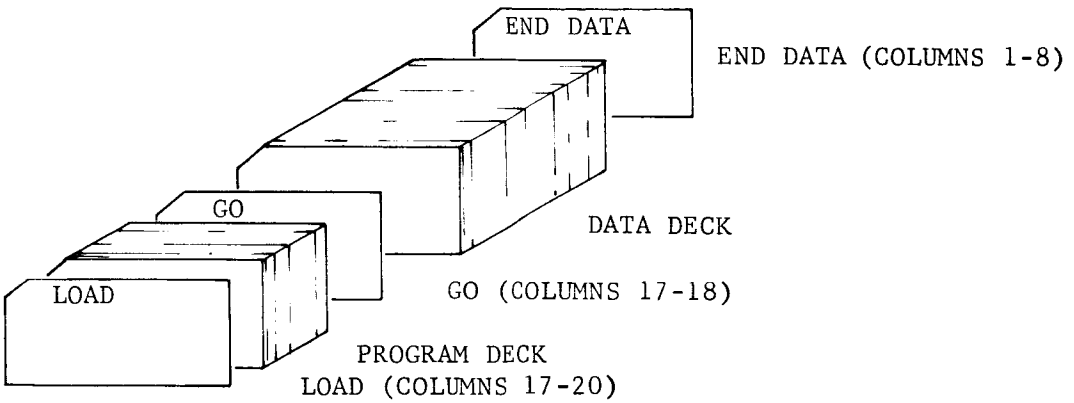

F03465 U

FIGURE 7-5 DECK SET-UP

VEHICLE CONSTANTS

J =	0.56100-001	A0 =	0.60400-001	N1 =	0.23300+001	M1 =	-0.14000+000
I1=	0.56100+000	A1 =	0.51800+000	N2 =	0.10990+000	M2 =	-0.66000-000
I2=	0.56100+000	A2 =	-0.12800+000	N3 =	0.	M3 =	0.
S =	0.61000+000	A3 =	0.92000-001	N4 =	-0.15344+000	M4 =	0.92000-002
M =	0.11440+001	A4 =	-0.10060+000			CMQ=	0.
L =	0.25000+001	DEL=	0.			CMC=	0.
						CNQ=	0.

ATMOSPHERIC CONSTANTS

C	=	0.37600+000
GAMMA	=	0.38400+000
BETA	=	0.45400-004
RHO*	=	0.23780-002
H*	=	0.
OMEG 1 SQ INITIAL	=	0.35400-001
OMEG 2 SQ INITIAL	=	0.35400-001

DAMPER CONSTANTS

LAMBDA 1	=	0.54000+001	MU1 =	0.20000+002
LAMBDA 2	=	0.45250+001	MU2 =	0.
BSQ 1	=	0.84000+000	MU3 =	0.
BSQ 2	=	0.84000+000	K1 =	0.15460-002
ALPHAL	=	0.39000+002	K2 =	0.15460-002
ALPHAM	=	0.38900+002	K3 =	0.15460-001
SMALL E	=	0.	E1 =	0.10000+001
			E2 =	0.10000+001
			E3 =	0.

INITIAL CONDITIONS

WX	=	0.	P1	=	0.
WY	=	0.	P2	=	0.
WZ	=	0.62800+001	ALPHA 1	=	0.38900+002
KX	=	0.	ALPHA 2	=	0.38900+002
KY	=	0.64279+000	H	=	0.38100+006
KZ	=	0.76604+000	V	=	0.22000+005
PHI	=	0.			

CONTROL INPUT

PHI OPTION IS 1 OMEGA OPTION IS 2
PRINT EVERY 1 PUNCH OPTION IS 1
TIME INITIAL IS 0. TIME FINAL IS 35.000000 DT = 0.100000
RELATIVE ERROR = 0.001000 ABSOLUTE ERROR = 0.000100

TIME	TAU/TAUO	Q	H	THETA	WZ	ALPHA 1	ALPHA 2
		V	WX	WY	PHI	P1	P2
		KX	KY	KZ	DPHI		
0.	1.000	0.02	381000.000	40.0004	6.2800	38.9000	38.9000
		22000.0000	0.	0.	0.	0.	0.
		0.	0.6428	0.7660	0.		

FIGURE 7-6. SAMPLE PRINT-OUT FOR 3D MODEL

7.2 PLANAR PROGRAM

7.2.1 PROGRAM MODEL

The planar computer program was used to obtain the results for the spherical entry body in Section 2 and for the Goddard probe in Section 4.

The equations for the planar model were derived in Paragraph 6.3. The equations which were actually programmed are listed in Table 7.2. Two comments are appropriate. First, the model is based on constant linear velocity. Second, a cosine term has been added to the series expansion for C_A.

7.2.2 FLOW DIAGRAMS

PEND (Figure 7-7) is the main routine performing the reading of the input data, the initilization, and the call of the Runge-Kutta integration subroutine. This integration routine was discussed in Paragraph 7.1.2.

The subroutine DERIV is called by the integration routine to compute the values of the derivatives.

The computation of auxiliary equations and printing of results is done in subroutine CNTRL (Figure 7-8). This routine also restricts the angle α. Upon entrance to CNTRL, α is compared to α_L, the user-set limit. When $\alpha \geq \alpha_L$, a new dt is computed and the integration step is repeated. The next entrance to CNTRL sets α equal to α_M, a value slightly below the limit. The slope of the angle, p_α, is multiplied by ϵ and the integration is reinitiated.

7.2.3 INPUT DATA AND FORMAT

Each case consists of eight cards. They have the following format:

Card	Columns	Program Name	Description
1	1-72 79-80	TITLE	Identification Card order, for convenience in deck set-up only.

Card	Columns	Program Name	Description
2	1-12	XK	k
	13-24	XLAMB	λ
	25-36	BSQ	b^2
	37-48	OMEGAO	Ω_0^2
	49-60	C	c
	79-80		Card order
3	1-12	AO	a_0
	13-24	A1	a_1
	25-36	A2	a_2
	37-48	A3	a_3
	49-60	A4	a_4
	61-72	SA5	a_5
	79-80		Card order
4	1-12	XN1	n_1
	13-24	XN2	n_2
	25-36	XN3	n_3
	37-48	XN4	n_4
	79-80		Card order
5	1-12	XM1	m_1
	13-24	XM2	m_2
	25-36	XM3	m_3
	37-48	XM4	m_4
	79-80		Card order
6	1-12	XMU1	μ_1
	13-24	XMU2	μ_2
	25-36	XMU3	μ_3
	37-48	ALPHAL	α_L
	49-60	ALPHAM	α_M
	61-72	E	ϵ
	79-80		Card order
7	1-12	PTO	p_θ initial
	13-24	PAO	p_α initial
	25-36	THETAO	θ initial
	37-48	ALPHAO	α initial
	79-80		Card order
8	1-12	TO	t initial
	13-24	TF	t final
	25-36	EA	Absolute error
	37-48	ER	Relative error
	49-60	DT	dt
	61-62	IPUN	Punch option
	63-64	IPRINT	Print option
	79-80		Card order

TABLE 7.2. EQUATIONS FOR THE PLANAR COMPUTER PROGRAM

$$\left\{1 + k\left[(1 - 2\lambda\cos\alpha + \lambda^2) - \frac{5}{7}\zeta^2\right]\right\}\dot{p}_\theta = -k\left[\lambda\,(2p_\theta + p_\alpha)\,p_\alpha)\sin\alpha + \frac{5}{7}\lambda\zeta\,p_\theta^2\sin\alpha - 2\zeta\delta_\alpha\right]$$
$$+\Omega^2 C_m + kb^2\Omega^2\left[\zeta\,(C_A\sin\alpha + C_N\cos\alpha) - \frac{7}{5}(C_A\sin\alpha + C_N\eta)\right] \tag{7-34}$$

$$\dot{p}_\alpha = -\frac{5}{7}(\zeta\dot{p}_\theta - \lambda p_\theta^2\sin\alpha) - 2\delta - b^2\Omega^2\,(C_A\sin\alpha + C_N\cos\alpha) \tag{7-35}$$

$$\dot{\theta} = p_\theta \tag{7-36}$$

$$\dot{\alpha} = p_\alpha \tag{7-37}$$

where

$$\Omega^2 = \Omega_o^2\,e^{ct} \tag{7-38}$$

$$\eta = \cos\alpha - \lambda \tag{7-39}$$

$$\zeta = 1 - \lambda\cos\alpha \tag{7-40}$$

$$\delta = \mu_1 p_\alpha + \mu_2 p_\alpha|p_\alpha| + \mu_3 p_\alpha^3 \tag{7-41}$$

$$C_A = a_o + a_1\sin\theta + a_2\sin 2\theta + a_3\sin 3\theta + a_4\sin 4\theta + a_5\cos\theta \tag{7-42}$$

$$C_N = n_1\sin\theta + n_2\sin 2\theta + n_3\sin 3\theta + n_4\sin 4\theta \tag{7-43}$$

$$C_m = m_1\sin\theta + m_2\sin 2\theta + m_3\sin 3\theta + m_4\sin 4\theta \tag{7-44}$$

$$\tau/\tau_o = e^{ct} \tag{7-45}$$

with the side conditions:

If $\alpha > \alpha_L$ set $p_\alpha = -\epsilon p_\alpha$, $\alpha = \alpha_M$ If $\alpha > \alpha_L$ set $p_\alpha = -\epsilon p_\alpha$, $\alpha = -\alpha_M$ (7-46)

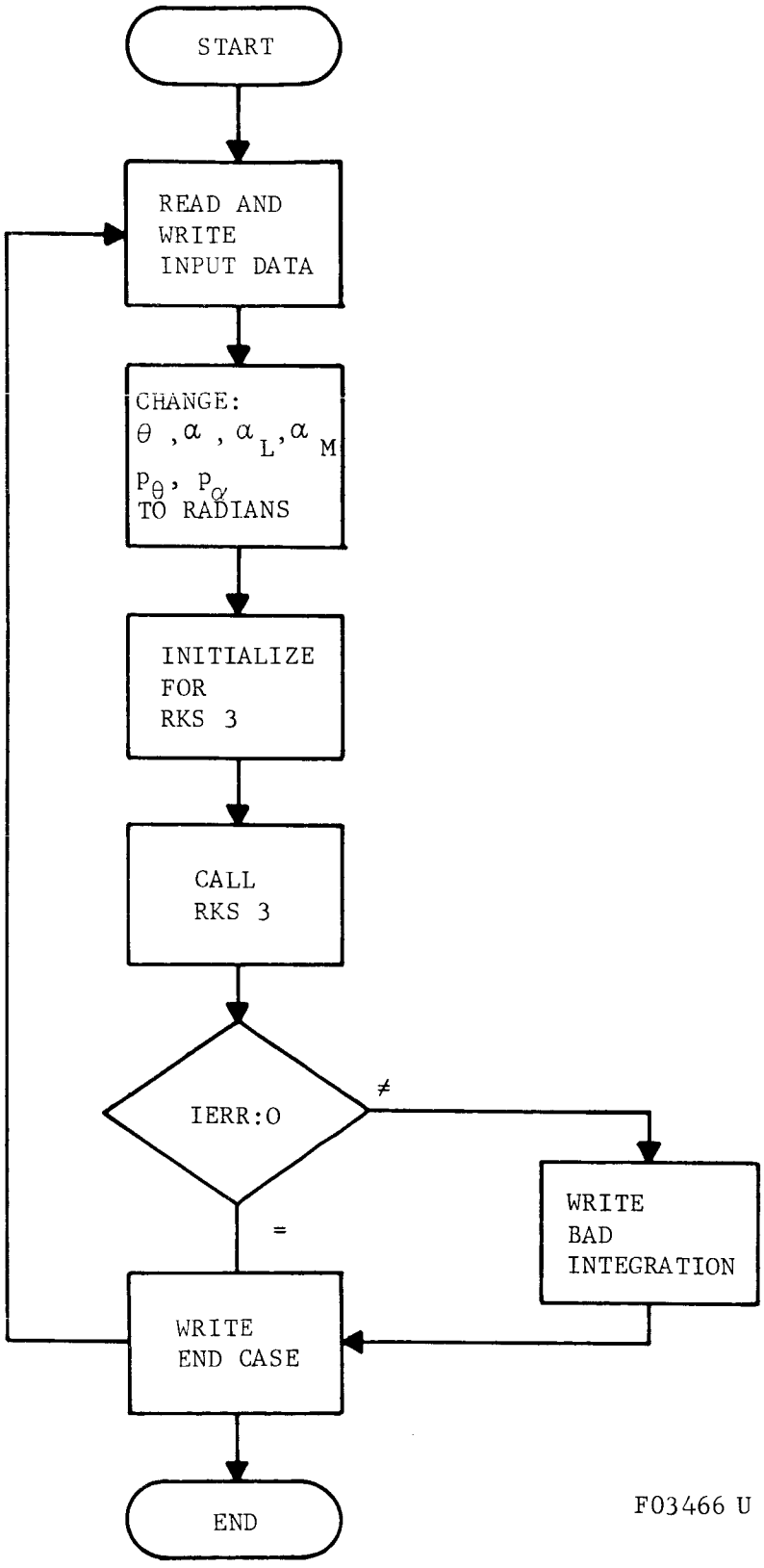

FIGURE 7-7. PEND

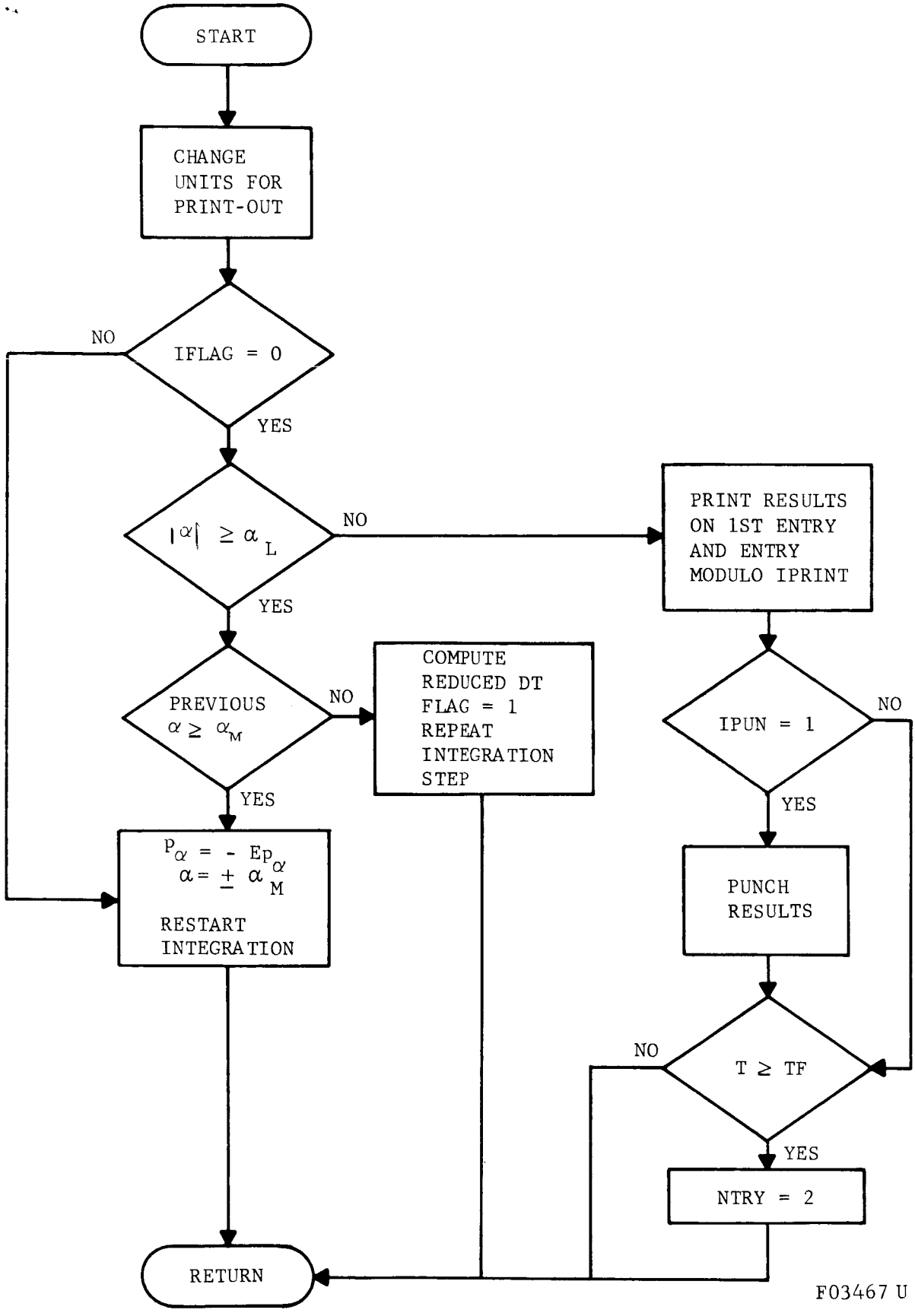

FIGURE 7-8. CNTRL

7.2.4 OUTPUT

The output will include all input data. The following calculated quantities are also output:

$t \quad \tau/\tau_o \quad \theta \quad \alpha \quad p_\alpha$

Figure 7-9 is a sample of the print-out.

```
RUN 47        PENDULUM DAMPER - PLANAR MODEL        GODDARD PROBE

K                  =       0.00622
LAMBDA             =       5.57500
B-SQUARED          =       1.97200
OMEGA SQ. INIT.    =       0.25000
C                  =       1.00000

A0 =       -0.31840
A1 =        0.45400
A2 =        0.10400
A3 =       -0.08600
A4 =       -0.03000 A5 =        0.44200

N1 =        3.75000
N2 =        0.05300
N3 =       -0.53000
N4 =        0.

M1 =       -1.83000
M2 =        0.23900
M3 =        0.09200
M4 =        0.

MU1       =       1.00000
MU2       =       0.
MU3       =       0.
ALPHA L   =      55.00000
ALPHA M   =      54.90000
EPSILON   =       0.

P THETA INITIAL =       0.
P ALPHA INITIAL =       0.
THETA           =     155.00000
ALPHA           =       0.

T INITIAL       =       0.
T FINAL         =      10.00000
ABSOLUTE ERROR  =       0.00010
RELATIVE ERROR  =       0.00100
DT              =       0.10000
PUNCH OPTION IS  0  --  PRINT EVERY  1
```

T	TAU/TAUO	THETA	ALPHA	P-ALPHA
0.	0.10000+001	0.15500+003	0.	0.
0.10000+000	0.10513+001	0.15494+003	-0.32433+000	-0.63782+001
0.25849+000	0.11380+001	0.15458+003	-0.20709+001	-0.15529+002
0.50968+000	0.12903+001	0.15324+003	-0.77312+001	-0.29685+002
0.90779+000	0.15744+001	0.14646+003	-0.24850+002	-0.58292+002
0.12932+001	0.19090+001	0.13909+003	-0.54900+002	0.
0.16785+001	0.23147+001	0.12161+003	-0.54900+002	0.
0.18320+001	0.24992+001	0.11109+003	-0.54900+002	0.
0.19854+001	0.26985+001	0.97637+002	-0.54900+002	0.
0.21388+001	0.29137+001	0.80844+002	-0.54900+002	0.
0.22922+001	0.31460+001	0.60659+002	-0.54900+002	0.
0.24457+001	0.33968+001	0.37622+002	-0.54900+002	0.
0.25991+001	0.36676+001	0.12823+002	-0.54900+002	0.
0.27525+001	0.39600+001	-0.12387+002	-0.54900+002	0.
0.29059+001	0.42758+001	-0.36402+002	-0.54900+002	0.
0.30027+001	0.44878+001	-0.49954+002	-0.54900+002	0.
0.30995+001	0.47104+001	-0.61425+002	-0.53638+002	0.37744+002
0.32530+001	0.50859+001	-0.73179+002	-0.32574+002	0.28931+003

FIGURE 7-9. SAMPLE PRINT-OUT FOR PLANAR MODEL

SECTION 8

INTERNAL DAMPER DYNAMICS

In order to understand the importance of the several parameters which affect the drag of the sphere-in-tube passive damper, a simple flow model has been developed. The drag values calculated from this model are roughly the same as the results of the experimental program.

8.1 FLOW MODEL

The important non-dimensional parameters which relate to the drag are the drag coefficient C_D, the Mach number M, the Reynolds number R_d, and a parameter λ which depends on the geometry of the sphere and tube. These are defined as follows:

$$R_d = \frac{\rho U d}{\mu}$$

ρ = fluid density

U = sphere velocity with respect to the tube

d = sphere diameter

μ = fluid viscosity

$$C_D = \frac{2D}{\rho U^2 A}$$

D = drag

A = sphere cross sectional area = $\frac{\pi d^2}{4}$

$\lambda = t/d$

t = tube inside diameter minus ball diameter

$M = V/A$ (Mach number)

a = speed of sound

and the appropriate V will be defined below in such a way that M will not be a significant parameter as long as M is much less than one. For most cases of interest, M will always be sufficiently small that the flow may be considered to be incompressible. The assumption of incompressibility will be used throughout the following analysis.

If the flow in the gap between the sphere and the tube is assumed to have a uniform velocity, this velocity, when measured with respect to the sphere center, can be shown to have the magnitude

$$V = U \left\{1 + \frac{1}{2\lambda + \lambda^2}\right\} \tag{8-1}$$

by appeal to the equation of mass conservation. This V is typical of the speeds in the gap, and is used in the definition of M.

The flow through this gap may be characterized by the Reynolds number R_t defined as

$$R_t = \frac{\rho V t}{\mu} \left(\frac{1}{1 + \lambda}\right) \tag{8-2}$$

which is simply related to R_d

$$R_t = \left\{\frac{1 + \lambda}{2 + \lambda}\right\} R_d \tag{8-3}$$

Whenever R_d or R_t is sufficiently small, the flow through the gap will be viscous, and it may be compared to the channel flow problem discussed by

Schlichting*. Schlichting calculates the inlet channel length required for fully-developed channel flow. From this calculation, it was decided to classify the flow past the sphere as "viscous" or fully-developed channel flow whenever

$$R_t < 50\lambda^{-\frac{1}{2}} \tag{8-4}$$

and "inviscid" whenever

$$R_t > 500\lambda^{-\frac{1}{2}} \tag{8-5}$$

The drag relation in the inviscid region has been estimated by assuming that C_D is given by the relation

$$C_{D_{\text{inviscid}}} = C_{D_S}\left(\frac{V}{U}\right)^2 \tag{8-6}$$

where $C_{D_S} = C_{D_S}(R_d)$ is the experimental sphere drag curve given by Schlichting.

For the region between the viscous and the inviscid limits, C_D has been obtained by fairing a smooth curve between the limits. This is analogous to the smooth C_{D_S} curve for the sphere alone, as given by Schlichting.

For the viscous case, the C_D estimate is more complex. The flow through the gap produces a difference in pressure between the front side and the back side of the sphere. The drag associated with this pressure drop was taken to be just the pressure drop times the sphere cross section area A. In addition, the viscous wall shearing stress acts as a drag on the ball. To estimate this pressure drop and shear stress, a parabola was fitted to match the sphere curvature. The parabola was used to define a two-dimensional channel, with the parabola as one side of the channel, and

*Schlichting, H., Boundary Layer Theory, McGraw-Hill, 1955, pp. 16 and 146.

a straight line representing the tube as the other side of the channel. The channel length was taken to be the ball diameter d. The parabola was placed so that the channel entrance and exit both had the width (t + d/4); halfway between the channel entrance and exit the width was only t, which represents the gap between the sphere and the tube. Then, with a given value of pressure drop through the channel, the flow rate was computed with the assumption that the pressure gradient dp/dx in the flow direction and the velocity profile across the channel were both the same as in a fully-developed, constant section channel.

The above calculation represents only the portion of the flow between the tube and the sphere where the gap distance is equal to t. At the diametrically opposite side of the sphere, the gap is zero since the sphere touches the tube. The gap varies from zero to t as one travels around the sphere. A calculation similar to that described above was done for each position around the sphere and for some given pressure difference between the front and back of the sphere. Thus, the assumption of a two-dimensional channel flow must be only a rather rough approximation. The flow around each part of the sphere was integrated to give the total volume flow rate, which by continuity is equal to the sphere cross-section area times the sphere speed U. The resulting drag formula, with some slight computational approximations, is

$$C_{D_{\text{viscous}}} = \frac{24}{R_d^{\frac{1}{2}}} \left\{ (2 + 3\lambda)\left(1 + \frac{\beta(\lambda)}{\beta(\lambda)}\right)\gamma(\lambda) + \frac{2\lambda^2\beta(\lambda)}{3} \right\} \tag{8-7}$$

where

$$\beta(\lambda) = \frac{1}{8}\left\{ \frac{2\lambda^2}{(\lambda + 1/4)^2} + \frac{3\lambda}{(\lambda + 1/4)} + 6\lambda^{\frac{1}{2}} \tan^{-1}\left(\frac{1}{2\lambda^{\frac{1}{2}}}\right) \right\}$$

$$\gamma(\lambda) = \left[\frac{3}{2\beta(\lambda)} + \frac{1}{\beta(\lambda/2)}\right]^{-1}$$

$$\delta(\lambda) = \frac{\lambda}{2(\lambda + 1/4)} + \lambda^{\frac{1}{2}} \tan^{-1} \left(\frac{1}{2\lambda^{\frac{1}{2}}}\right)$$

Results from equations (8-6) and (8-7) are plotted in Figure 8-1. This shows the wide range of C_D as λ is varied. In particular, for the viscous case and for $\lambda \ll 1$, C_D varies like $\lambda^{-5/2}$.

8.2 RELATING C_D - R_d CURVE TO DRAG AND VELOCITY

Figure 8-1 is a generalized curve containing a wide range of cases. Some of these cases have been tested by the experimental program. As the experiments were completed, the approximate results of Figure 8-1 were replaced by the experimental data.

In any case, the transformation from the C_D - R_d plane to a drag versus velocity plot is straightforward. From the definitions of C_D and R_d we can write the relations

$$U = \frac{R_d \mu}{\rho d} \tag{8-8}$$

and

$$D = 1/2 \rho A C_D U^2 \tag{8-9}$$

Thus, U is a linear function of R_d, and D is a linear function of $C_D U^2$.

8.3 HEATING PARAMETER

The passive damper action generates heat. Whether or not this is a problem can be answered by defining a heating parameter θ as

$$\theta = \frac{\text{energy expended by the sphere drag}}{\text{fluid heat energy per degree temperature rise}}$$

where the fluid heat energy is that contained in the tube volume swept out by the motion of the sphere. That is,

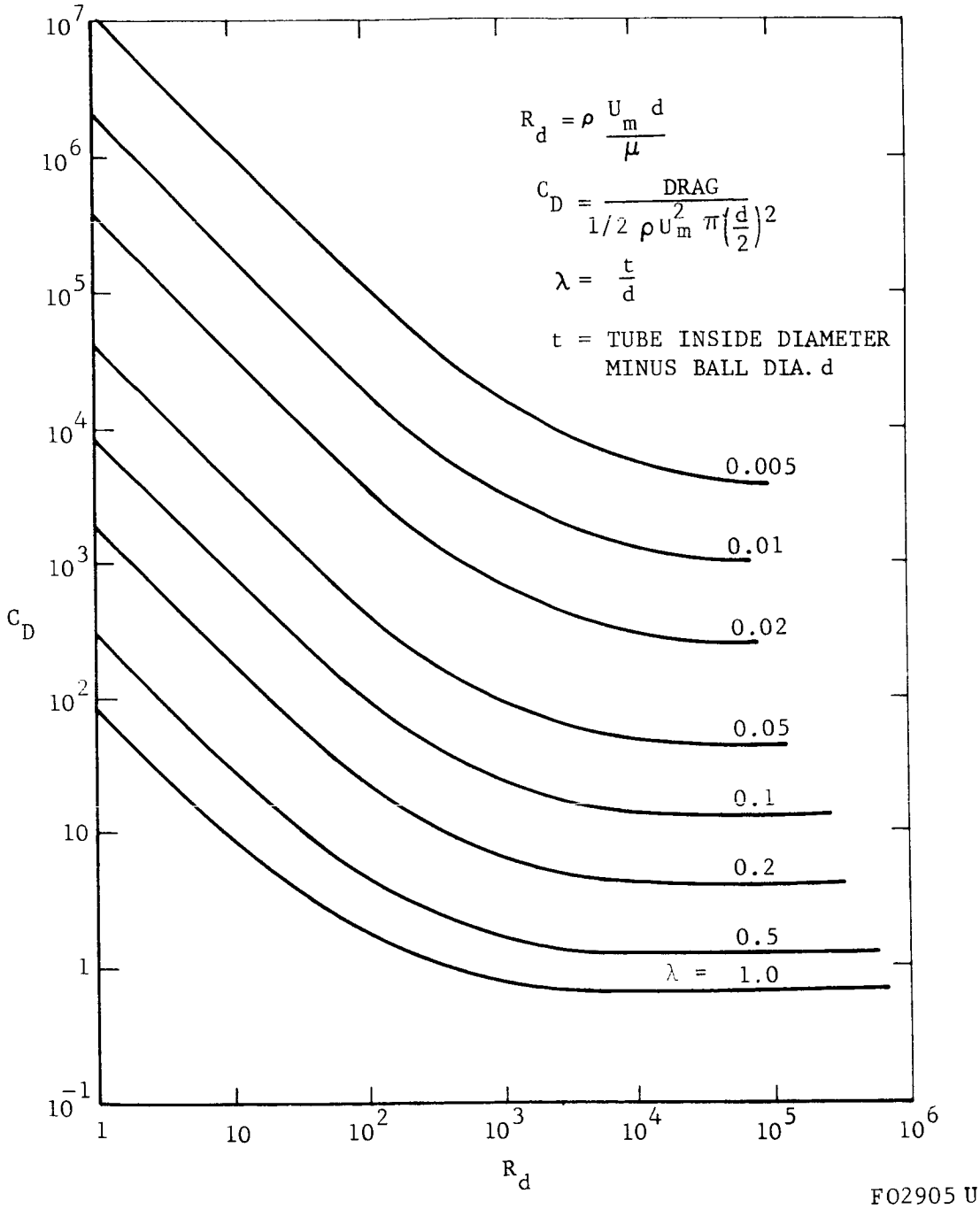

F02905 U

FIGURE 8-1. DRAG COEFFICIENT VERSUS REYNOLDS NUMBER (THEORY)

$$\theta = \frac{DU}{\frac{\pi}{4}d^2(1 + \lambda)^2 U\rho g C_p} \tag{8-10}$$

or

$$\theta = \frac{C_D U^2}{2(1 + \lambda)^2 g C_p} \tag{8-11}$$

where most symbols are defined above, g is the acceleration of gravity, and C_p is the fluid specific heat.

A typical value of θ can be found by using the drag coefficient for the case where the sphere drag is just equal to the inertial driving force. This is expressed by

$$C_D = \frac{4wd^3 N\rho}{3\mu^2 R_d^{\ 2}} \tag{8-12}$$

where w is the weight of the sphere material per unit volume, and N is the number of "g's" of accelerating force on the sphere in the direction of the tube.

By using this and the Reynolds' number

$$R_d = \frac{\rho U d}{\mu}$$

one obtains the relation

$$\theta = \frac{2wdN}{3\rho(1 + \lambda)^2 g C_p} \tag{8-13}$$

Typical numbers of interest are

$w = .544$ lb/in^3 (tungsten carbide)

$d = 2$ in.

$N = 1$

$\rho = .002378$ slugs/ft^3 (air at one atmosphere)

$g = 32.2$ ft/sec^2

$C_p = 187$ ft lb/lb$^\circ$F (air)

$\lambda = .01$

then

$\theta = 7.2^\circ$F.

Thus, one pass of the sphere through the tube for one "g" acceleration produces only 7.2°F temperature rise. Successive passes or higher "g" loadings will increase this heating, but this does not appear to be a problem. Also, the effective heating is reduced by the fact that the sphere may travel over only a small portion of the total length of the tube during each cycle of a re-entry oscillation.

8.4 EXPERIMENTAL CONSIDERATIONS

Experiments have been performed by rolling several stainless steel balls through aluminum tubes and measuring the resulting velocities. When the sphere has reached its equilibrium or terminal speed, its drag is just equal to the driving force, as expressed by equation (8-12). This shows that the range of C_D which may be tested for some given value of R_d is proportional to wd^3N and to the fluid parameter ρ/μ^2.

Since atmospheric air has a value of ρ/μ^2 which is almost as large as or much larger than all other readily available fluids, it was the only fluid utilized in the experimental program.

The parameter N was varied experimentally over a range of about 0.01 to 0.75 by changing the slope of the tube. With these values of N and ρ/μ^2, most of the interesting range of the C_D - R_d plane can be covered using a stainless steel ball with a diameter of approximately 2 inches. Other experiments were performed using nominally 1-inch diameter balls in order to verify the experiments performed with the larger balls.

A third set of experiments was completed in which the larger balls ($d \cong 2$ inches) were subjected to "g" loads corresponding to $.5 \leq N \leq 10$. In these tests a short inclined tube was placed in a centrifuge, and the component of the centrifugal force in the direction of the tube axis provided the high "g" environment.

Another experimental consideration which affected all experiments is the distance necessary for the ball to travel before reaching its equilibrium speed. This, effectively, places an upper limit on the sphere velocities which can be obtained with laboratory facilities. An estimate of this "equilibrium" distance may be obtained as follows.

Consider a sphere of weight W rolling down an inclined plane and being acted upon by the propulsive force WN, and a retarding drag force which we assume to be proportional to its translational velocity, U. The net force, F, acting on the ball may be expressed as

$$F = WN \left(1 - \frac{U}{U_m}\right) \tag{8-14}$$

so that when $U = U_m$, no net forces will be influencing the ball and it will no longer accelerate. U_m is therefore referred to as the equilibrium velocity.

When appropriate rolling inertia considerations are made, it may be shown that the acceleration, $\ddot{x}$, is given by

$$\ddot{x} = \frac{5}{7} gN \left(1 - \frac{\dot{x}}{U_m}\right) = A - B\dot{x} \tag{8-15}$$

where $A = \frac{5}{7} gN$ and $B = \frac{A}{U_m}$

(If the ball should slide rather than roll, this equation would not be valid.)

Equation (8-15) may be rewritten as

$$\dot{V} + BU = A \tag{8-15a}$$

or

$$\frac{dV}{dt} = A - BU \tag{8-15b}$$

When equation (8-15b) is integrated and solved for t, we find that

$$t = \frac{1}{B} \log \left(\frac{A}{A - BU}\right) = \frac{1}{B} \log \left(\frac{1}{1 - \frac{U}{U_m}}\right) \tag{8-16}$$

and

$$\left(1 - \frac{U}{U_m}\right) = e^{-Bt} \tag{8-17}$$

We may now change equation (8-17) to the form

$$\frac{dx}{dt} = U = U_m \left(1 - e^{-Bt}\right) \tag{8-17a}$$

and after the proper integration we have an expression for the distance x required by velocity U_m and time t.

$$x = U_m t + \frac{U_m^2}{A} \left[e^{-Bt} - 1\right] \tag{8-18}$$

We now let the time t_n and the distance x_n correspond to the time when

$$\left(1 - \frac{U}{U_m}\right) = \frac{1}{e^n}$$

Then from equation (8-16) we find that

$$t_n = \frac{1}{B} \log e^n = \frac{n}{B} \tag{8-16a}$$

and

$$x_n = \frac{U_m}{B} \left\{(n - 1) + e^{-n}\right\} \tag{8-18a}$$

For cases of interest to these experiments n may assume any value from $n = 1$ to $n = \infty$. Therefore the ratio (U/U_m) may be made to approach unity as close as desired by merely letting n be sufficiently large.

If we now consider the same rolling sphere system in the absence of any drag forces, a consideration of the kinetic and potential energies of the system shows that the kinetic energy must be equal to the potential energy lost in traveling a distance x_o. Therefore we have

$$K.E. = \frac{7}{5}\left(\frac{1}{2}\frac{W}{N}U_m^2\right) = WNx_o \tag{8-19}$$

and

$$x_o = \frac{7}{10}\frac{U_m^2}{gN} \tag{8-19a}$$

Given the velocity, U_m, and equations (8-18a) and (8-19a) we develop the following results.

$$x_o = \frac{7}{10}\left(\frac{U_m^2}{gN}\right) = k_o\left(\frac{U_m^2}{gN}\right) \tag{8-19a}$$

$$x_n = \{(n - 1) + e^{-n}\}\frac{U_m}{B} = k_n\frac{U_m^2}{gN} \tag{8-18a}$$

where $n = 1,2,3 \ldots$

$k_o = 0.700$ (no drag - 100% U_m)

$k_1 = 0.515$ $(U/U_m = 0.63)$

$k_2 = 1.588$ $(U/U_m = 0.87)$

$k_3 = 2.87$ $(U/U_m = 0.95)$

$k_4 = 4.22$ $(U/U_m = 0.98)$

In view of these results, it may be shown that a ball falling through a vertical distance of 10 feet under the influence of a one-"g" load will achieve a velocity (with little or no drag) of approximately 21 ft/sec. In order to reach 95% of this velocity in the presence of retarding drag

forces, the same ball would have to travel through a distance x_3 given by

$$x_3 = \left(\frac{k_3}{k_o}\right) (x_o) = \left(\frac{2.87}{.70}\right) (10) = 41 \text{ ft}$$

This problem was circumvented by providing a length of tubing which is slotted on its top side. The slot allows air to escape so that the drag force in this portion of the tube is much less than in a second portion of the same tube, which is not slotted. The first part is used to bring the sphere up to the desired testing speed; in the second part, the speed is measured by passing a light beam across the tube at three equidistant stations. A light-sensitive device is used to record the passage of the ball. If the time between the breaking of the first and the second light beams is less (or more) than that between the second and third light beams, the ball is slowing (or speeding) in the tube, and the equilibrium velocity was exceeded (or was not attained). From this information, the vertical fall distance in the first part of the tube can be either decreased (or increased) so as to decrease (or increase) the velocity the sphere attains in the first portion of the tube. After several trials, a starting height is found that accelerates the sphere to just its terminal speed. In the above example, this slotting technique would decrease the required tube length for sphere acceleration from something greater than 40 feet to about 10 feet.

Similar considerations were applied to the centrifuge experiments and the results, in conjunction with physical size limitations, determined which ball sizes could be studied.

8.5 EXPERIMENTAL FACILITIES

A photograph of the experimental apparatus used in the inclined tube studies (low "g") is shown in Figure 8-2, and a schematic representation of the facility is presented in Figure 8-3. As was mentioned in a previous section, the apparatus consists of a 9 foot long aluminum tube which is

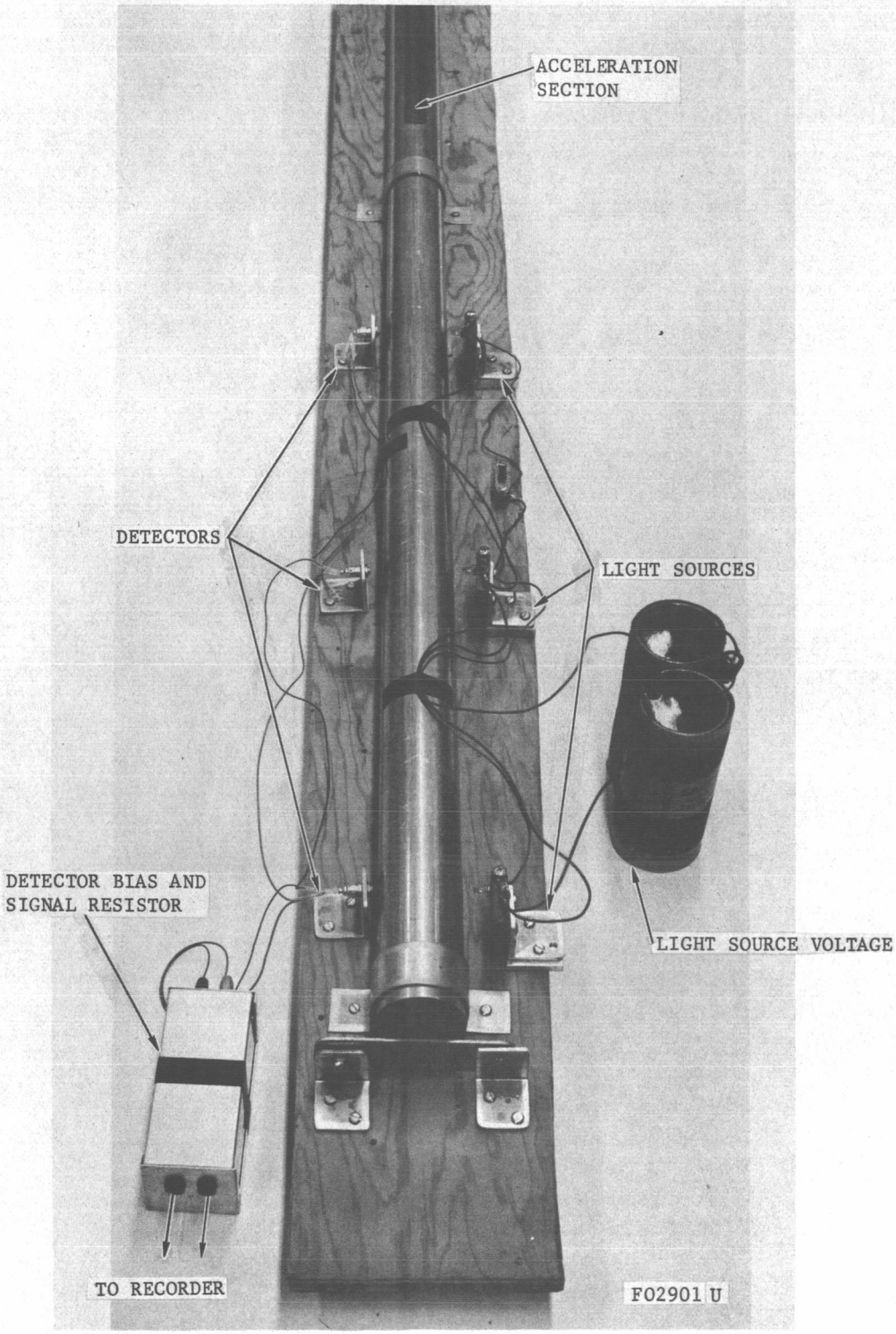

FIGURE 8-2. LOW -"g" EXPERIMENTAL APPARATUS

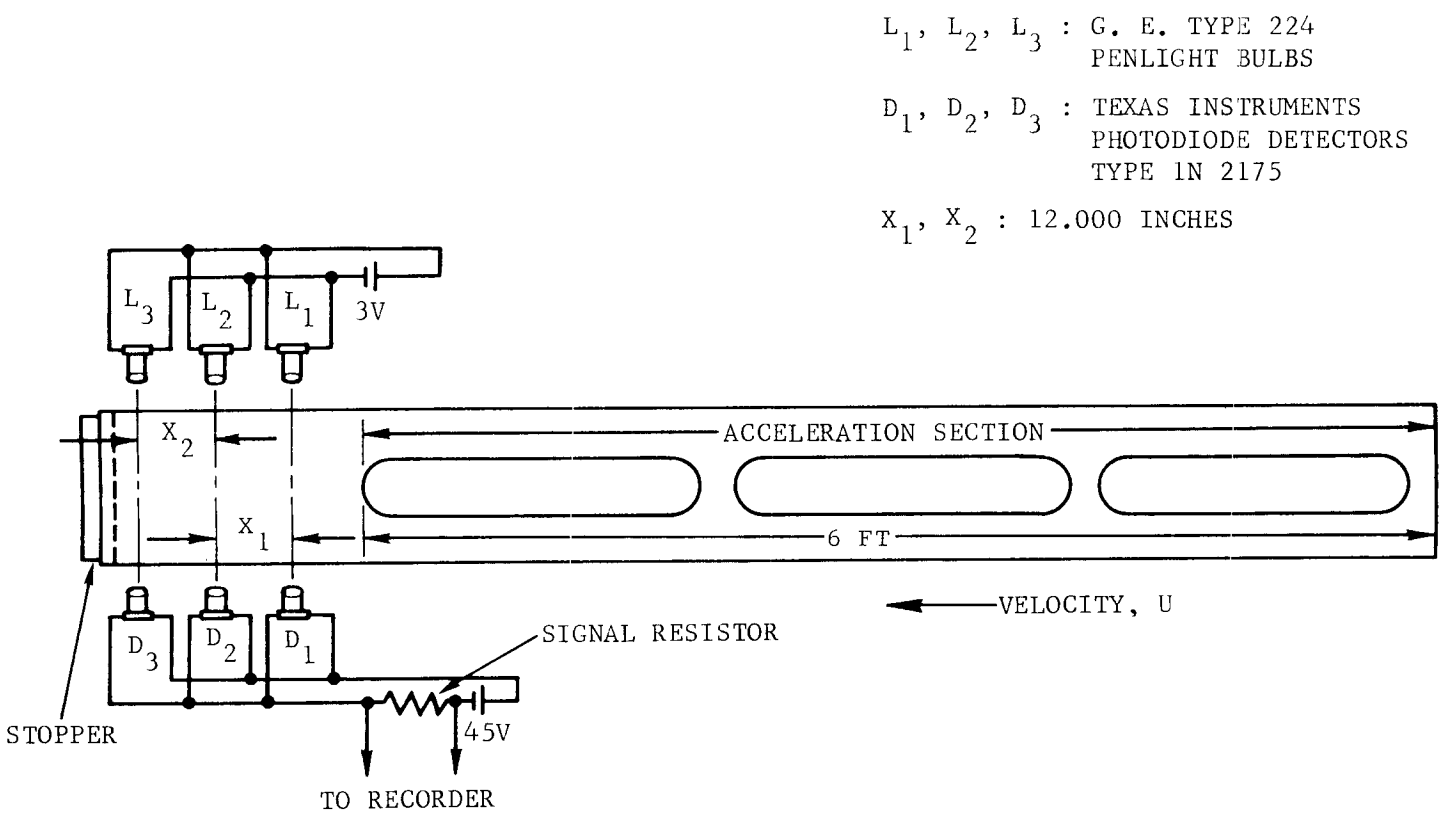

F02908 U

FIGURE 8-3. SCHEMATIC OF LOW - "g" EXPERIMENTAL APPARATUS

divided into a slotted accelerating section (6 feet long) and a test section. The test section is in turn divided into two portions. The first foot of the tube is merely a closed portion (no slots) one foot long, which is used to help the sphere reach equilibrium before it enters the actual test section. The test section is comprised of three small holes (0.040 inches diameter) placed 12.000 inches apart, and which have been covered and sealed with a thin (0.015 inch thick) clear mylar film to prevent air leakage. Details concerning the light sources and the detectors are presented in Figure 8-3.

The detectors are photoconductive devices whose resistance decreases as light is made incident upon them. Therefore, as the sphere rolls down the inclined tube past each detector, the total impedance of the circuit changes and expresses itself as a change in the voltage drop across the series resistor. The resulting signal approximates a square wave and is shown in Figure 8-4. This figure is actually a tracing of a typical test run.

The output signal mentioned above is placed into an amplifier whose output is then used to drive a galvonometer-type recorder. The recorder used in these experiments was a Visicorder Model 1108 used in conjunction with a 1000 cps fluid-damped galvonometer. The recorder has several drive speeds and a timing line generator. This mechanism places a signal on the record at discrete intervals of 1.0, 0.1, and 0.01 seconds. These marks are also shown in Figure 8-4. Therefore, if one assumes a constant recorder speed, the travel time between detectors may be measured to about 0.002 seconds by interpolating between 0.01 second markers.

A 32-inch long version of the inclined tube model was constructed for use in a series of centrifuge experiments. Figures 8-5 and 8-6 are photographs of the apparatus prior to mounting in the centrifuge, and as it appeared in the centrifuge, respectively. The inside vertical height of the centrifuge facility dictated the maximum length of tubing which could be

11-19-65
RUN #52 (d = 1.938 IN.)
STAINLESS STEEL BALL
X = 36 IN.
N = 0.558

NOTE: X IS STARTING POSITION RELATIVE TO TEST SECTION ENTRANCE

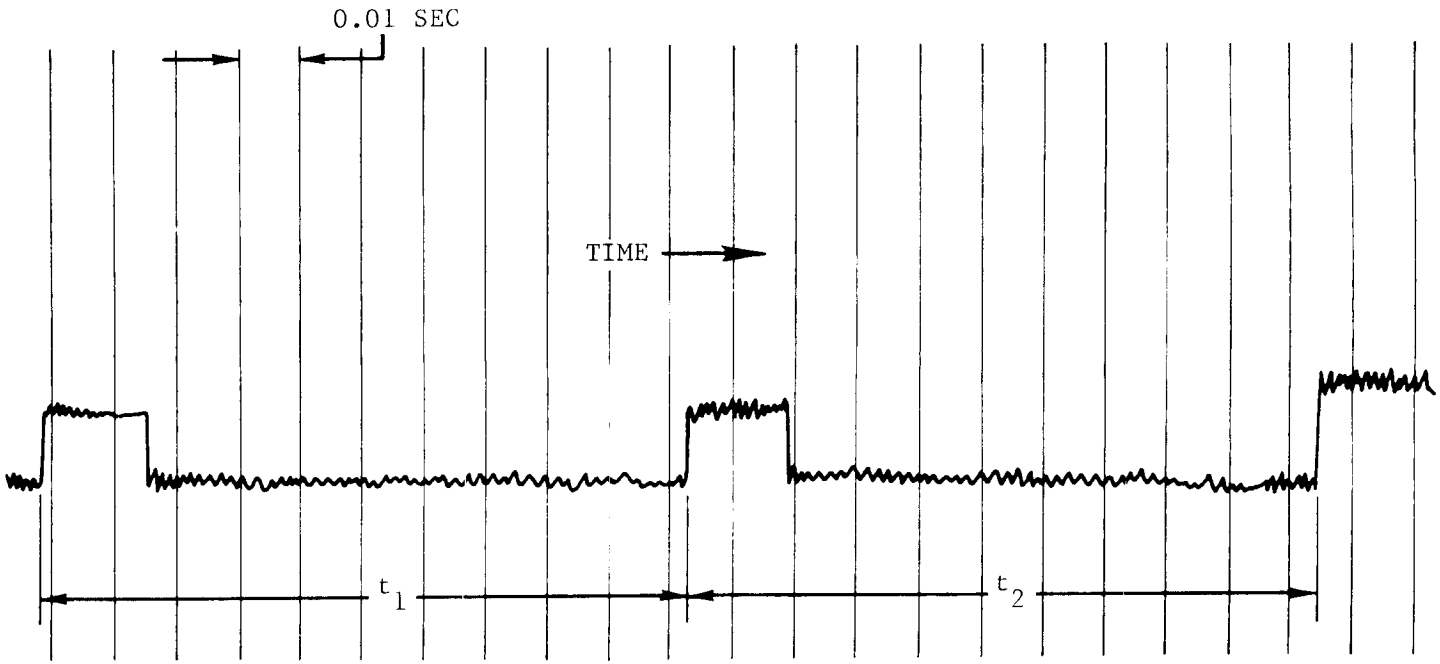

t_1 = 0.104 SEC.
U_1 = 9.62 FT/SEC.

t_2 = 0.102 SEC.
U_2 = 9.80 FT/SEC.

F02914 U

$$U_i = \frac{12.000 \text{ IN.}}{t_i \text{ SEC}} = \frac{1.0 \text{ FT}}{t_i \text{ SEC}}$$

FIGURE 8-4. OSCILLOGRAPH OUTPUT

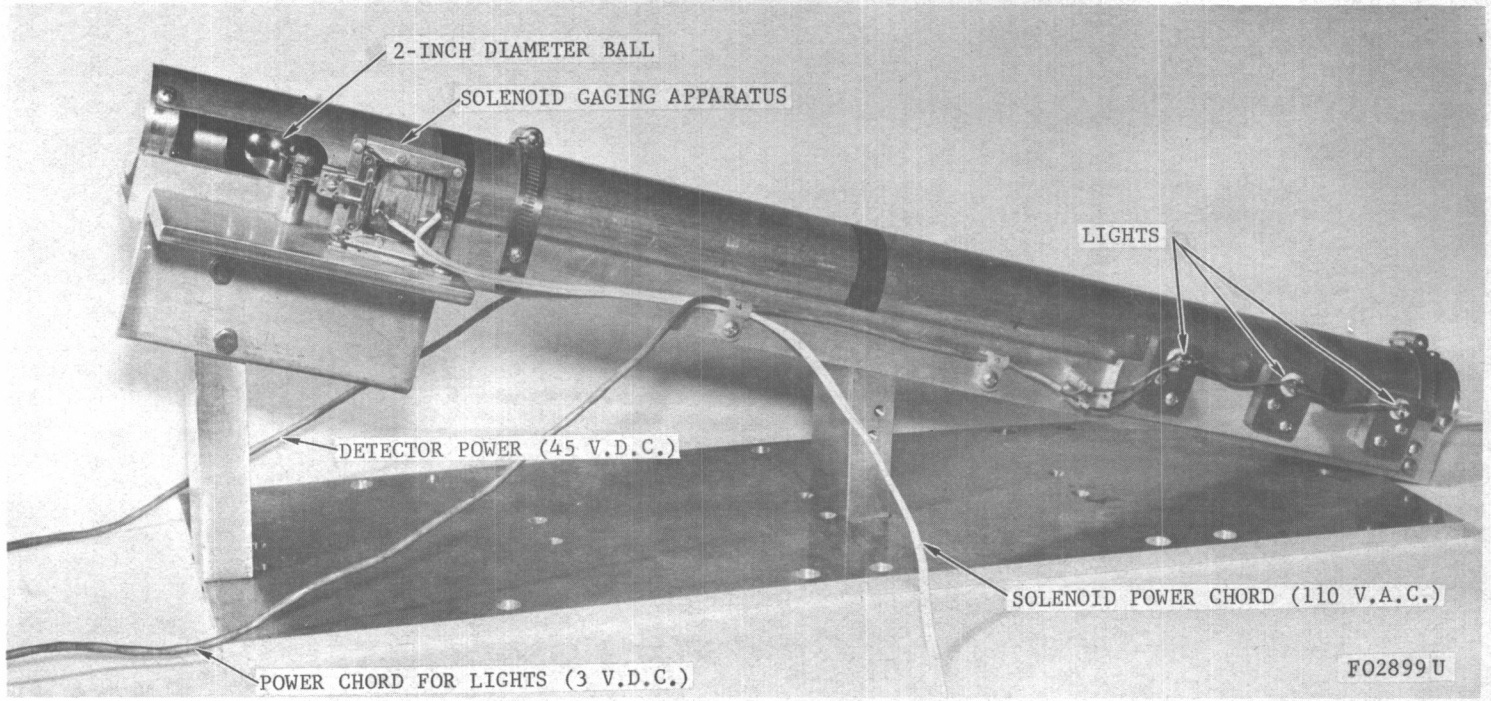

FIGURE 8-5. EXPERIMENTAL APPARATUS FOR CENTRIFUGE STUDIES

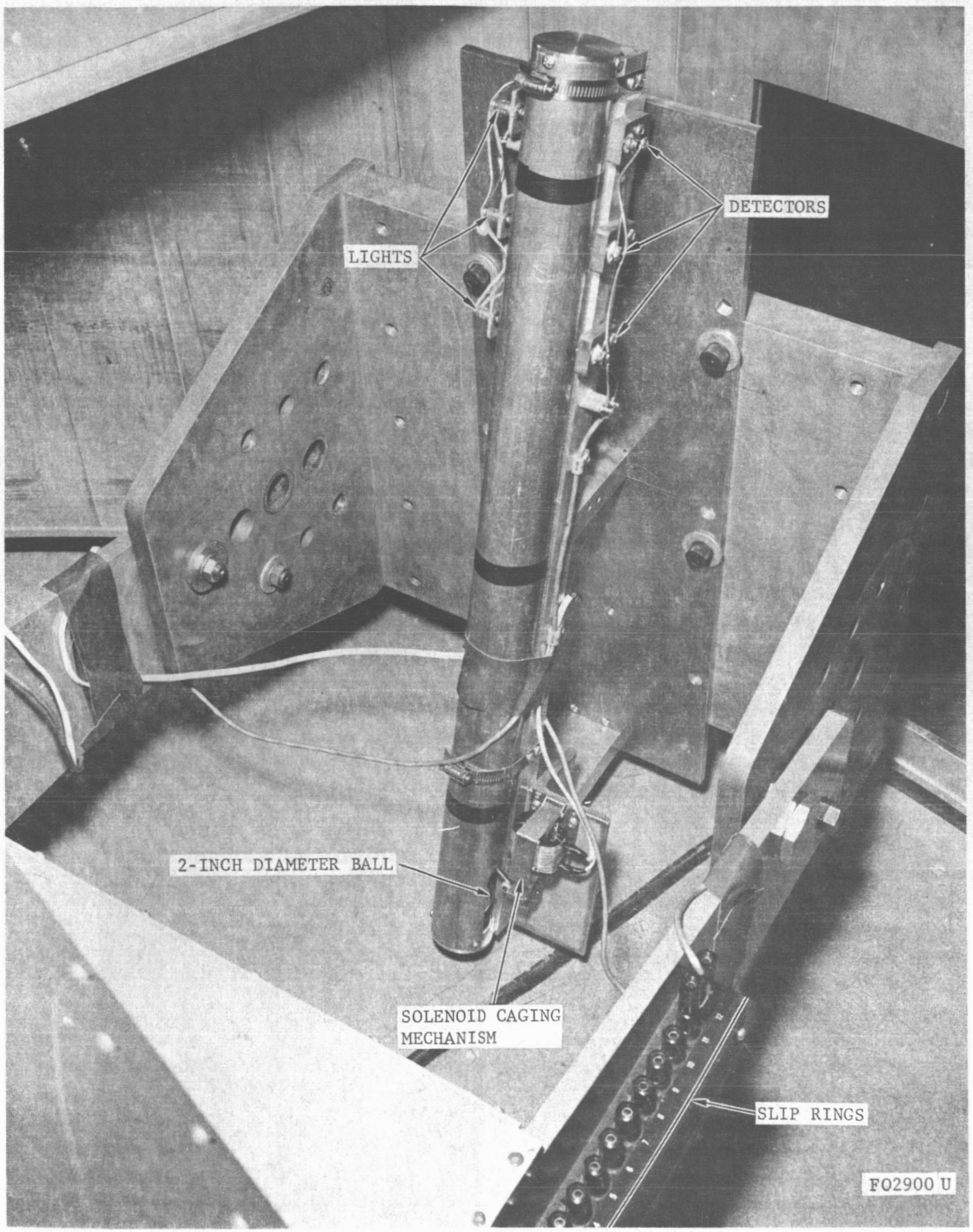

FIGURE 8-6. EXPERIMENTAL APPARATUS AS VIEWED FROM TOP OF CENTRIFUGE

used, and the tube length in turn determined which ball sizes could be studied. Calculations indicated that the largest λ which could be studied while allowing the ball to reach equilibrium velocity inside the tube was 0.01. Therefore, only balls corresponding to λ-values of 0.004 and 0.008 were used. Figure 8-7 is a sketch of the test apparatus showing the actual radial positions of the detectors.

Details of the centrifuge facility used are as follows:

Manufacturer:	Geniso, Inc.
Model:	A-1030
Rating:	10,000 g-lb maximum 0.1 to 150 g at 38-in radius 100 lb to 100 g
Stability:	Stability is 0.05 percent of steady-state g averaged over a three-minute period
Speed:	Variable from 10 to 400 rpm, measurement accuracy is $\pm$ 0.1 rpm
Rate:	3-1/3 rpm/sec maximum
Radius of Arm:	Variable from 27 in. to 45 in.
Slip Rings:	16 each at 1 amp, 5 amp, and 10 amp

As in the previous studies, the motion of a ball past a photo-detector was used to determine the ball velocities. The ball velocity at each of the two detectors was determined by dividing the ball diameter by the time that the ball interrupted the light beam. Since the light beam was less than 0.040 in. in diameter, the resolution of the time measurement was good.

No slotted accelerating section was used on the centrifuge model. Since the parameter (U_m^2/gN) appearing in equations 8-18a and 8-19a was small compared to the tube length, no slotted section was needed. Also, the range of tests was limited to small values of (U_m^2/gN) because the distance from the centrifuge axis of rotation to the ball varied somewhat with ball height (see Figure 8-7). The precaution of using only small values of

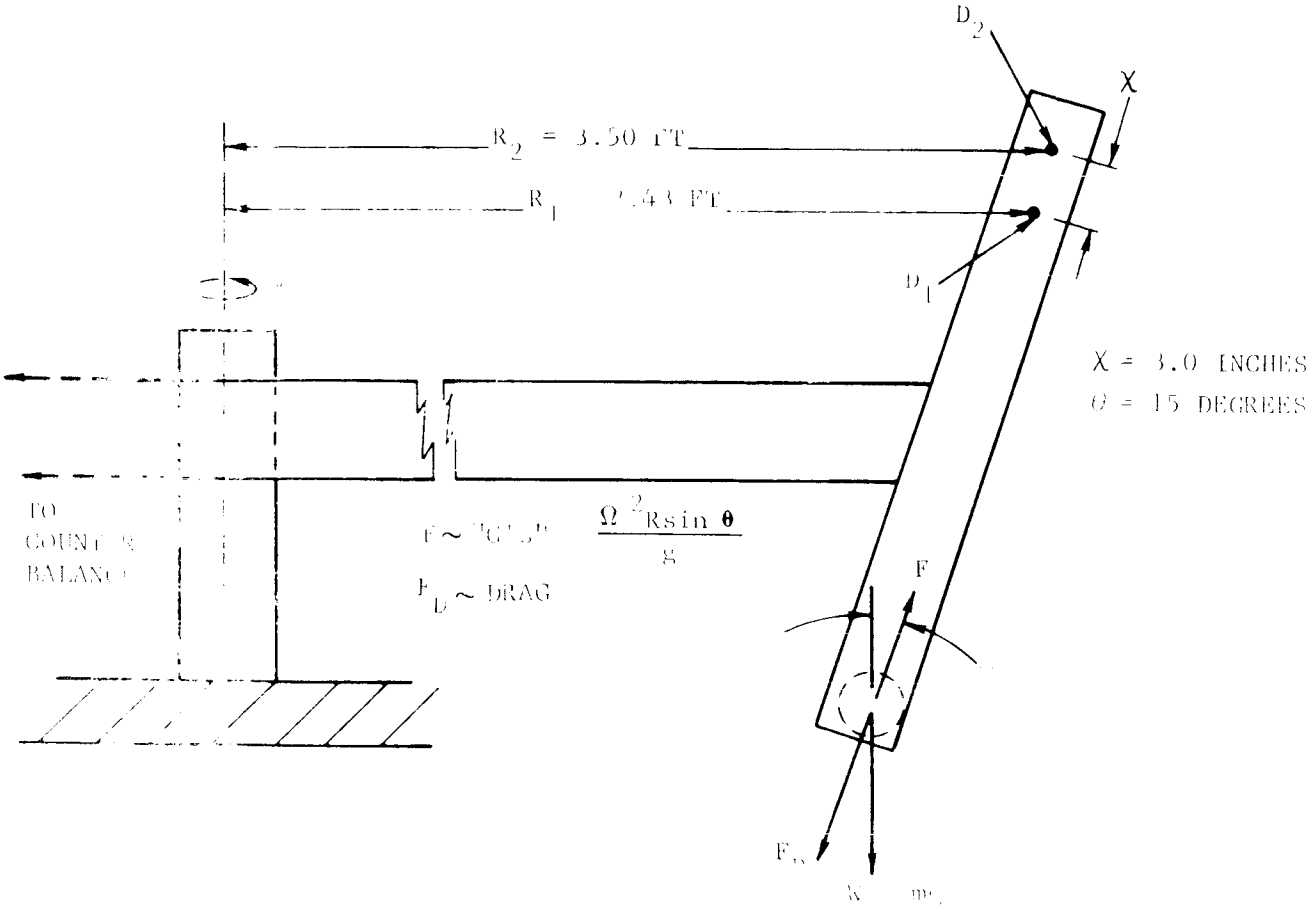

F029111U

FIGURE [illegible] CENTRIFUGE APPARATUS; DIMENSIONS AND FORCE DIAGRAM

(U_m^2/gN) meant that the ball should approach its equilibrium speed with only a short travel distance.

The procedure employed to obtain the high-"g" data was as follows. A solenoid-operated caging apparatus was used to hold the ball in place at the bottom of the tube until the centrifuge reached a predetermined angular velocity. Once it was determined the centrifuge was operating steadily at the desired speed, power to the solenoid was interrupted, the ball proceeded up the tube, and the resulting velocities were measured. An electrical "trip" wire at the top of the tube was connected to a small light outside the centrifuge in order to determine when the ball reached the top. The centrifuge was then stopped and prepared for another run.

8.6 EXPERIMENTAL RESULTS

The inclined tube configuration was used to complete the low-"g" experiments using nominally 2-inch diameter balls. Four gap sizes with corresponding λ-values of 0.004, 0.008, 0.015, and 0.036 have been studied, and the drag coefficient data are shown in Figures 8-8 and 8-9. The solid lines represent the analytical predictions against which the experimental results may be compared, and are large scale reproductions of the analytical results shown in Figure 8-1.

As was expected, the lower λ case (λ = .004) was by far the easiest to study. Drag forces in this instance were relatively large, and the sphere reached equilibrium velocity in a very short distance. The tube used in these experiments had a nominal inside diameter of 2.008 inches. However, minor variations in the tube diameter were present from the extrusion process, and at extremely low values of λ these variations create a significant error in λ. In order to overcome this difficulty, the diameter fluctuations of the entire test section were carefully measured. The results indicated that a value of 2.009 inches should be used for the length between the first two detectors, and 2.007 inches between the second pair

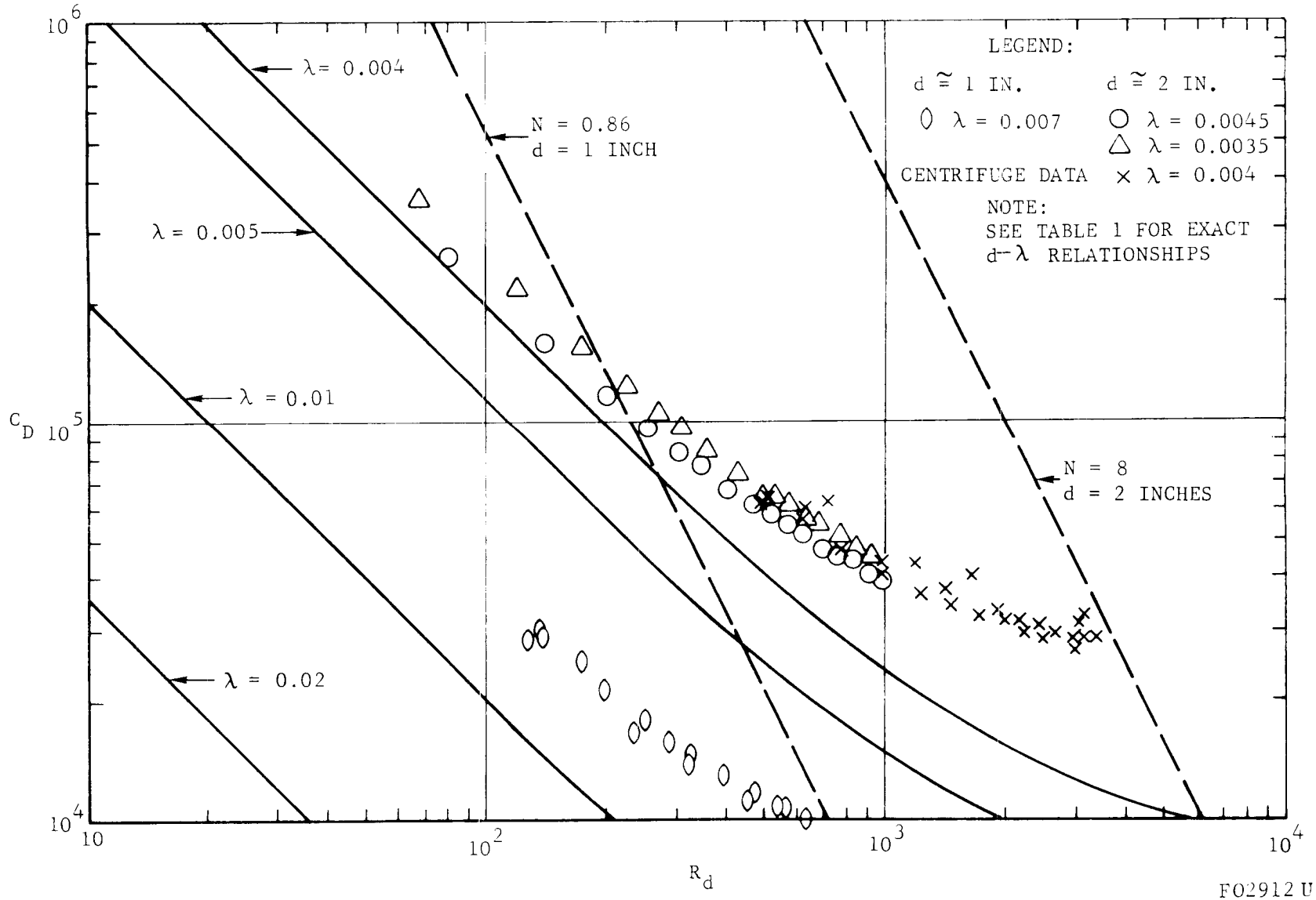

F02912 U

FIGURE 8-8. REYNOLDS NO. VERSUS DRAG COEFFICIENT THEORY AND EXPERIMENT

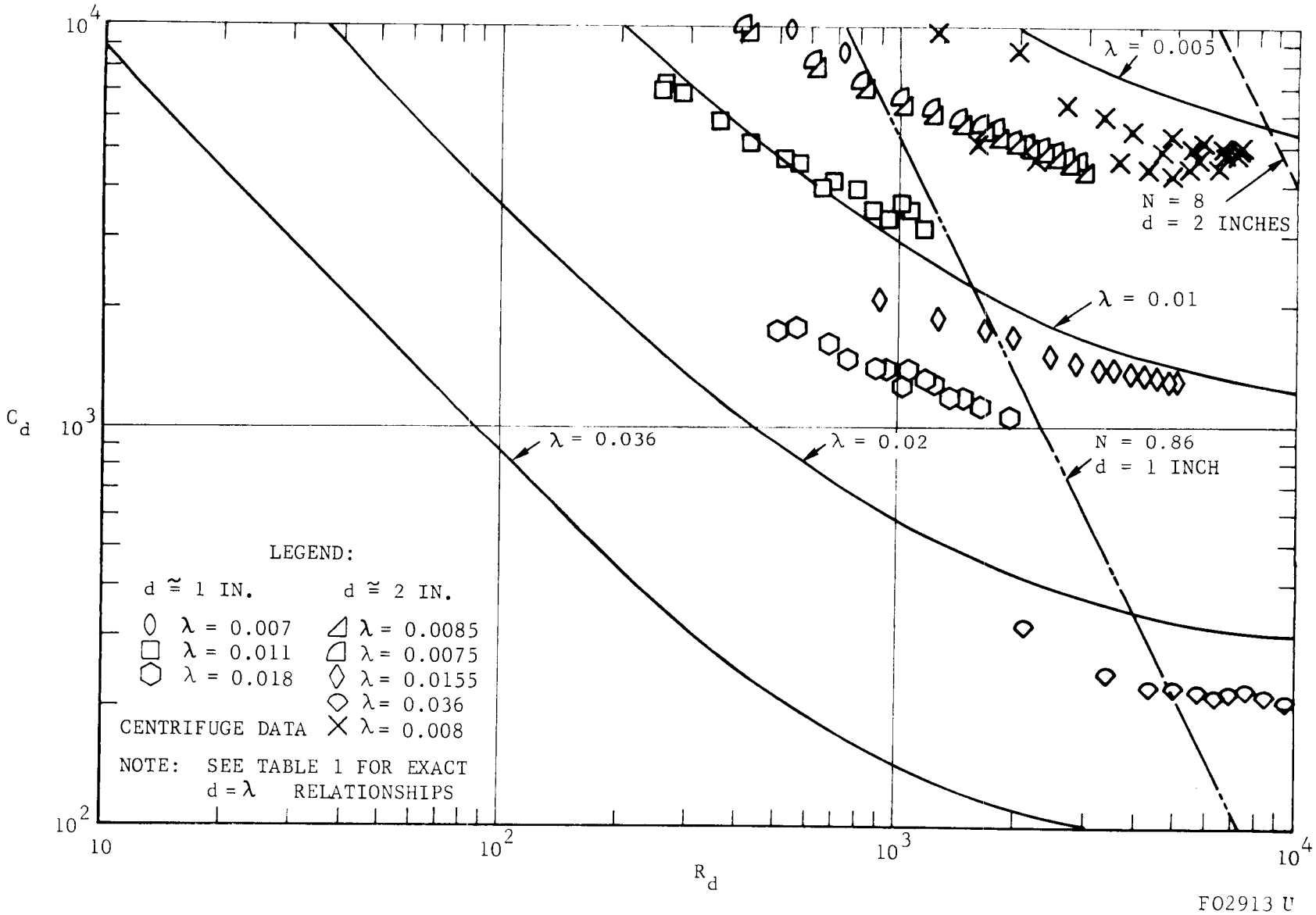

FO2913 U

FIGURE 8-9. REYNOLDS NO. VERSUS DRAG COEFFICIENT THEORY AND EXPERIMENT

of detectors. This explains the appearance of the two sets of data points shwon in Figure 8-8. In practice, it became impossible to obtain identical velocities between the two pairs of detectors for the lower λ-values, and this led to the inspection mentioned above. For values of λ greater than about 0.1, this effect was sufficiently small to be undetectable, as may be seen in Figure 8-9.

Similar experiments were performed using nominally 1-inch diameter balls (λ = 0.007, 0.011, 0.018) as a check on the previous results. These are also shown in Figures 8-8 and 8-9. Although the Reynolds number range of the two ball sizes is somewhat different, enough data points are shown to indicate consistent results regardless of ball size. The broken diagonal lines appearing in Figure 8-8 and 8-9 represent the 0.86 "g" testing limit for a 1-inch ball (which is about the largest "g" testing that can be done using a fixed tube - that is, without the centrifuge), and the 8 "g" limit for a 2-inch ball. These limits were calculated from equation 8-12.

Figures 8-10 and 8-11 are the resulting velocity profiles obtained in the centrifuge. It should be noted that two distinct sets of data points appear on each figure. Although reference to Figure 8-6 shows that three detectors were present, only two were actually used at one time. Since the detectors are at slightly different radial positions from the center of the centrifuge, the balls experience slightly different centrifugal forces and necessarily different velocities result. The resulting velocities are shown in Figures 8-10 and 8-11. It should be noted that in referring to the "g"-load, N, we are always speaking of the load in the direction of the axis of the tube unless specified otherwise.

Two difficulties appear upon examination of the velocity data. The first is the fact that the curves of velocity versus N of the centrifuge data do not even closely agree with those obtained earlier using the fixed tube. These are compared in Figures 8-12 and 8-13. Because of this

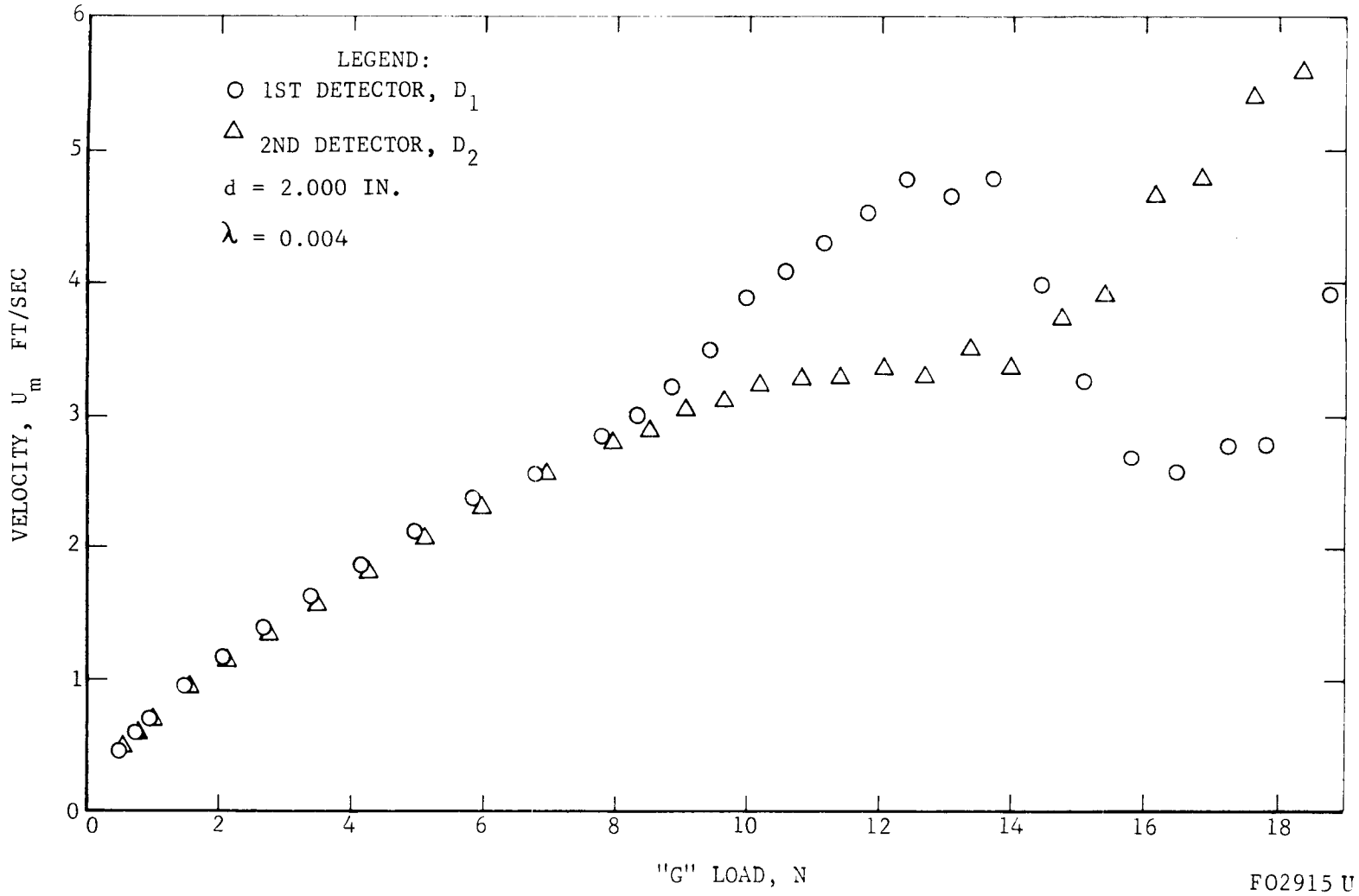

FIGURE 8-10. CENTRIFUGE VELOCITY PROFILE FOR 2-INCH BALL ; $\lambda = 0.004$

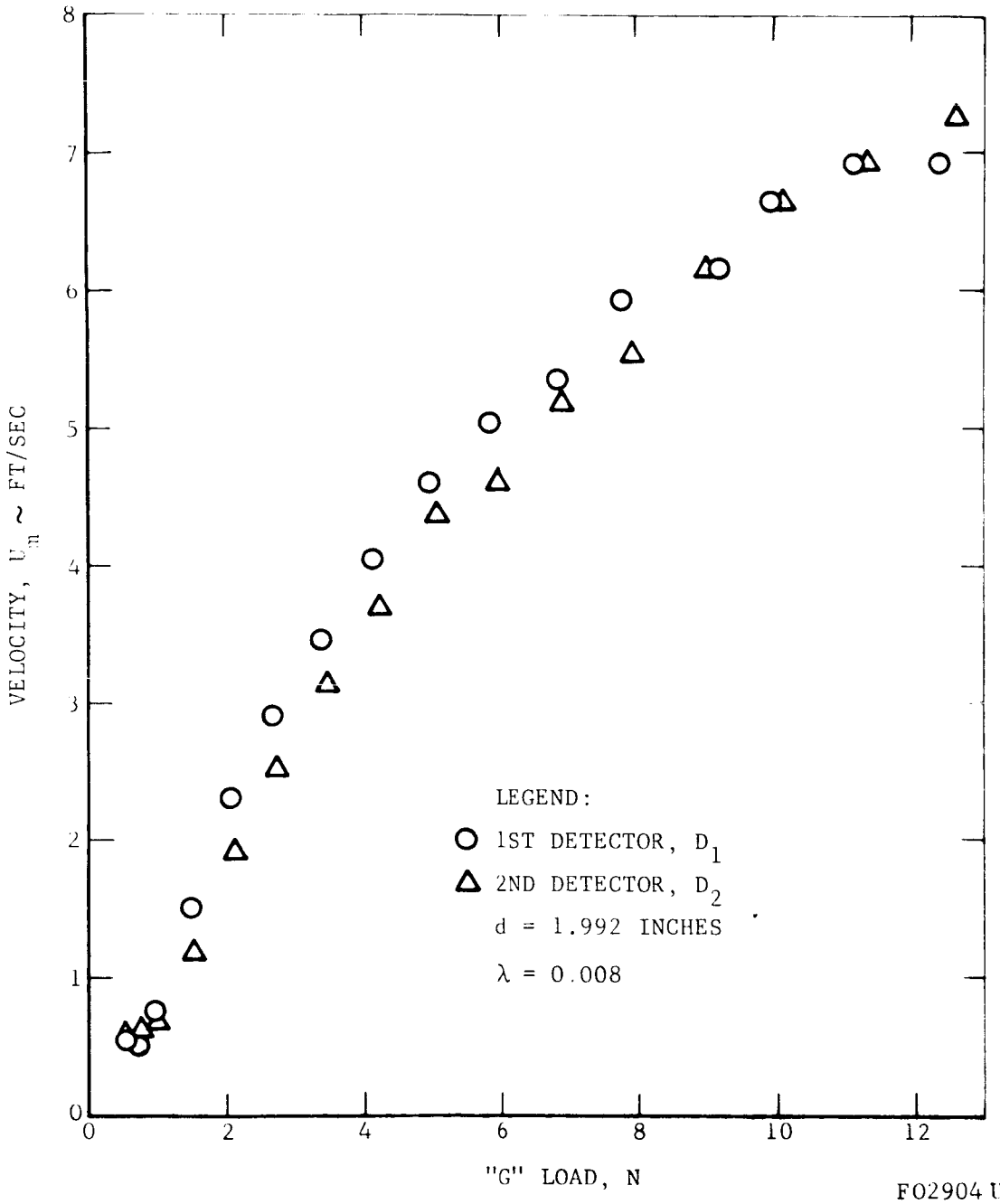

F02904 U

FIGURE 8-11. CENTRIFUGE VELOCITY PROFILE FOR 2 INCH BALL; λ = 0.008

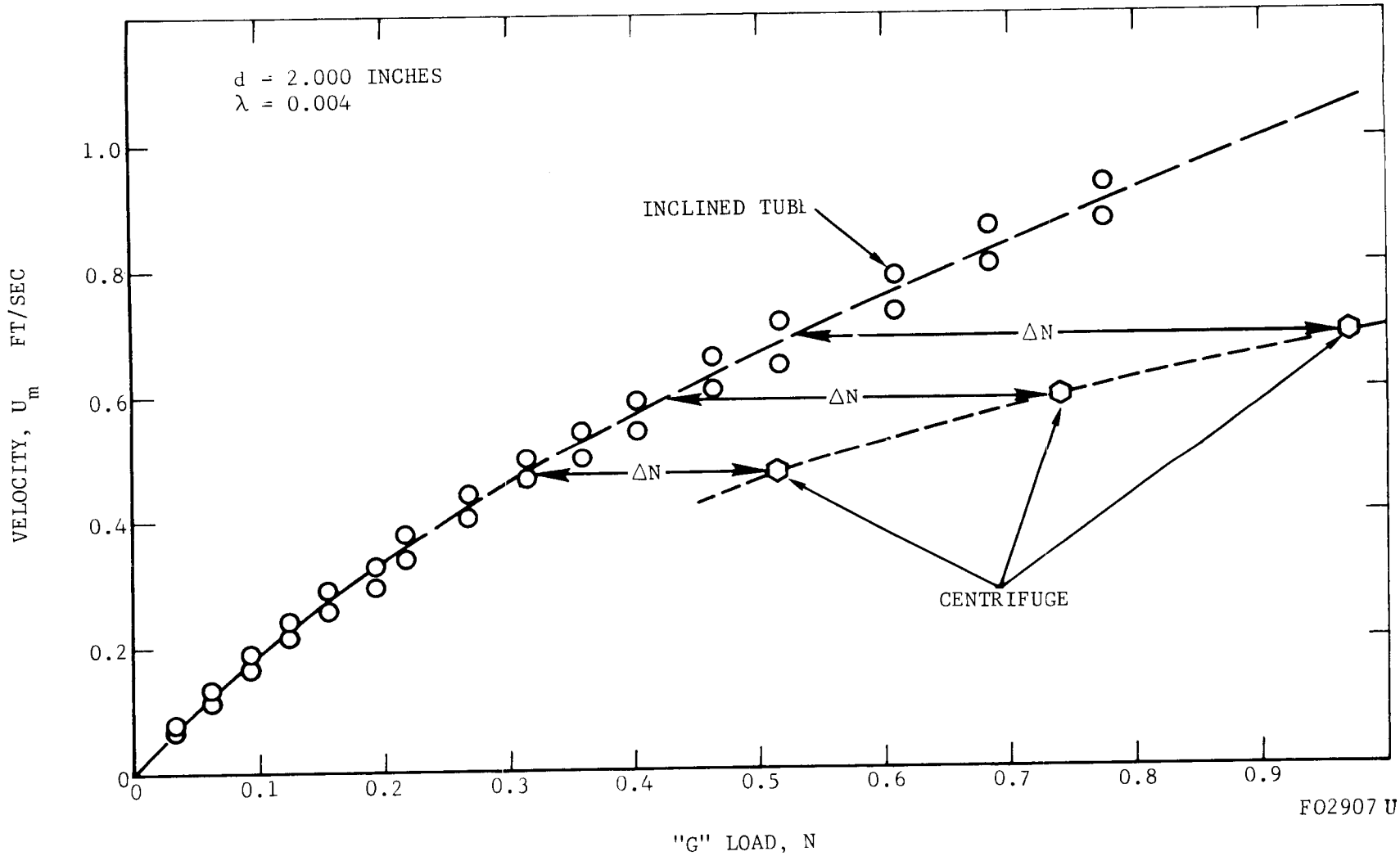

FIGURE 8-12. COMPARISON OF VELOCITY PROFILES FROM INCLINED TUBE AND CENTRIFUGE

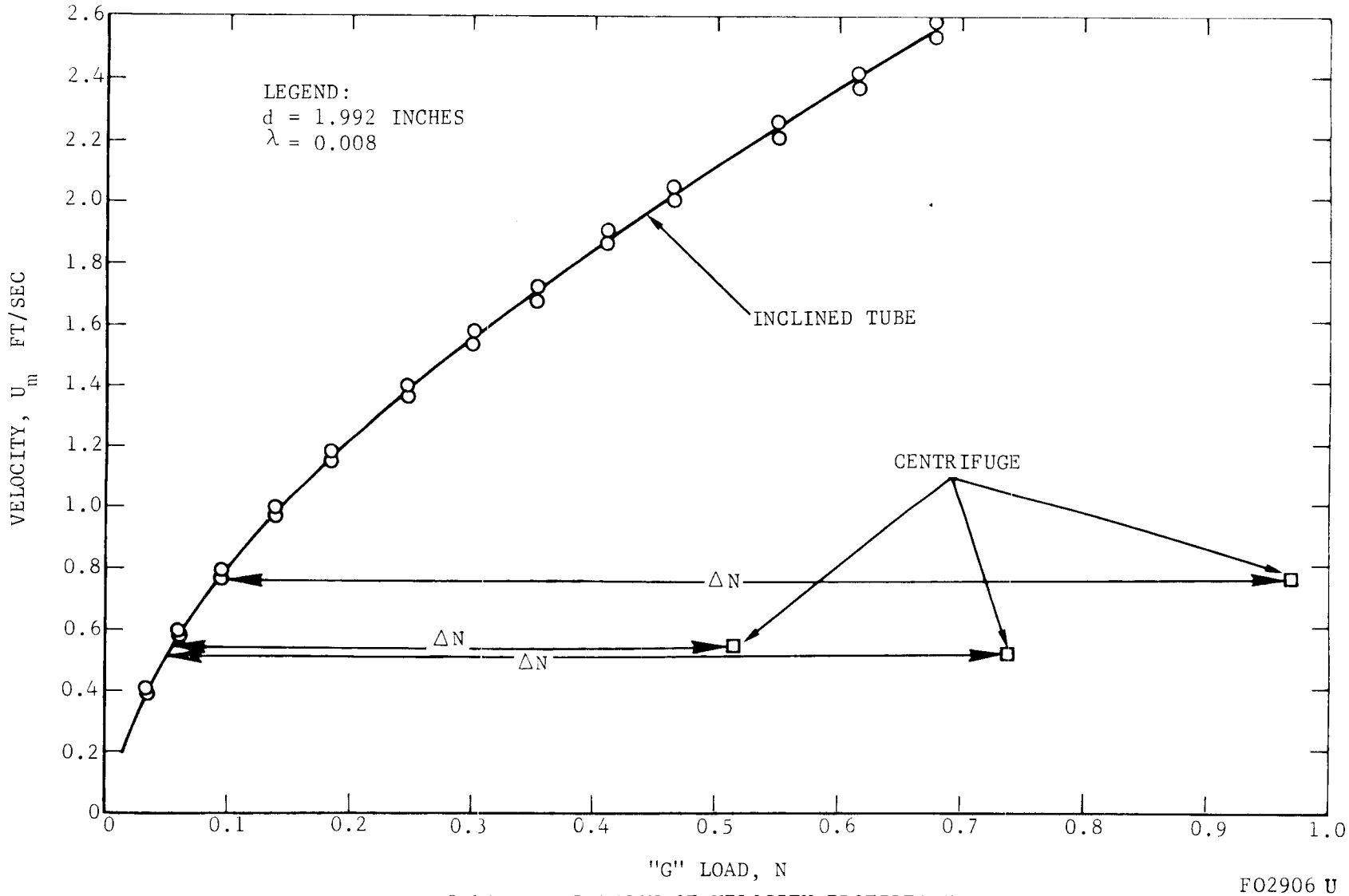

F02906 U

FIGURE 8-13. COMPARISON OF VELOCITY PROFILES FROM INCLINED TUBE AND CENTRIFUGE

disagreement, the two types of experiments were carefully analyzed to discover a reason for the disagreement. The Coriolis force was present only for the centrifuge tests, but a careful consideration of this did not show a significant effect. The ball rolling friction was measured, and the retarding force was found to be slightly less than 0.002 times the normal force between the ball and the tube; this also produced no significant effect to explain the disagreement. A third effect, the so-called "spinning phenomenon", was discovered and is used here to explain the difference.

The idea of the spinning phenomenon is a result of the observation that if the ball were to roll along the tube while the tube was being rotated by the centrifuge, as first had been supposed, then the vector $\dot{\phi}$ which represents the ball rotational velocity must change its direction at the rate Ω, where Ω is also the angular velocity of the centrifuge arm. This is shown in Figures 8-14 and 8-15, where $\dot{\phi}$ is the angular velocity of the ball. Figures 8-14 and 8-15 are unrealistic because the centrifuge fails to provide a torque to the ball that would cause $\dot{\phi}$ to change in the manner indicated.

Since Figures 8-14 and 8-15 are not correct, the investigators supposed that the ball must <u>slide</u> rather than roll through the tube. Furthermore, it was supposed that the vector $\dot{\phi}$ remained constant with respect to the centrifuge arm and at some angle α as shown in Figure 8-16. This assumption was made because the problem would be greatly increased in complexity if $\dot{\phi}$ were not constant. Now, since the ball is sliding upward in the tube, the friction force imposes on the ball a torque T which is constant with respect to the centrifuge. The torque adds a rotational acceleration to the ball, so that $\dot{\phi}$ must be changing absolutely. Since $\dot{\phi}$ is assumed fixed with respect to the centrifuge, the angle α must be zero. If α were any other angle, the magnitude of $\dot{\phi}$ would change in time. The torque T serves to change the direction of $\dot{\phi}$ absolutely; this change is just fast enough

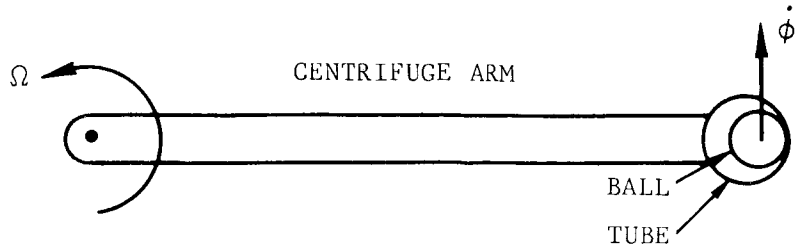

FIGURE 8-14. TOP VIEW OF CENTRIFUGE WITH BALL ROLLING UPWARD IN TUBE

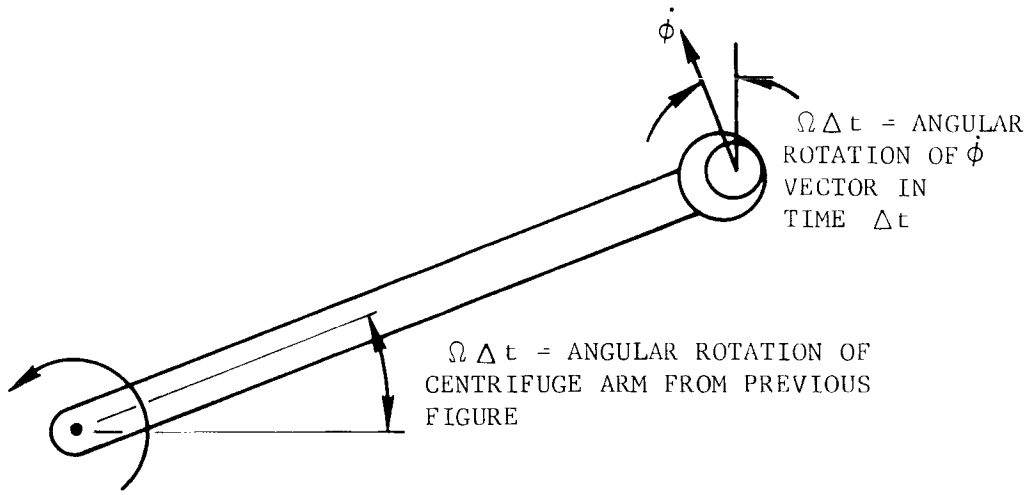

FIGURE 8-15. TOP VIEW OF CENTRIFUGE, BALL, AND TUBE A SHORT TIME AFTER THAT OF FIGURE 8-14.

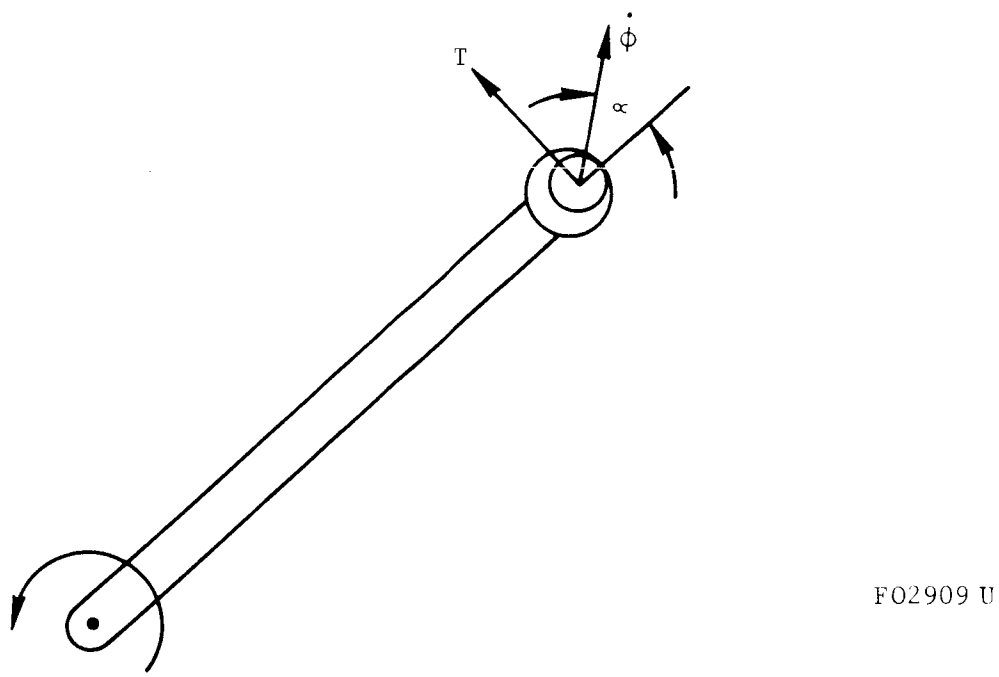

FIGURE 8-16. SUPPOSED EQUILIBRIUM ANGULAR VELOCITY OF BALL WITH RESPECT TO CENTRIFUGE

that $\dot{\phi}$ rotates with the centrifuge speed. Hence $\dot{\phi}$ remains constant with respect to the centrifuge. The important result is that the ball must be both spinning with velocity $\dot{\phi}$ and sliding in the tube. Therefore, the difference between the centrifuge and the fixed-tube results on Figures 8-12 and 8-13 is primarily the result of the sliding of the ball.

A correction for this sliding friction loss was applied to the centrifuge data, and is shown in a succeeding section.

The spinning of the ball should also make some change in the aerodynamic drag force on the ball, and this has not been separated from the friction force in the above paragraph. However, since the rotational velocity of the ball surface can be shown to be much smaller than that of the air near the ball surface, this should make only a quite small change in the aerodynamic drag. For this reason, the change has been neglected.

The second difficulty encountered appears in the data of Figures 8-10 and 8-11 (although the effect is more pronounced in Figure 8-10). At ball velocities of 3 ft/sec for $\lambda = 0.004$ and 7 ft/sec for $\lambda = 0.008$ the velocities at the two detectors differ greatly. An examination of this problem indicates that it is a Mach number effect. Reference to equation 8-1 shows that the average velocity, V, of the flow in the gap is related to the ball velocity, U, and the gap parameter, λ, by the relationship

$$\frac{V}{U} = \left\{1 + \frac{1}{2\lambda + \lambda^2}\right\} \tag{8-1}$$

If we calculate the quantity within the bracket for λ-values of 0.004 and 0.008, we get $(V/U)_{\lambda = .004} = 126$ and $(V/U)_{\lambda = .008} = 64$. If we now associate with each λ the respective ball velocities 3 ft/sec and 7 ft/sec we find the corresponding V-values to be $V_{\lambda = .004} = 378$ ft/sec and $V_{\lambda = .008} = 444$ ft/sec. Although these values are considerably lower than the sonic velocity (V = 1100 ft/sec) it must be remembered that they

represent the average velocity of the flow through the gap. It is not inconceivable that the maximum gap velocities could be two to three times the average velocity, in which case part of the flow would approach or exceed the speed of sound. Therefore, Mach number would be an important parameter in determining the ball drag, and shock waves could develop in the flow. The shock waves might be expected to produce unsteady values of drag and hence the separation of data points as shown on Figures 8-10 and 8-11.

Since the passive damper studies have been limited to cases where Mach number effects are not significant, the data points on Figure 8-10 exceeding 3 ft/sec and on Figure 8-11 exceeding 7 ft/sec will not be used in the final data. The tests indicate that Mach number effects will be significant whenever Mach number, the ratio of V to the sonic speed, exceeds about 0.35.

8.7 SLIDING FRICTION CORRECTIONS

In order to estimate the friction losses which appeared in the centrifuge experiments, reference must first be made to Figures 8-12 and 8-13. At some given velocity U, and specified λ (say, Figure 8-12; λ = .004) let ΔN be the difference between the two sets of data. Then the sliding friction coefficient μ_f must be given by

$$\mu_f = \frac{\Delta NW}{F_n} \tag{8-20}$$

where F_n is the force on the ball in the direction normal to the tube axis. The values of μ_f calculated from Figures 8-12 and 8-13 for the regions in which the velocities overlapped are shown in Figure 8-17. Although many data points were not available, an upper limit appears to exist which is a function of the gap parameter, λ. The upper limit for λ = .004 was rather arbitrarily chosen as μ_f = 0.09 whereas μ_f = 0.13 was taken as the upper limit for the λ = .008 data. In each instance the faired curves were

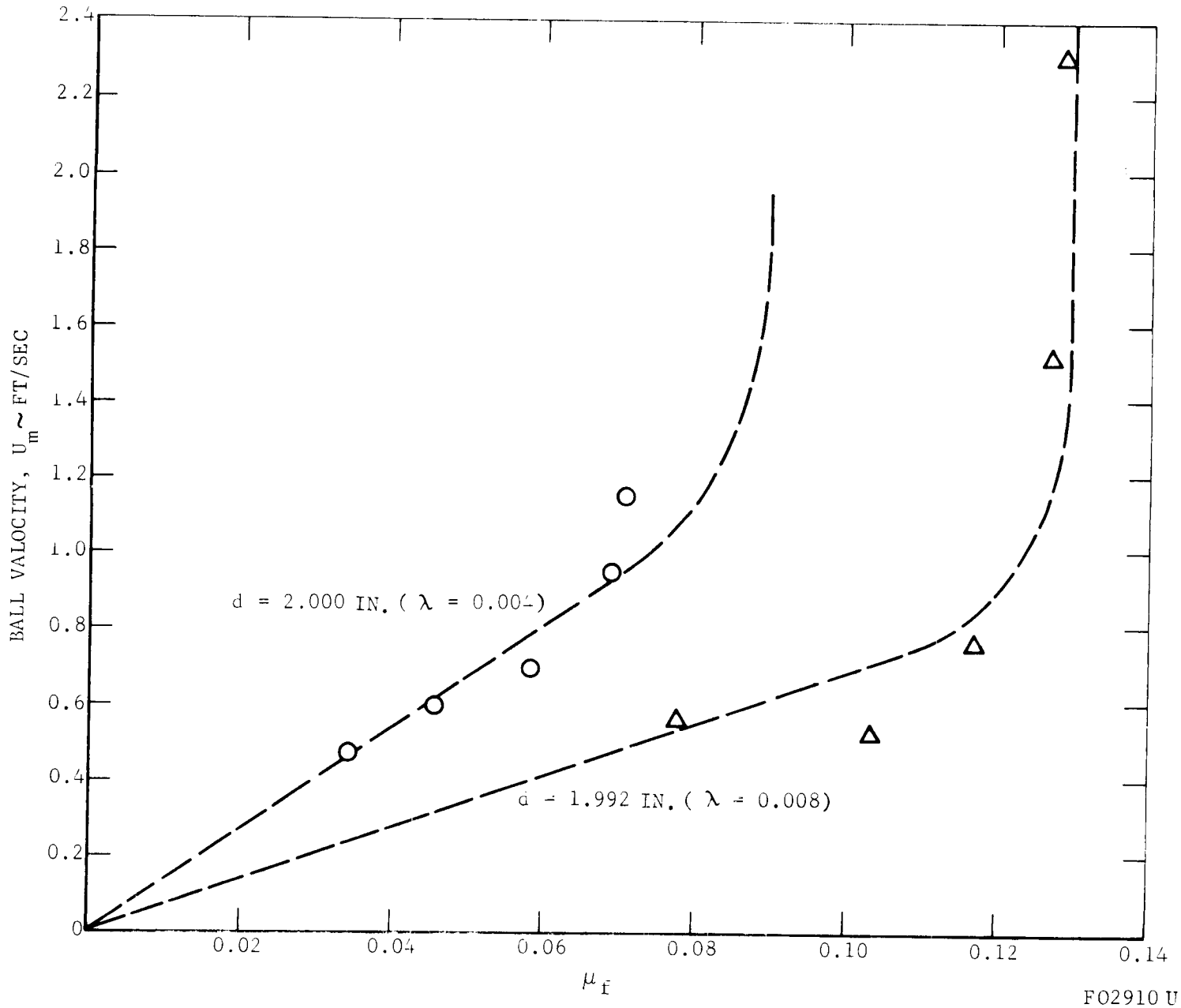

FIGURE 8-17. CENTRIFUGE AVERAGE SLIDING FRICTION COEFFICIENT

applied to the experimental results. The resulting C_D - R_d points are shown in Figures 8-8 and 8-9.

The final numerical data for both the low "g" and high "g" cases are presented in Table 8-1.

8.8 CONCLUSIONS

The results of this tudy have led to the following conclusions. In some instances, limitations exist and are also disclosed.

1. The experiments performed have indicated the feasibility of the inclined tube technique in accurately determining drag data for a rolling sphere when the accelerating force is such that $N < .8$.

2. The results indicate good agreement with the analytical formulations at the low values of λ (say, $\lambda \leq .01$).

3. For λ-values such that $\lambda \geq .01$ agreement is not as good, but the experimental and analytical results differ only by a factor of about three.

4. The experimental results were further substantiated by performing tests with two different sizes of balls ($d_2 \cong 2d_1$) for similar values of λ.

5. The high-"g" experiments ($0.5 \leq N \leq 10$) were completed in the centrifuge, and the results indicated that the centrifuge is not fully adequate as a tool for determining meaningful drag data.

6. Approximate corrections applied to the centrifuge data can be used to calculate ball drag values at "g" levels approaching $N = 8$.

7. Care must be taken to insure in a given damper configuration that the mean fluid velocity in the gap between the ball and the tube does not exceed the critical Mach number $M \cong .35$.

8. For Mach numbers approaching or exceeding $M \cong .35$, the flow in the gap approaches sonic conditions, and the drag values must be corrected to account for compressibility.
9. The experiments performed at $M > .35$ indicate that the ball motion becomes erratic rather than approaching an equilibrium speed. This implies that attendant shock formations may be reflected from the closed end of the tube. Such a phenomenon would mean that the ball drag would be a complicated function of ball position, past time history, and Mach number as well as Reynolds number; this would greatly complicate a passive damper design procedure.

NOMENCLATURE

N	numerical value of "g" forces acting on a body - a body of mass m experiences force F given by $F = Nmg$
g	acceleration due to gravity = 32.2 ft/sec^2
λ	gap parameter = t/d
t	tube inside diameter minus ball diameter
d	ball diameter
U	ball translational velocity with respect to the tube
U_m	ball maximum or "equilibrium" velocity
V	average velocity of the air flow through the gap, t
ω	angular velocity of the centrifuge arm
$\dot{\phi}$	angular velocity of the ball in the tube
μ_f	total friction coefficient - includes sliding as well as rolling friction
R_d	Reynolds number = $\rho Ud/\mu$
ρ	fluid density
μ	fluid viscosity
C_D	drag coefficient = $2D/\rho U^2 A$
D	sphere drag
A	sphere area = $\pi d^2/4$
M	Mach number - $M = V/a$
a	speed of sound
W	ball weight
w	Ball specific weight - $w = W/$ball volume

Note 1: The symbols listed above apply only to Section 8.

Note 2: Not all symbols used in the text are presented in this nomenclature. Those parameters which were momentarily introduced and defined to illustrate a specific concept (i.e., heating parameter, sliding effects, etc.) and which are not employed in the development of the flow model are not repeated in this nomenclature.

TABLE 1 EXPERIMENTAL RESULTS

Low "g" Studies - 2-inch spheres

Tube Specifications:

Material - 2024 T-3 aluminum

Length - 9 ft

Outside diameter - 2.250 inches

Inside diameter - 2.008 inches

Ball Specifications:

Material 440-C stainless steel

Diameter - nominally 2- inches - varies with λ

Sphericity - $\pm$ 0.0001 inches

Density - 0.277 lb/in^3

$$d = 2.000 \text{ inches}$$

$$R_d = (1.06 \times 10^3)\ (U_m)$$

$$C_D = (5.0 \times 10^{10})\ (N/R_d^{\ 2})$$

$\lambda = 0.0045$				$\lambda = 0.0035$			
N	U_m ~ft/sec	$R_d \times 10^{-2}$	$C_D \times 10^{-4}$	N	U_m ~ft/sec	$R_d \times 10^{-2}$	$C_D \times 10^{-4}$
.033	.076	.806	25.7	.033	.064	.678	36.3
.062	.132	1.40	15.8	.062	.113	1.20	21.5
.093	.189	2.00	11.6	.093	.164	1.74	15.2
.124	.241	2.55	9.55	.124	.212	2.25	12.25
.155	.289	3.06	8.30	.155	.258	2.73	10.4
.186	.328	3.48	7.70	.186	.293	3.11	9.60
.217	.379	4.02	7.60	.217	.340	3.60	8.35
.267	.441	4.67	6.15	.267	.403	4.28	7.30
.314	.392	5.21	5.80	.314	.467	4.95	6.40
.358	.540	5.72	5.45	.358	.497	5.27	6.45
.402	.588	6.23	5.17	.402	.541	5.73	6.12
.463	.657	6.97	4.77	.463	.606	6.42	5.60
.517	.712	7.55	4.54	.517	.645	6.84	5.50
.608	.785	8.32	4.46	.608	.727	7.70	5.13
.684	.862	9.13	4.11	.684	.800	8.48	4.76
.775	.929	9.85	3.99	.775	.871	9.23	4.55

$d = 1992$ inches

$R_d = (1.053 \times 10^3)\ (U_m)$

$C_D = (4.91 \times 10^{10})\ (N/R_d^2)$

$\lambda = 0.0085$

N	U_m ~ft/sec	$R_d \times 10^{-2}$	$C_D \times 10^{-3}$
.035	.402	4.23	9.57
.062	.593	6.25	7.78
.097	.788	8.30	6.91
.140	.990	10.43	6.28
.186	1.177	12.40	5.94
.248	1.395	14.7	5.63
.302	1.57	16.55	5.41
.353	1.72	18.11	5.26
.411	1.90	20.0	5.03
.551	2.25	23.7	4.81
.617	2.41	25.4	4.69
.678	2.58	27.2	4.50
.760	2.82	29.7	4.23

$\lambda = 0.0075$

N	U_m ~ft/sec	$R_d \times 10^{-2}$	$C_D \times 10^{-3}$
.035	.391	4.12	10.11
.062	.577	6.08	8.22
.097	.766	8.07	7.31
.140	.965	10.17	6.64
.186	1.148	12.10	6.23
.248	1.361	14.35	5.90
.302	1.53	16.12	5.70
.353	1.67	17.6	5.58
.411	1.86	19.6	5.25
.511	2.20	23.2	5.02
.617	2.36	24.9	4.88
.678	2.53	26.65	4.68
.760	2.70	28.45	4.60

$d = 1.978$

$R_d = (1.048 \times 10^3)\ (U_m)$

$C_D = (4.84 \times 10^{10})\ (N/R_d^2)$

$\lambda = 0.0155$

N	U_m ~ft/sec	$R_d \times 10^{-3}$	$C_D \times 10^{-3}$
.035	0.86	0.901	2.08
.062	1.21	1.268	1.86
.101	1.59	1.67	1.75
.132	1.86	1.95	1.68
.186	2.33	2.44	1.51
.240	2.70	2.83	1.45
.302	3.07	3.22	1.40
.357	3.34	3.50	1.41
.426	3.70	3.88	1.37

$d = 1.938$ inches

$R_d = (1.028 \times 10^3)\ (U_m)$

$C_D = (4.54 \times 10^{10})\ (N/R_d^2)$

$\lambda = 0.036$

N	U_m ~ft/sec	$R_d \times 10^{-3}$	$C_D \times 10^{-2}$
.031	2.05	2.11	3.16
.062	3.35	3.44	2.38
.093	4.25	4.37	2.21
.124	4.90	5.04	2.215
.155	5.55	5.71	2.16
.186	6.15	6.33	2.11
.225	6.70	6.89	2.155
.275	7.30	7.51	2.175
.334	8.25	8.48	2.11

$\lambda = 0.0155$

N	$U_m \sim$ ft/sec	$R_d x10^{-3}$	$C_D x10^{-3}$
.489	4.00	4.19	1.35
.555	4.27	4.47	1.34
.620	4.59	4.81	1.30
.683	4.78	5.01	1.31

$\lambda = 0.036$

N	$U_m \sim$ ft/sec	$R_d x10^{-3}$	$C_D x10^{-2}$
.411	9.30	9.57	2.04

Low "g" Studies - 1-inch spheres

Tube Specifications:
- Material - 6061 T-6 aluminum
- Length - 9 ft
- Outside diameter - 1.125 inches
- Inside diameter - 0.998 inches

Ball Specifications:
- Material - 440-C stainless steel
- Diameter - nominally 1-inch - varies with λ
- Sphericity - $\pm$ 0.0001 inches
- Density - 0.277 lb/in^3

d = 0.991 inches

$R_d = (5.26 \times 10^2)\ (U_m)$

$C_D = (6.10 \times 10^9)\ (N/R_d^2)$

$\lambda = 0.007$

N	$U_m \sim$ ft/sec	$R_d x10^{-2}$	$C_D x10^{-4}$
.074	.241	1.266	2.82
.093	.261	1.372	3.01
.124	.337	1.740	2.50
.139	.380	1.998	2.135
.152	.451	2.37	1.650
.186	.477	2.51	1.800
.217	.551	2.90	1.572
.236	.616	3.235	1.38
.256	.621	3.265	1.463
.333	.751	3.95	1.30

d = 0.987 inches

$R_d = (5.23 \times 10^2)\ (U_m)$

$C_D = (6.025 \times 10^9)\ (N/R_d^2)$

$\lambda = 0.011$

N	$U_m \sim$ ft/sec	$R_d x10^{-2}$	$C_D x10^{-3}$
.074	.484	2.53	6.96
.081	.495	2.59	7.27
.093	.548	2.87	6.80
.124	.685	3.58	5.82
.155	.814	4.26	5.15
.209	.991	5.18	4.70
.240	1.081	5.65	4.54
.272	1.228	6.42	3.98
.318	1.305	6.83	4.10
.395	1.495	7.82	3.89

$\lambda = 0.007$			
N	$U_m \sim$ ft/sec	$R_d x10^{-2}$	$C_D x10^{-4}$
.383	.869	4.57	1.12
.426	.888	4.67	1.19
.465	1.020	5.36	0.988
.512	1.02	5.36	1.088
.558	1.072	5.64	1.070
.675	1.213	6.38	1.012
.737	1.375	7.23	0.860

$\lambda = 0.011$			
N	$U_m \sim$ ft/sec	$R_d x10^{-2}$	$C_D x10^{-3}$
.427	1.643	8.59	3.48
.480	1.79	9.36	3.30
.527	1.750	9.15	3.80
.625	1.956	10.23	3.59
.667	2.05	10.72	3.49
.737	2.22	11.61	3.29

$$d = 0.980 \text{ inches}$$
$$R_d = (5.20 \times 10^2)\ (U_m)$$
$$C_D = (5.90 \times 10^9)\ (N/R_d^{\ 2})$$

$\lambda = 0.018$			
N	$U_m \sim$ ft/sec	$R_d x10^{-3}$	$C_D x10^{-3}$
.074	.961	.500	1.746
.093	1.074	.559	1.758
.124	1.295	.673	1.616
.1395	1.432	.745	1.480
.186	1.702	.885	1.402
.209	1.813	.943	1.386
.232	1.992	1.036	1.274
.264	2.04	1.060	1.386
.310	2.27	1.180	1.310
.341	2.40	1.247	1.293
.379	2.635	1.370	1.192
.426	2.81	1.460	1.180
.512	3.14	1.632	1.132
.656	3.71	1.929	1.038

High "g" Studies - 2-inch spheres

Tube Specifications: Material - 2024 T-3 aluminum
Length - 32 inches
Outside diameter - 2.250 inches
Inside diameter - 2.008 inches

Ball Specifications: Material - 440-C stainless steel
Diameter - nominally 2-inches - varies with λ
Sphericity - $\pm$ 0.0001 inches
Density - 0.277 lb/in^3

Note: For these tests the quantity N refers to the net accelerating force after the friction and gravity losses have been subtracted.

$$d = 2.000 \text{ inches}$$
$$R_d = (1.06 \times 10^3)\ (U_m)$$
$$C_D = (5.0 \times 10^{10})\ (N/R_d^{\ 2})$$

$\lambda = 0.004$				$\lambda = 0.004$			
N	$U_m \sim$ ft/sec	$R_d x10^{-3}$	$C_D x10^{-4}$	N	$U_m \sim$ ft/sec	$R_d x10^{-3}$	$C_D x10^{-4}$
.311	.471	.500	6.22	.333	.479	.508	6.44
.447	.590	.626	5.70	.476	.592	.628	6.02
.582	.689	.781	4.77	.622	.681	.722	6.35
.828	.942	.990	4.16	.865	.927	.983	4.47
1.122	1.158	1.228	3.725	1.267	1.128	1.196	4.43
1.498	1.378	1.461	3.51	1.549	1.344	1.425	3.81
1.91	1.618	1.716	3.245	2.270	1.558	1.653	4.15
2.405	1.852	1.962	3.255	2.487	1.812	1.922	3.36
2.963	2.11	2.24	2.955	3.040	2.06	2.185	3.19
2.536	2.35	2.49	2.85	3.633	2.285	2.425	3.09
4.262	2.53	2.68	2.965	4.260	2.53	2.68	2.965
5.825	2.83	3.00	2.68	4.942	2.78	2.95	2.84
5.732	2.98	3.16	2.87	5.844	2.88	3.05	3.14
6.644	3.21	3.40	2.875	6.794	3.035	3.22	3.28

$$d = 1.992 \text{ inches}$$
$$R_d = (1.053 \times 10^3)\ (U_m)$$
$$C_D = (4.91 \times 10^{10})\ (N/R_d^{\ 2})$$

$\lambda = 0.008$				$\lambda = 0.008$			
N	$U_m \sim$ ft/sec	$R_d x10^{-3}$	$C_D x10^{-3}$	N	U_m = ft/sec	$R_d x10^{-3}$	$C_D x10^{-3}$
.263	1.509	1.589	5.11	.307	1.168	1.25	9.64
.564	2.305	2.43	4.69	.72	1.909	2.01	8.77
.878	2.91	3.06	4.59	.919	2.52	2.655	6.40
1.25	3.46	3.64	4.62	1.30	3.13	3.30	5.96
1.635	4.05	4.27	4.41	1.69	3.69	3.885	5.50
2.063	4.61	4.86	4.29	2.121	4.37	4.60	4.92
2.536	5.03	5.30	4.43	2.583	4.61	4.86	5.37
2.997	5.36	5.65	4.61	3.065	5.19	5.47	5.03
3.51	5.93	6.25	4.41	3.597	5.53	5.83	5.18
4.052	6.15	6.48	4.73	4.154	6.15	6.48	4.96
4.624	6.64	6.99	4.65	4.744	6.64	7.00	4.76
5.234	6.92	7.29	4.83	5.364	6.92	7.28	4.97